Imperial College London
Department of Life Sciences

Characterisation of novel motility proteins in flagellar motors using cryo-electron microscopy

Nanki Kaur Singh

Submitted in part fulfilment for the degree of Doctor of Philosophy, July 2024

Copyright declaration

The copyright of this thesis rests with the author. Unless otherwise indicated, its contents are licensed under a Creative Commons Attribution-Non Commercial 4.0 International Licence (CC BY-NC).

Under this licence, you may copy and redistribute the material in any medium or format. You may also create and distribute modified versions of the work. This is on the condition that: you credit the author and do not use it, or any derivative works, for a commercial purpose.

When reusing or sharing this work, ensure you make the licence terms clear to others by naming the licence and linking to the licence text. Where a work has been adapted, you should indicate that the work has been changed and describe those changes.

Please seek permission from the copyright holder for uses of this work that are not included in this licence or permitted under UK Copyright Law.

Declaration of originality

I declare that all work presented in this thesis is my own work unless otherwise acknowledged. This work presented was done under the supervision of Dr. Morgan Beeby. Any work that has been done in collaboration with other labs and with colleagues has been appropriately cited and mentioned in this thesis. All published work is appropriately referenced and reprinted with permission.

Dedicated to my family, forever by my side.

Abstract

Little is known about the evolution of macromolecular complexes. A prime example of a macromolecular machine is the bacterial flagellar motor. This rotatory molecular motor is embedded in the cell membrane of many bacteria and provides motility. Bacterial flagellar motors have diversified over the course of evolution and vary in structure across different species of bacterium. The core flagellar motor structure remains the same but additional structures have been incorporated into motors which are specific to each species. These structures benefit the bacterium because they act as scaffolds to keep the motor in place or form wider flagellar motors which make more powerful motors that generate high torque and modulate swimming speeds. A flagellar motor that provides high torque benefits bacteria that reside in high viscous environments for example *Campylobacter jejuni*. The flagellar motor can also 'sense' its surrounding environment and signal the bacterium to change its cell morphology as observed in *C. crescentus*. To power the flagellar motor, transmembrane proteins embedded in the inner membrane rotate against the rotor which generates torque. To understand the evolution of the flagellar motor I first studied these transmembrane proteins using cryo-electron microscopy. I showed significant improvements in the *in situ* structure of the ring of transmembrane proteins that surround the rotor. I further showed that these transmembrane proteins behave differently in *C. jejuni*'s high-torque motor compared to low-torque bacteria. To understand the role of the flagellar motor in morphological changes I study two novel proteins known to contribute to this process in *C. crescentus* using cryo-electron tomography. By studying novel proteins in the flagellar motor of two distinctly diverse species of bacteria *C. jejuni* and *C. crescentus* I showed how macromolecular structures have evolved in different species to aid biological function.

Acknowledgements

Firstly, a massive thank you to Morgan. I am grateful for your constant guidance and mentorship throughout my PhD. Since the day I started during the middle of a pandemic to now, you have helped me navigate my thoughts, think like a scientist and see the bigger picture. I have learnt through you the meaning of being a good scientist and the art of telling a story through my science. I am incredibly grateful to have had your supervision and enthusiasm for science to guide me through this journey.

To the Beeby lab members, Trishant, Eli and Tina, thank you for taking me on as part of the team and making me feel so welcome. I have learnt so much from all of you whether it was genetics, microscopy or weird Linux code. I am grateful to have been part of a fun and scientifically stimulating lab. To my 5th floor friends thank you for making the floor so fun. From hosting all the socials to the laughs and interesting conversations, you truly made my time at Imperial a memorable experience, one I will truly miss. To Yassin, Ambre and Tanvi, thank you, I can't think of a better bunch of people to go through my PhD with.

Thank you to Bernadette Byrne and Tiago Costa, my progress review panel for all the feedback, guidance and wisdom during my PhD. Thank you to Paul Simpson for teaching me all about microscopes and for your help with troubleshooting and data collection whilst making the EM facility a fun place to learn.

Thank you to my closest and dearest friends for being my support throughout the years through all my ups and downs. To Soundarya, for always being there with a big hug and going through life together. Rama, Lia, Francesca and Amrit, I will never forget the long phone calls, coffee catch-ups and our trips around London. Your presence made London feel home. To Mar, thank you for being my amazing long-distance bestie, for all our phone calls and being by my side. To my undergraduate group, thank you for reminding me that I have the best people around me for which I always feel grateful.

To my family, who have supported me through every step of this journey. My mum and dad who always put their kids first and encouraged me to go get my PhD. Thank you for believing in me and for reminding me that whatever the obstacle was, that things would be okay. Thank you for all the love, food visits to London and for always making me smile. To my grandma (nani) who has always given us so much love and her million-dollar smile. To my siblings, Angad and Bani, thank you for always having my back and being the best brother and sister I could ask for. I am lucky to have a group of incredible people by my side.

Contents

Chapter 1 Introduction 16
1.1 The evolution of macromolecular machines 17
1.2 The flagellar motor is an ideal model system to study the evolution of molecular machines. 17
1.3 We can study molecular machines using cryo-electron microscopy 18
1.4 What is cryo-electron microscopy and why is it important? 18
1.4.1 Sample preparation in Cryo-Electron Microscopy 19
1.4.2 How are samples imaged using cryo-electron microscopy? 21
1.4.3 How are scattered electrons converted into images? 25
1.4.4 Data processing in cryo-electron microscopy depends on the 'central slice theorem'. 27
1.5 Types of cryo-electron microscopy 28
1.5.1 Single Particle Analysis 28
1.5.2 Cryo-Electron Tomography 28
1.6 Cryo-electron microscopy is a tool for studying the evolution and mechanism of rotation in motors 33
1.7 The mechanism of assembly for core motor structures is conserved in flagellated bacteria 34
1.8 The core motor structure is built to generate torque 35
1.8.1 Stator units are pentameric proteins that interact with the cytoplasmic ring to drive rotation 36
1.8.2 Stator units in certain bacterial motors incorporate into the motor as load on the motor increases 39
1.8.3 Studying stator dynamics using biophysical assays 39
1.8.4 Stator dynamics in the motor are not conserved between species 40
1.9 High-torque motors have incorporated additional structures to support torque generation 42
1.10 *C. jejuni* as a model system for studying multiple components in the flagellar motor 43
1.10.1 *C. jejuni* has novel proteins that scaffold stator complexes 46
1.11 Summary 47
Chapter 2 Single Particle Analysis of stator complexes *in situ* 48
2.1 Chapter Summary 48
2.2 Introduction 49
2.2.1 The flagellar motor is a macromolecular complex important for motility with a conserved core architecture 49

2.2.2 Protein structures provide an understanding of the mechanism of torque generation....50
2.2.3 Cryo-electron tomography as a tool to study macromolecular complexes *in situ* (limitations)....51
2.2.4 Using minicells in combination with Single Particle Analysis to provide a higher resolution flagellar motor structure....52
2.2.5 *C. jejuni* minicells to study stator complexes *in situ*....52
2.3 Aims....53
2.4 Results....54
2.4.1 *C. jejuni* minicells for Single Particle Analysis....54
2.5 Discussion....74
2.6 Methods....79
2.6.1 Bacterial strains and growth conditions....79
2.6.2 Strain construction in *C. jejuni*....79
2.6.3 Cryo-EM sample preparation and freezing (by Eli Cohen)....80
2.6.4 CryoEM data collection....80
2.6.5 Cryo-EM processing....80
Chapter 3 Are stators in *C. jejuni* static or dynamic?....83
3.1 Chapter Summary....83
3.2 Introduction....85
3.2.1 Differences between 'high torque motor' and 'low torque motors'....85
3.2.2 Cryo-electron tomography can be used for studying stator dynamics....87
3.2.3 Biophysical experiments provide functional data on stator dynamics....87
3.2.4 The structure of stator complexes are conserved across species....88
3.3 Aims....88
3.4 Results....89
3.4.1 Are stators in *Campylobacter jejuni* present when there is no load on the motor?....89
3.4.2 Subtomogram average of *C. jejuni* motor in CCCP confirms stators are static 89
3.4.3 Extra densities around stators are accessory proteins are required for full motor function....91
3.4.4 Stators disappear when FlgX is deleted from the motors....93
3.4.5 Resurrection experiments in *C. jejuni* suggests stators are permanently attached to the motor....95
3.4.6 Functional data to show that stators are dynamic when no FlgX is present....95
3.4.7 Locating FlgX using AlphaFold2 CollabFold (v1.5.5) and Cryo-tomography….....96

3.4.8 Stators and putative FlgX missing densities in FlgX-tagged C. jejuni subtomogram average 100
3.5 Discussion 102
3.5.1 Summary of results 102
3.5.2 Stators are statically placed around the motor 102
3.5.3 Biophysical assays support statically placed stators 103
3.5.4 Additional proteins keep stators in place in *C. jejuni* 103
3.5.5 Stator motility without FlgX is restored by a mutation in MotA 104
3.5.6 Locating FlgX *in situ* using a tag did not confirm its placement in the flagellar motor 104
3.6 Methods 106
3.6.1 Cell growth 106
3.6.2 Swimming speed videos 106
3.6.3 Motility Plates 107
3.6.4 Preparing *C. jejuni* for freezing grids 107
3.6.5 Cryo -Electron Tomography Data Acquisition 107
3.6.6 Tomogram Reconstruction and Processing 107
3.6.7 AlphaFold2 CollabFold (v1.5.5) Models 108
Chapter 4 Additional proteins are incorporated into the motor to control rotor speed 109
4.1 Chapter summary 109
4.2 Introduction 110
4.2.1 *C. jejuni'* s flagellar motor modulates viscosity dependent motor output 110
4.2.2 *C. jejuni*'s flagellar motor structure is built to favour a high viscous environment 110
4.2.3 A subset of motility proteins in the flagellar motor control velocity of *C. jejuni* 111
4.2.4 Aims 113
4.3 Results 115
4.3.1 Initial Screening of Mutants 115
4.3.2 VidA deletion reduces the size of the density between the MS- and N-terminus of FliG 115
4.3.3 Deleting VidA and VidB does not remove the density between FlhA and FliG 117
4.3.4 CJJ81176_1732 deletion removes the FlgV density in *C. jejuni* 118
4.3.5 The putative FlgV ring is 20-fold symmetric in *C. jejuni* 121
4.3.6 Attempting to obtain a 20-fold symmetric ring in the single particle flagellar motor structure in *C. jejuni* 121
4.4 Discussion 126

4.4.1 Summary of previous research and results 126
4.4.2 VidA interacts with FlgV to control velocity 126
4.4.3 CJJ81176_1732 is important for the stability of FlgV and VidA 127
4.4.4 FlgV is important for the stability of CJJ81176_1732 and VidA 127
4.4.5 The inner ring between the MS-ring and FliG N-terminus is 20-fold symmetric 128
4.4.6 20-fold symmetric structure could not be imposed on the single particle structure of the flagellar motor in *C. jejuni* minicells 128
4.4.7 VidB's location is unknown 129
4.4.8 Conclusion 130
4.5 Methods 131
4.5.1 Cell Growth and Freezing Conditions 131
4.5.2 Cryo -Electron Tomography Data Acquisition 131
4.5.3 Tomogram Reconstruction and Processing 132
4.5.4 Single Particle Analysis and subtraction of the FlgV ring 132
Chapter 5 Locating flagellar signalling suppressor (fss) proteins required for holdfast in *C. crescentus* 134
5.1 Chapter Summary 134
5.2 Introduction 135
5.2.1 Bacteria have advanced developmental cycles for colonization of solid surfaces…… 135
5.2.2 Holdfast promotes adhesion by a yet unknown mechanism. 135
5.2.3 FssA and FssB contribute to late stage flagellar disassembly 136
5.2.4 Subtomogram averages of *C. crescentus* reveal yet unknown densities 137
5.2.5 Aims 137
5.3 Results 138
5.3.1 NA1000 cells versus CB15 cells for cryo-electron tomography 138
5.3.2 Synchronization separates pre-divisional cells from swarmer cells 139
5.3.3 Subtomogram averaging of mutants reveals flagellar motor without the cogwheel 142
5.4 Discussion 144
5.5 Methods 146
5.5.1 Cell Growth and Synchronization process 146
5.5.2 Freezing cells for cryo-electron tomography 146
5.5.3 Cryo -Electron Tomography Data Acquisition 147
5.5.4 Tomogram Reconstruction and Processing 147
Chapter 6 Conclusions 148
6.1 Summary 148

6.2 Present conclusions and future work 149
6.2.1 A higher resolution flagellar motor structure provides insight into molecular evolution 149
6.2.2 A step forward in understanding stator dynamics in *C. jejuni* 149
6.2.3 STA to locate novel proteins 150
6.2.4 Limitations 151
7 Bibliography 153

List of Figures

Figure 1.1 A schematic diagram of the cryo-electron microscopy workflow (both single particle analysis and tomography taken from Umrekar et al., 2021). 20
Figure 1.2 A schematic diagram of the lenses in a cryo-electron microscope. 23
Figure 1.3 Spherical aberration and the contrast transfer function. 27
Figure 1.4 A schematic diagram showing the process of collecting a tilt series. a) the sample rotating when collecting a tilt series; b) A collection of tilts forming a tilt series; c) A back projection of the tilt series to form a series of images d) A reconstruction of 2D tilt images to form a 3D tomogram. 30
Figure 1.5 Subtomogram averages of motors from different bacteria show diverse architectures of bacterial flagellar motors. 33
Figure 1.6 The bacterial flagellar motor is a multi-megadalton self-assembling rotatory motor. 36
Figure 1.7 MotA interacts with FliG of the C-ring to drive rotation. 38
Figure 1.8 Biophysical methods to measure torque. 40
Figure 1.9 A comparison of a subtomogram average of *S. enterica* versus *C. jejuni* 41
Figure 1.10 High torque flagellar motors present wider C-ring. 43
Figure 1.11 A comparison between a subtomogram averages of *S. enterica* and *C. jejuni* highlighting differences in the architecture of their flagellar motor. 45
Figure 1.12 A schematic diagram highlighting four novel proteins in *C. jejuni* which are yet to be characterised. 47
Figure 2.1 Stator units diffuse and interact with the rotor, specifically the C-ring to rotate the flagellar motor. 50
Figure 2.2 Comparison of *C. jejuni* wild type cell versus *C. jejuni ΔflhG ΔflaAB* minicells. . 55
Figure 2.3 Single Particle Analysis work flow processing the minicell dataset results in higher resolution flagellar motor. 57
Figure 2.4 Signal subtraction and focused refinement using a lathe mask around the stator and C-ring improves resolution of pentameric stator units. 59
Figure 2.5 Localised reconstruction hints differences in conformational states of a stator unit. 60

Figure 2.6 Changes in classification workflow did not provide a higher resolution stator unit structure or different conformational states of stator units provided some indication of C-ring spokes. 62
Figure 2.7 Homogeneous refinement of subtracted stator complexes reveal improved visibility of pentameric stators. 65
Figure 2.8 Masked alignment in CryoSPARC does not improve alignment. 66
Figure 2.9 Masking out singular/range of stator units reduces alignment at C1 symmetry. 68
Figure 2.10 Mask encompassing part C-ring and one stator unit did not reveal C-ring spokes against a stator unit. 69
Figure 2.11 Homogeneous refinement and signal subtraction with a tighter mask reveals unknown density but also provides some artefactual data. 71
Figure 2.12 Overview of the overall processing pipeline. Stator complexes were processed in RELION, CryoSPARC and Scipion in attempt to find different conformational states of stator complexes. 73
Figure 3.1 Differences in stator dynamics in *C. jejuni* versus *S. enterica*. 86
Figure 3.2 Subtomogram averages of *C. jejuni* cells with the addition of CCCP confirm stator units are static in *C. jejuni* 90
Figure 3.3 Single Particle Structure of the *C. jejuni* flagellar motor shows pentameric stators in situ to a resolution where we can model individual stator complexes. 92
Figure 3.4 MotB density can be observed in wild type but not in *C. jejuni ΔflgX motA*^{H138Y} which is motile. 94
Figure 3.5 Linear and semi-log x plots of average angular speed vs. time for *C. jejuni* and *E. coli* showing the difference in the rate of resurrection for each bacterium (Dr. William H. Hoffmann, Postdoctoral Researcher, Pedaci Lab, CNRS - Centre de Biologie Structurale) 95
Figure 3.6 Resurrection experiments on *C. jejuni ΔflgX motA*^{H138Y} exhibit faster incorporation of stator units compared to *E. coli* but slower incorporation speeds compared to wild type *C. jejuni.* 96
Figure 3.7 The designed tag included FlgX in red with its extended alpha helix at the C-terminal fused to Lysozyme in yellow. 97
Figure 3.8 Different tag designs of FlgX fused to lysozyme. FlgX density: green is FlgX, blue is lysozyme, light blue is FlgX without the tag. 98
Figure 3.9 *C. jejuni* mutants with the designed tags were grown on motility agar to measure swimming abilities. 99

Figure 3.10 Subtomogram average of the tagged FlgX mutant lacked the presence of stators but the mutant is motile which suggests dynamic stator units. 101
Figure 4.1 Subtomogram averages of *H. pylori*. 112
Figure 4.2 Shows the putative location of proteins FlgV (CJJ81176_0100), VidA (CJJ81176_0996), VidB (CJJ81176_1107) and CJJ81176_1732 and their potential interactions in the motor to control velocity. 114
Figure 4.3 *C. jejuni* cells were screened on the T12 microscope (Thermofisher Scientific™) before data collection.. 115
Figure 4.4 Subtomogram average of *C. jejuni ΔvidA* reveals a smaller density between the MS-ring and C-ring compared to *C. jejuni* wild type. 116
Figure 4.5 Subtomogram average of *C. jejuni ΔvidA* reveals unknown density interacting with the C-ring. 117
Figure 4.6 Subtomogram average of *C. jejuni ΔvidA ΔvidB* reveals the same missing density as observed in *C. jejuni ΔvidA* but the hypothesized VidB density remains. 118
Figure 4.7 Subtomogram average of *C. jejuni ΔflgV* reveals part-ring formation between the MS-ring and C-ring and a density interacting with the C-ring. 120
Figure 4.8 Subtomogram average of wild type *C. jejuni* reveals 20-fold symmetric ring between the MS-ring and C-ring. 121
Figure 4.9 Single Particle analysis of minicells shows the density between MS-ring and C-ring encompasses 4 subunits. 123
Figure 4.10 DeepTMHMM transmembrane topology plots of a) FlgV and b) CJJ81176_1732. 125
Figure 4.11 Region of sequences from *C. jejuni* and *H. pylori* from an MSA analysis highlighting residues in FliF which are hypothesized to interact with FlgV. 128
Figure 5.1 Cryo-electron microscopy images comparing CB15 cells with NA1000 cells. 138
Figure 5.2 Negative stain images to check for filaments in *C. crescentus* NA1000 *ΔfssA* and *ΔfssB* cells. 139
Figure 5.3 Synchronization separates swarmer cells from stalked cells but residual Percoll® remains in the samples. 141
Figure 5.4 Tomograms of *C. crescentus ΔfssA* (a) and *ΔfssB* (b) were collected on the Glacios 200 keV cryo-transmission electron microscope. 142
Figure 5.5 Subtomogram averages of *ΔfssA* and *ΔfssB* lack the cogwheel structure. 143

List of Tables

Table 2.1 List of strains used in Chapter 2 79
Table 2.2 Data collection statistics of minicell SPA dataset 80
Table 3.1 Diameter of growth on 0.4% w/v agarose gel (motility plate). 99
Table 3.2 Strains used for this project 106

Abbreviations

2D	2-dimensional
3D	3-dimensional
BSA	Bovine serum albumin
CCCP	Carbonyl cyanide m-chlorophenyl hydrazone
Cryo-EM	Cryo-electron microscopy
CTF	Contrast transfer function
DDD	Direct detection devices
DNA	Deoxyribonucleic acid
DQE	Detective Quantum Efficiency
FEG	Field emission gun
FSC	Fourier shell correlation
GFP	Green fluorescent protein
IM	Inner membrane
kDa	Kilo Daltons
Km	Kanamycin
keV	Kiloelectron Volts
LaB6	Lanthanum hexaboride
MAP	Monolithic active pixel sensor
MH	Mueller Hinton
MTF	Modulation Transfer Function
Nm	Nanometres
NMR	Nuclear magnetic resonance
OM	Outer membrane
PAE	Predicted align error
PCR	Polymerase chain reaction
PG	Peptidoglycan
PDB	Protein Data Bank
PMF	Proton motive force
PYE	Peptone yeast extractRNA Ribonucleic acid
SIRT	Simultaneous iterative reconstruction technique
Sm	Streptomycin
SOE	Splicing-by-overhang-extension
SPA	Single particle analysis
STA	Subtomogram averaging
T3SS	Type III secretion system
TEM	Transmission Electron Microscope
TMH	Transmembrane helices
TPR	Tetratricopeptide repeat
WBP	Weighted back projection

Chapter 1

Introduction

In this thesis I study the evolution of flagellar motors mainly using a technique called cryo-electron microscopy. Below I present a brief outline of the work presented in each chapter.

In Chapter 1, I describe the diversity of flagellar motors and why the flagellar motor is a good case study for studying macromolecular complexes. I start my thesis by providing a summary of cryo-electron microscopy and its function in studying large macromolecular structures such as the flagellar motor. I then provide a more detailed introduction of the flagellar motor and its use as a case study to study molecular diversity in macromolecular complexes.

In Chapter 2, I present the first *in situ* structure of transmembrane proteins called stator complexes that power the flagellar motor. I also show how we used 'minicells' as a tool to solve a higher resolution SPA structure of the *C. jejuni* flagellar motor.

In Chapter 3, I investigate a novel protein and find that it is required to keep stator complexes in place so it can swim in a high viscous environment.

In Chapter 4, I show that *C. jejuni* can control its swimming speed. The speed C. jejuni swims at depends on its surrounding viscosity therefore C. jejuni has evolved specific proteins in its flagellar motor for this purpose. These proteins are required for *C. jejuni* to increase speeds at low viscosity and reduce speeds at high viscosity.

In Chapter 5, I attempt to locate proteins in the flagellar motor of *Caulobacter crescentus* required to start changes in cell morphology during cell adhesion to a solid surface.

In Chapter 6, I provide overall conclusions of the presented work and outline future studies that build upon the results of the thesis to further understand the flagellar motor. I focus on concluding my findings on *C. jejuni* and *C. crescentus*.

1.1 The evolution of macromolecular machines

How molecular machines have evolved has been a long-standing question in evolutionary biology. A common observation when studying the evolution of macromolecular complexes is its ability to re-purpose and re-use proteins as well as incorporate novel proteins (Beeby, 2019; Denise et al., 2020). The existence of macromolecular complexes poses questions like how do molecular machines incorporate these novel proteins? How do macromolecular machines gain functionality? How do novel proteins interact with existing complexes to benefit the macromolecular machine? How do proteins develop new binding interfaces? Most case studies involve smaller structures where it is difficult to study these questions (Finnigan et al., 2012; Hochberg et al., 2020). The best-known case study of a large macromolecular machine is the bacterial flagellar motor. The flagellar motor has provided examples of re-purposed proteins that have been incorporated into the motor and examples of non-homologous additional structures that have incorporated into conserved core flagellar motor (Beeby et al., 2016; Chaban et al., 2018; Chang et al., 2021; Moon et al., 2016).

1.2 The flagellar motor is an ideal model system to study the evolution of molecular machines.

A prime example of a complex molecular machine is the flagellar motor which is important for motility in many bacteria (Beeby et al., 2016; Chaban et al., 2018; Chen et al., 2011). Its core structure remains conserved throughout species, but additional structures have incorporated which are specific to each species. The conserved core of the motor provides the bacterium with its ability to swim. The diversity in structures between each bacterium affect swimming speeds, make larger motors and overall affect bacterial motor function. These structures have gained, lost and re-purposed proteins to help with their specific function (Beeby, 2019; Denise et al., 2020; Finnigan et al., 2012). These motors, therefore, serve as contemporary examples of evolution. The flagellar motor is an important case study for macromolecular evolution. By studying how some of these proteins have incorporated into the flagellar motor we gain a snapshot into how macromolecular machines have evolved. In my PhD, I use cryo-electron microscopy as the main technique to study the molecular architecture of the flagellar motor. Therefore, I will start by introducing cryo-electron microscopy and I will then return to discussing the flagellar motor.

1.3 We can study molecular machines using cryo-electron microscopy

Motors amongst varied species look different but this diversity is poorly understood. The differences amongst motors might be related to their niche environments but further studies are yet to be done to confirm this. Studies have already sampled a library of motors, these range from simple motors that only consist of the core motor structures to more complex larger motors which have incorporated additional proteins (Chen et al., 2011). For example, *Escherichia coli* and *Salmonella enterica* have small simple motors and have peritrichous flagella; *Caulobacter crescentus* which is found in freshwater environments has a slightly more complex motor with some additional structures and has only one flagellum on its cell body; whereas *Campylobacter jejuni* is a polarly flagellated bacterium found in the gut that has a complex motor with large scaffold like structures that hold the motor in place (Gao et al., 2014; Wallis, 1994).

By studying additional structures that benefit the flagellar motor we can better understand how rotation has evolved in the flagellar motor. To understand how motors have evolved we can generate mutants (deletion mutants, chimeric mutants) and then use cryo-electron tomography to image the mutant *in situ* (Beeby et al., 2016; Nishino et al., 2015). Cryo-electron tomography involves imaging a specimen over incremental tilts which is then reconstructed, a tilt series is collected and averaged to form a 3D image of the specimen called a tomogram (Umrekar et al., 2021). Tomograms can be averaged by a process called subtomogram averaging (STA). This provides us the location of the protein and its effect on bacterial motility and some insight on how/why the motor evolved to incorporate this protein. To understand how we can use this method to study motors I first discuss the basics of cryo-electron microscopy.

1.4 What is cryo-electron microscopy and why is it important?

Cryo-electron microscopy is a technique which uses electrons focused by magnetic lenses to image biological samples (cell) or purified samples (for example RNA, DNA, proteins) (Cheng et al., 2015). These two-dimensional images can then be used to produce a high-resolution three-dimensional structure of the protein or cell. Structures solved by cryo-electron microscopy are used for understanding macromolecular complexes *in situ* (e.g., embedded in membrane or organelle) and protein complexes to atomic resolution. Cryo-EM is a less invasive technique compared to other imaging techniques such as those that require staining. Using cryo-EM to solve structures is beneficial

when solving structures of proteins that cannot be crystalized, are heterogeneous, are membrane proteins or are large macromolecular complexes that cannot be solved by NMR or crystallography.

1.4.1 Sample preparation in Cryo-Electron Microscopy

Cryo-electron microscopy is the optimal method for studying macromolecular machines because electrons scatter readily through thin samples unlike photons in light microscopy. The smaller wavelength of the radiation provides a higher resolution image in comparison to other microscopy methods such as light microscopy. To study a sample in its native state we need to first preserve the sample to limit damage from electrons. This is done by embedding the sample in a thin layer of ice to protect it. To prepare the sample for cryo-electron microscopy, a few microlitres of the specimen/or purified protein is added to a carbon/copper grid (other variations exist) (Dobro et al., 2010; Dubochet and Mcdowall, 1981). The grid is then embedded in a thin layer of vitrified ice. The sample is plunge frozen quickly (a few milliseconds) into liquid ethane/propane at cryogenic temperatures to keep the ice vitrified or 'glass like' before it turns into crystalline ice which would expand and damage the sample (Figure 1.1, sample preparation). Most of the sample is wicked away by blotting paper to provide a thin layer of sample in ice for imaging. The sample should be thin, certainly under 500 nm to prevent too many electrons from inelastic or multiple scattering which produces noise. The sample can then be inserted into the microscope which keeps the sample in high vacuum (Figure 1.1, image processing). The thin layer of ice limits damage from the electrons in the beam and the high vacuum prevents scattering of electrons by air molecules therefore providing a consistent electron beam. In cryo-electron microscopy no stains are required, instead contrast is achieved by changing optics using the lenses. Over time cryo-electron microscopy has become more high-throughput. The development of machines such as the Vitrobot (ThermoFisher Scientific) has allowed for us to control temperature, blotting conditions and humidity in the freezing chamber. In addition to this, advances in microscope software have allowed for faster automated data collection with minimum manual user interference.

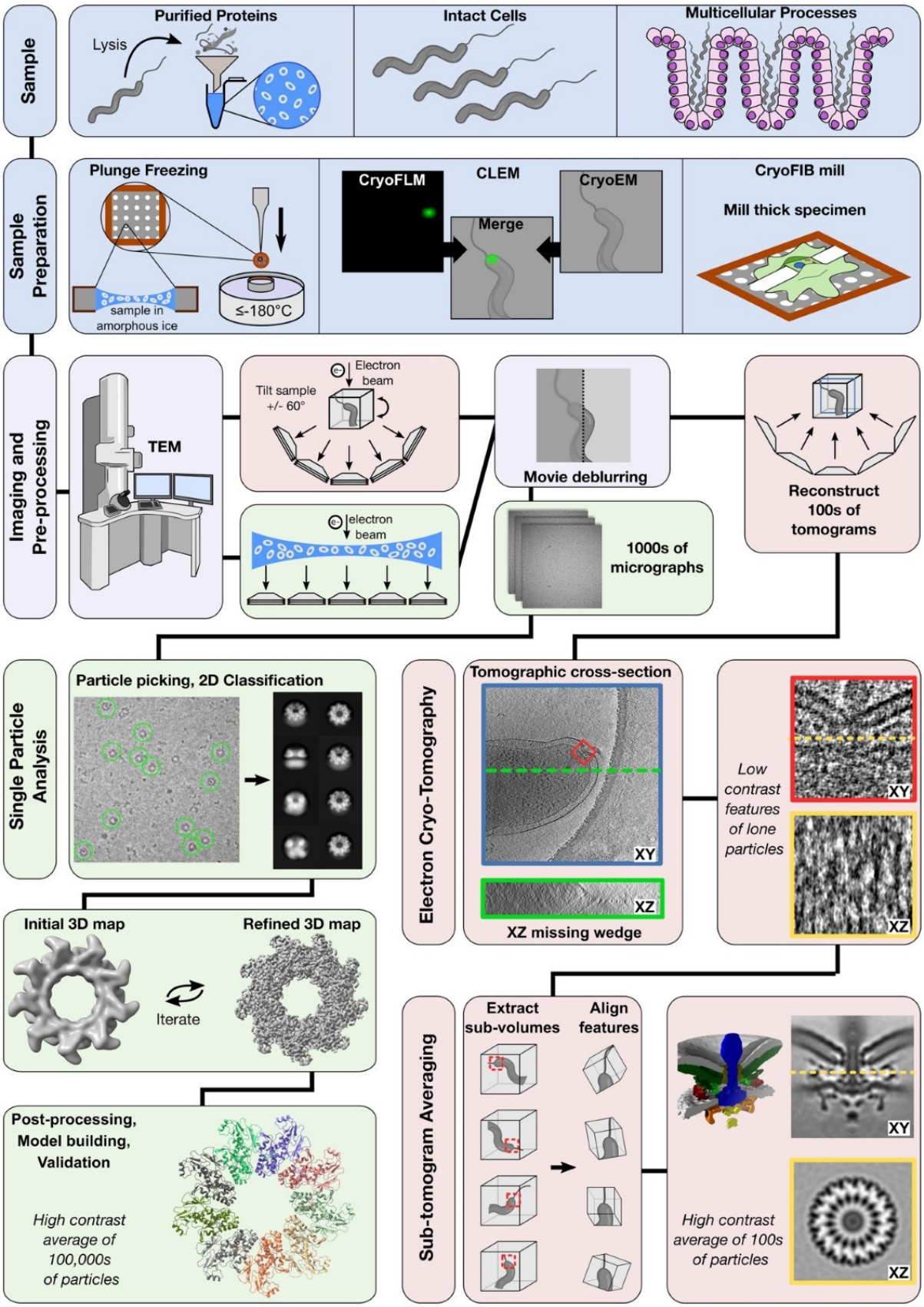


Figure 1.1 A schematic diagram of the cryo-electron microscopy workflow (both single particle analysis and tomography taken from Umrekar et al., 2021).

1.4.2 How are samples imaged using cryo-electron microscopy?

To image a sample using cryo-electron microscopy an electron beam is focused on the specimen (Carter and Williams, 2016; Thompson et al., 2016; Umrekar et al., 2021). Electromagnetic lenses are used to focus the electrons before and after the electrons hit the specimen. The electrons are accelerated down the microscope column which is under a vacuum to prevent any unwanted scattering of electrons by gaseous particles. Finally, the camera is used to detect scattered electrons and form an image of the specimen.

1.4.2.1 An electron gun is the electron source to produce a beam

Electrons are produced by a device referred to as an electron gun. There are different types of electron guns, which produce electron beams of differing coherences. The Tungsten filament is the simplest form of electron gun, which produces beams of lowest coherence (Carter and Williams, 2016). Tungsten filaments are a bent tungsten wire which are heated and through which a current is passed. At a certain temperature, electrons can escape the wire. Other radiation sources can provide more coherent beams compared to tungsten filaments for example the LaB6 crystals which operate similarly to tungsten filaments but have a sharper more focused electron beam which in turn produces a higher resolution final image. The field emission gun, or FEG, is found in more sophisticated microscopes (Hamaguchi et al., 2019; Nakane et al., 2020). Field emission guns have a sharp Tungsten tip (~100 nm or Schottky), when a strong electric field is applied to the Tungsten tip, high-energy electrons are released producing a narrow and coherent electron beam with high intensity. FEGs do not all require heating to function. An extraction anode is placed under the electron gun to control the acceleration of electrons. This is important because electrons should have spatial coherence which means that they come from the same direction to the same position on the object and temporal coherence which means electrons should have the same wavelength to provide a less noisy image.

Once electrons are excited, a tool called the Wehnelt cylinder held at a voltage higher than the extraction voltage focuses the beam that is excited from the radiation source. A series of disks of increasing voltage are placed under the Wehnelt cylinder called accelerator stacks which accelerate the electrons towards the specimen as they gain voltage. The resulting electrons have an energy conferred on them by the acceleration voltage that is expressed in kilo-electron Volts (keV).

Electron microscopes use high voltages in the electron gun so electrons can pass through the specimen. Electrons in microscopes suited to biological specimen imaging usually accelerate electrons with 300 keV, although is also common 200 keV electron energy – the chief difference being that lower voltage

microscopes are cheaper to build and maintain (Egerton, 2014; Henderson, 1995; Herzik et al., 2017). Higher voltage microscopes are also more beneficial as the number of electron interactions with the sample will be lower but the penetration of the beam through the sample will be higher. Therefore, a higher resolution structure could be obtained on a 300 keV microscope compared to a 200 keV microscope, but it also depends on other hardware equipment in the microscope.

The inside of the microscope is kept in a high vacuum environment because many electrons scatter in gases, therefore having a high vacuum means that the electron will only scatter once it hits the specimen. A high vacuum reduces the probability of non-specimen scattering events. The electrons are then re-focused by lenses. Under the gun are a series of electromagnetic lenses that focus the electron beam on the specimen. Electron lenses are an electromagnetic field which is generated using copper wires covered in an ion cast. Current is passed through the copper wires which generates a magnetic field to focus the negatively charged electron beam.

1.4.2.2 Types of lenses

The microscope has three types of lenses condenser, objective and projector lenses. The condenser lens helps focus and control the intensity of electrons. The objective lens is used to focus and magnify the image. The projector lenses help magnify the image (Figure 1.2) (Orlova and Saibil, 2011). Condenser lenses are located above the specimen and projector lenses are located under the specimen. In more sophisticated microscopes, a third condenser lens is added to provide a parallel beam to maintain beam coherence. The main projector lens which magnifies the image under the specimen is called objective lens. The final image is a magnified object observed on a fluorescent screen or detector.

A biproduct of imperfect magnetic lenses is spherical aberration (Figure 1.3 a). Spherical aberration means that different objects of different resolution within a sample are focused differently. As a result, some electrons fail to converge at the same point. Spherical aberration causes a change in the phase of these electrons. A change in phase means that there is a change in spatial frequency which changes the contrast of the image but negatively affects resolution. Spatial frequencies can have negative contrast and positive contrast. The lowest spatial frequency equalling to zero is known as the ‘first zero’ where the wave changes from positive contrast to negative contrast (Figure 1.3 b). The practical outcome of these aberrations is that features at some resolutions have positive contrast, some have negative contrast, and some have no contrast.

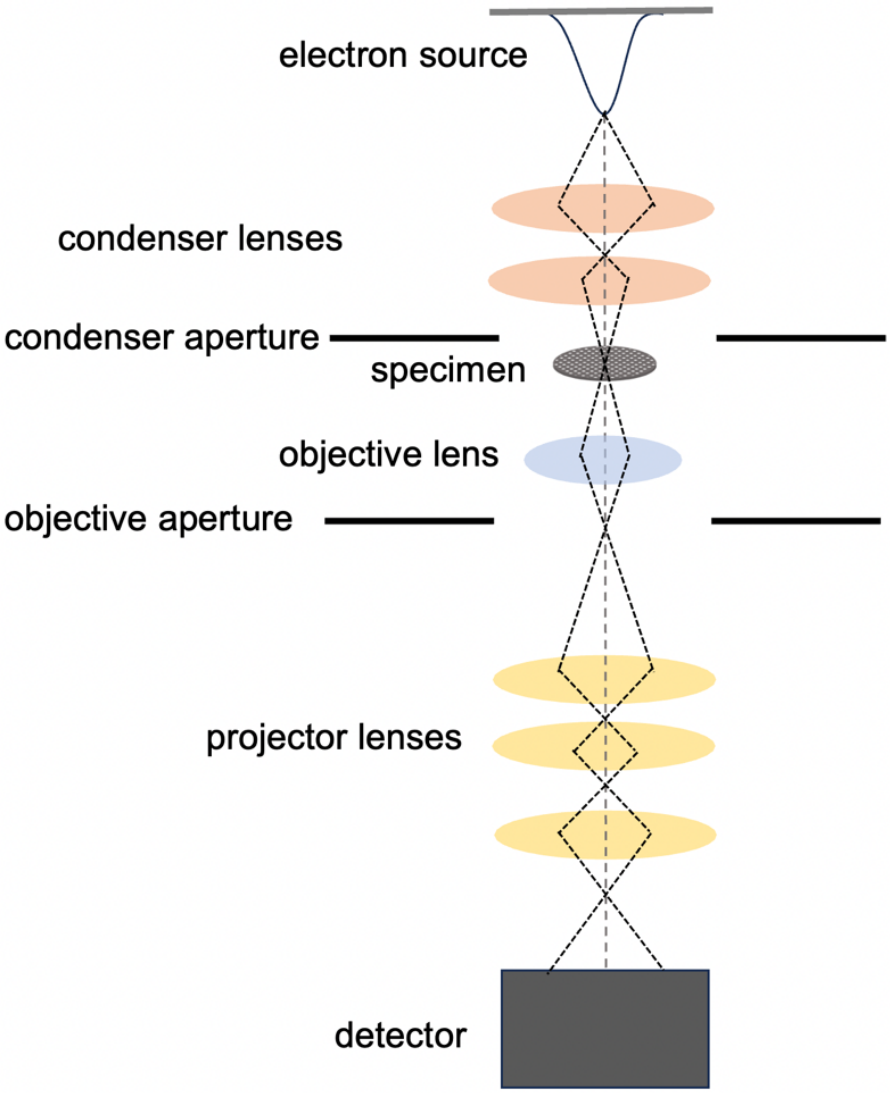


Figure 1.2 A schematic diagram of the lenses in a cryo-electron microscope. The electron source provides electrons which are focused by a series of electromagnetic lenses. Apertures are used to remove any inelastic scattering electrons. The final magnified image of the specimen is projected onto a detector.

1.4.2.3 Tools for generating contrast at the time of data collection

Biological samples have little amplitude contrast, thus necessitating phase contrast to see them. The main way to produce contrast is by increasing defocus. But tools can help to increase contrast which minimizes the amount of defocus that needs to be changed. One tool that can be used is an energy filter. An energy filter can be used to reduce noise from inelastic scattering. Energy filters are made of magnetic prisms that focus the electron beam to 90° angle. The un-scattered electrons and elastically scattered electrons pass through the slit (Baker and Rubinstein, 2010). The inelastically scattered electrons have lower energy and do not pass through the slit because they bend more strongly. By

allowing certain electrons with a specific energy to hit the detector, it reduces noise added by inelastic scattering and increases contrast. Because the contrast is higher than usual, a lower defocus can be used to image the object resulting in a higher resolution image (Henderson, 1995; Rohou and Grigorieff, 2015).

1.4.2.4 Detection devices detect scattered electrons to form an image of the specimen

Detectors are used to detect electrons to produce an image and are placed right at the end of the column. At present most microscopes use direct detection devices (DDD's). DDD's are used because they are more sensitive and can directly detect scattered electrons resulting in a crisper image of the object. Direct detection devices are particularly useful because they have a rapid frame rate and can detect electrons in counting mode which means each electron is detected separately (Li et al., 2013). This reduces scattering and improves Detective Quantum Efficiency (DQE) which measures contrast and spatial frequency between pixels. Having a rapid frame rate means that if multiple electrons hit a pixel, it can still be counted with precision which prevents coincidence loss. Coincidence loss is when the count-rate cannot keep up with the internal frame rate. When multiple electrons hit the detector at the same pixel and the detector cannot detect each individual electron which leads to inaccuracies in the final signal. By collecting short videos (of multiple frame rates), we can super-impose and average them to remove blurred data. Short movies with sub frames are also useful to predict the CTF of an object which can later be used for CTF correction. Lastly, DDD's have monolithic active pixel sensor (MAP) which are back thinned to prevent unwanted back scattering of electrons and reducing noise.

1.4.2.5 The Shannon-Nyquist frequency is used to choose the correct magnification for imaging

Prior to collecting data in cryo-EM, an appropriate magnification should be considered. The correct magnification for imaging is based on field of view and pixel size. The pixel value chosen to image a sample is based on the Nyquist-Shannon Sampling theorem. The theorem states that a signal can be reconstructed if the frequency components are lower than half the sampling frequency also known as Nyquist frequency.

1.4.2.5.1 The effects of pixel size on the final image

It is important to choose the correct pixel size because this effects the final resolution of the image. We obtain waves that are of high spatial frequency and low spatial frequency. By collecting high spatial frequency information provides a higher resolution image and low spatial frequency provides a low-

resolution image. An image itself is a 2-dimensional matrix of pixel intensity values. Therefore, to visualise images of high spatial frequency (high resolution) we need a small pixel size. In practical terms, at low magnifications fewer pixels are used to make an image resulting in a low-resolution image. At high magnifications more pixels are used to make up the same features in an object. At higher magnification we can take information from higher spatial frequencies which provides a high-resolution image. Therefore, pixel size needs to be a number that is half of the resolution you wish to obtain.

1.4.2.5.2 The effects of magnification on the final image

It is important to choose the correct field of view for the object since imaging at high magnification means that the field of view decreases, but the final image can be used to obtain a higher resolution structure. A deduction in the field of view means that information from the surrounding environment is lost. A wider field of view in cryo-electron microscopy is important because a wider field of view means more particles per image means fewer total images required. Magnification is a trade-off between number of particles and sufficiently small pixels. Information from the surrounding environment is important in tomography where we look at the cellular context of an object or when more than one particle can be obtained from a tomogram.

1.4.3 How are scattered electrons converted into images?

Once electrons hit the sample they are scattered and refocused. To understand how these scattered electrons form an image we first need to understand Fourier transforms which explains how electron waves can be used to form an image.

1.4.3.1 Fourier transforms can represent an image as a series of sine waves

Fourier transforms in cryo-electron microscopy are required for determining molecular structures. Fourier transforms are a series of sine waves formed from the original data collected when electrons interact with the specimen and produce a diffraction pattern. These sine waves collectively form an image of the object this process is known as Fourier synthesis. In practical terms this means that Fourier transforms are used in 3D reconstruction algorithms to reconstruct an image and for filtering images. The process of combining these waves is known as convolution. We can then use the information from a Fourier transform to represent a power spectrum in a process known as deconvolution. The power spectrum is the Fourier transform of these spatial frequency patterns which is squared to provide a more readable set of numbers. By combining each wave that we have analysed in the power spectra we can produce the original image.

1.4.3.2 Contrast Transfer Function represents the changes in contrast due to the microscope

The Contrast Transfer Function (CTF) is a function of the contrast of the image, the amplitude and spatial frequency. The effects of the microscope on the sample such as spherical aberration and differences in contrast can be mathematically represented using CTF. By knowing the CTF we can correct for any distortions in the image created by imperfect microscope function using a method called CTF correction. We can use CTF to look at how a change in defocus affects contrast at various spatial frequencies, we can use it to generate optimal contrast to visualise the specimen. We can then use CTF correction to correct for this defocus and spherical aberration of the microscope to recover information from the specimen image (Fernández et al., 2006).

1.4.3.3 Thon rings represent the zeros of the CTF

A visual representation of the zeroes in the CTF is known as Thon rings which are set of concentric rings representing the 2D Fourier space of an image (Figure 1.3 c). The power spectra of cryo-EM images are collected using a higher level of defocus often exhibiting more of these concentric rings (Orlova and Saibil, 2011; Wade, 1992). In a power spectrum, low spatial frequency is shown in the centre and the rings for high spatial frequency are at the edges. Thon rings not only provide information on contrast and defocus but also on the quality of ice, the nature and thickness of the object being imaged and astigmatism of the beam. Thicker samples cause more scattering and change the ring pattern compared to thinner samples. In thicker samples the Thon rings are clearer because the defocus oscillations are more pronounced. The quality of ice can also be determined by looking at Thon rings. Vitrified ice will produce distinct continuous Thon rings whereas crystalline ice or contaminants will produce spots or streaks in the Thon rings.

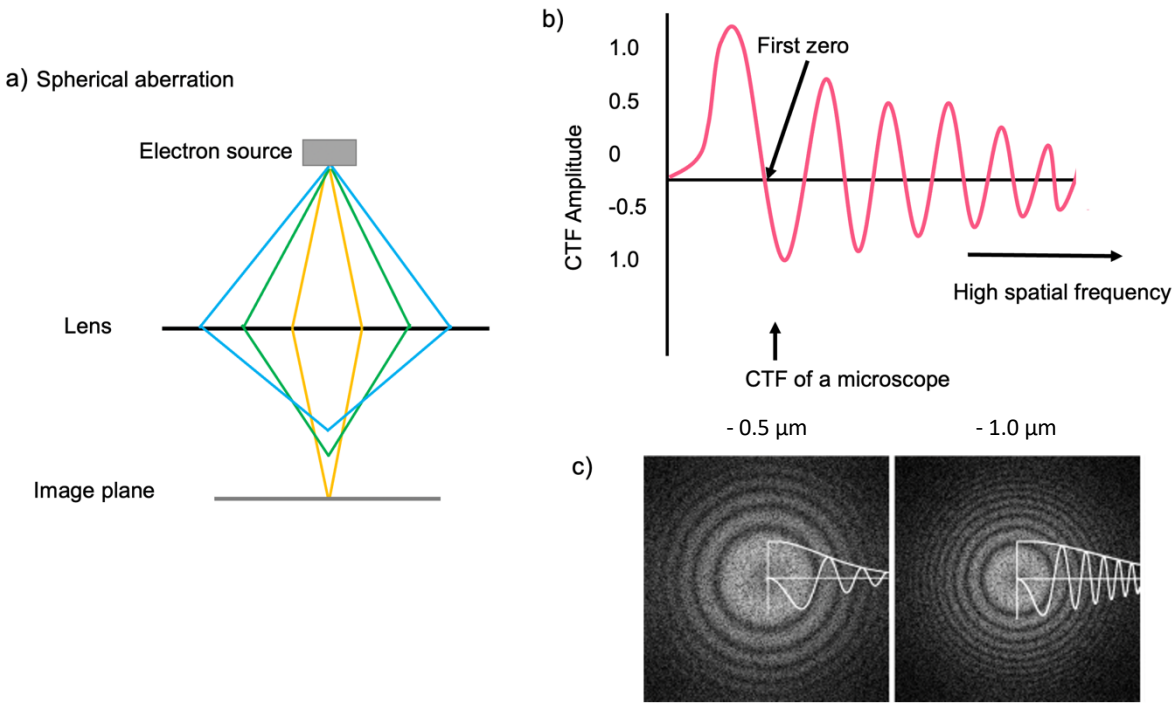


Figure 1.3 Spherical aberration and the contrast transfer function. a) Spherical aberration is a result of imperfect which scatter electrons. This provides more contrast to the image but reduces resolution. b) Is the contrast transfer function which is a series of oscillations as a function of spatial frequency. The increase in oscillations and decrease in amplitude shows high resolution information. c) Is an example of Thon rings which are a visual representation of the CTF oscillations, adapted from Orlova and Saibil, 2011.

1.4.4 Data processing in cryo-electron microscopy depends on the 'central slice theorem'.

The basis of data processing algorithms in both SPA and cryo-electron tomography are based on the 'central slice theorem' to provide a final three-dimensional output. In cryo-electron microscopy 2D projections are used to construct a three-dimensional object (Crowther et al., 1970; Crowther and Klug, 1971; De Rosier and Klug, 1968; Penczek, 2010). To reconstruct a 3D object from 2D projection images it is important to understand the central slice theorem.

The central slice theorem states that Fourier transforms of a 2D projection image can be used to derive information about the 3D structure of the original object. The Fourier transform of a 2D projection image of the object of interest is equivalent to a slice passing through the origin of a 3D Fourier transform (Crowther et al., 1970; De Rosier and Klug, 1968). Therefore, projection images at different angles can be used to detect an inverse Fourier transform to produce a 3D structure.

1.5 Types of cryo-electron microscopy

There are two main types of cryo-electron microscopy used to collect data. The first is single particle analysis (SPA) which is used for purified complexes and the second is cryo-electron tomography used to study structures *in situ* (Cheng et al., 2015; Ferreira et al., 2018). Both methods have the same methods to prep samples but have slightly different data collection techniques and outputs.

1.5.1 Single Particle Analysis

SPA is a method by which two-dimensional images of randomly oriented particles are collected to provide a three-dimensional final object (Cheng et al., 2015). SPA is an important technique because we can solve structures of purified proteins to molecular resolution. This provides us with information such as interaction between proteins and finding key residues important for protein function.

In most cases the process of solving a protein structure using SPA starts with a purified protein sample usually >100 kDa in size. The sample is then frozen on grids as explained in section 1.3.1. The samples on the grid are in random orientations as a result of it being in a solution prior to freezing (Cheng et al., 2015). The grid is inserted into the microscope after which thousands of multi-frame movies of the sample are collected. The movies are motion-corrected which result in micrographs. These micrographs are CTF corrected to correct for defocus and spherical aberration (Wade, 1992). CTF corrected micrographs are used to pick particles, this can be either done manually or using particle picking algorithms. The particles are then grouped depending on their orientation into different classes of two-dimensional images. These 2D averages can then be combined to provide a final 3D structure which is at a resolution between 2 to 4 Å. The particles in 2D classification are classified based on Maximum Likelihood Approach which decides the classification of particles based on the objects features and statistical calculations. The 2D averages already provide a higher signal to noise image which can then be used to make a 3D initial model. The initial model is a low-resolution structure of the object used as a reference in 3D classification for iterative refinement where the model is iteratively improved based on the previous model. After a final model is achieved validation tools can be used to improve the 3D reconstruction and build an atomic model.

1.5.2 Cryo-Electron Tomography

In cryo-electron tomography a single object is rotated laterally at different angles (Ferreira et al., 2018). By tilting the object around an axis, multiple projection images of the object can be collected at different views throughout a range of tilts. This is like SPA which also images different orientations of an object but in 2D and the orientations are random. To distinguish between the different orientations a large

number of images are required. In cryo-electron tomography, these 2D images taken at different angles can be used to reconstruct a tomogram.

Cryo-electron tomography is a useful tool to study biological structures *in situ* in their native environment. It is also an important tool for visualising a structure from different angles to provide an informative three-dimensional structure. In contrast to SPA, cryo-tomography repeatedly images one object to collect a single tilt series. Many tilt series are collected where each tilt series is the same object in a different specimen. Each tilt series can then be reconstructed to form a tomogram. Multiple tomograms can be averaged in a process known as subtomogram averaging (STA).

1.5.2.1 Sample preparation and data collection in cryo-electron tomography

To prepare samples for cryo-electron tomography cells are frozen on grids as explained in section 1.3.1. These cells are usually mutants which could answer a biological question or could be wild type cells of which we know little about. A tilt series can then be collected which is reconstructed into a tomogram.

1.5.2.1.1 Collecting a tilt series

To collect data, usually, a few hundred tilt series are collected to provide a sub-nanometre resolution structure but the amount of data collected mainly depends upon sample abundance (Bharat et al., 2015). A tilt series is a set of images collected of an object at different angles. At each tilt increment a 2D projection image is taken which can then be aligned to produce a three-dimensional short volume of the object known as a tomogram. For most of our projects, the maximum tilt angles are -60° to +60° or sometimes ±70° at 3° increments (Figure 1.4). In terms of collecting data usually we opt for a dose-symmetric, bi-directional tilt scheme (Bouvette et al., 2021; Hagen et al., 2017). This is because high-resolution information (thin sample) is found at lower tilts whereas low resolution images are collected at higher tilts. Therefore, the electron beam hits the low tilt angles first (+3◦, -3◦, +6◦, -6◦) to prevent imaging low tilt angles once the sample is exposed to electrons and damaged the sample.

1.5.2.1.2 Limitations of collecting a tilt series in cryo-electron tomography

There are some limitations to using cryo-electron tomography for data collection. When collecting a tilt series, the resolution at higher tilts is reduced because the ice thickness increases at an angle that is not perpendicular to the ice plane at higher tilts resulting in anisotropic resolution. As a result, the final tomogram looks less defined with fewer features. Another limitation of this procedure is that we cannot image at 180-degree tilt angles because at ± 90° the sample is parallel to the beam. The disk like structure of the grid and the metal ring of the sample holder block electrons from passing through the

sample. The missing information is represented as a ‘missing wedge’ because the space where no tilts are collected is a wedge-shaped structure in 3D Fourier space (Ferreira et al., 2018). A way to fill in this information is to collect data of an object at a different orientation to the beam to fill in missing information. By aligning and averaging tomograms, we can fill in this missing information. Averaging tomograms results in a subtomogram average (STA).

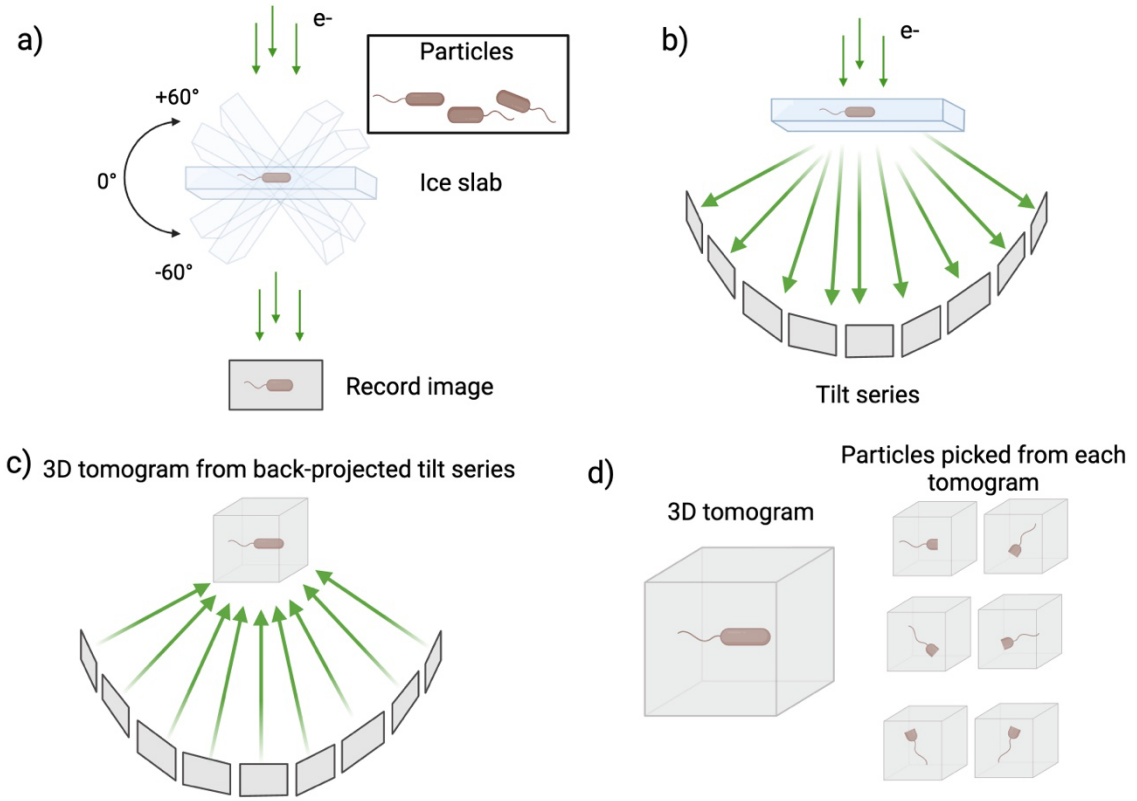


Figure 1.4 A schematic diagram showing the process of collecting a tilt series. a) the sample rotating when collecting a tilt series; b) A collection of tilts forming a tilt series; c) A back projection of the tilt series to form a series of images d) A reconstruction of 2D tilt images to form a 3D tomogram.

1.5.2.1.3 Collecting data over a range of defocus settings can fill in the zeros to fill in missing information

For cryo-electron tomography it is important to find a defocus where we obtain sufficient contrast to observe our feature of interest without losing too much resolution (Ferreira et al., 2018). By increasing defocus, you can increase contrast of particles but at the cost of high resolution. A change in defocus results in enhancing of certain spatial frequencies which allows for the visibility of certain features. Parts of the structure that are not visible can then be compensated for in other views of the dataset.

Contrast in images shows an oscillating behaviour as a function of resolution. We can fill in missing information by using data collected with a different defocus which focus on unique features. To acquire an image at higher contrast, phase contrast can be altered by imaging under focus (< -2 μm) using lenses this allows enough contrast see objects of interest. The defocus depends on the sample being imaged and contrast required to see the object of interest.

1.5.2.2 Data processing in cryo-electron tomography

To process data in cryo-tomography, each tilt series is reconstructed to form a tomogram. Tomogram reconstruction requires pre-processing of each 2D tilt image. Each tilt series is first motion corrected, CTF estimated and CTF corrected. The 3D CTF correction can also be done in later stages of processing. Using known information such as the acceleration voltage and spherical aberration we can calculate the defocus of the dataset and compare the Thon rings to the calculated defocus. CTF correction is then done by phase flipping the frequencies with inverted contrast (Heel et al., 2000). The tilt series can then be aligned to form a tomogram.

1.5.2.2.1 Two-dimensional tilt series are reconstructed to provide three-dimensional tomograms.

To align a tilt series, we determine the orientation of each 2D tilt image in relation to each other. To help with alignment, fiducials are added into the sample prior to freezing. Fiducials are gold beads between 5 to 10 nm in size. These gold beads are high in density, high-scattering, high-contrast objects and easily tracked in tilt series. The fiducials are widely spread in the sample and can be tracked in each tilt image for optimal alignment. These gold beads help finding translations and rotational angles between images since we cannot rely on an imperfect microscope stage. Usually, 10 to 20 fiducials per 2D image are sufficient for aligning a tilt series. The lattice of fiducials formed is a 3D model of the fiducials for subsequent accurate alignment of tilt series for back-projection using cross-correlation algorithms. At later stages of processing fiducials can be ‘removed’ from the tomogram using algorithms. The final 3D model generated using fiducials describes exact translations, rotations, and angles between images. This information from the 3D model is then used by reconstruction algorithms to convert 2D images into a 3D tomogram.

1.5.2.3 Subtomogram averaging can result in a sub-nanometre resolution structure.

Subtomogram averaging also helps increase signal to noise ratio and produce a higher resolution image providing a higher resolution image compared to one tomogram. For subtomogram averaging 2D

projection images are first converted to 3D tomograms. In most cases weighted back projection (WBP) is used where the 2D projection images from the tilt series are back projected to form a 3D volume (Kremer et al., 1996). Each 2D projection is placed back into its corresponding position in 3D space. Reliability in data varies in each tomogram therefore the data is weighted depending on the tilt angle and signal to noise ratio. Data with high-spatial frequencies such as data collected at lower tilt angles contribute more than data from low-spatial frequencies. The result is a low signal to noise tomogram. Filtering techniques can be used for aligning tilt series and for providing higher contrast tomograms. The second method for aligning tilt series is simultaneous iterative reconstruction technique (SIRT) (Agulleiro and Fernandez, 2011). It is a method by which an initial 3D volume is reconstructed using the tilt series after which the 3D volume goes through iterative refinements. This is done by computationally forming 2D synthetic projections from the original 3D volume then comparing the 2D synthetic projections to the original data to find artefacts and errors. Similarly, to WBP the focus is on high spatial frequency information. Iterative refinement of the 3D volume eventually leads to a more defined 3D structure. Although SIRT is more thorough compared to WBP it is more computationally expensive.

1.5.2.3.1 The object of interest determines the parameters used for subtomogram averaging

The object is aligned computationally over many iterations. Usually six dimensional searches are conducted, starting with global searches over a wider search range and ending with more local searches over smaller angles using a deterministic approach. Previous knowledge about the object of interest determines some of the search ranges. Subtomogram averaging increases signal to noise ratio and resolves features that are not visible in a single tomogram recovering high spatial frequency information resulting in a higher resolution structure. Since it assumes all objects being aligned are the same, any variations between objects in tomograms will be averaged out. With enough particle number symmetry of the structure can be detected, we can then impose this symmetry to increase signal to noise ratio and refine the structure further.

1.5.2.3.2 Fourier Shell Correlation is required to determine the final resolution of the subtomogram average.

After subtomogram averaging the dataset, the final FSC coefficient is calculated (Rosenthal and Henderson, 2003). Similarly, to single particle analysis the dataset can be randomly halved, aligned and processed separately which is the gold standard approach. The FSC then measures how similar (the correlation between) each half of the dataset. Inverse of the spatial frequency at a particular resolution is given as a cut off.

1.6 Cryo-electron microscopy is a tool for studying the evolution and mechanism of rotation in motors

Cryo-electron microscopy has been used to study the evolution of motors. It is important to study the motor *in situ* to study protein structures in their native environment and keep information which is lost when purifying proteins. Differences between motors in different species are visualised by cryo-electron tomography and subtomogram averaging (STA). Subtomogram averages of motors from different species serve as fossil records of motors. These subtomogram averages are often compared to find similarities and differences in motor architecture. The flagellar motor is a large macromolecular complex embedded in the inner and outer membrane of the cell. cryo-electron tomography has shown that the core motor structures remain the same (although could differ slightly) but motors have diverged to add additional proteins which are species specific.

To gain insight into the evolution of motors it is important to identify and locate proteins in the motor. To identify proteins as part of a larger complex deletion assays are commonly used in combination with cryo-electron tomography and STA (Rossmann and Beeby, 2018). The gene encoding for the protein is deleted, the motor is then imaged and compared with wild type. Often densities are missing which shows where the protein is located. In some cases, multiple proteins disappear which means these structures somehow depend on the deleted protein. An alternative is to add tags to the protein of interest and then check for the extra density (the tag). Often this does not work because subtomogram averaging involves averaging tomograms and tags are mostly flexible, so the density is lost in averaging step.

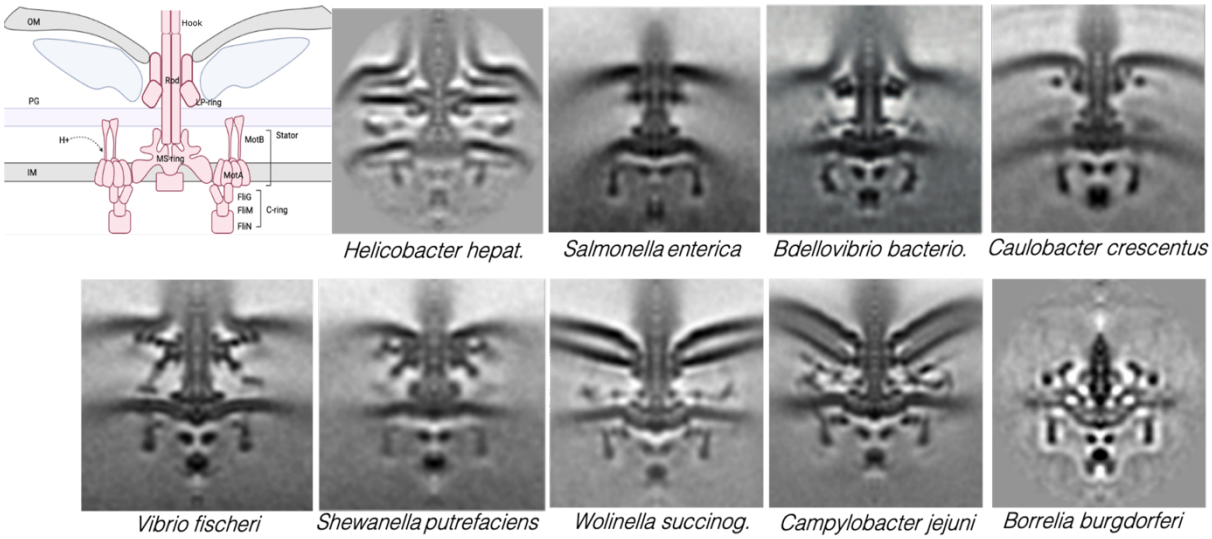


Figure 1.5 Subtomogram averages of motors from different bacteria show diverse architectures of bacterial flagellar motors. Top left: a schematic cartoon of the flagellar motor. The area highlighted in pink are the

conserved components of the motor. The area highlighted in light blue is the part of the motor that is variable. Subtomogram averages taken from Chen et al., 2011; Zhao et al., 2013; Beeby *et al*., 2016; Rossmann et al., 2020.

SPA has been used to study individual protein complexes. The high-resolution structures (usually between 3 - 4 Å) obtained from SPA are useful to understand how individual proteins look, function and interact with each other. For example, motility protein A in the rotor, initially thought to be tetrameric was shown to be pentameric using single particle analysis (Deme et al., 2020; Santiveri et al., 2020). Information from this structure such as conserved residues were modelled against the torque helix of FliG (a protein in the rotor required to generate rotation) to provide a mechanism for rotation (Lloyd et al., 1999). Protein FliM (another protein in the rotor required to generate rotation) was solved by SPA and provided insight into how the motor switches direction (Park et al., 2006).

STA and SPA can be combined to build models which helps us understand protein function in a larger context. To build models of macromolecular complexes we can use single particle structures to model into sub-nanometre *in situ* structures. To help fill in structures of proteins that have not been solved, protein prediction tools can be used. Typically, these have been monomeric proteins that are non-flexible and small, whereas larger protein complexes and membrane proteins are more difficult to predict. AlphaFold2 CollabFold (v1.5.5) is a neural network-based model, using Critical Assessment of protein Structure Prediction (CASP14) to predict novel protein structures (Jumper et al., 2021). AlphaFold2 CollabFold (v1.5.5) was used to predict the interaction between a protein called FliL and stator complexes in the *B. burgdorferi* motor which was then used to build a large model (Guo and Liu, 2022). AlphaFold2 CollabFold (v1.5.5) was used to predict the structures of proteins from the basal disk and other parts to complete much of the periplasmic region of the *C. jejuni* motor (Drobnič et al., 2023). To understand how motors have evolved I first discuss the core motor structures and how they assemble.

To identify the evolutionary changes in motors we first need to understand the current structure of the motor which consists of 100's of proteins working together in a synchronous manner to provide torque to rotate the motor. Here I explain the function and assembly and mechanism of rotation of the core motor structures.

1.7 The mechanism of assembly for core motor structures is conserved in flagellated bacteria

The flagellar motor is assembled over multiple stages. The first stage starts with the type III secretion system (T3SS) which is homologous to the injectosome structure (Abby and Rocha, 2012; Egan et al.,

2014). The flagellar type III protein export system binds to proteins that form axial components which are transported through the central region of the apparatus. Unfolded proteins are then translocated through the axial components to provide the rest of the protein structures. This export process is driven by proton motive force. The motor is assembled by first making a scaffold in the periplasm. The scaffold is made of FliF proteins which is part of the MS-ring (stands for membrane and supra-membrane ring). After that the P-ring (peptidoglycan ring) and L-ring (lipopolysaccharide ring) assemble which provides a channel for the axial components of the motor (Abrusci et al., 2013; Hu et al., 2015; Li and Sourjik, 2011; Morimoto et al., 2014). These include the central components of the motor which are the rod, hook, the hook-filament junction. The extracellular filament is last to form and extends to many microns (Minamino, 2014).

1.8 The core motor structure is built to generate torque

An average flagellar motor is usually about 50 nm wide and comprising of repeating protein units that function to allow rotation (Chen et al., 2011; Minamino and Imada, 2015). The flagellar motor is classified in three parts – the basal body, the hook, and the filament (Figure 1.6) (Berg, 2003; Macnab, 2003). The basal body is a reversible rotor embedded in the membrane. At the centre of the motor is the rod which is surrounded by large disk like components that provide rotation around an axis to produce torque. Above the rod is the hook which is a flexible structure that bridges the rotor to the filament. The extracellular filament rotates once torque is generated by the rotor.

The motor is powered by trans-membrane proteins called stator units which take in ions from bacterial respiration to power the motor. Stator units push rotation towards the basal body like a mesh of two cogwheels which generated torque. Each stator unit interacts with the cytoplasmic ring (C-ring) in a cogwheel like fashion, this rotation travels to the MS-ring (stands for membrane and supra-membrane ring) located in the periplasm. The generate torque the basal body rotates around the rod which transports torque towards the hook and then the filament. The basal body has two main parts the MS-ring and cytoplasmic ring which control speed of rotation and direction of rotation. Through tight interaction between the cytoplasmic ring and the MS-ring (proteins FliG and FliF) the rotor rotates (Francis et al., 1994; Guo and Liu, 2022; Ogawa et al., 2015). The hook acts as a universal joint between the filament and the basal body which provides flexibility in movement. The filament acts as a helical propeller to push the bacterium forward.

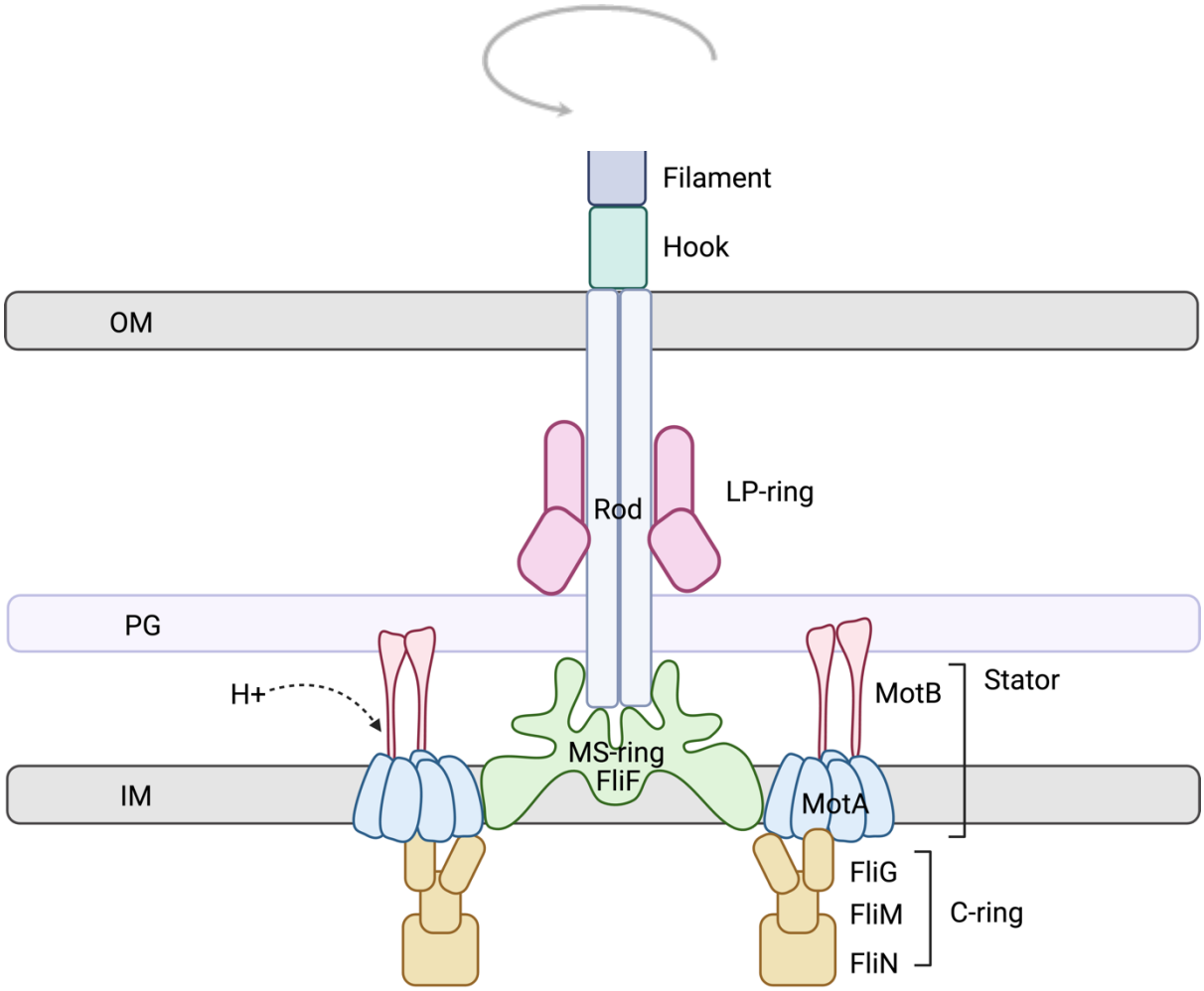


Figure 1.6 The bacterial flagellar motor is a multi-megadalton self-assembling rotatory motor. This schematic structure represents the core components in the flagellar motor. To rotate the motor, protons enter transmembrane proteins called stator units which comprise of MotA and MotB. This pushes the C-ring which transfers rotation to the MS-ring and further to the rod around an axis which is highlighted by the dotted line through the rod. The direction of rotation is highlighted by a grey arrow. IM: inner membrane. PG: peptidoglycan OM: outer membrane.

1.8.1 Stator units are pentameric proteins that interact with the cytoplasmic ring to drive rotation

The rotor is powered by stator units which take in protons from the proton gradient established by cellular respiration. Each stator unit interacts with the cytoplasmic ring in the rotor to drive rotation. The cytoplasmic ring is made up of repeated units of three proteins that form a complex. One of the three proteins is FliG which interacts with stator units to drive rotation and 'switching' allowing the bacterium to swim and change direction.

The stator complex comprises of motility protein A (MotA) and motility protein B (MotB). MotA is a pentameric structure embedded in the membrane (Figure 1.7 a) (Deme et al., 2020; Santiveri et al., 2020). MotB is a dimeric transmembrane helix that reaches up to the peptidoglycan layer to allow the influx of protons into MotA. This induces a conformational change in MotA which allows it to rotate. There are five copies of MotA that make up its pentameric structure. Each monomer has four transmembrane helices (TMH), TMH1 and TMH2 stabilize MotA by interacting with surrounding subunits (Figure 1.7 b). TMH3 and TMH4 interact with transmembrane helices of MotB to make the plug. Unplugging of MotB then initiates a conformational change in MotA. MotA rotates 36° around MotB producing a 'power stroke'. MotA has charged residues in the cytoplasmic region towards the base of the stator which are important for interacting with the 'torque helix' of FliG (Figure 1.7 c) (Zhou et al., 1998, 1998a; Zhou and Blair, 1997). Current research suggests that MotA does not change position but instead the FliG torque helix makes a 180° turn around MotA so the C-ring appears larger (Carroll et al., 2020).

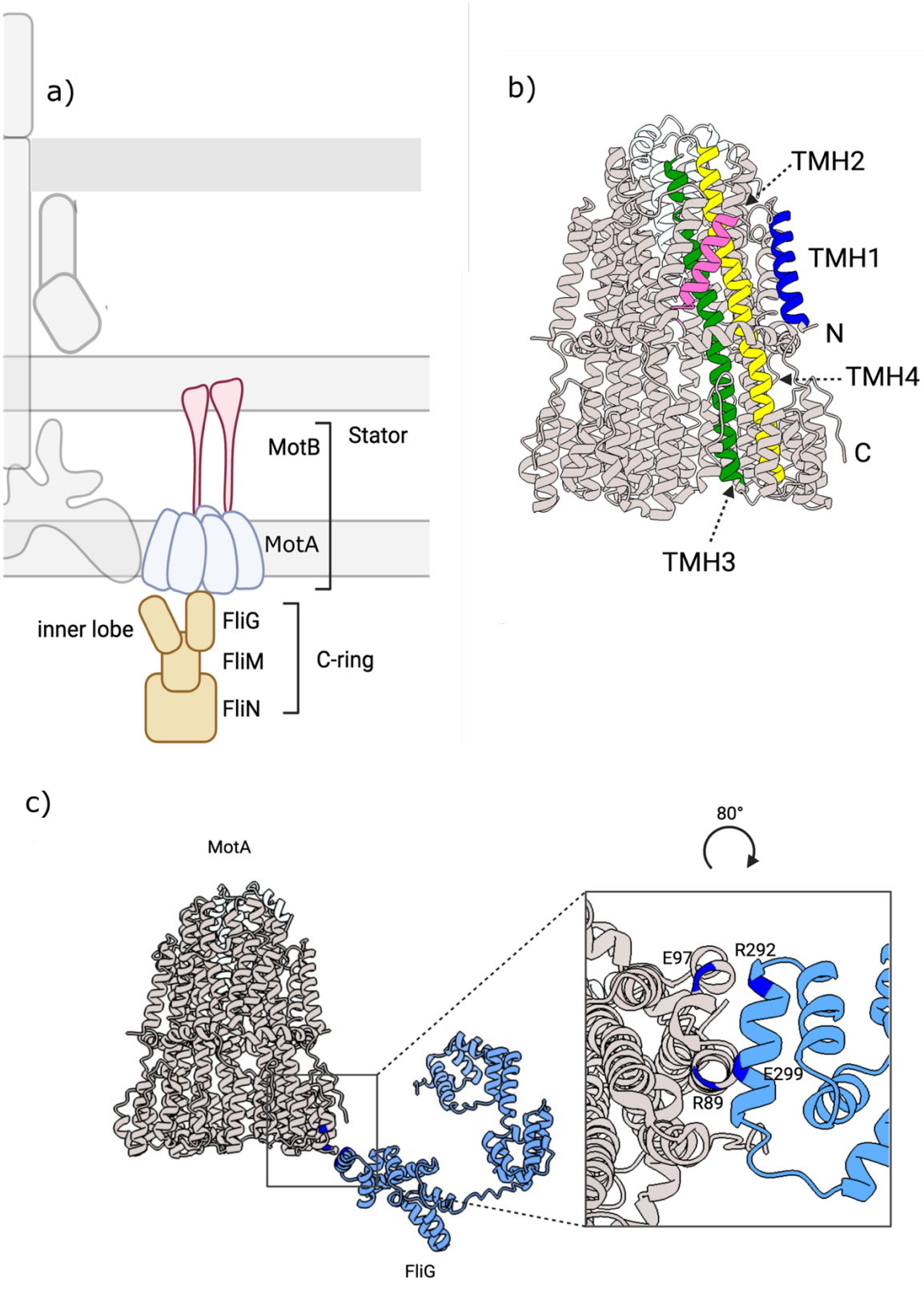


Figure 1.7 MotA interacts with FliG of the C-ring to drive rotation. a) Cartoon depicting the motor highlighting the C-ring (yellow), and stator unit MotA (blue) and MotB (red) b) Each monomer is MotA contains four transmembrane helices, these are important for rotation. c) MotA interacts with the torque helix of FliG at two specific residues to drive rotation in *C. jejuni*.

1.8.2 Stator units in certain bacterial motors incorporate into the motor as load on the motor increases

The recruitment of stators is dependent on the load a bacterium experiences. Stators are known to be mechanosensitive this means that it can modulate the number of stators required at any given time depending on the surrounding viscosity (Lele et al., 2013; Nirody et al., 2016; Ryu et al., 2000). At low viscosity only one or two stators are required to swim. An increase in viscosity means more stator units are recruited into the motor until the maximum number of stator units are reached. In *E. coli* and *S. enterica* this is around 11 stators, but this number varies amongst varied species. In addition to recruiting more stators the existing stators grip more tightly to the peptidoglycan layer when exposed to higher load, this is known as the catch-bond mechanism (Nord *et al.*, 2017). This allows the motor to be powered as surrounding viscosity increases.

1.8.3 Studying stator dynamics using biophysical assays

Stator dynamics has traditionally been studied in *E. coli* using biophysical experiments. There are three main ways of measuring torque. The first is the *tethered cell assay* which involves sticking the filament to a microscope slide and measuring rotation of the cell body (Figure 1.8 a) (Nord and Pedaci, 2020). The second is the *bead assay* where the cell body is stuck to the microscope slide and a bead is attached to the hook of the motor (Figure 1.8 b) and the rotation of the bead is measured. As the number of stator units increase, there is a linear increase in speed, once the maximum number of stators is reached the motor has reached its 'knee speed' which is the maximum torque the motor can produce (Figure 1.8 c). Lastly, the *Resurrection assay* is used to show that the stator units incorporate into the motor (Figure 1.8 d). A protonophore is used to dissipate the proton gradient. Once the protonophore is washed away and the motor senses proton motive force we see a stepwise increase in stator units which re-attach themselves to the motor one at a time. These experiments have helped understand the dynamic nature of stators.

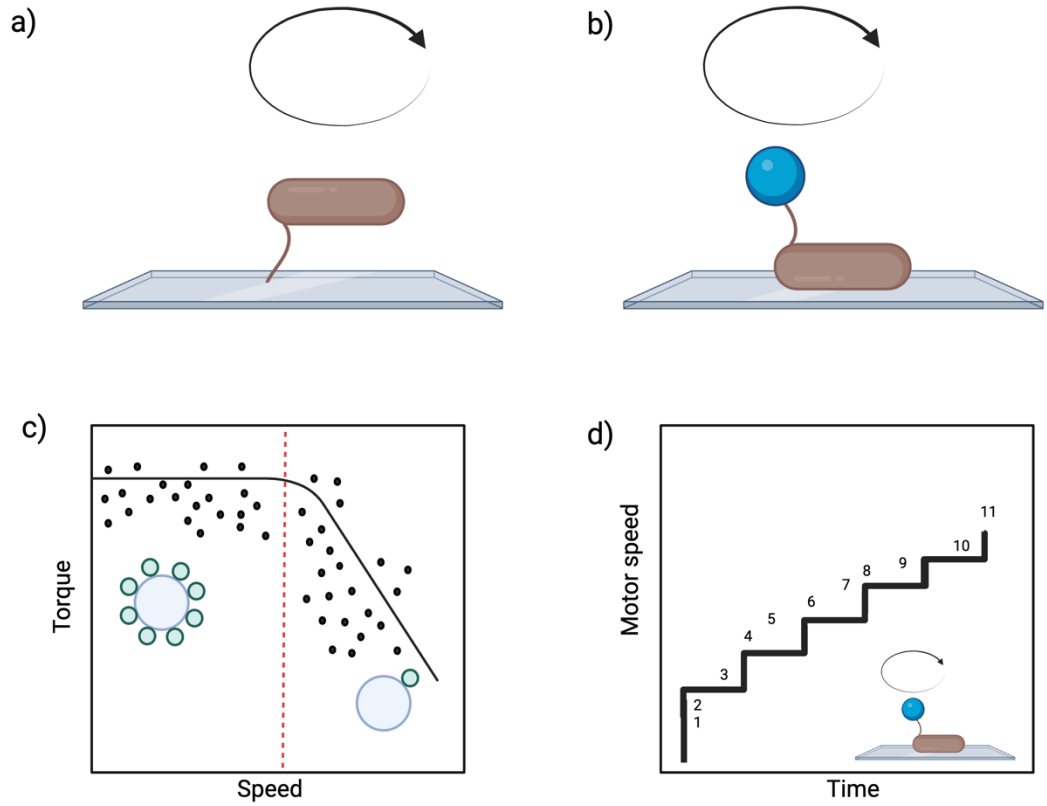


Figure 1.8 Biophysical methods to measure torque. a) Torque can be measured by attaching the filament to a slide and measuring the rotation of the cell body. b) Torque can be measured by attaching the cell body to a glass slide and attaching a bead to the hook of the motor, differences in bead size provide different loads on the motor. c) Representing torque speed curve where the motor has reached knee speed then declines in torque and speed (dissociation of stators). d) Representing an increase in load which allows for a step wise incorporation of stators.

1.8.4 Stator dynamics in the motor are not conserved between species

Motors of bacteria such as *E. coli* and *S. enterica* look fundamentally different compared to motors of *C. jejuni* and *Vibrio fischeri*. The motor architecture of *E. coli* and *S. enterica* looks simple and only consists of core motor structures. Whereas motors of *C. jejuni* and *V. fischeri* are more complex. Subtomogram averages of these motors have shown that stators are not visible in *E. coli* and *S. enterica* but are visible in *C. jejuni* and *V. fischeri*. This suggests that stator dynamics in motors not conserved between species. In *E. coli* and *S. enterica* each motor that a tilt series is collected from will have a different number of stators. An average of these tomograms will average out the stator densities. Although there are hints of stator densities, the maximum stators cannot be observed (Figure 1.9 a, b) (Chen et al., 2011). In more complex motors subtomogram averaging has shown that stators are

consistently present (Chaban et al., 2018). For example, in *C. jejuni* these stators are visible indicating that the maximum number of stators either remain attached to the motor for extended periods of time exhibiting high occupancy or they remain statically present around the rotor (Figure 1.9) (Chaban et al., 2018; Chen et al., 2011). At present little is known about the dynamics of such motors. Studying dynamics of high occupancy stators using biophysical assays will provide context to the constant stators.

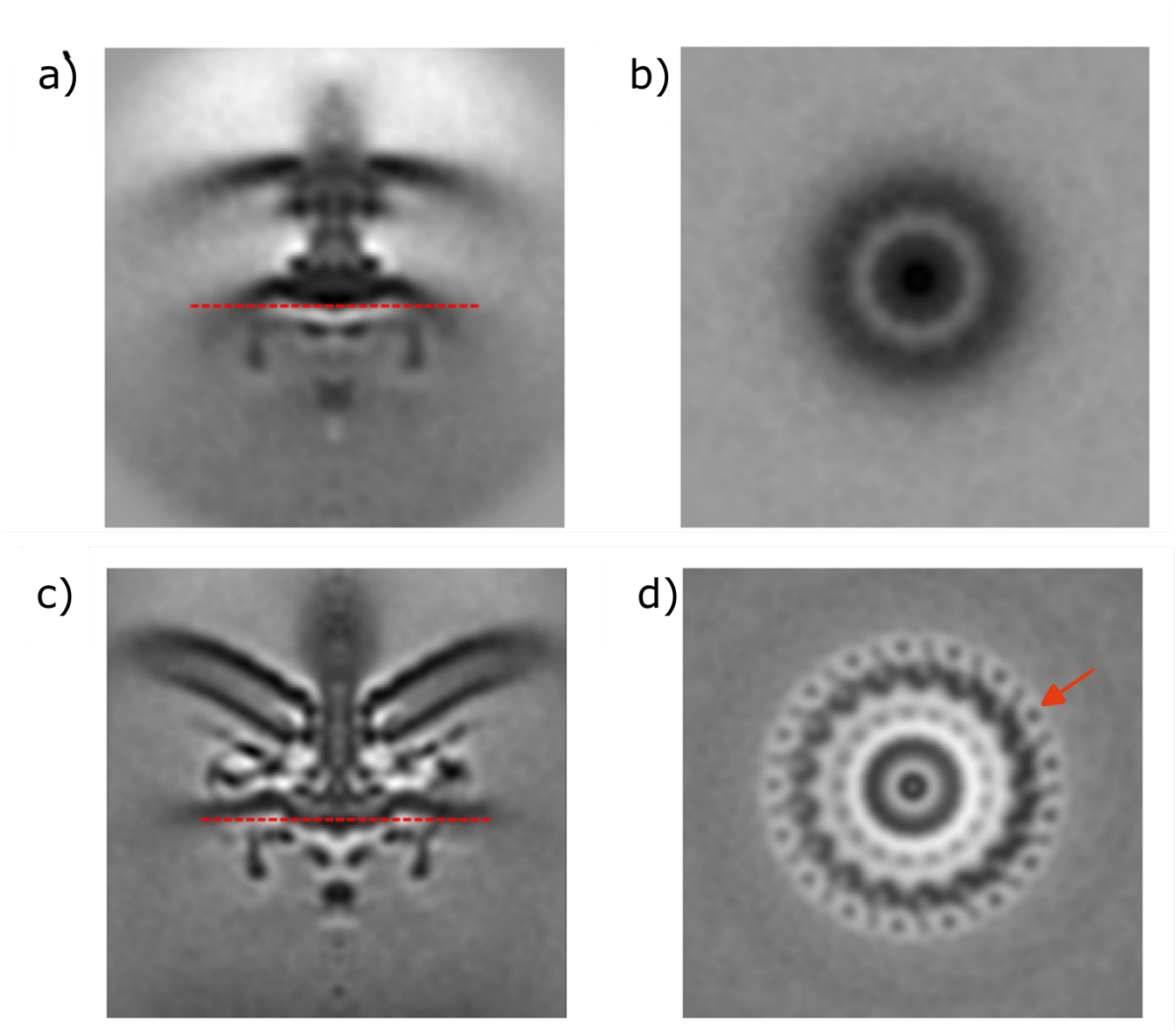


Figure 1.9 A comparison of a subtomogram average of *S. enterica* versus *C. jejuni*. a) The subtomogram average of *S. enterica* shows it is a 'simpler' motor which consists of core components in a flagellar motor (Chen et al., 2011). The red dotted line represents a cross-section through the stator region. b) presents the subtomogram average in (a) through a Z slice showing that we cannot observe MotA subunits. c) A subtomogram average of the *C. jejuni* flagellar motor shows it has evolved to a more complex flagellar motor architecture. The red dotted line represents a cross-section through the stator region. d) presents the subtomogram average in (b) through a Z slice showing that we indeed do observe all 17 MotA subunits. One MotA subunit is highlighted using a red arrow (Beeby et al., 2016).

1.9 High-torque motors have incorporated additional structures to support torque generation

For this thesis, bacteria will be categorised into ‘low torque’ motors and ‘high torque’ motors. Bacteria such as *E. coli* and *S. enterica* have architecturally simple motors that produce lower rotational speeds thus referred to as ‘low torque’ motors. Other species have adapted more powerful motors to swim solely in high viscous environments such as *C. jejuni* and *Helicobacter Pylori* have incorporated additional proteins to maintain a high torque (Chaban et al., 2018).

High-torque motors have gained key molecular features that allow it to swim in a high viscous environment. These include additional proteins surrounding its core motor structure, a wider cytoplasmic ring, more stators, and high stator occupancy (for example, Figure 1.9 c, d) (Beeby et al., 2016; Chaban et al., 2018). Having a wider cytoplasmic ring is beneficial to acquire a higher torque because applying force on a larger diameter ring means the force can act over a greater distance. A wider diameter also allows for more stator units to be incorporated into the rotor providing more energy to power the motor. The average C-ring powering a motor can range anywhere between 34-57 nm in diameter depending on the species. Motors such as those of *S. enterica* which has a cytoplasmic ring radius of 22 nm and can generate around 1300 pN·nm with 11 stator complexes wider (Figure 1.10 a) (Che et al., 2014; Sowa and Berry, 2008). Although the torque of *C. jejuni* has not been calculated, we know that *H. pylori* a bacterium closer in the taxa to *C. jejuni* produces torque of ~3600 pN·nm, has a maximum of 18 stator complexes and a C-ring radius of 26 nm, providing more power to rotate the motor (Figure 1.10 b) (Celli et al., 2009).

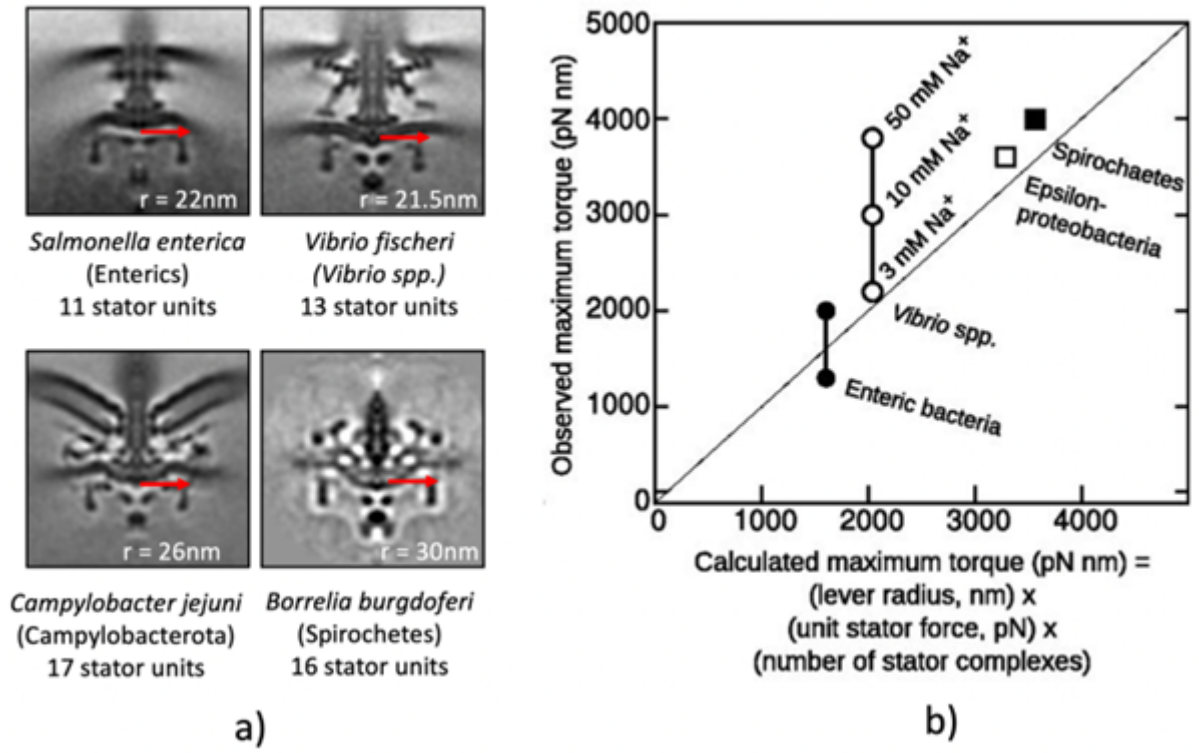


Figure 1.10 High torque flagellar motors present wider C-ring. a) The radius and number of stator units in a subset of bacteria representing the increase in radius of the C-ring also increases the number of stator units. b) Represents an increase in torque as the C-ring radius and number of stators increases. Figures adapted from (Beeby et al., 2016; Chen et al., 2011).

1.10 *C. jejuni* as a model system for studying multiple components in the flagellar motor

C. jejuni a prime model system for studying the evolution of flagellar motors. *C. jejuni* has one of the most divergent flagellar motors and exhibits many proteins which are unique to its motor. These novel proteins that are somehow beneficial to motor function, therefore, from an evolutionary perspective it is an interesting motor to study (Chaban et al., 2018). The specific proteins which act as a part of a more complex macromolecular machinery most likely help *C. jejuni* with producing high torque. How these proteins have incorporated to produce high-torque is largely elusive, unlike low-torque motors such as the *E. coli* motor which is widely studied.

C. jejuni is a member of the Campylobacterota phylum, has evolved to colonize the lower epithelium of hosts (Ferrero and Lee, 1988; Hazell et al., 1986). It is a helical shaped cell with a filament on each end. To swim, the leading filament wraps around the cell body and the other one rotates towards a niche of interest (Cohen et al., 2020). The corkscrew like motility of *C. jejuni* means that it can swim through

the high viscous environment of the gut. Although not lethal to avian hosts, it is pathogenic to humans and causes diarrheal disease (Newell, 2002).

In comparison to low torque motors such as *S. enterica*, *C. jejuni* has incorporated additional proteins that are essential for its motility (Figure 1.11). The motor in *C. jejuni* has three disks that are not present in *S. enterica.* The three disks are the "basal disk" under the outer membrane, the "medial disk" in the periplasmic space and the "proximal disk" in the inner membrane (Beeby et al., 2016). These disks are also found in other high torque motors such as *H. pylori*.

C. jejuni is an optimal bacterium for cryo-electron microscopy and subtomogram averaging because it is a small, thin, and polarly flagellated bacterium so fewer unwanted electron scattering from thin specimen. To study unknown/ uncharacterised proteins in *C. jejuni* deletion assays are used. For example, the function and location of FlgP was identified by solving the structure of a Δ*flgP* mutant by STA and comparing the subtomogram average with that of wild type. Results showed that FlgP subunits make up concentric rings which functions as a buttress to support the motor. Similarly, the medial and proximal disks were also characterised. The proximal disk is partly made of PflA and PflB, deleting PflB also removes the MotB density and most of the proximal disk (Beeby et al., 2016). Therefore, PflB is important for stator stability in the motor and deleting it will negatively affect *C. jejuni*'s swimming capabilities. Without these scaffold proteins *C. jejuni* fails to swim. These are few of many proteins in *C. jejuni* that are yet to be characterised.

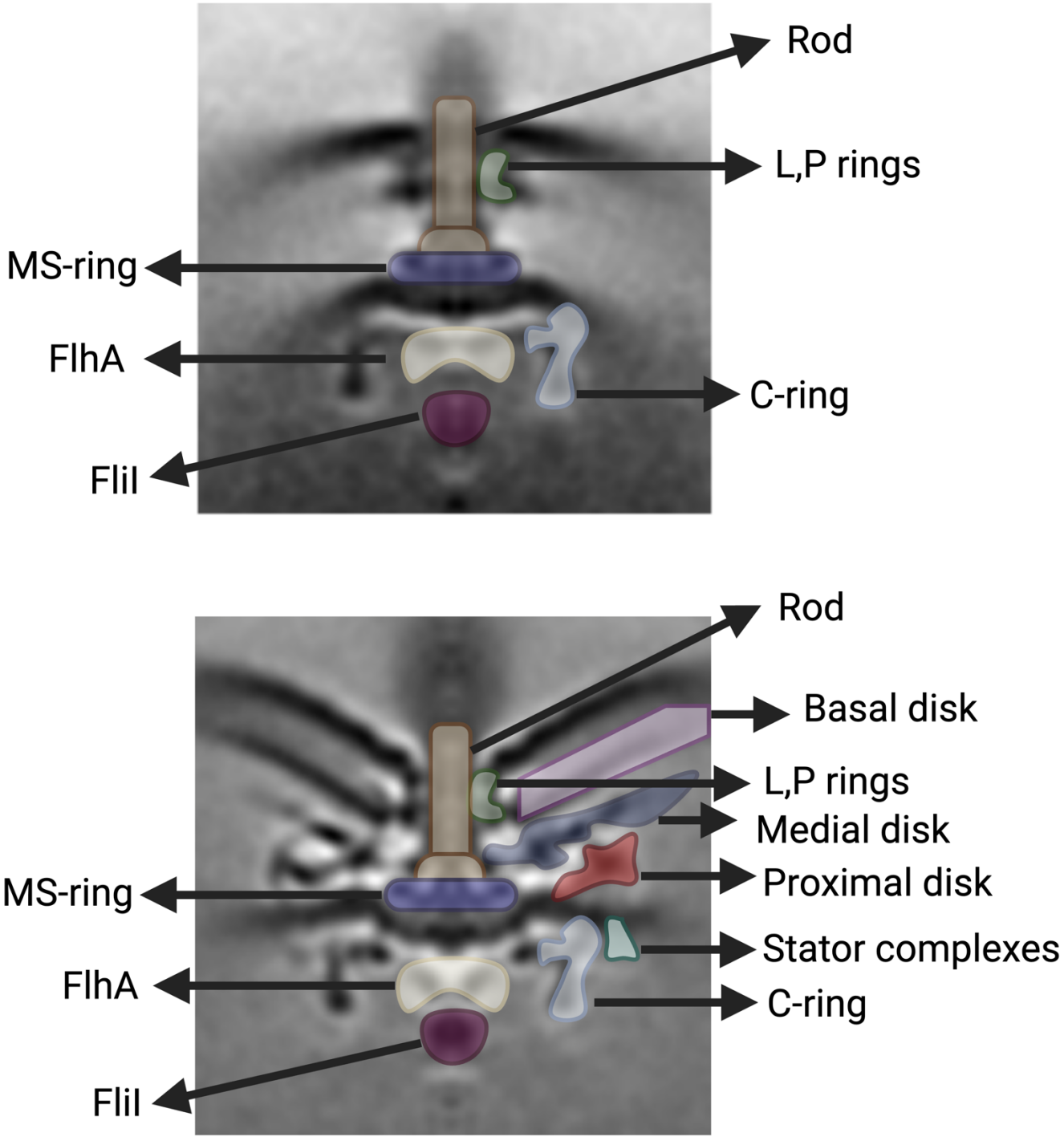


Figure 1.11 A comparison between a subtomogram averages of *S. enterica* and *C. jejuni* highlighting differences in the architecture of their flagellar motor. *C. jejuni* possess more structural components which are not found in *S. enterica*. The core flagellar motor structure remains largely the same (Beeby et al., 2016).

1.10.1 *C. jejuni* has novel proteins that scaffold stator complexes

C. jejuni has additional structures many of which are uncharacterised. The architectural differences between *C. jejuni* compared to other motors leads to believe that these differences have selectively benefited the *C. jejuni* motor in some way. Differences in *C. jejuni* are found on a genetic level. Bacteria from the Campylobacterota have developed a highly regulated flagellar apparatus which expresses proteins when it is in the right environment. *C. jejuni* also has a unique two-component system and the transcription factors σ^{54} and σ^{28} to regulate gene expression (Balaban and Hendrixson, 2011; Joslin and Hendrixson, 2009; Pereira and Hoover, 2005). These translate to several unique proteins that have yet been uncharacterised. For some of these proteins there is functional, biochemical, and *in vivo* imaging analysis to provide some evidence of assembly and function in flagellar apparatus, but little structural information exists. Novel motility proteins have been identified using transposon mutagenesis and high-throughput screening (Gao *et al.*, 2014). Co-immunoprecipitation assays showed that the identified proteins directly affect motility and were shown to interact with conserved proteins. For example, an identified protein CJJ91176_0100 interacts with FliF a protein located in the membrane and supramembrane region of the motor required for motility and direction switching (Figure 1.12). Another motility protein cjj81176_0199 was shown to interact with MotA of the stator complex. To check for direct interaction between the two proteins we can image deletion mutants of these proteins *in situ*. More proteins like these have been identified but are yet to be characterised (shown in Figure 1.12).

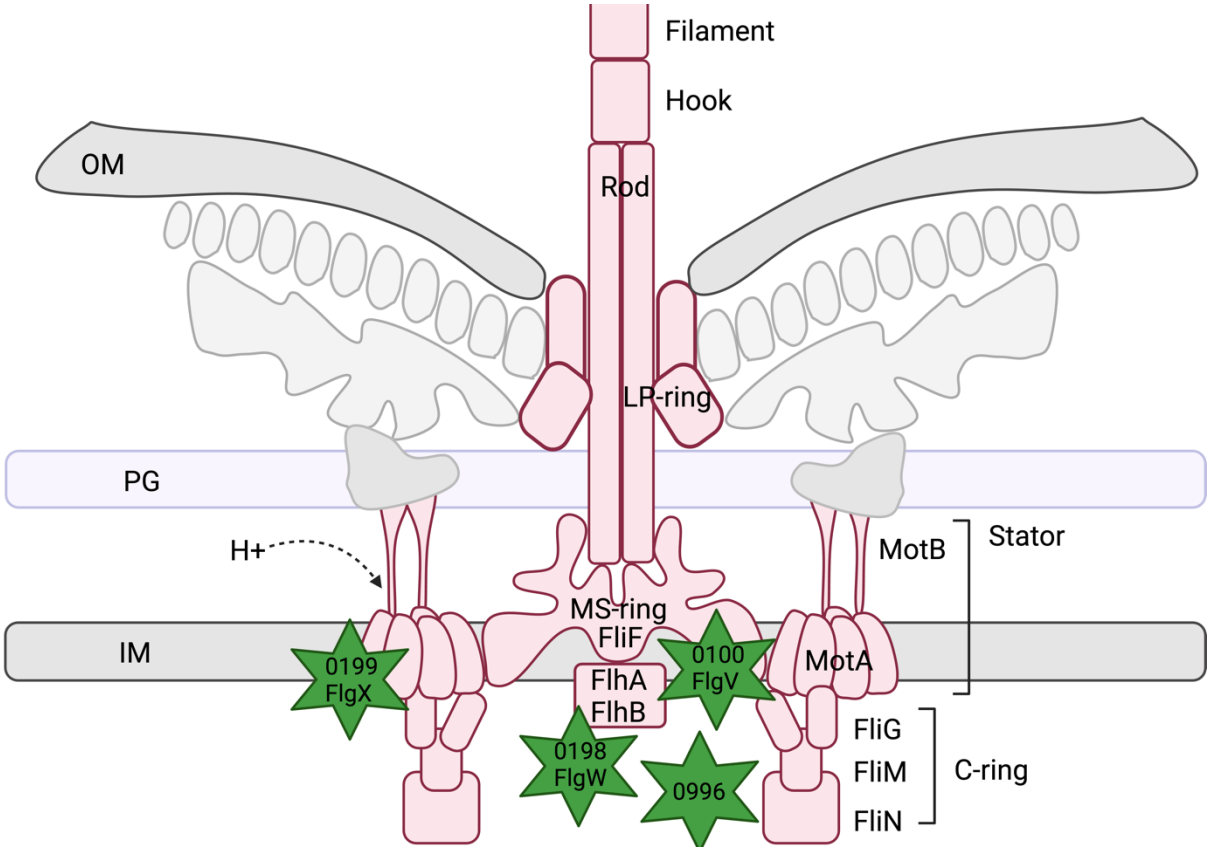


Figure 1.12 A schematic diagram highlighting four novel proteins in *C. jejuni* which are yet to be characterised.

1.11 Summary

We do not know how molecular machines have evolved to incorporate novel proteins. The flagellar motor is a complex macromolecular machine which has evolved to look different in different bacterial species. A previous study from our lab largely characterised novel periplasmic regions of *C. jejuni*'s flagellar motor to yet unprecedented detail and shows how *C. jejuni* has taken up additional proteins as well as modified core flagellar motor proteins for generating torque (Drobnič et al., 2023). My aim is to characterise novel proteins in the cytoplasmic region specific to *C. jejuni* that help *C. jejuni* swim. My research will provide an understanding for how *C. jejuni* has evolved and the possible function of these proteins which has not been visualised before.

Chapter 2

Single Particle Analysis of stator complexes *in situ*

2.1 Chapter Summary

To understand subsequent chapters about the incorporation of novel proteins to drive rotation we first need to understand the mechanism of rotation. Rotation in the bacterial flagellar motor is dependent on transmembrane proteins called stator complexes which power the flagellar motor. We still do not understand how these stator complexes interact with the flagellar motor to drive rotation. Studying the proteins such as the stator complexes *in situ* has been limited by resolution from sample thickness and limited particle number in cryo-electron tomography. By studying the flagellar motor *in situ* at a higher resolution we can obtain more information about how proteins interact with each other. To overcome limitations in resolution, a post doc in our lab Eli Cohen made minicells of *C. jejuni* which are smaller, thinner, hyper flagellated cells. Minicells largely overcome the limitations of sample thickness and increase particle size by 10-fold. The final *C. jejuni* flagellar motor structure was solved to 9.4 Å resolution by single particle analysis using minicells. I used this structure to gain mechanistic insight into generating rotation. We know torque is generated by stator units which interact with the cytoplasmic ring (Blair, 2003). By gaining an increased resolution structure of *C. jejuni*'s flagellar motor we study these proteins *in situ* at unprecedented detail. I attempted to use the minicell dataset to decipher conformational states of each stator unit to show stator rotation against the C-ring, but I was limited by orientation bias in the sample and few particles in other conformational states. My results show that stator units maintain one conformational state most of the time and suggest that stators do not continuously rotate against the C-ring.

2.2 Introduction

2.2.1 The flagellar motor is a macromolecular complex important for motility with a conserved core architecture

The bacterial flagellar motor is a large rotatory complex important for bacterial motility. It is used as motility machine in many bacterial species. The flagellar motor is of interest because the motor has evolved to look different in different bacteria. Although the architecture of the flagellar motor looks different it still maintains a core flagellar motor structure. This makes the flagellar motor an interesting model system to study the evolution of macromolecular complexes (Chen et al., 2011). We do not fully understand the mechanics of the core flagellar motor structure. This is important to understand to grasp the full concept of how the flagellar motor has evolved.

The core structures of the flagellar motor are composed of a basal body, a rod, the hook and a filament (Berg, 2003; Macnab, 2003). The flagellar motor is powered by intermembrane complexes called stators situated in the basal body region which take in protons to drive rotation (Coulton and Murray, 1978; Khan et al., 1988; Stader et al., 1986; Wilson and Macnab, 1990). Each stator unit somehow interacts with the cytoplasmic ring also situated in the basal body to generate torque. One stator unit is composed of a pentameric MotA and a dimeric MotB in the inner membrane (Deme et al., 2020; Kojima et al., 2009; Roujeinikova, 2008; Santiveri et al., 2020).

The flagellar motor rotates once it senses its surrounding viscosity which translates to the ‘load’ sensed by the flagellar motor. Once the flagellar motor senses load, MotB dimerizes and attaches itself to the peptidoglycan layer (Kojima et al., 2018; Roujeinikova, 2008), this conformational change in MotB unplugs MotA which can then take in protons and rotates against the cytoplasmic ring (Figure 2.1). MotA specifically interacts with FliG, which is one of three proteins that make up a C-ring subunit. The C-terminus of FliG known as the ‘torque helix’ is the contact point at which MotA interacts with the C-ring (Kojima and Blair, 2001; Lee et al., 2010; Minamino et al., 2019; Zhou et al., 1998). The C-ring then interacts with the MS-ring which drives rotation up to the rod and the filament to drive rotation of the filament.

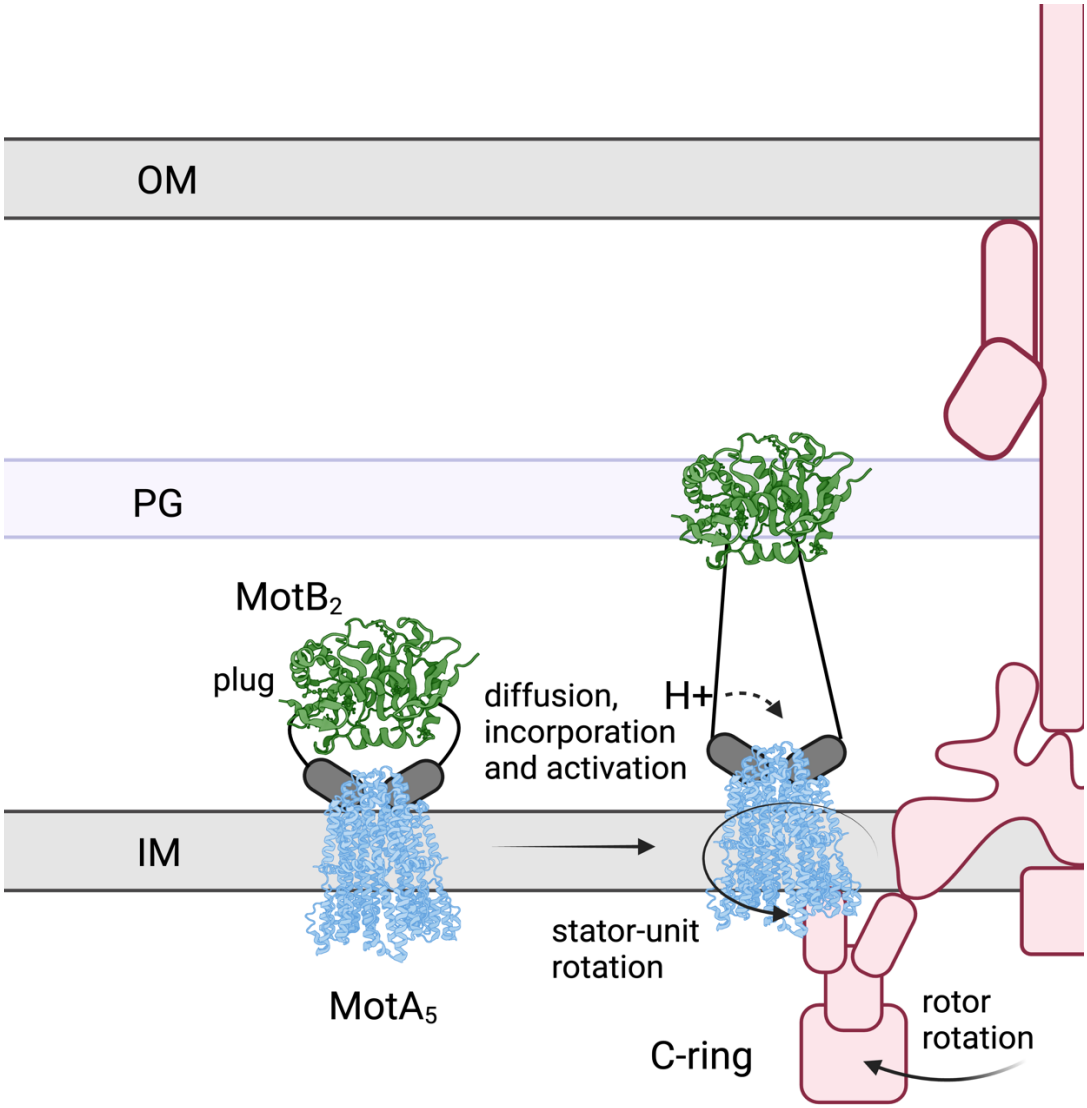


Figure 2.1 Stator units diffuse and interact with the rotor, specifically the C-ring to rotate the flagellar motor. Once a stator unit interacts with the rotor it induces a conformational change in the stator unit. MotB reaches up to interact with the peptidoglycan layer which allows ions to pass through MotA resulting in torque generation.

2.2.2 Protein structures provide an understanding of the mechanism of torque generation

Solving protein structures of the bacterial flagellum has been crucial for understanding how stator units interact with the cytoplasmic ring to produce torque in the flagellar motor. The crystal structure of the C-terminal periplasmic fragment of MotB showed that it can dimerize and interact with the peptidoglycan layer using its peptidoglycan binding domain which is similar to the OmpA protein (Kojima et al., 2018, 2009, 2008; Roujeinikova, 2008). The single particle structure of MotA showed that MotA is pentameric and has two alpha helices of MotB situated in the MotA pentamer, this MotA structure was previously thought to be tetrameric. Two research groups that solved the structure of MotA further identified residues essential for rotation of the stator unit (Deme et al., 2020; Santiveri et

al., 2020). The crystal structure of the FliG protein from *Aquifex aeolicus*, showed a structure made entirely of alpha helices, N-terminal alpha helix, Middle alpha helix, and C-terminal alpha helix (Lee et al., 2010). The C-terminal torque helix interacts with MotA to rotate the flagellar motor. Although high resolution structures of purified proteins have provided good evidence for the mechanism of torque generation, we can only generate models using these structures. We also do not gain a full understanding of this mechanism because often information is lost through harsh purification methods when extracting proteins. Purifying these proteins also does not provide us with an overview of its location and interaction with other proteins as a complex as a part of a large macromolecular structure. Therefore, we need to think of alternative methods to study macromolecular structures to gain a full understanding of the biological complex.

2.2.3 Cryo-electron tomography as a tool to study macromolecular complexes *in situ* (limitations)

To gain a better structural understanding of the mechanism of rotation in the flagellar motor *in situ* usually cryo-electron tomography and subtomogram averaging (STA) are used. Cryo-electron tomography and STA are important tools for studying the flagellar motor because they provide information about the overall architecture of the motor and location of proteins in the macromolecular machine. Both cryo-electron tomography and STA together have provided evidence for the evolutionary diversity in flagellar motor architecture between different species (Beeby et al., 2016; Carroll et al., 2020; Chaban et al., 2018; Chen et al., 2011). These tools have also been important for location protein structures using deletion assays (section 1.6).

To understand the core structure of the flagellar motor and how it generates torque, cryo-electron tomography and STA serves as a tool to visualise the structure of the whole stator ring with the intact basal body including the C-ring which gives structural evidence of this mechanism of torque generation. One limitation of studying stators and C-ring is the low-resolution structure STA provides compared to Single Particle Analysis. Using STA, we cannot visualise pentameric stators or the torque helix of FliG. Although, STA has been useful for providing a wider context to these protein structures we need a higher resolution *in situ* structure of the flagellar motor to understand how the flagellar motor produces torque.

2.2.4 Using minicells in combination with Single Particle Analysis to provide a higher resolution flagellar motor structure

The flagellar motor has many moving parts and proteins embedded in the membrane which make it difficult to study the structure of the complex beyond a certain resolution. Cryo-electron tomography and STA have provided structures of resolution between 16 to 18 Å-resolution and purified protein complexes of the bacterium flagellum using SPA has provided higher resolution structures (between 2 to 4 Å-resolution) but do not provide information about dynamic components such as stator units working against the C-ring (Abrusci et al., 2013; Chang et al., 2019; Deme et al., 2020; Santiveri et al., 2020; Tachiyama et al., 2021). We are therefore limited to the knowledge that can be achieved by both techniques. For this reason, we pivoted towards SPA and used minicells as our sample to image the flagellar motor *in situ* to obtain a higher resolution structure. A minicell is essentially a bi-product of unregulated cell division. A minicell lacks most machinery for growth and division. Minicells contain cell organelles such as the RNA, protein, plasmids, membranes, peptidoglycan but they do not contain chromosome (Farley et al., 2016).

For cryo-electron microscopy, minicells are a good model system because it is thinner than a wild type cell therefore prevents multiple electrons scattering events. Minicells are smaller in size therefore would increase particle number per field of view, we will therefore have more particles to work with. Both thinner sample and increased number of particles should contribute to a higher resolution structure. Since minicells provide more particles per grid hole we can treat these grids as samples for single particle analysis to collect more particles in a smaller space of time. This allows us to aim for a higher resolution by collecting more particles, faster collection rate and collecting only at 0° as opposed to cryo-electron tomography where at higher tilt angles you lose resolution because of ice thickness.

2.2.5 *C. jejuni* minicells to study stator complexes *in situ*

Previous research has shown that stator units are made of a pentameric MotA and a dimeric MotB. We also know that MotA directly interacts with FliG to transfer torque to the rest of the flagellar motor (Deme et al., 2020; Kojima et al., 2008; Lee et al., 2010; Santiveri et al., 2020). To understand exactly how these proteins generate torque we must first solve the flagellar motor's structure to a resolution where we can see these pentameric stators inside the cell. We also need to know the number of FliG subunits to gain a full understanding of the stoichiometry between MotA and FliG to understand how they interact. We predominantly use *C. jejuni* as a model system to study the flagellar motor, this is because *C. jejuni* has one of the most complex flagellar motors and stator units are visible in *C. jejuni* because it is a high torque flagellar motor (Beeby et al., 2016) (section 1.9). The flagellar motor is located at the polar regions of *C. jejuni* which are the thinner regions of the cell, this makes it a good

model system to study the flagellar motor. By working with *C. jejuni* minicells we have even thinner and smaller cells which take us to higher resolution structures.

2.3 Aims

The aim of this project was to understand the interaction between stator units and the C-ring to get a better understanding of the mechanism of torque generation. I studied this mechanism using a novel *C. jejuni* minicell mutant developed in our lab. I used the minicell mutant to obtain a higher resolution structure of the flagellar motor then focused on the stator and C-ring to see if I can classify different conformational states of the stator unit. This provided us with a better understanding of how the stator unit interacts with FliG to generate torque.

2.4 Results

To gain a better understanding of how the flagellar motor generates torque and recruits novel proteins we looked at *C. jejuni*'s flagellar motor. We characterised *C. jejuni*'s flagellar motor in minicells by collecting an SPA dataset of these minicells and processing it in RELION to obtain a sub-nanometre global resolution structure of the motor. By processing this single particle dataset using signal subtraction and focused refinement we were able to resolve *C. jejuni*'s flagellar motor between 8 Å to 20 Å, an improvement from cryo-electron tomography where resolutions are limited to 30 Å to 40 Å. Multiple resolutions in the *C. jejuni* minicell flagellar motor structure are reported because different parts of the flagellar motor are resolved to different resolutions. Higher resolution complexes are found in the central and periplasmic regions of the flagellar motor whereas the resolution decreases in the cytoplasmic region where the proteins are more flexible.

2.4.1 *C. jejuni* minicells for Single Particle Analysis

2.4.1.1 Engineering the *C. jejuni* minicell strain

Here I briefly describe the work conducted by a postdoc in our lab, Dr. Eli Cohen (Imperial College London). He engineered the minicell strain, optimised the minicell purification protocol and froze grids which were used for data collection. Minicells are a bi-product of imperfect cell division. We can create minicells by introducing mutations that disrupt cell division machinery. In most cases, the Min system, which controls cell division, is disrupted. Mutations in MinD and MipZ are usually made in many bacteria which result in minicells (Farley et al., 2016; Thanbichler and Shapiro, 2006). *C. jejuni* does not have a Min system but it does have a MinD/MipZ ortholog called flhG. This can be mutated to make minicells in *C. jejuni*. *flhG* is also interesting because in *C. jejuni* it regulates the number of flagella per cell (Balaban and Hendrixson, 2011). Therefore, by mutating *flhG,* you not only get minicells, but hyperflagellated minicells with many flagella per cell. This is useful because we could image multiple flagella, hence multiple motors, in a single field of view. They concluded that by isolating *C. jejuni* Δ*flhG* minicells we can have more cells per hole on the grid as opposed to one cell per hole. *C. jejuni* Δ*flhG* minicells are hyperflagellated, which means more than one motor per cell. Both number of cells per hole and number of flagellar motors per cell would vastly increase particle number and provide a high-resolution structure.

To isolate *C. jejuni* minicells from whole cells, Eli knocked out *flaA* and *flaB* which make up the filament. This was important to separate minicells from whole cells during centrifugation since

filaments are heavily glycosylated and longer than *C. jejuni*'s cell body (Cohen et al., 2020; Ewing et al., 2009; Inoue et al., 2018). By deleting the glycosylated filaments, the whole cells sediment much faster and allows for a larger separated distance between minicells and whole cells based on their density (Sharpe, 1988).

2.4.1.2 Preparing minicells for SPA data collection

Eli conducted the sample preparation for this dataset. He first grew around ten MH/agar plates of minicells (*C. jejuni* Δ*flhG* Δ*flaAB*). Once the cells grew, he washed the cells off the plate using MH media. The minicells were separated from wild type cells by multiple rounds of centrifugation until only minicells were remaining. He then concentrated the minicells using centrifugation and froze the cells on cryo-EM grids. He screened these grids which showed that in comparison to wild type cells (Figure 2.2 a, b), minicells (Figure 2.2 c, d) are indeed much smaller and thinner. Grids with wild type cells had one cell per hole whereas grids with minicells had around 10 cells per hole.

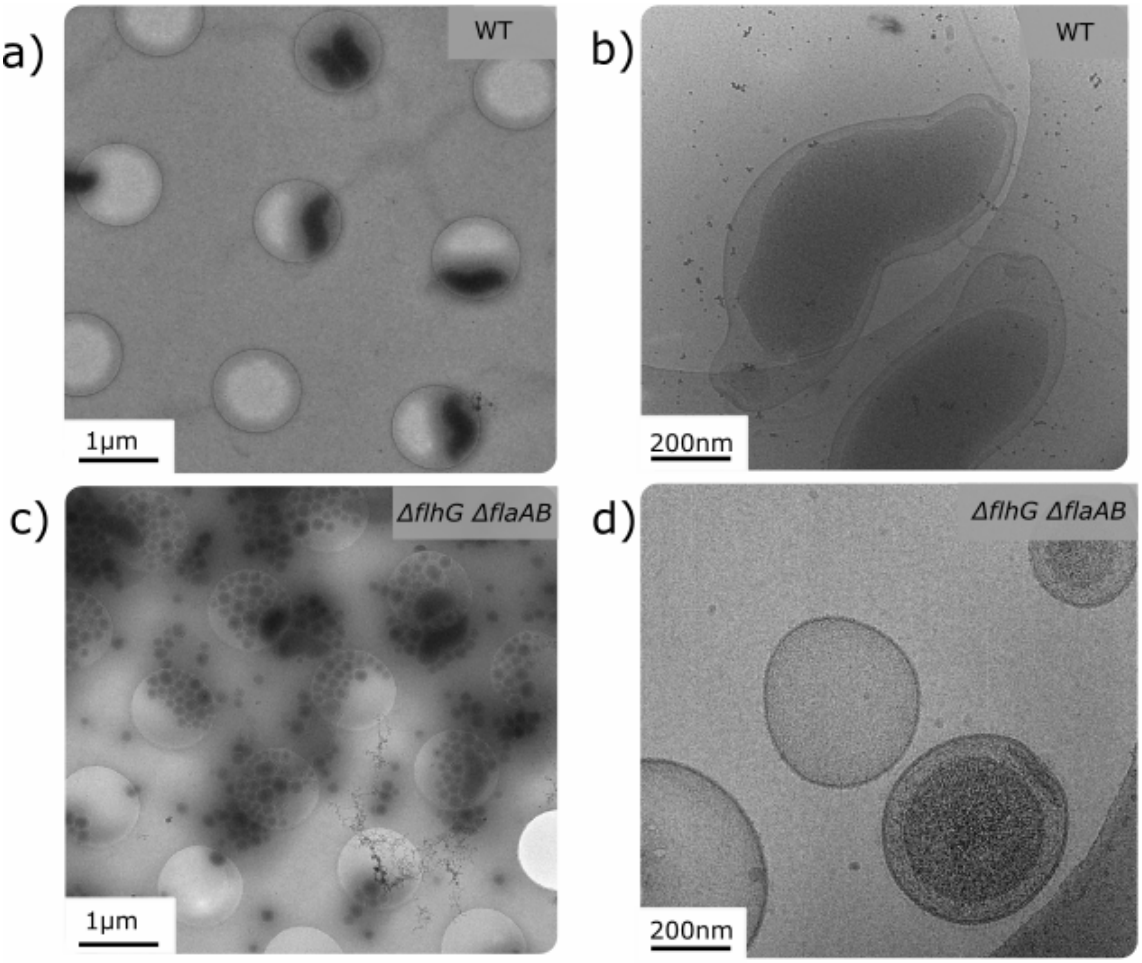


Figure 2.2 Comparison of *C. jejuni* wild type cell versus *C. jejuni* Δ*flhG* Δ*flaAB* minicells. a) A low magnification image showing wild type *C. jejuni* cells on a grid used for cryo-electron microscopy. Each grid hole accommodates 1 to 2 *C. jejuni* cells b) A higher magnification image of a *C. jejuni* wild type cell on a grid for cryo-electron microscopy. c) A low magnification image of *C. jejuni* minicells on a grid. Each grid hole can accomadate over

10 minicells per grid hole. d) A higher magnification image of minicells. Data in a) and b) Collected by Eli Cohen and Trishant Umrekar (Imperial College London). Data in c) and d) collected by Andrea Nans (the Francis Crick Institute).

2.4.1.3 Processing the *C. jejuni* minicell dataset in RELION

The *C. jejuni* flagellar motor structure was solved to 13.96 Å resolution using the minicell dataset collected by SPA. Post-processing was performed by a previous PhD student in our lab Tina Drobnič which resulted in a flagellar motor structure with a global resolution of 9.4 Å.

Wild type *C. jejuni* cells are large and accommodate one cell per hole (Figure 2.3 a). The use of minicells allowed us to collect more flagellar motors to increase particle number and provided a thinner specimen for imaging (Figure 2.3 b). As a result, we could collect data at high-throughput and the final structure was much higher resolution compared to a subtomogram average of the flagellar motor. The minicell dataset was collected by Dr. Andrea Nans at the Francis Crick institute. Coordinates from micrographs were picked by lab members Tina, Eli and I (Figure 2.3 c). The particles picked were combined in RELION 3.1 (Scheres, 2012). In 2D classification we could already observe major features such as the C-ring, flagellar type III secretion system and basal disk (Figure 2.3 d). I selected 2D classes of the flagellar motor and removed the junk classes which focused mainly on the membrane. The chosen particles then went through 3D classification and refinement with C17 symmetry imposed on the dataset because *C. jejuni* is 17-fold symmetric in the proximal and medial ring regions (Chaban et al., 2018). 3D classification with C17 symmetry imposed resulted in in whole-motor reconstruction from 27164 particles. RELION estimated the global resolution to be 13.9683 Å after 3D refinement but the cytoplasmic regions of the motor were restricted to 20 Å (Figure 2.3 e). This was a major improvement from cryo-electron tomography structure of *C. jejuni*'s flagellar motor which had an estimated resolution of 30-40 Å (Beeby et al., 2016). All 17 stator units could be observed which provided a starting point for further refinement of stator units (Figure 2.3 f, i). Figure 2.3 (g) highlights the core flagellar motor structures; these can be compared to our first 3D refined single particle structure of *C. jejuni*'s flagellar motor (Figure 2.3 h) which resolves a number of these proteins to a higher resolution.

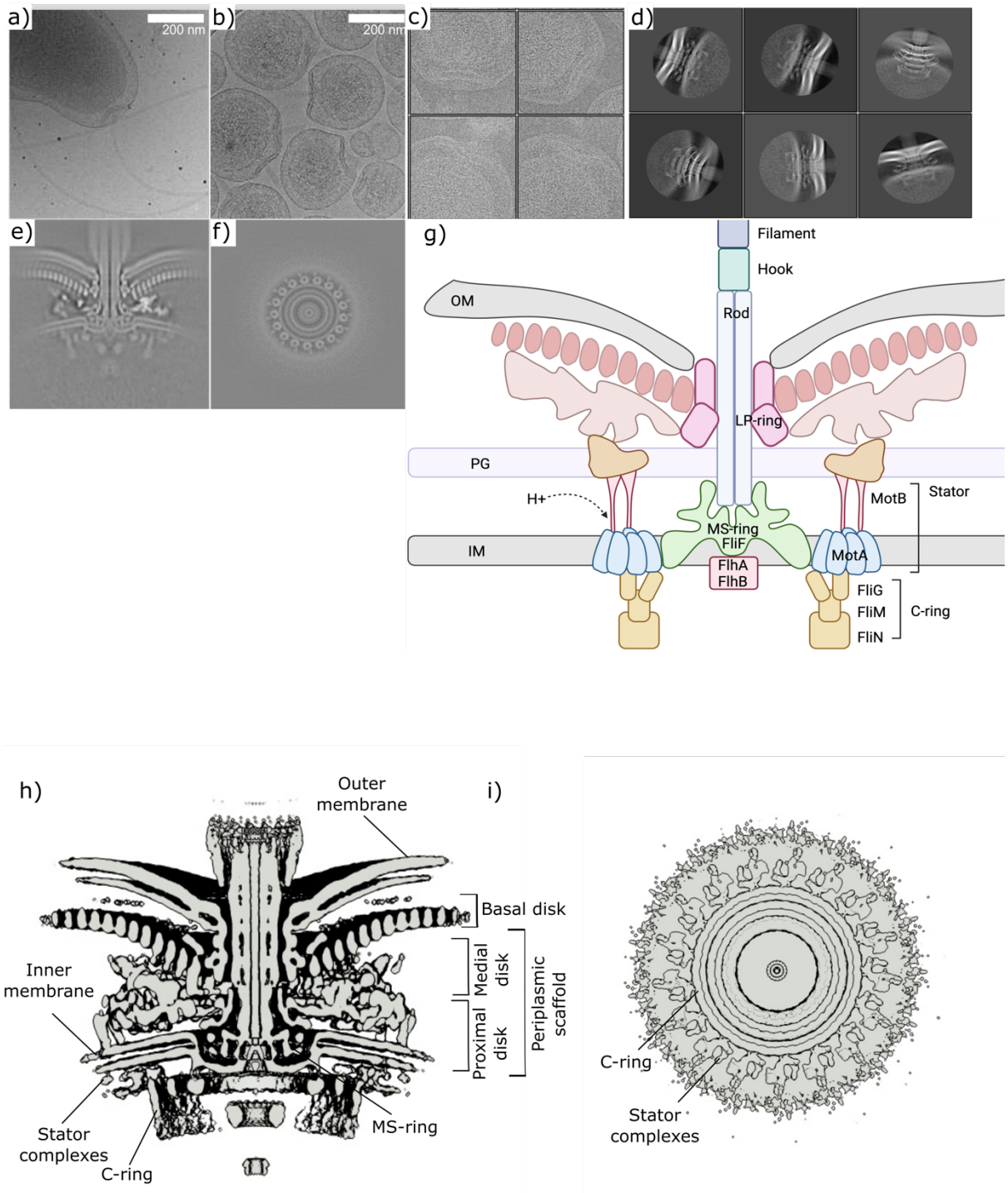


Figure 2.3 Single Particle Analysis work flow processing the minicell dataset results in higher resolution flagellar motor. a) A micrograph of minicells used for picking flagellar motors, these coordinates are then used to extract particles. b) Picked particles are then entered in 2D classifcation c) 2D classification averages showed structures previously not observed in flagellar motor subtomogram averages. d) Structure of *C. jejuni* flagellar motor after 3D classification and refinement with imposed C17 symmetry is at an estimated resolution of 9.4 Å. f) The whole motor structure shows very evident stator units. g) A cartoon highlighting core components in C. jejuni's flagellar

motor. h) 3D classified and refined structure from (d) shown through an isosurface in greyscale using ChimeraX. i) The same isosurface shown in (h) but from the Y/Z axis showing stator units attached to the C-ring.

The whole flagellar motor structure provided sufficient resolution to decipher protein structures (Figure 2.4 a) including pentameric stator units (Figure 2.4 b). To better understand the flagellar torque-generation machinery we performed focussed refinement of the stator complexes and the outer edge of the periplasmic scaffold enabling us to resolve the pentameric structure of MotA contacting the C-ring. By adding a lathe mask for signal subtraction and focused refinement we could focus alignment on the stator ring (Figure 2.4 c, d). In RELION this provided a final resolution of ~19Å (Figure 2.4 e, f). The isosurface of the stator ring provided sufficient signal of pentameric stator units which to our knowledge is the first *in situ* structure of the stator ring (Figure 2.4 g, h).

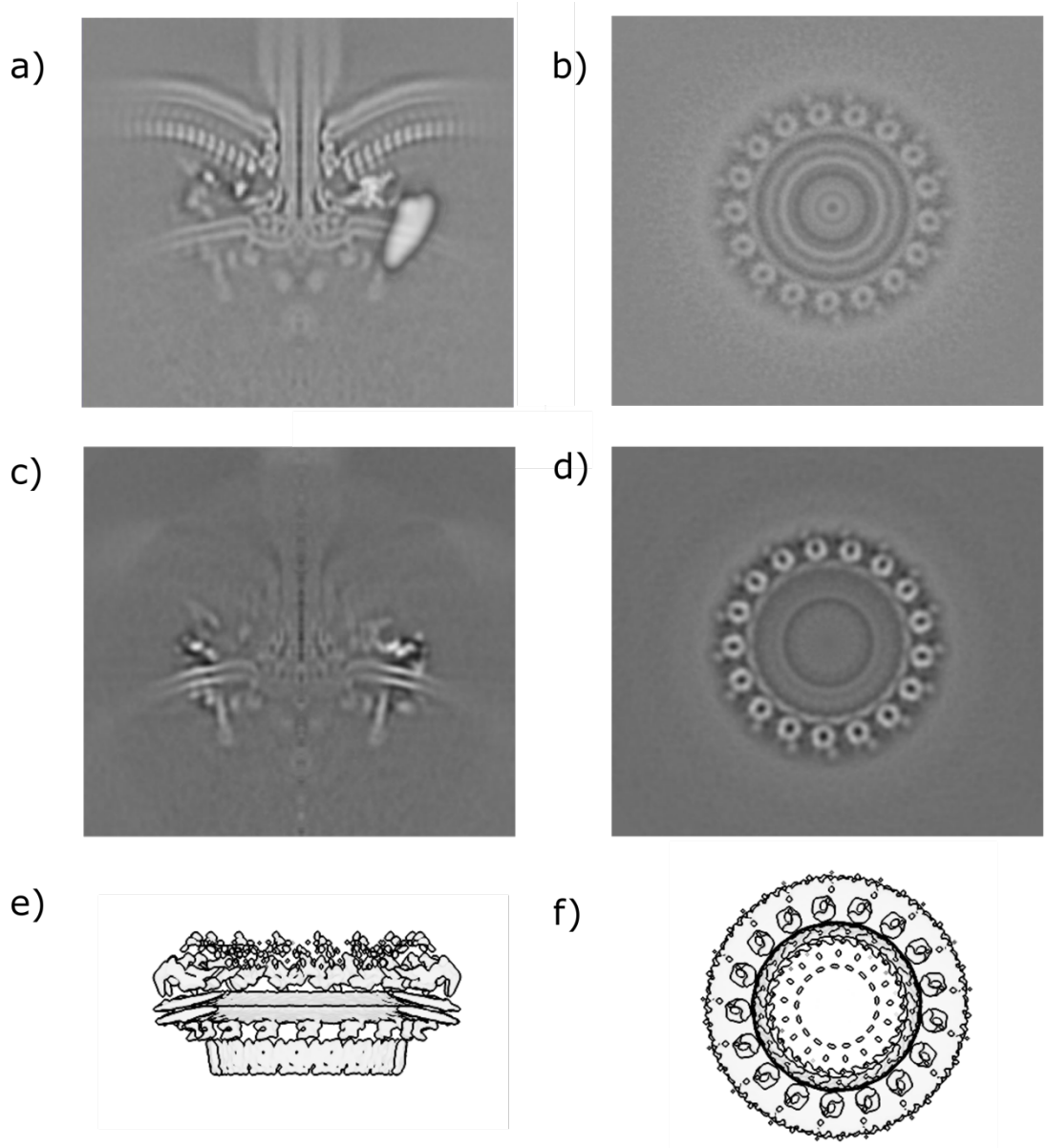


Figure 2.4 Signal subtraction and focused refinement using a lathe mask around the stator and C-ring improves resolution of pentameric stator units. a) 3D refined structure with a lathe mask in white imposed on the stator and C-ring. b) Stator ring before signal subtraction and focused refinement. c) 3D refined structure of the flagellar motor after signals subtraction and refinement d) Signal subtracted and focused refined structure of the stator highlighting pentameric stator units. e) isosurface of the flagellar motor after signal subtraction f) Isosurface of the stator ring after signal subtraction.

2.4.1.4 Local reconstruction to decipher different conformations of one stator unit

Local reconstruction using RELION in the Scipion software did not directly provide different conformational states of MotA rotating. After local reconstruction and particle extraction, the particles were classified using RELION 3D Classification in Scipion. Particles were divided between two classes. In both classes the position of MotA does not change, this suggests that MotA mostly remains in one conformation (Figure 2.5). In the C17 symmetric structure of stators, the C-ring obtains C17 symmetry as an artefact of imposing symmetry on the structure (Figure 2.5, green arrow). This artefact is still present in the localised reconstructed C1 structure of the stator ring. Interestingly, the first class presented two densities around the stator unit (Figure 2.5 red arrow). In the second class the density on the left disappears (Figure 2.5, white-red arrow), this could indirectly suggest conformational changes in the stator unit which displaces this protein. Further classification of both refined structures did not reveal more information about conformational states of stator units.

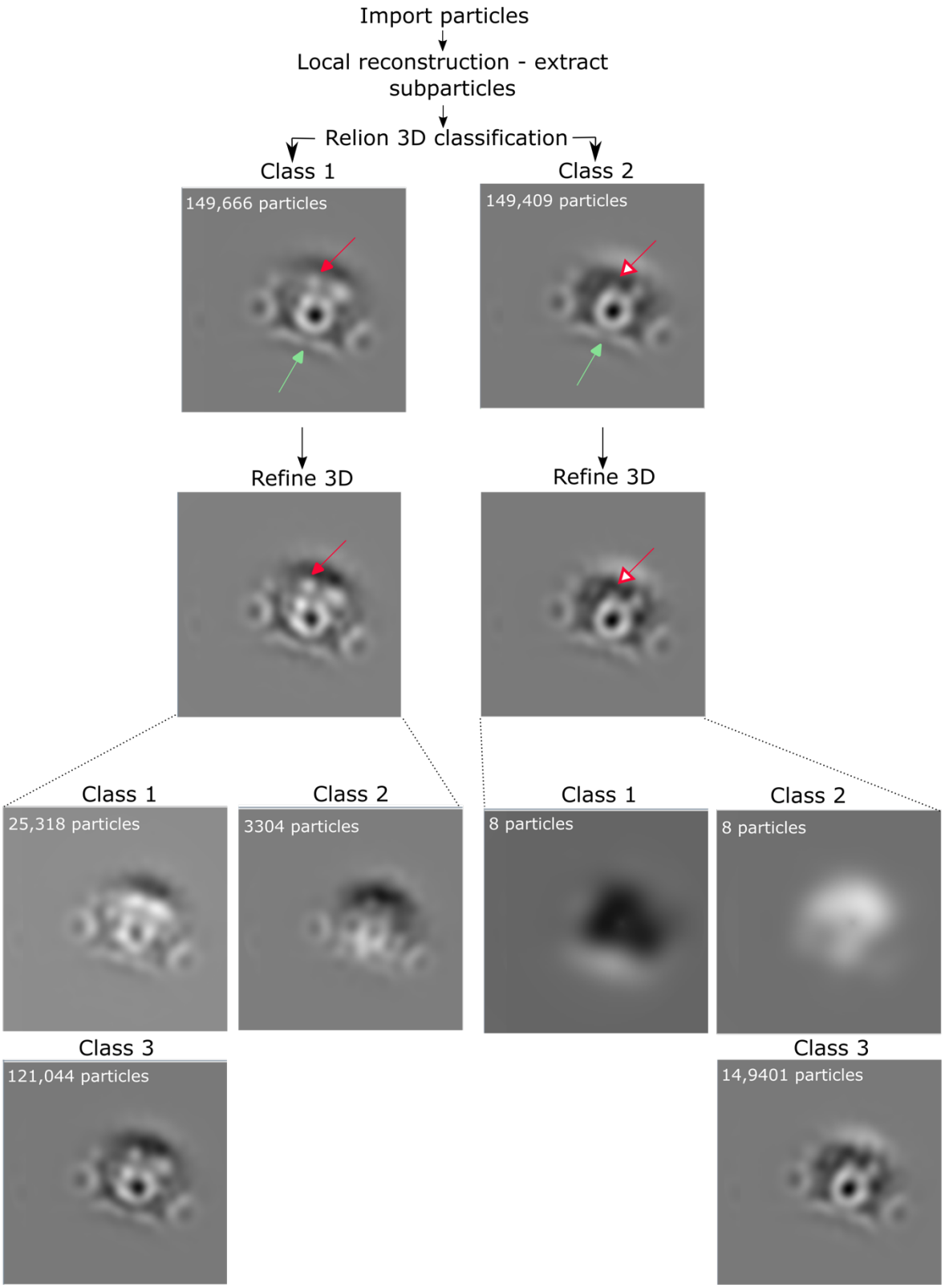


Figure 2.5 Localised reconstruction hints differences in conformational states of a stator unit. In localised reconstruction particles are first imported then sub-particles are extracted, so each particle is independent of each

other. After conducting 3D classification, the 2 classes did not show variation in the conformational states of stator units, but missing densities were observed in Class 1 which surround stator units (red arrow in class1 versus red/white arrow in class 2), these protein densities were observed in Class 2. Class 1 and Class 2 were refined and re-classified to check for different conformational states in stator units. Of 3 classes for each refinement one class provided a stator unit of the same conformation but the other two classes were noise.

I performed local reconstruction and classified particles into three classes (Figure 2.6). This provided one class of a single pentameric stator unit. This structure was refined and further classified. The final classification and refinement resulted in low resolution noisy stator unit structures which meant it was difficult to search for differences between each class.

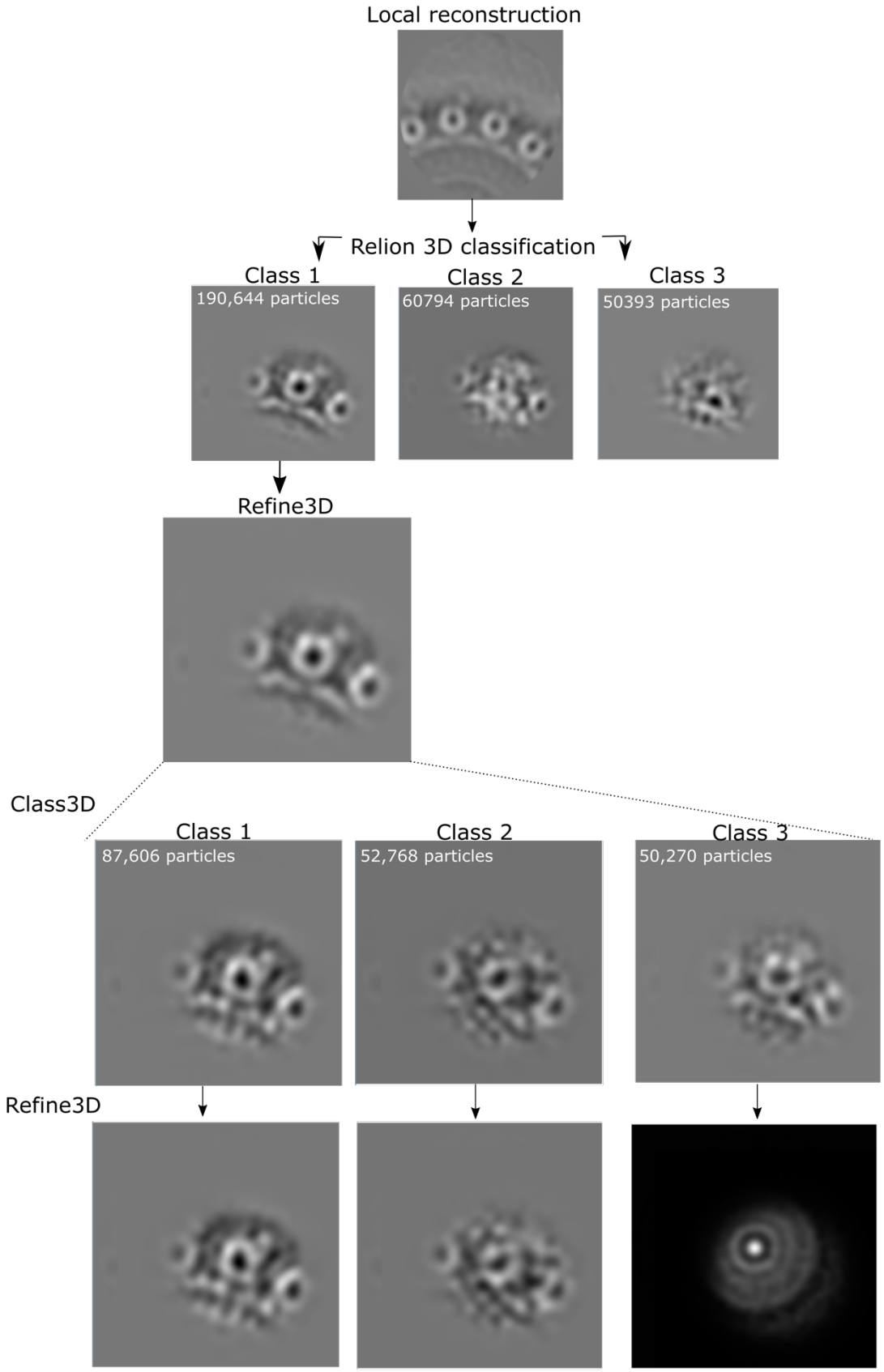


Figure 2.6 Changes in classification workflow did not provide a higher resolution stator unit structure or different conformational states of stator units provided some indication of C-ring spokes. Local reconstruction was

conducted to focus on a single stator unit to classify. Classification provided one good class and two noisy classes which lacked pentameric stator unit features. I refined the first class and conducted another 3D classification. Each class looked noisy with lowered resolution stator unit. C-ring showed spokes but due to high noise the features are not reliable.

2.4.1.5 Processing in CryoSPARC to improve the resolution of pentameric stator units

I used CryoSPARC to further process the stator ring in attempt to obtain a higher resolution structure. I imported signal subtracted, refined particles from RELION 3.1 into CryoSPARC (Punjani et al., 2017). Homogeneous refinement revealed a ring of pentameric stator units with an estimated resolution of 15.95 Å (Figure 2.7 a, b, d, e) according to its FSC graph (Figure 2.7 c). The clear pentameric structure of each MotA subunit in the ring meant that we could model the single particle analysis structure of *C. jejuni* MotA (Figure f, g) solved by Santiveri *et al* (Santiveri et al., 2020). Other protein structures around MotA became more apparent. This was novel since previously we were limited by resolution *in situ* using cryo-electron tomography therefore these structures were not previously visible. The novel densities are located under MotA in the cytoplasmic region and are at the same radius as the periplasmic cage. The cytoplasmic densities could directly link to form a continuous lattice around MotA to keep it statically in place (Drobnič et al., 2023).

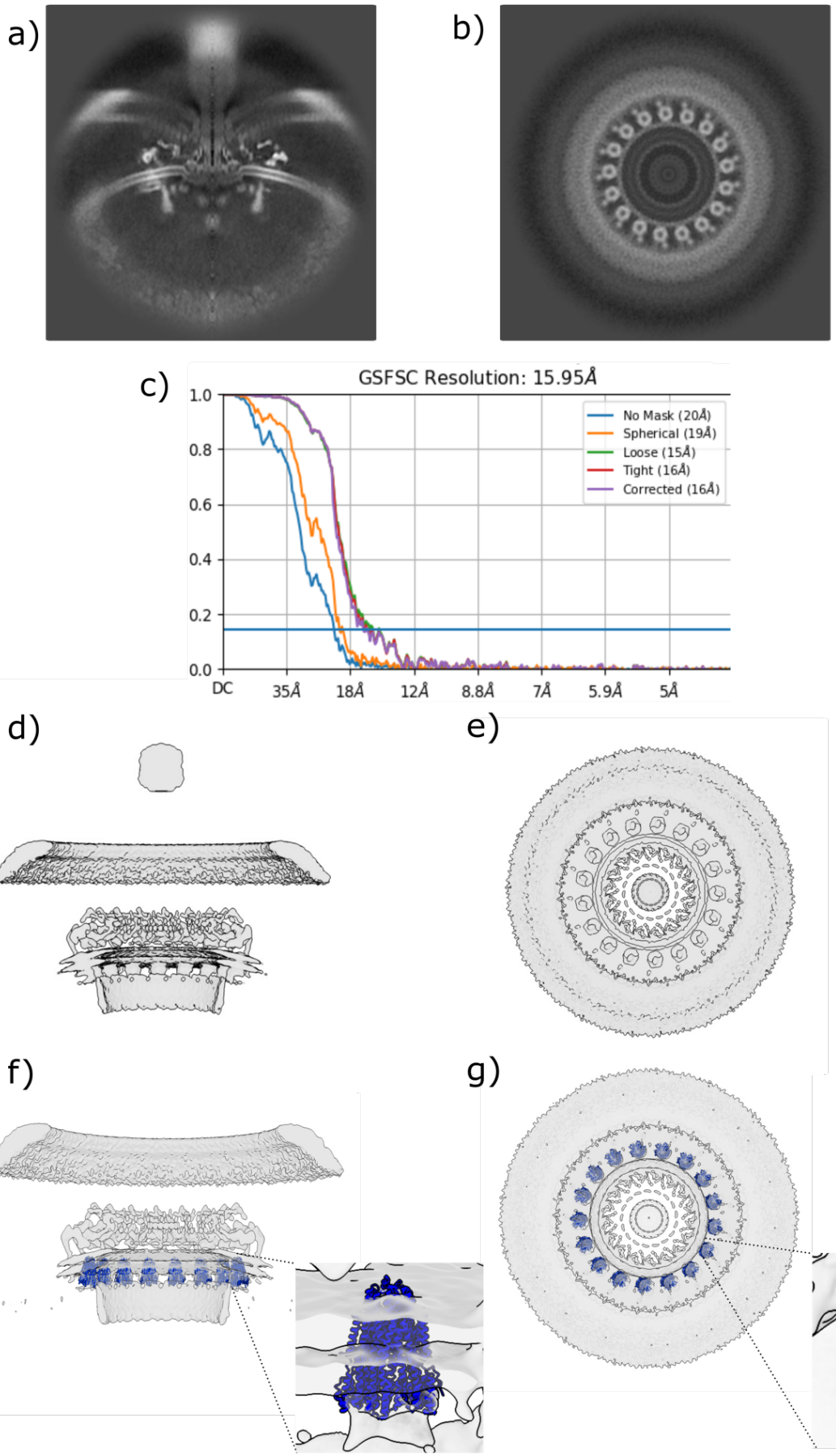

a)
b)
c)
GSFSC Resolution: 15.95Å
No Mask (20Å)
Spherical (19Å)
Loose (15Å)
Tight (16Å)
Corrected (16Å)
1.0
0.8
0.6
0.4
0.2
0.0
DC
35Å
18Å
12Å
8.8Å
7Å
5.9Å
5Å
d)
e)
f)
g)

Figure 2.7 Homogeneous refinement of subtracted stator complexes reveal improved visibility of pentameric stators. a) Homogeneous refined structure of the flagellar motor using signal subtracted, refined particles from RELION 3.1. b) Stator ring after homogeneous refinement shows more pronounced pentameric stators. c) Global resolution of the map is estimated from FSC plot 19.72 Å as calculated in CryoSPARC.

The pentameric structure was more evident compared to the structure obtained from RELION 3.1. I imported the same mask used for signal subtraction in RELION 3.1 to CryoSPARC (Figure 2.8 a) shows first homogeneous refinement with the mask in white used for following runs (b) and (c). Homogeneous refinement of subtracted particles with this mask and C17 symmetry imposed resulted in pentameric stators of similar resolution with less focus on densities surrounding MotA (Figure 2.8 b). This homogeneous refinement was also performed with C1 symmetry which provided a lower resolution stator ring (Figure 2.8 c). This SPA volume was considered unreliable. As observed in these runs and previous runs it was challenging to revert a C17 structure to a C1 structure. To obtain a true C1 structure the initial processing must also be done in C1.

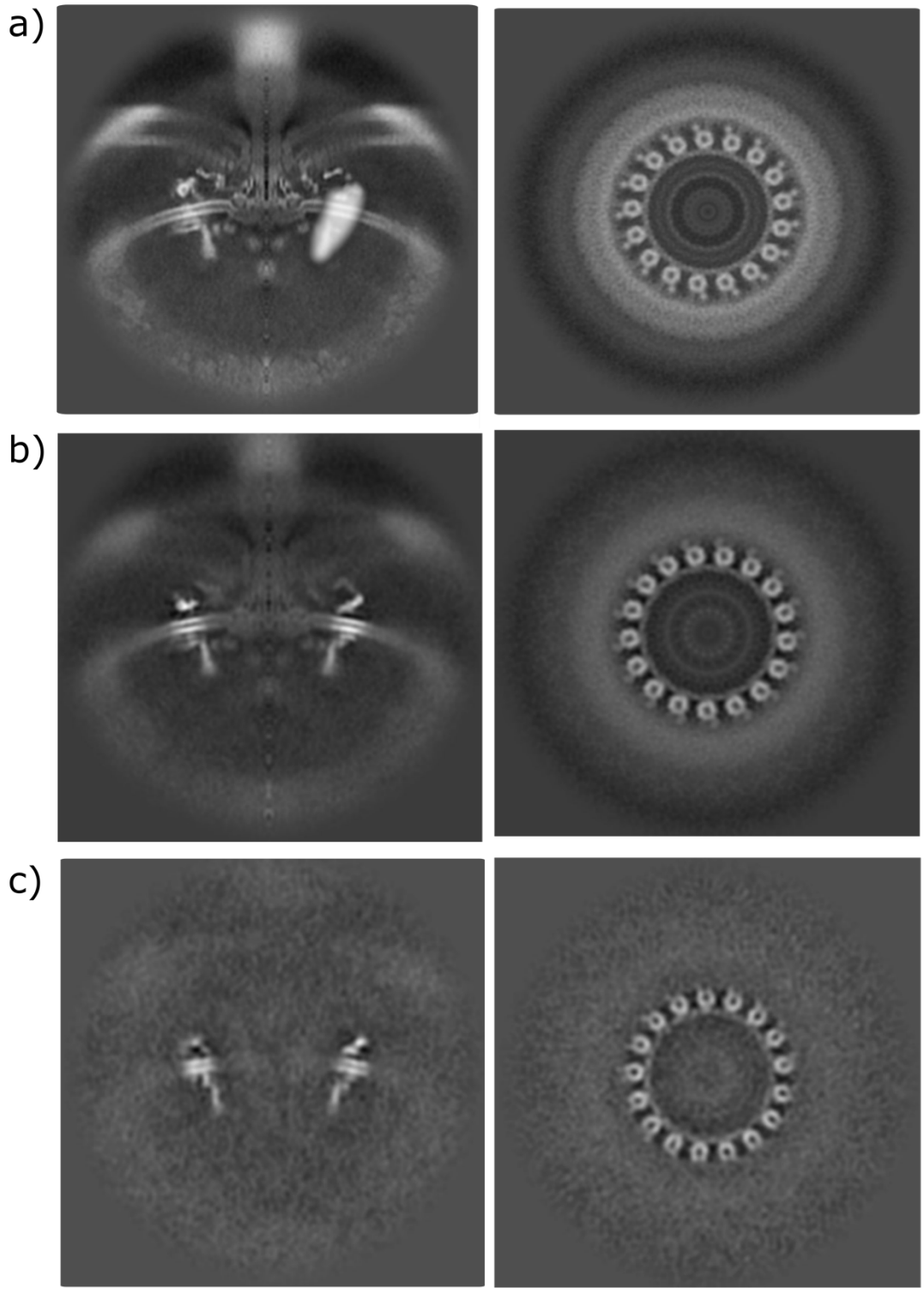


Figure 2.8 Masked alignment in CryoSPARC does not improve alignment. a) Homogeneous refined stator ring was re-aligned with the same lathe mask used in CryoSPARC which focused on the stator ring. b) The lathe mask focused on the stator ring shown in (a) and lowered signal of proteins surrounding the stator units, but the stator ring did not improve in resolution. c) The same job homogeneous refinement job in (b) was performed with C1 symmetry which did not reveal C-ring symmetry and lowered resolution of each stator unit.

2.4.1.6 Masking out a subset of stator units in CryoSPARC

Next, I attempted to mask out a stator unit to see if I could discern confirmations of one stator unit in CryoSPARC by allowing the stator unit to drive alignment as opposed to the whole stator ring. I made different lathe masks to segment out a small part of the C-ring and one to three stator units depending on the mask. In each mask stator units were visible, but the resolution remained the same or lowered in both XY view and YZ view the subtracted MotA and C-ring became less visible indicating problems in alignment (Figure 2.9 and 2.10).

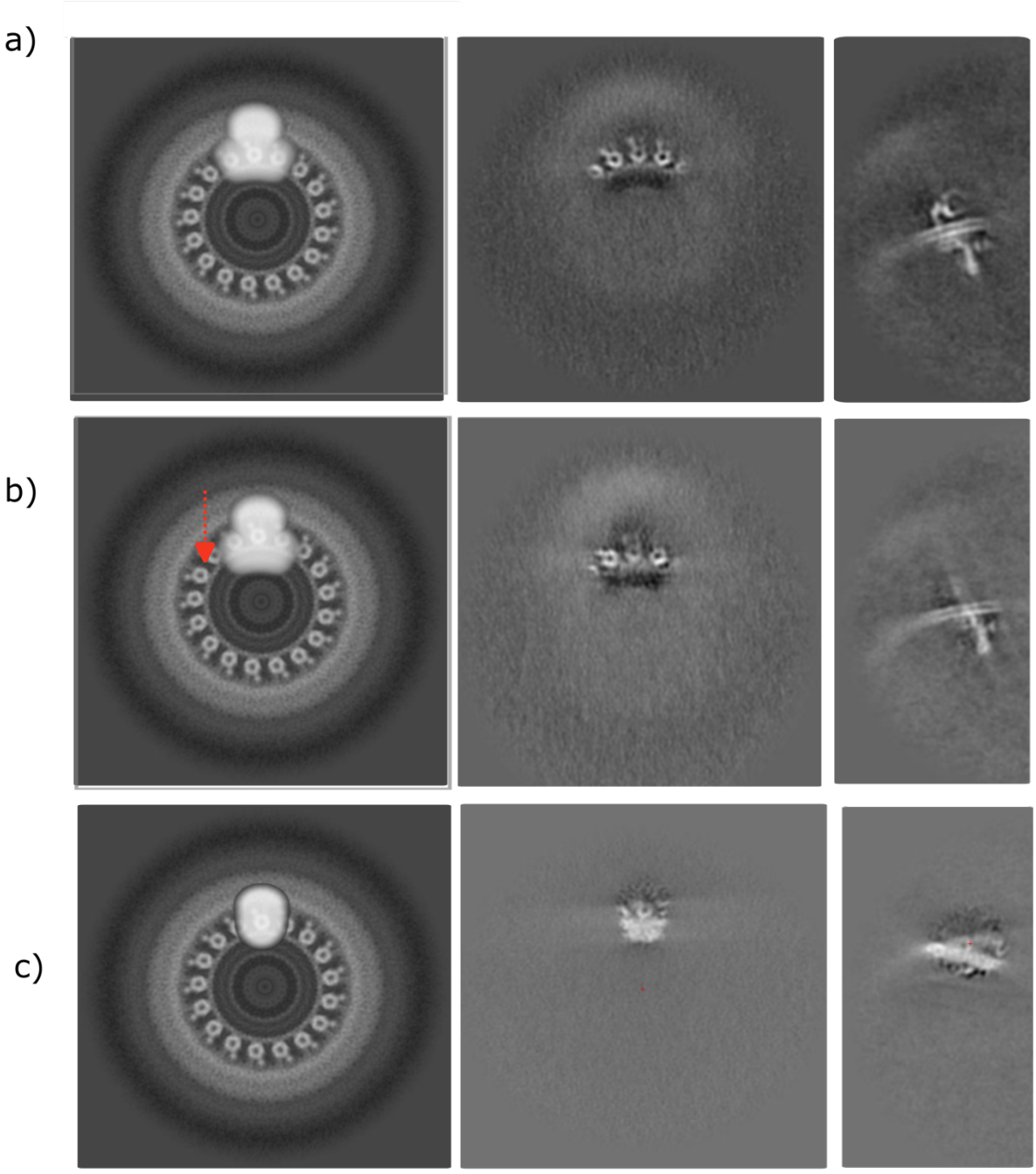


Figure 2.9 Masking out singular/range of stator units reduces alignment at C1 symmetry. a) Mask encompassing three whole stator units reduces alignment. b) Moving the mask used in (a) down to reduce the number of stator units and use the C-ring for alignment reduces the resolution further c) Focusing on a singular stator unit reduces resolution further which makes it difficult to derive different conformational states since stator units are flexible proteins and most likely present slightly different conformations.

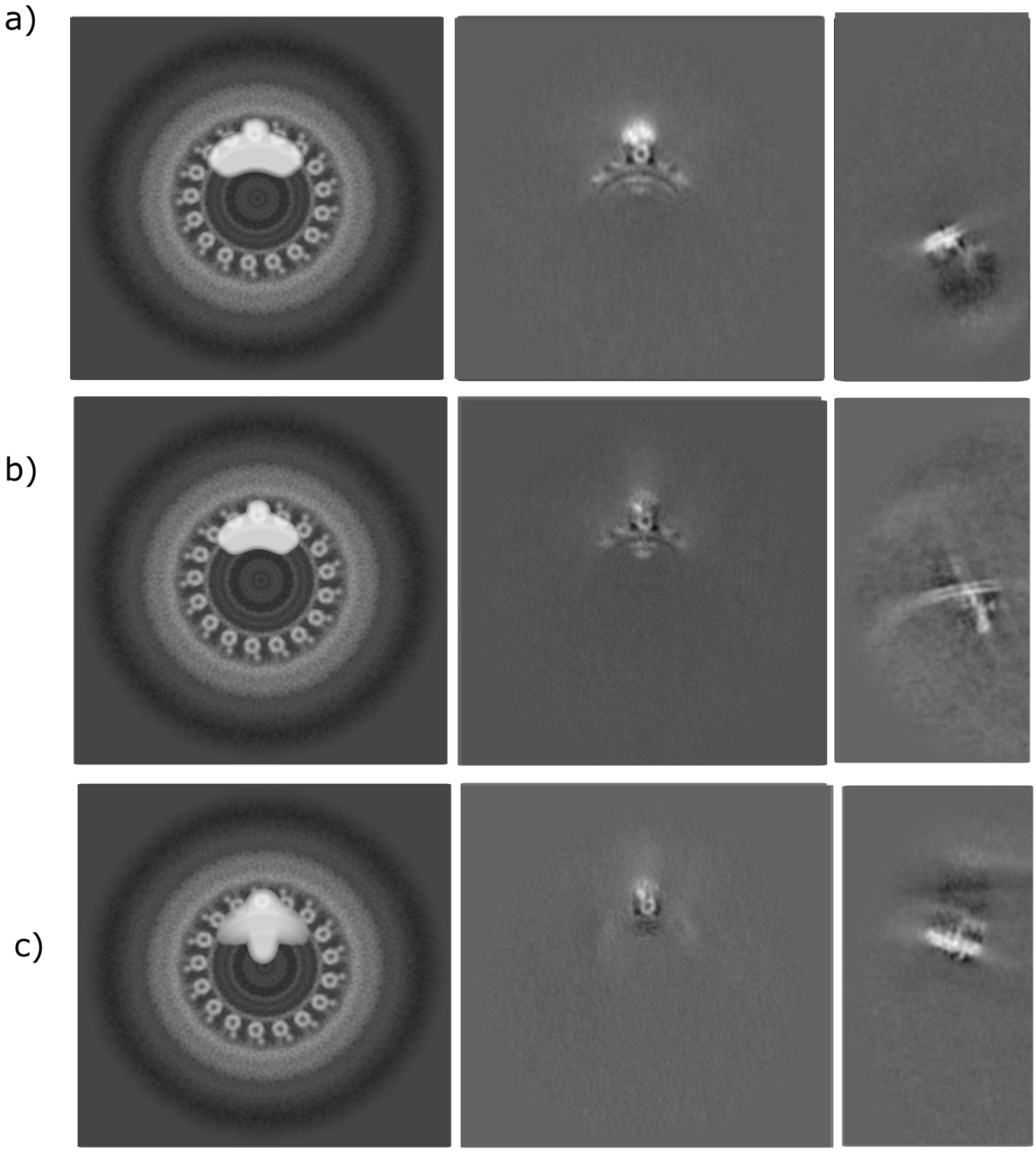


Figure 2.10 Mask encompassing part C-ring and one stator unit did not reveal C-ring spokes against a stator unit. a) Shows a mask encompassing one stator unit and part C-ring, in this density the alignment is driven by a density adjacent to a stator unit. Spokes in the C-ring were not visible and stator unit was not pentameric b) The mask was lowered to encompass more of the C-ring and less of the extra density around the stator unit. The C-ring spokes could not be deciphered, and the stator unit was of lower resolution compared to the starting model. c) Lastly, I attempted a different mask to encompass one stator unit which again aligned to the density adjacent to the stator unit suggesting it could be a more rigid structure to align to.

To investigate whether I could boost resolution even further, I used a mask that exactly encompasses part of the cytoplasmic regions of the motor for signal subtraction and focused refinement. I used ChimeraX to generate to the initial volume and used CryoSPARC to transform the volume to a mask and applied it to the initial subtracted volume (initial homogeneous refinement) to remove the densities around the membrane and the basal disk that were not the stator or C-ring (Figure 2.11 a, b, c). The result from this subtracted homogeneous refinement provided an artefactual non-pentameric ring of stators which did not comply to the biological stator unit structure (Figure 2.11 b). The subtracted cytoplasmic region of the motor in XY axis provided a clear subtracted structure of the C-ring and MotA (Figure 2.11 c), the estimated resolution was 13.19 Å which considering the structure is an over estimation. But an extra density was observed just under MotA which previously had not been observed. In the first subtracted homogeneous structure the area under MotA appears blurry merging the C-terminus of FliG and a smaller unknown density (Figure 2.11 d). After the second subtraction with a tighter mask, the density under MotA is more visible (Figure 2.11 (e) green arrow pointing to unknown density, red arrow pointing to MotA and C-ring). A summary of the processing steps used to process the minicell dataset using RELION, CryoSPARC and Scipion is shown in Figure 2.12.

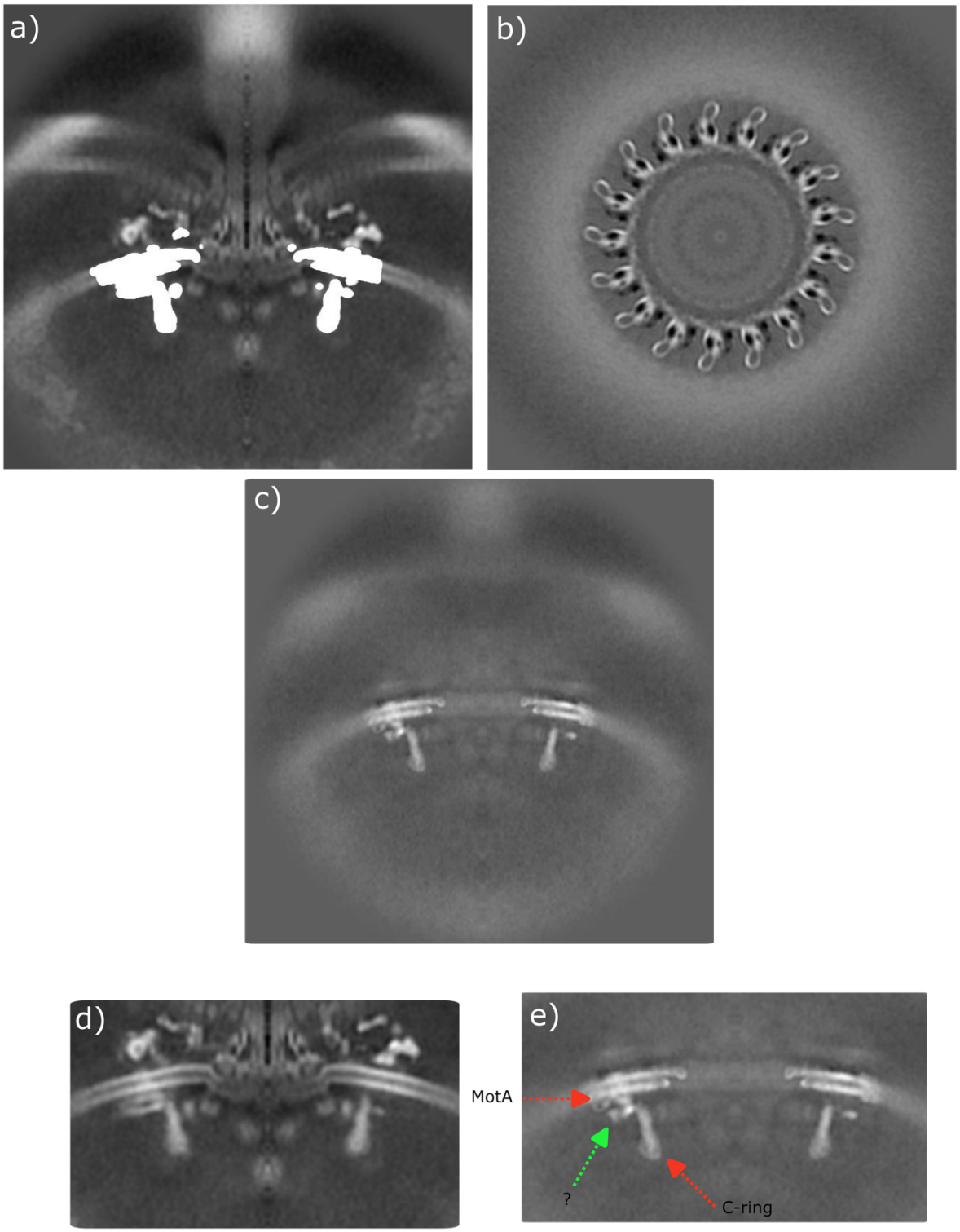
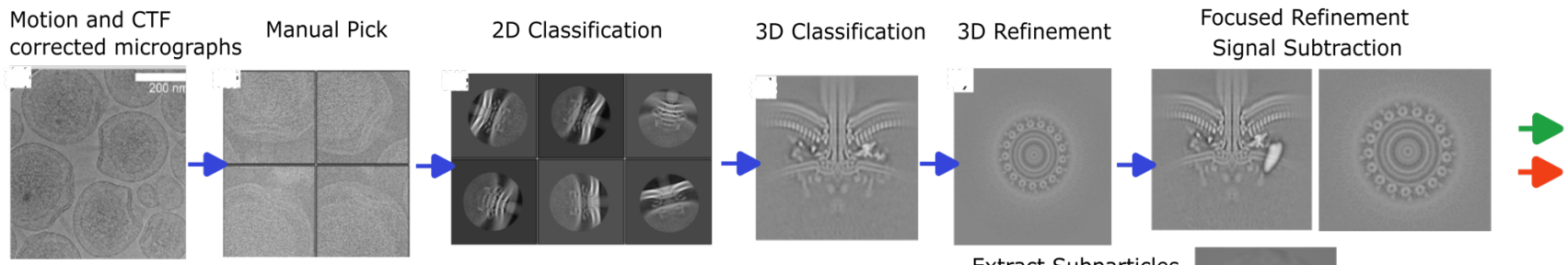
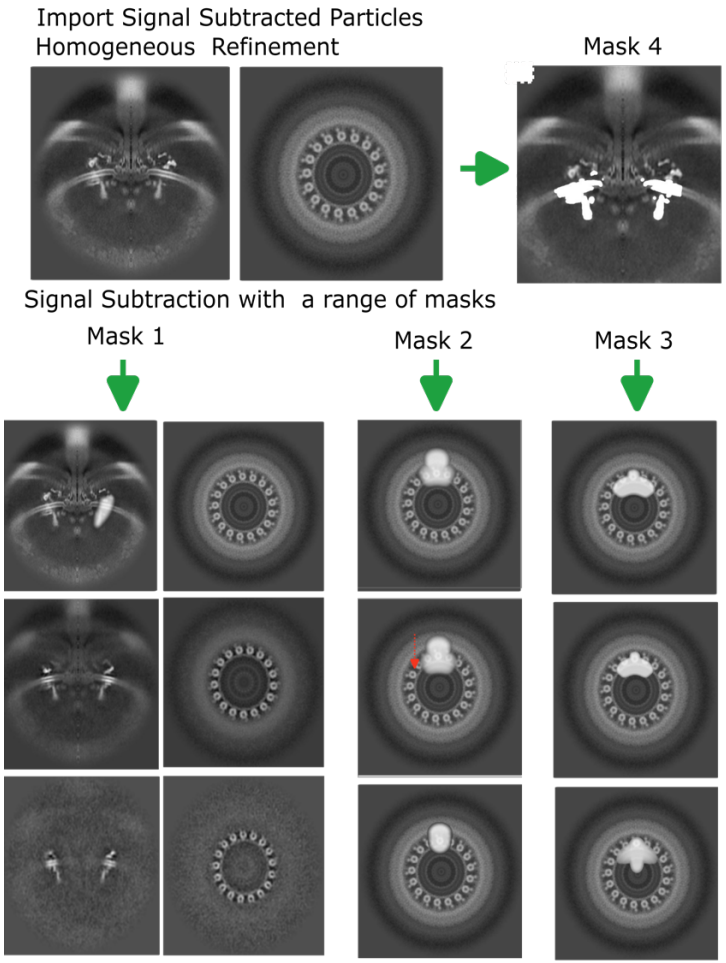


Figure 2.11 Homogeneous refinement and signal subtraction with a tighter mask reveals unknown density but also provides some artefactual data. a) Initial structure (homogeneous refinement and signal subtracted) with mask (highlighted in white). b) YZ axis stator ring showing artefactual ring and non-pentameric stators after signal subtraction. c) XY axis of stator unit and C-ring, signal subtracted structure d) Periplasmic and cytoplasmic region of flagellar motor e) Subtracted region of the flagellar motor, extra density highlighted with a green arrow.

RELION



Cryosparc



Scipion

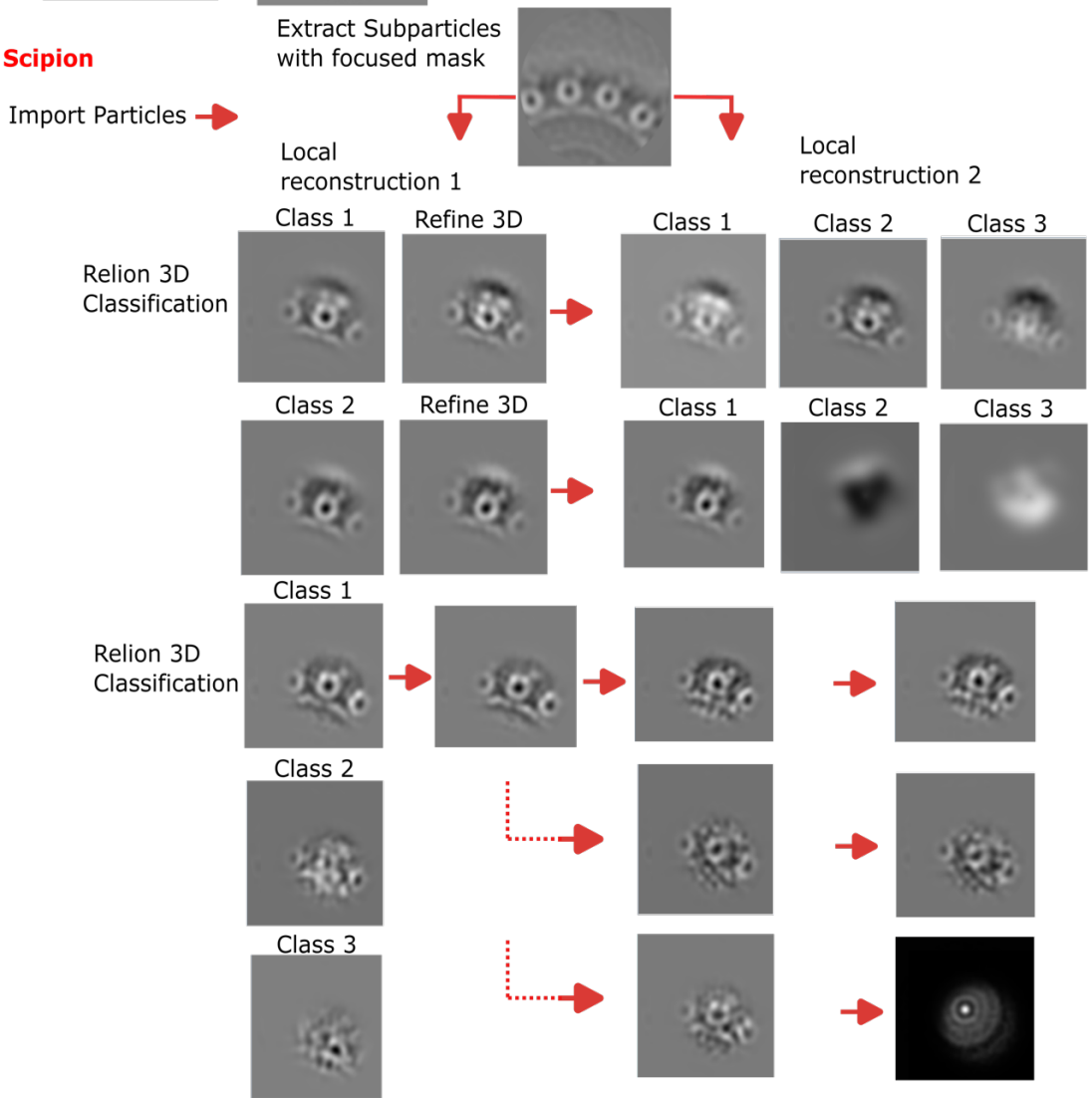


Figure 2.12 Overview of the overall processing pipeline. Stator complexes were processed in RELION, CryoSPARC and Scipion in attempt to find different conformational states of stator complexes.

2.5 Discussion

The low particle number obtained using cryo-electron tomography means we cannot collect enough particles for subtomogram averaging to obtain a higher resolution structure. In cryo-electron tomography we image one cell per hole. This means each tilt series acquired only contains one particle. The number of days to collect a typical dataset of 200 tomograms can range between 2 to 3 days since each tilt series collected takes around 20 minutes. To collect a dataset of tens of thousands of particles could easily take months and in most cases is not feasible. Although cryo-electron tomography has greatly improved its data collection software which improves stage-movement and as a result we can collect data as fast as 5 minutes per tilt series (Bouvette et al., 2021; Branon et al., 2018). This still does not fully allow for the number particles that usually we obtain by Single Particle Analysis to significantly increase resolution.

In our minicell dataset, the number of particles significantly increased because most cells were hyperflagellated due to the deletion of *flhG* and we could easily separate out the minicells by deleting the genes for the filament (*flaA* and *flaB*). Having almost 10 times more particles per grid hole because the cells are much smaller also means we increased particle number. Another important characteristic of the minicells is that although they were much smaller compared to wild type *C. jejuni* cells, the minicells assembled full flagellar motors and did not have any proteins missing as a part of the wild type flagellar motor structure. We could confirm this by comparing the *C. jejuni* minicell flagellar motor structure to the already solved *C. jejuni* wild type flagellar motor subtomogram average (Beeby et al., 2016). Another important aspect to consider was to check whether the flagellar motor in minicells rotate, since we wanted to not only study *C. jejuni*'s flagellar motor structure to a high resolution but also study the structural dynamics of the flagellar motor structure, including different conformational states of stator units. A post-doc in our lab Eli Cohen verified this by growing minicells with filaments and tagging it with maleimide, with this he could visualise filaments of the cells rotating. This experiment validated that we imaged active flagellar motors (data not shown).

We were able to process the minicell dataset to a global resolution of 9.9 Å. There were differences in resolution in different parts of the flagellar motor. The periplasmic region of the flagellar motor was further processed by a previous PhD student in our lab Tina Drobnič, she was able to solve the periplasmic ring to around 7 Å. The periplasmic region of the flagellar motor is a more rigid structure and mainly acts as scaffolding to maintain torque and movement of the flagellar motor (Drobnič et al., 2023). Particles could therefore align to each other without the issue of inherent flexibility of the structure. The periplasmic region, as Tina found, templates C17 symmetry which is why imposing C17 symmetry aligned the particles to solve the structure. We also know from previous *C. jejuni* flagellar

motor subtomogram averages that most of the motor is 17-fold symmetric, this information helped us process the minicell dataset.

With structures that are more flexible such as the stator units and C-ring which are constantly moving to generate torque, it was more difficult to align particles and solve complex interactions between stator units and the C-ring. By imposing C17 symmetry, the 17-fold symmetric stator ring became more apparent. By subtracting out the rest of the flagellar motor and focused refinement I was able to clearly show a pentameric stator ring. The atomic structure of *C.jejuni*'s MotA pentamer was already solved using cryo-electron microscopy (Santiveri et al., 2020). This structure was then used to dock into the stator ring (Figure 2.7). There were many attempts of solving other symmetries by members of the lab and I, but we were not able to obtain a full structure of the C1 symmetric flagellar motor. This could be due to the lack of top views leading to preferred orientation that already became apparent in the 2D classes. We could not collect top views for two reasons, the first being that the hook most likely drives alignment of the cell which means that in most cases the cell is orientated sideways and perpendicular to the rotation axis. One could collect a dataset of hookless minicells to allow for more cells in different orientations. A post doc, in our lab is currently working on this project. The next limitation is that the particles are embedded in the membrane inner and outer membrane of cells. To collect top and bottom views the electrons would have had to pass through the thickest part of the cell which usually leads to more elastically scattered electrons by the cytoplasm. For the current dataset oblique views and imposed C17 symmetry was used to understand this anisotropic structure.

This dataset was used to focus on stator units with the idea that we could classify out different conformational states of stator units against the C-ring. A mask encompassing the stator units and part of the periplasmic region including MotB was used for signal subtraction and focused by alignment (Figure 2.4). By focusing alignment on the stator ring and imposing C17 symmetry the 17-fold pentameric stators became more prominent (Figure 2.4). The final resolution according to RELION 3.1 was around 19 Å. This was the first time to our knowledge we saw pentameric stators *in situ*. Although I attempted to a higher resolution structure of the stator ring, the flexibility in stator units and C-ring limited its resolution.

To tease out different conformational states of the stator unit I used localised reconstruction. In localised reconstruction each particle has sub-particles which contain information about the original orientation of each particle in its original image (Abrishami et al., 2021; Ilca et al., 2015). Local reconstruction does not require a high-resolution structure which was beneficial for processing this dataset which presented a range of different resolutions. Each sub-particle is extracted and treated independently from one another and can then be used for classification and refinement. This method is useful for studying symmetry mismatch components and flexible components which limit the resolution of the final

structure since stator units when averaged and C17 symmetrized will take on the most predominant conformation available. Local reconstruction focused on one to three stator units. After local reconstruction and extraction of particles I ran 3D classification using a mask on one stator only. In each class MotA was in the same conformation. After further refinement each class showed slight differences between classes. Once class had slightly better resolution and more particles. Although the conformational state of the stator unit remained the same, the first class had two densities surrounding the stator unit whereas the second class had one density surrounding the stator unit. This might be an indirect indication of stator unit changing conformational states which displaces this unknown protein. Previous studies have identified proteins in the cytoplasmic region in *C. jejuni*'s flagellar motor but their exact location is yet unidentified (Gao et al., 2014). Even though local reconstruction classification and refinement was run in C1 symmetry, the final structure did not look so different from the C17 symmetric stator ring including dents in the C-ring which were caused by imposing C17 symmetry even though the C-ring has a different symmetry. The initial C17 subtracted and focused structure could not be changed back to C1.

Another reason for the lack of different conformations could be that each stator spends most its time in one conformation. The cytoplasmic region of the stator against the torque helix of FliG in the C-ring which means that when collecting data very few stator units would be in a different conformation. A different method of local reconstruction would have been doing local reconstruction on the centre of one stator unit to edge of one stator unit as opposed to the centre of the stator ring to the centre of one stator unit, however the lack of resolution suggests it would have failed to acquire different conformational states.

Since I could not decipher conformational states using localised reconstruction in Scipion. I attempted to use CryoSPARC to increase the resolution of the stator ring and then classify stator units in CryoSPARC. I imported the original signal subtracted and focused dataset into CryoSPARC. I conducted homogeneous refinement with this dataset and found that the pentameric stator ring became more apparent (Figure 2.7 b) and the C-ring did not have small dents as observed in the RELION structure (Figure 2.4 f). The FSC graph provided a resolution of 19.72 Å without a mask and 9.9 Å with a tight mask which is the highest *in situ* resolution of stator units achieved as per our knowledge. Using this model, I was able to fit in the single particle pentameric stator units previously solved by Santiveri *et al*. By fitting each pentamer, the structure highlighted that additional densities around the stator were also present these are novel and have not previously been observed because of the low resolution subtomogram averaged previously obtained. We are yet to characterise many surrounding structures but one candidate FlgX that is known to stabilise MotA I have characterised further in Chapter 3.

To improve alignment further, I used the same mask for CryoSPARC as I had used in RELION which encompassed stator units and a small part of the periplasmic region. In the previous homogeneous refinement, there were still areas of the inner and outer membrane and features in the rest of the motor such as rod and basal body that were still somewhat visible and possibly driving alignment (Figure 2.8). The final subtracted structure showed that the subtraction itself was quite successful, highlighting only areas of the C-ring and stator unit and removing any other additional structures including proteins surrounding MotA, here we see that the stator unit the mask is tight and also does not improve the resolution (Figure 2.8 a, b) in the Y/Z axis. The same job was also conducted with C1 symmetry to check whether imposing C1 symmetry in CryoSPARC would provide a true C1 symmetric structure (Figure 2.8 c). However, the final structure had more noise and a lower resolution structure, I could not validate whether it was truly a C1 structure.

To investigate the interaction between a stator unit and the C-ring, I made a mask that encompassed one stator unit and part of the C-ring this would use the single stator unit to drive alignment. We hypothesized that aligning to one stator and part of the C-ring and imposing C1 symmetry would show C-ring spokes interacting with one stator. Although I tried a range of masks (Figure 2.9 and Figure 2.10) the stator unit significantly decreased in resolution and increased in noise and spokes were not observed in the C-ring. This again is because of the inherent flexibility of the proteins and the inability of changing a C17 structure back to C1. Since then, other students have worked on obtaining a C1 structure of the flagellar motor using this SPA dataset. A previous undergraduate student in our lab (Joshua Parks, Imperial College London) was able to obtain a C1 structure of the *C. jejuni* flagellar motor. But the resolution was not sufficient to yet tease out different conformational states.

Lastly, I created a specific mask to the stator and C-ring (Figure 2.11) using ChimeraX and CryoSPARC. This allowed for a mask that specifically outlined the densities as opposed to a wider lathe mask. This mask was used subtract out the rest of the flagellar motor. The stator, C-ring and part of the inner membrane remained in the homogeneous refined structure. In the X/Y axis under MotA we see an extra density which I suggested is FlgX (Chapter 3). The Y/Z provided an artefactual ring with non-pentameric stator units.

Results in this project suggest that *C. jejuni*'s stator complexes have evolved. *C. jejuni*'s stator complexes are surrounded by proteins PflA, PflB, FliL and miscellaneous proteins that keep MotA statically in place. A previous PhD student in our lab, Tina docked the MotB in the periplasmic region of the flagellar motor and showed that MotB does not reach the peptidoglycan layer and could indirectly bind to the peptidoglycan layer via other proteins. Both results suggest that stator units in *C. jejuni* behave differently compared to other species such as *S. enterica*. We were able to see pentameric stator units in the flagellar motor. Focused classification to decipher different conformational states of stator

units was not successful. But we see static stator complexes (further explained in Chapter 3) and the symmetry mismatch between FliG protomers and the 17 stator units in *C. jejuni* suggest low duty ratio since the stator units are found largely in one position as opposed to constantly changing conformational states in which case the pentamer would be less obvious *in situ*. As opposed to *S. enterica* and *E. coli* which have a high duty ratio and move at a dynamic rate and MotA is constantly rotating (Nirody et al., 2016; Ryu et al., 2000).

2.6 Methods

2.6.1 Bacterial strains and growth conditions

C. jejuni DRH212, a streptomycin-resistant derivative of *C. jejuni* 81-176 and the minicell strain (*C. jejuni* Δ*flhG* Δ*flaAB*) was grown in MHT agar (1.5% w/v agar, 10 μg/mL trimethoprim). To select for antibiotic resistant colonies, antibiotics were added to the agar medium. The following antibiotics were used when required, Kanamycin (Km) at 50 μg/mL, streptomycin (Sm) at 2 mg/mL. *C. jejuni* was grown under microaerophilic conditions (5% O2, 10% CO2, 85% N2) in a Heracell 150i trigas incubator (Thermo Fisher Scientific). The strains grown are listed in table 2.1.

Table 2.1 List of strains used in Chapter 2

Use	Bacterial strain or plasmid	Source
Base 'wild-type' DRH212	*C. jejuni* 81-176 rpsL^{Sm} (Sm^{R})	(Hendrixson et al., 2001)
Minicell-producing strain	*C. jejuni* Δ*flhG* Δ*flaAB*	This study (Eli Cohen, Imperial College London)

2.6.2 Strain construction in *C. jejuni*

The *C. jejuni* minicell strain was made by a post doc in our lab Eli Cohen. Strain construction is done by natural transformation of linear splicing-by-overhang-extension (SOE) PCR. This process involves mutations that are chromosomally encoded and does not require any plasmids. The mutants were constructed by a two-step protocol as described in (Cohen et al., 2020). To mutate the genomic locus of interest, the aphA3'-rpsL cassette which codes for kanamycin resistance and sensitivity to streptomycin in the strain DRH212 was altered by designing primers that were homologous to the genomic locus of interest and the cassette of interest. The homologous regions were around 500 bp in length. This fragment after SOE is methylated using EcoRI methyltransferase (New England Biolabs), incubating with S-adenosylmethionine (New England Biolabs) at 37°C for an hour. The methylated DNA around 5 μg is taken and transformed into the *C. jejuni* strain of interest using the biphasic method (Van Vliet et al., 1998). The plate with cells and methylated DNA is incubated for 4 hours under microaerophilic conditions. The cells were washed off and plated on kanamycin plates. Kanamycin resistant colonies were picked from these plates after 48 hours. The SOE PCR and transformation was repeated with the mutated DNA fragment of interest with 500 bp homology to the locus on each end to replace the aphA3'-rpsL cassette. Each colony was then checked again for kanamycin sensitivity and streptomycin resistance (plated on 2mg/ml streptomycin plates). The colonies were then purified and sent for Sanger sequencing (Source Bioscience).

2.6.3 Cryo-EM sample preparation and freezing (by Eli Cohen)

C. jejuni Δ*flhG* Δ*flaAB* cells (minicell) were first grown on MH plates (1.5% w/v agar, 10 μg/mL trimethoprim). Between 8 to 10 MH plates were streaked to harvest enough minicells. To purify the minicells from whole cells, the cells were washed off the plates and spun at 4,000 rpm for 20 minutes which pelleted the whole cells. The minicells remain in the supernatant which was extracted from the tube and divided into Eppendorf tubes which were spun at 15,000 rpm for 5 minutes. The final OD_{600} of the sample was around 15. Minicells were frozen on QUANTIFOIL® R0.6/1 and R1.2/1.3 carbon grids. Each grid was plunge frozen in liquid ethane using a Vitrobot Mark IV (Thermo Fisher Scientific) using the following parameters, blot force of 2, and blot time of 2 seconds.

2.6.4 CryoEM data collection

Micrographs were collected at the Francis Crick Institute by Dr. Andrea Nans. The microscope used for data collection was a 300 keV Titan Krios TEMs (Thermo Fisher Scientific). Dataset was collected using a K2 direct electron detector with a GIF energy filter (Gatan) with a slit width of 20 eV. One shot per hole was collected and the Gain correction was conducted as the data was collected. The parameters used for data collection are shown in Table 2.2.

Table 2.2 Data collection statistics of minicell SPA dataset

Data Parameters	K2 Dataset
Voltage [keV]	300
Detector	K2
Pixel size [Å/pix]	2.2
Exposure dose per frame [e-/Å/frame]	1.53
Total exposure dose [e-/Å]	50
Defocus range [μm]	-1.5 to -3.0
Total micrographs	42,988

2.6.5 Cryo-EM processing

To process the collected minicell dataset collected, the movie frames were aligned, and dose weighted using MotionCorr 2.1 (Zheng et al., 2017). The rest of the processing was done in RELION 3.1 (Scheres, 2012; Zivanov et al., 2018). First CTF correction was conducted using CTFFIND4 (Rohou and Grigorieff, 2015) in RELION. Then Eli, Tina and I picked particles from these micrographs resulting in a total of 79,287 coordinates. These particles were extracted using a box size of 800 pixels. 2D classification removed junk particles which left us with particles where we could observe clear flagellar motor features. The 2D classification was averaged and C17 symmetry was imposed to create an initial

model. We knew *C. jejuni*'s flagellar motor templated 17-fold symmetry from previous structural characterisation using cryo-electron tomography (Beeby et al., 2016). Then I performed 3D classification and refinement using applied C17 symmetry with a 1200 Å diameter spherical mask with 27164 selected particles. The final volume without masking was estimated to be 13.9683 Å. This final volume was signal subtracted and focused on the ring of stators, C-ring and part of the periplasmic region including MotB using a lathe mask. After signal subtraction, I performed another round of 3D classification and refinement with the focused lathe mask which resulted in 17753 particles and a 19.3407 Å structure.

I attempted to use Local Reconstruction to investigate the interaction of a singular stator unit against the C-ring. I imported signal subtracted/refined particles into Scipion. Then an initial and terminal point was defined to target the location and orientation of sub-particles using Chimera. The two markers highlighting initial and terminal points were saved in a .cmm file and imported into Scipion. Sub-particles were extracted using 'local rec – extract subparticles' at a box size of 200 pixels. Sub-particles were then used for 3D classification (RELION 3.1) to extract different conformational states of stator units (T = 4, number of classes = 3, particle diameter = 400 Å). Class 1 had 149,666 particles, Class 2 had 149,409 particles, Class 3 had 2726 particles. Of the three classes, two showed pentameric stators which were further refined using RELION 3.1 (initial angular sampling (deg) = 1.8, initial offset range 5.0 (pix), initial offset step 1 (pix), Local search from auto-sampling 1.8, particle mask diameter 400 Å) for both classes. The refined structure was classified again. Refined volume 1 had 3 classes, class 1 121,044 particles, class 2 25,318 particles, class 3 3304 particles. Refined volume 2 had 3 classes, class 1 14,9401 particles, class 2 8 particles, class 3 8 particles.

Local reconstruction was performed with a box size of 200 pixels encompassing 4 stator units. Sub-particles were defined using the same .cmm file. A box size of 100 pixels was used to extract particles. A total of 50301 sub-particles were extracted. 3D classification was performed to classify out junk particles (T = 4, number of classes = 3, particle mask diameter = 400 Å). Class 1 had 190644 particles, Class 2 had 60794 particles and Class 3 = 50393 particles. I performed 3D refinement on the best class initial (angular sampling (deg) = 1.8, initial offset range 5.0 (pix), initial offset step 1 (pix), Local search from autosampling 1.8, particle mask diameter 400 Å). The refined stator unit structure was then re-classified and refined to find different conformations of one stator unit. Class 1 had 87,606 particles, Class 2 had 52,768 particles, Class 3 had 50,270 particles.

To investigate whether I could increase the resolution of the stator ring, I imported the subtracted and refined structure from RELION into CryoSPARC (Punjani et al., 2017). I performed mask-free homogeneous refinement with 17,753 particles which resulted in a structure with an estimated

resolution of 15.95 Å. I imported the lathe mask encompassing the stator ring and the C-ring from RELION 3.1 to CryoSPARC. I performed two homogeneous refinement jobs with this mask, the first was performed with C1 symmetry imposed (17,752 particles, estimated resolution 15.88 Å). The second homogeneous refinement job was performed with C17 symmetry imposed (17,752 particles, estimated resolution 19.78 Å). In attempts to improve alignment I performed a second homogeneous refinement with the lathe mask in CryoSPARC in both C1 and C17 symmetry.

Lastly, I made a tight mask by importing a signal subtracted, refined stator ring into ChimeraX. I deleted parts of the volume and kept only the C-ring and MotA densities in the volume. This new volume was imported into CryoSPARC. I used 'Vol Tools' to convert the volume into a mask. The mask was then used to run a homogeneous refinement in CryoSPARC with 17,753 particles which resulted in structure with an estimated resolution of 13.19 Å.

Chapter 3

Are stators in *C. jejuni* static or dynamic?

3.1 Chapter Summary

A bacterial flagellar motor incorporates membrane proteins called stators to power the motor enabling bacterial movement. To drive rotation, stator units interact with the cytoplasmic ring (C-ring) which transports rotation towards the axial regions of the motor. Protons are taken up by stators which change conformation and rotate. The interaction between stator units and C-ring is described as a mesh between one rotor cogwheel interacting with many stator complex cogwheels where each stator unit interact with the C-ring to drive rotation of the motor. In bacterial species with simple motors such as those of *E. coli*, stator units are dynamic and incorporate as the surrounding load increases. However, in more complex motors which take up a lot of energy to bore through high viscous environments, for example, in that of *C. jejuni*, it remains unclear whether stators are continuously anchored in the cell membrane (i.e. static), or intermittently, either during longer ("high occupancy") or shorter periods ("dynamic"). We hypothesize that stator units are statically present around the motor because in subtomogram averages we can see 17 stator complexes. Stator complexes cannot be observed in flagellar motors with dynamic stators such as those in *E. coli* suggesting differences in stator dynamics between *C. jejuni* and *E. coli*. *C. jejuni* has evolved its existing core motor structures to provide higher torque. For example, *C. jejuni* has 17 stator units and *S. enterica* and *E. coli* have between 11 to 13 stator units. The C-ring in *C. jejuni* has a much bigger radial distance (26 nm radius) than other bacterial species such as *S. enterica* (22 nm radius) which allows for more stators to incorporate onto the *C. jejuni* C-ring. Cryo-electron tomography has shown that stator units are visible in *C. jejuni* but not visible in *S. enterica* and *E. coli* because of their dynamic nature.

A limitation of studying stators using cryo-electron tomography and subtomogram averaging is that we cannot differentiate between "high occupancy" stator units and static stator units. Most stator units are anchored to the motor in *C. jejuni,* as a result the average of these motors shows the maximum number of stator units which is 17, but this does not confirm whether stator units are high-occupancy (attached for an extended period) or static.

To confirm stator dynamics, we can use a protonophore to dissipate the proton gradient (PMF) which increases the permeability of the cell membrane to protons and dis-engages mechanosensitive stator units leading to stator complex dissociation. This is a well-established technique previously used to stator dynamics in *E. coli*/ *S. enterica*. If stator units are dynamic in *C. jejuni* stator units will dis-engage from the motor once the proton gradient is dissipated (Chang et al., 2019; Motaleb et al., 2000; Nord et al., 2022; Perez-Carrasco et al., 2022). To study stator dynamics a protonophore carbonyl cyanide m-chlorophenyl hydrazone (CCCP) is usually used. By imaging *C. jejuni* cells incubated in CCCP using cryo-electron tomography and subtomogram averaging we can check whether stators remain engaged to the motor and are static or disengage from the motor and are high occupancy. I show that in *C. jejuni* 17 stators remain present with the addition of CCCP.

To understand how stators are statically anchored I speculated that additional proteins surrounding stators keep statically anchored stators in place. FlgX is known to interact with MotA and help it incorporate into the motor and prevent degradation of MotA. In this project I show the potential location of FlgX and how it plays a role in stabilizing MotA using cryo-electron microscopy. I also show that in a motile FlgX deletion mutant with a missense mutation in MotA causes loss of stators in the membrane even though the cell still swims, suggesting dynamic stators.

3.2 Introduction

Campylobacter jejuni has adapted selected features over the course of evolution. These features have helped *C. jejuni* to survive in high viscous environments such as the gastrointestinal epithelium (Chaban et al., 2018). Some key features include corkscrew cell shape which allows it to swim through mucous membranes and a powerful flagella motor to produce high torque. The *C. jejuni* flagellar motor is one of the most divergent motors compared to other flagellar motor systems in different species. Cryo-electron tomography and subtomogram averaging has been crucial for highlighting architectural differences in the flagellar motor between species. In subtomogram averages of *C. jejuni* we observe accessory proteins which have incorporated into the flagellar motor. Using subtomogram averaging we also observe evolutionary adaptations to core motor proteins such as stators units which are required to power the flagellar motor, these stator units are shown as static or possibly high occupancy. By understanding how the *C. jejuni* motor has evolved to produce higher torque we gain insight into molecular evolution of motor systems.

3.2.1 Differences between 'high torque motor' and 'low torque motors'

Adaptations that contribute to *C. jejuni* having a powerful motor are, firstly, its 17 stator units compared to well-studied bacteria such as *E. coli* and *S. enterica* which are known to have between 11 to 13 stator units (Khan et al., 1988; Reid et al., 2006). Secondly, the diameter of the cytoplasmic ring (a large ring of repeating protein complexes that rotates to generate torque of the motor) is larger radial distance (26 nm radius) in *C. jejuni* compared to other bacterial species such as *S. enterica* (22 nm radius) this allows for more stators to incorporate onto the C-ring (Beeby et al., 2016). Stator units in *C. jejuni* are thought to be either high occupancy where they mostly engaged to the motor or static where stator units are permanently placed around the motor (Figure 3.1) (Lele et al., 2013; Tipping et al., 2013). In contrast, stators in *E. coli* and *S. enterica* are known to be dynamic where there are fewer stator complexes when *E. coli* swims at low viscosity but as the load on the motor increases the number of stators incorporated into the motor also increases. Little is known about how stator units interact with the motor in *C. jejuni* but evidence from cryo-electron tomography suggests that the *C. jejuni* stator units are locked in place instead of dynamic.

These evolutionary adaptations are important because they provide us with a deeper understanding of how/why *C. jejuni* has evolved and adapted to produce faster swimming speeds. *C. jejuni* most likely has these adaptations because it resides in high viscous high nutrient environment of the gut. Therefore, in terms of cost benefit analysis it makes sense for *C. jejuni* to favour high-torque compared to *E. coli* and *S. enterica* which do not necessarily require such adaptations. It is likely that the initial evolutionary

adaptations in *C. jejuni* started with proteins PflA and PflB which make up the periplasmic ring and then the outer membrane scaffold which is made up of FlgP subunits which keep the motor in place (Chaban et al., 2018). We still do not understand the later stages of flagellar assembly and stator dynamics in high torque flagellar motors.

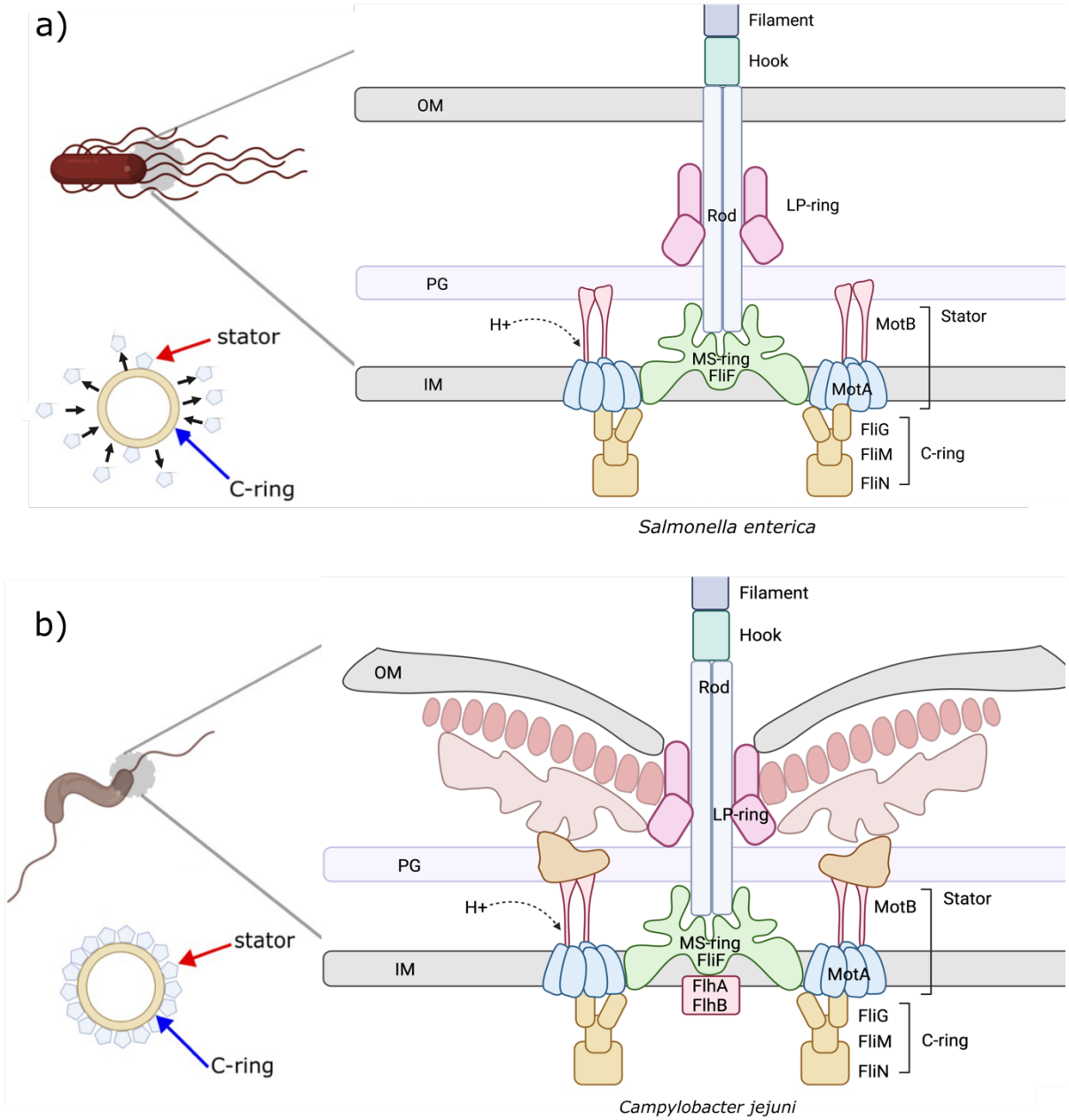


Figure 3.1 Differences in stator dynamics in *C. jejuni* versus *S. enterica*. a) In *C. jejuni* the flagellar motor has many different components and stator units are 'high occupancy' or permanently positioned around the C-ring. b) In *S. enterica* the flagellar motor is made of core flagellar components only and stator units are dynamic which means they frequently associate and dissociate from the C-ring.

3.2.2 Cryo-electron tomography can be used for studying stator dynamics

Cryo-electron tomography has shown architectural differences between motors of *C. jejuni* (high-torque motor) and *S. enterica* (low-torque motor). These differences are also found in core flagellar motor proteins which have evolved to behave differently in different species. For example, stator units, which power the flagellar motor behave differently in high torque bacterium versus low torque bacterium. In subtomogram averages of the flagellar motor in *C. jejuni* 17 stator units were attached to the flagellar motor. Whereas in subtomogram averages of a bacterium that produces lower torque such as *S. enterica* no stator units are observed. The dynamic nature of simple motors such as that of *S. enterica* and *E. coli* means that the number of stator units in each bacterium will be different compared to *C. jejuni* where each bacterium has the same number of stators in contact with the rotor. Therefore, the result of averaging many low-torque bacterium motors is a blurred ring which means no stator units are visible (Figure 1.9). These subtomogram averages suggest that stator dynamics have evolved in high torque bacterium which have diverged from low torque bacterium.

Stator units in *C. jejuni* are visible in subtomogram averages. But limitations in the averaging step of subtomogram averaging make it difficult to explain whether stator units are visible because they are statically attached to the motor or because they are high occupancy where they are mostly attached to the motor and dissociate less frequently than low torque motors. If stator units in *C. jejuni* are high occupancy, then it would still provide the same subtomogram average as statically attached stator units because stator units in *C. jejuni* are mostly attached to the motor therefore averaging the motor would provide the maximum number of stator units.

3.2.3 Biophysical experiments provide functional data on stator dynamics

Biophysical experiments are used to study stator dynamics as explained in section 1.8.3. Studies like the bead assay which a bead is attached to the flagellum to measure rotation and the resurrection assay where a protonophore is added and then washed to out to measure the incorporation of stator units have been crucial for understanding how stators incorporate into the motor (Nirody et al., 2017). In simple motors of low-torque, stators are incorporated in stepwise manner as the load is increased on the motor (Blair and Berg, 1988; Ryu et al., 2000). These studies were done in *E. coli* a bacterium which we know may not exhibit the same stator dynamics as *C. jejuni* because their subtomogram averages look different (Beeby et al., 2016; Chen et al., 2011). It is important to perform the same studies in high torque motors such as *C. jejuni* to confirm stator behaviour in high torque motors. I hypothesize that high torque motors do not exhibit the same behaviour as low torque motors. But studies on these are yet to be done.

3.2.4 The structure of stator complexes are conserved across species

Stator complexes are conserved across species. These stators are powered by protons, which are a product of cellular respiration (Blair and Berg, 1988; Ryu, Berry and Berg, 2000). The stators are made up of two proteins, motility protein A (MotA) a pentameric, pseudo-symmetric protein situated in the inner membrane and motility protein B (MotB) a transmembrane helix with a large periplasmic domain which forms a homodimer in MotA making a 5:2 complex (Deme et al., 2020; Santiveri et al., 2020). MotB acts as a plug and is located on MotA. The transmembrane domain of MotB contains a conserved aspartate residue (D22) which is involved in proton transport (Zhou et al., 1998). To rotate the motor, MotB reaches up to the peptidoglycan layer to allow protons into MotA which then changes conformation. MotA interacts with FliG of the C-ring which rotates the rotor (Wilson and Macnab, 1990; Kojima and Blair, 2004). Purified structures of MotA solved by Single Particle Analysis show that each monomer of MotA (specifically residues R89 and E97) interacts with the C-terminal of FliG (specifically residue D299 and R292) also known as the torque helix to rotate against MotA (Figure 1.7 c) (Santiveri et al., 2020). A hydrophobic residue of MotA (F186) protects the periplasm from the hydrophilic region of MotAB complex. When MotB reaches up to the peptidoglycan layer the MotA F186 moves to allow for protons to pass through. Once protons go through MotA it rotates 36° in a stepwise manner around MotB. For each step, MotB chain alternates in protonation.

3.3 Aims

The aim of this project was to understand the dynamics of the stators in *C. jejuni*, specifically, whether stators are statically placed around the motor. In Chapter 2, I showed that the stators have extra densities that surround the stator. In this chapter I showed that the extra density is a protein called FlgX which provides support to the stator and statically places it around the motor. FlgX not only stabilizes the stators but allows for the stators to be readily present to operate a high torque motor in a high viscous environment. I do this by using a protonophore to dissipate the proton gradient in wild type *C. jejuni*. I image wild type *C. jejuni* in the proton dissipated environment using cryo-electron tomography. I imaged a deletion mutant of FlgX and a FlgX tagged mutant to locate the FlgX protein. I collaborated with a lab that showed biophysical data which corresponded with our structural results.

3.4 Results

3.4.1 Are stators in *Campylobacter jejuni* present when there is no load on the motor?

To test whether stators remain statically present in *C. jejuni*, I first needed to remove the load on the motor since the motor is mechanosensitive. Previous studies in *E. coli* have shown that stators disengage from the motor when there is no load on the motor. This is done by adding CCCP a protonophore which binds to H+ ions to transport these ions through the membrane to dissipate the proton gradient. When CCCP is washed out from the cells, the cells can swim again because the proton gradient reinitiates itself. When the proton gradient is stabilized stators are recruited back into the motor and this stepwise increase in stator units is observed. These experiments have been done in *E. coli*, a well characterized bacteria which has dynamic stators, but such studies have not been done in *C. jejuni*.

To check the concentration of CCCP required to dissipate the proton gradient in *C. jejuni*, a range of concentrations of CCCP were added to *C. jejuni* cells. In each Eppendorf tube 20 µL of *C. jejuni* cells at OD 0.5 was pipetted. The concentration of CCCP ranged from 10 µM to 200 µM but already at 10 µM of CCCP the cells stopped swimming. The cells swimming under a microscope was compared to Δ*motB C. jejuni* which are immotile. For freezing cells, cell pellets of much higher concentrations are used. Therefore, I used cells which were at OD 56 and added 50µM, 250µM, 500µM of CCCP to 20µL of cells to each Eppendorf tube. I confirmed that at each of these concentrations the cells stopped swimming.

3.4.2 Subtomogram average of *C. jejuni* motor in CCCP confirms stators are static

To investigate whether stators are dynamic in *C. jejuni.* I added CCCP to wild type *C. jejuni* whole cells. CCCP was added in excess to a pellet of wild type *C. jejuni* cells for cryo-electron tomography. 146 tomograms were used for the subtomogram average and compared to wildtye and Δ*motB*. In C1 and C17 showed that all 17 stators were present. This confirmed that stators are statically present around the motor (Figure 3.2).

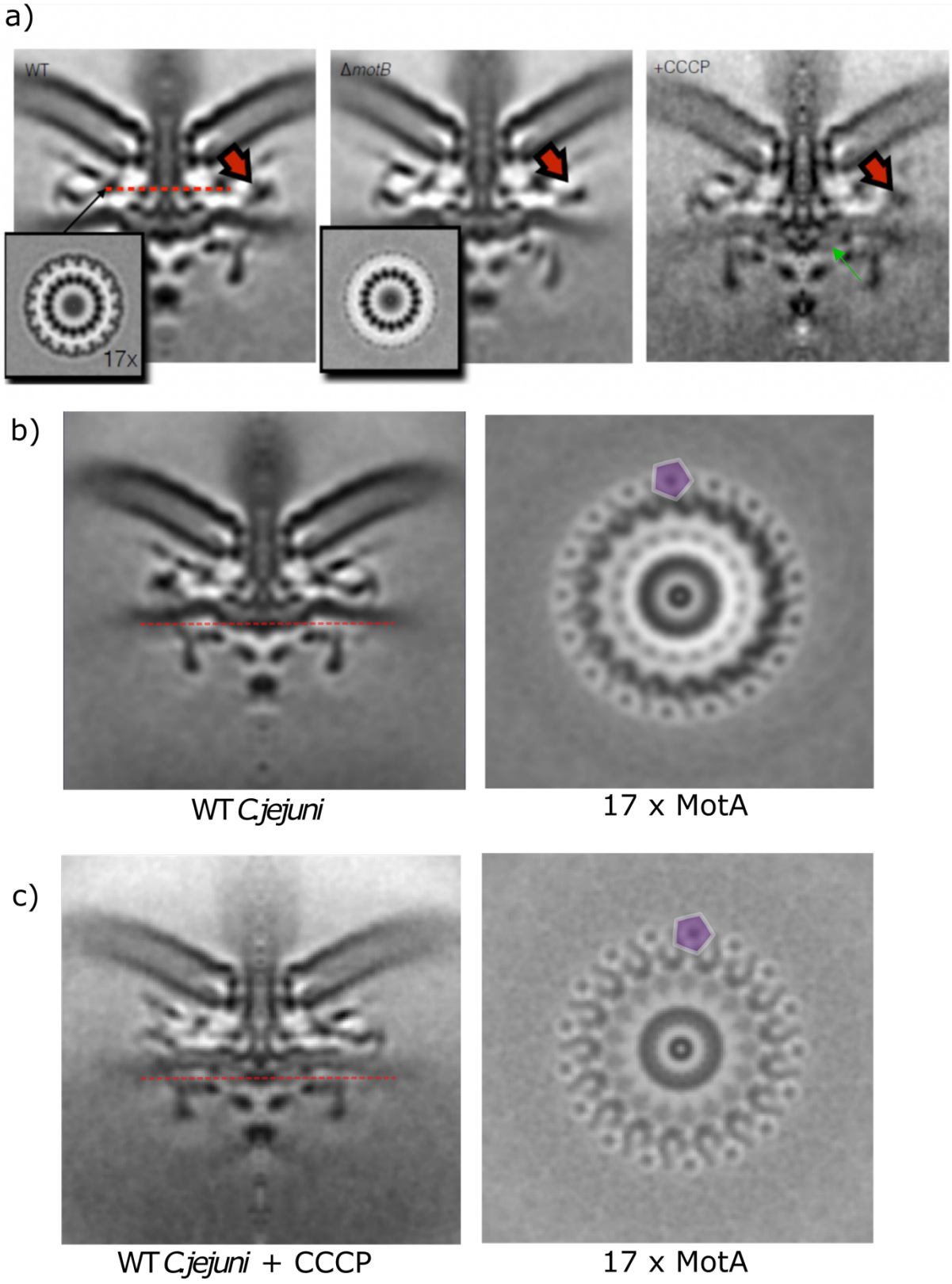


Figure 3.2 Subtomogram averages of *C. jejuni* cells with the addition of CCCP confirm stator units are static in *C. jejuni*. a) Compares subtomogram averages of wild type, Δ*motB* and wild type with the addition of CCCP *C. jejuni* cells. 17 MotB subunits are observed in WT *C. jejuni* which are deleted in Δ*motB C. jejuni* and 17 subunits of MotB are observed in Wild type *C. jejuni* with CCCP. The red line represents a cross-section through MotB in

Z. b) Subtomogram average of wild type *C. jejuni*, red dotted line highlights cross-section through the stator region to show 17 MotA densities. c) Subtomogram average of wild type *C. jejuni* with the addition of CCCP, red dotted line highlights cross-section through the stator region on the right the stator ring also shows 17 MotA densities(Beeby et al., 2016).

3.4.3 Extra densities around stators are accessory proteins are required for full motor function

As found in Chapter 2, extra densities were observed around the stators (Chapter 2, Figure 2.11). To check which proteins could possibly hold the stators statically in place I looked at study which screened for uncharacterized motility proteins in *C. jejuni* (Gao *et al.*, 2014). A paper by Gao *et al* showed that protein Cjj_0199 (FlgX) was shown to interact with MotA. This was further confirmed by Ribardo and co-authors, they showed using pull-down assays and immune precipitation assays that FlgX indeed directly interacts MotA. FlgX is a chaperone for MotA that required for the retention of MotA. FlgX prevents MotA from degradation protein FtsH (Ribardo et al., 2019). Therefore, FlgX was hypothesized to be an extra density under the stators. First, I used AlphaFold2 CollabFold (v1.5.5) to predict the structure of FlgX. Then I used CollabFold to predict a structure of FlgX with MotA (Figure 3.3 b). FlgX is predicted to be a small protein that fits in the small density under MotA as shown in the single particle analysis structure from the *C. jejuni* minicell dataset processed in chapter 1 (Figure 3.3 a), the structure highlighted in red is FlgX and the structure highlighted in blue is the pentameric MotA that is stabilized by FlgX. The stator ring is about 15.95 Å in resolution and shows pentameric stators (Figure 3.3 c), in the single particle *in situ* structure of the stator, the predicted structure of FlgX was fitted into a density under MotA (Figure 3.7 c), this low-resolution structure was not enough to validate the location of FlgX.

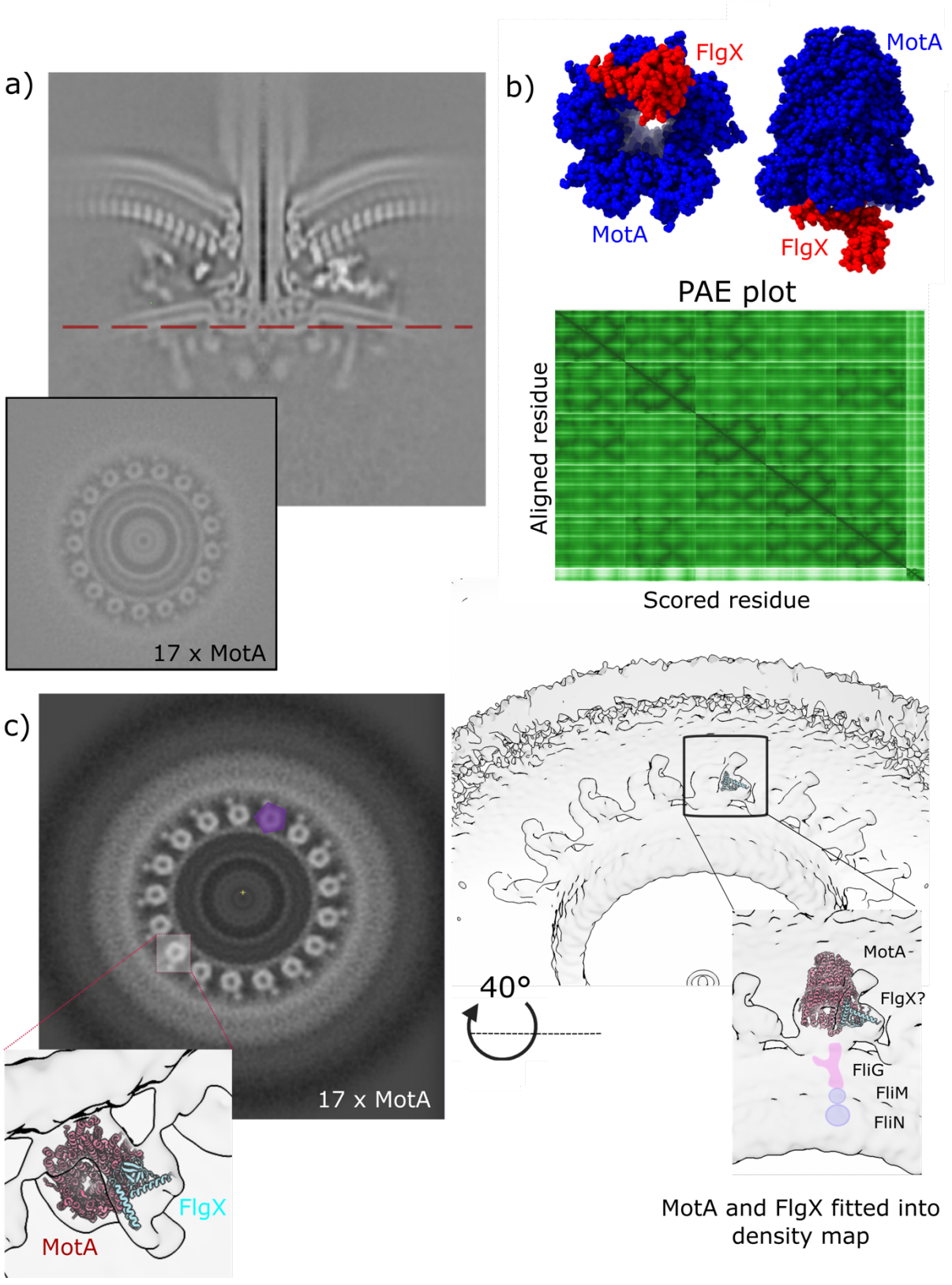


Figure 3.3 Single Particle Structure of the *C. jejuni* flagellar motor shows pentameric stators in situ to a resolution where we can model individual stator complexes. A higher resolution structure of the stator ring highlights extra densities that previously were not visible such as FlgX which is suggested to be located under MotA. a) Single

Particle structure of the *C. jejuni* flagellar motor which shows 17 MotA units processed in RELION 3.1. b) predicted protein complex of MotA (blue) with FlgX (red) using AlphaFold2 CollabFold (v1.5.5). c) Single particle signal subtracted/ focused refined structure of the stator ring processed in CryoSPARC. Bottom left shows a single particle MotA structure fitted into the density map of one of the pentameric MotA densities in the stator ring. Right: shows an isosurface of the flagellar motor with MotA and FlgX fitted into the stator ring. FliG, FliM and FliN are also highlighted.

3.4.4 Stators disappear when FlgX is deleted from the motors

Our collaborators showed that deleting FlgX made *C. jejuni* immobile but mobility was restored with a point mutation in MotA, specifically changing the histidine in position 138 to threonine (H138Y) (Ribardo et al., 2019). The mutants from the paper sent by Dave Hendrixson's lab and I put them on motility plates to check for swimming. As written by our collaborators paper Δ*flgX motA*^{H138Y} showed a halo ring, therefore swam whereas Δ*flgX C. jejuni* did not swim but we still do not know the mechanism by which the mutant swims (Figure 3.4 c). To check whether the density disappears when FlgX is deleted, I imaged *C. jejuni* Δ*flgX motA*^{H138Y}, with the aim of seeing stators but not the putative FlgX density under MotA. Subtomogram average from 247 tomograms showed that the stator ring had disappeared as well as the extra density under MotA (Figure 3.4 b) compared to wild type where the stators and putative FlgX is still visible (Figure 3.4 a). This suggested that although the mutant is motile the stators are not statically engaged to the motor, it is not known whether all 17 stators are present, or a smaller number of stators are engaged to the motor. The lack of stators did not change the diameter of the C-ring or any other part of the motor.

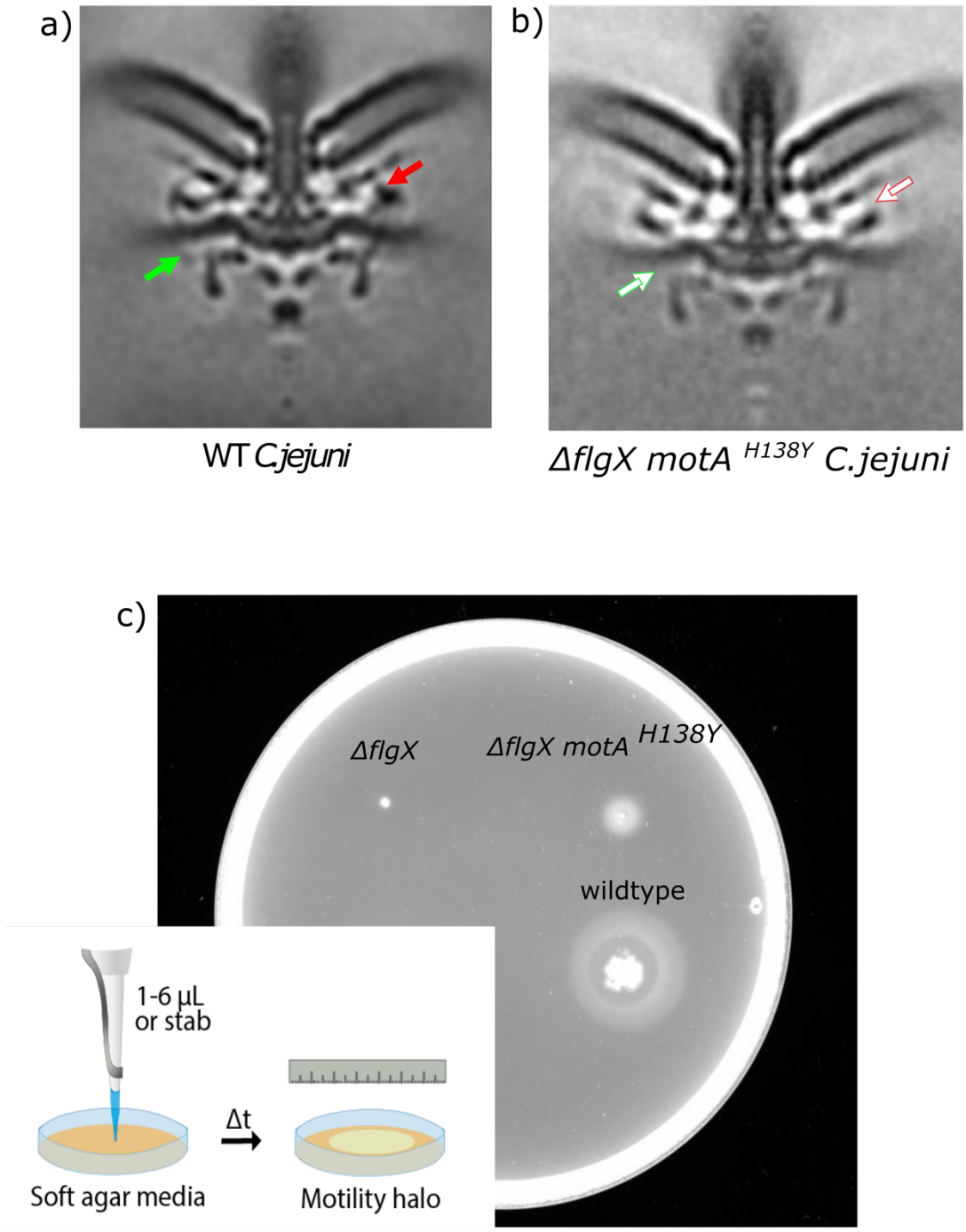


Figure 3.4 MotB density can be observed in wild type but not in *C. jejuni* ΔflgX motAH138Y which is motile. This suggests stator units in *C. jejuni* ΔflgX motAH138Y be dynamic rather than static. a) Subtomogram average of wild type *C. jejuni* (Beeby et al., 2016; Ribardo et al., 2019), bottom red arrow points to MotA/FlgX densities and top red arrow points to MotB. b) Subtomogram average of mutant *C. jejuni* where bottom white arrow points to missing MotA/FlgX densities and top white arrow points to missing MotB density. c) Motility plate showing Δ*flgX* mutant does not swim, Δ*flgX* motAH138Y swims but not as good as wild type, wild type *C. jejuni*. Cartoon on the bottom left shows the use of motility plates to measure motility halos edited from (Palma et al., 2022).

3.4.5 Resurrection experiments in *C. jejuni* suggests stators are permanently attached to the motor

To test our speculation that this mutant *C. jejuni* Δ*flgX motA*^{H138Y} has stator complex behaviour similar to *E. coli* our collaborator (Dr. William H. Hoffmann, Postdoctoral Researcher, Pedaci Lab, CNRS - Centre de Biologie Structurale) conducted resurrection assays. CCCP was added to remove the load on the motors then CCCP is washed away, cells experience load again and stator units re-incorporate into the motor. In *E. coli* stator units incorporate in a step-wise manner. In *C. jejuni* these measurements are yet unknown. In a resurrection assay, first, a steady trace is measured with CCCP for 5 minutes. Then 5μM of CCCP is added to dissipate the proton gradient. After 5 to 8 minutes CCCP is washed away. Videos are recorded at the time of resurrection. To compare the velocity increase between *E. coli* and *C. jejuni* the angular speed versus time was plotted (Figure 3.5). Both plots show that *C. jejuni* has an increased rate of resurrection compared to *E. coli*.

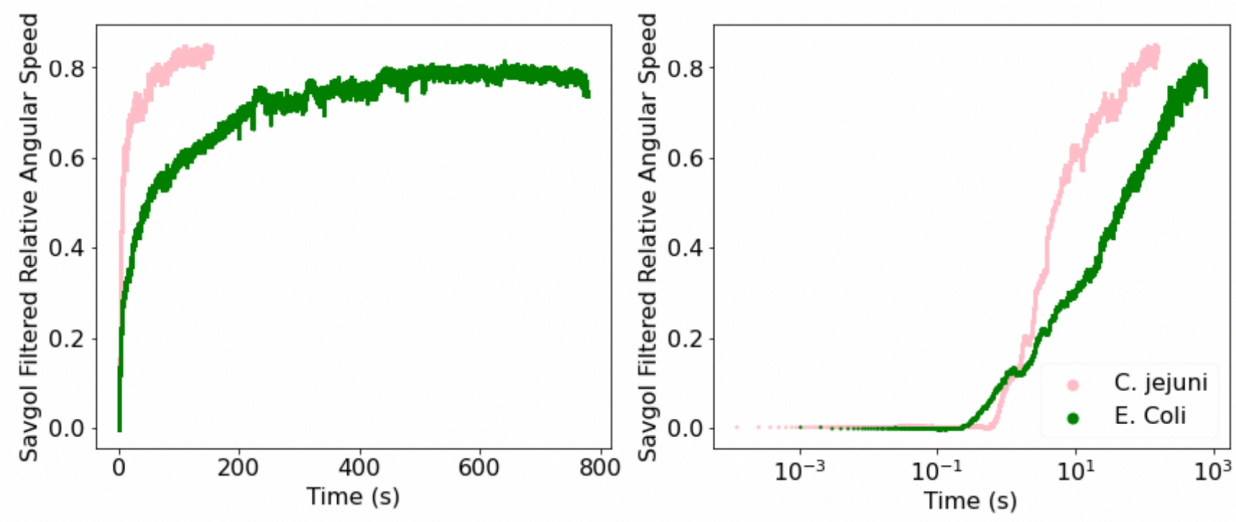


Figure 3.5 Linear and semi-log x plots of average angular speed vs. time for *C. jejuni* and *E. coli* showing the difference in the rate of resurrection for each bacterium (Dr. William H. Hoffmann, Postdoctoral Researcher, Pedaci Lab, CNRS - Centre de Biologie Structurale).

3.4.6 Functional data to show that stators are dynamic when no FlgX is present

To investigate whether *C. jejuni* Δ*flgX motA*^{H138Y} exhibits dynamic stators the mutant was sent to our collaborator Francesco Pedaci's lab to perform resurrection assays. Our collaborator (Dr. William H. Hoffmann, Postdoctoral Researcher, Pedaci Lab, CNRS - Centre de Biologie Structurale) found that *C. jejuni* Δ*flgX motA*^{H138Y} exhibits an intermediate resurrection pattern. that *C. jejuni* Δ*flgX motA*^{H138Y} does not resurrect as fast as wiltype *C. jejuni* but does not take as long as *E. coli* to re-incorporate stator units

(Figure 3.6). *C. jejuni ΔflgX motA*^{H138Y} exhibits a part step-wise increase of stator units and could be partially dynamic.

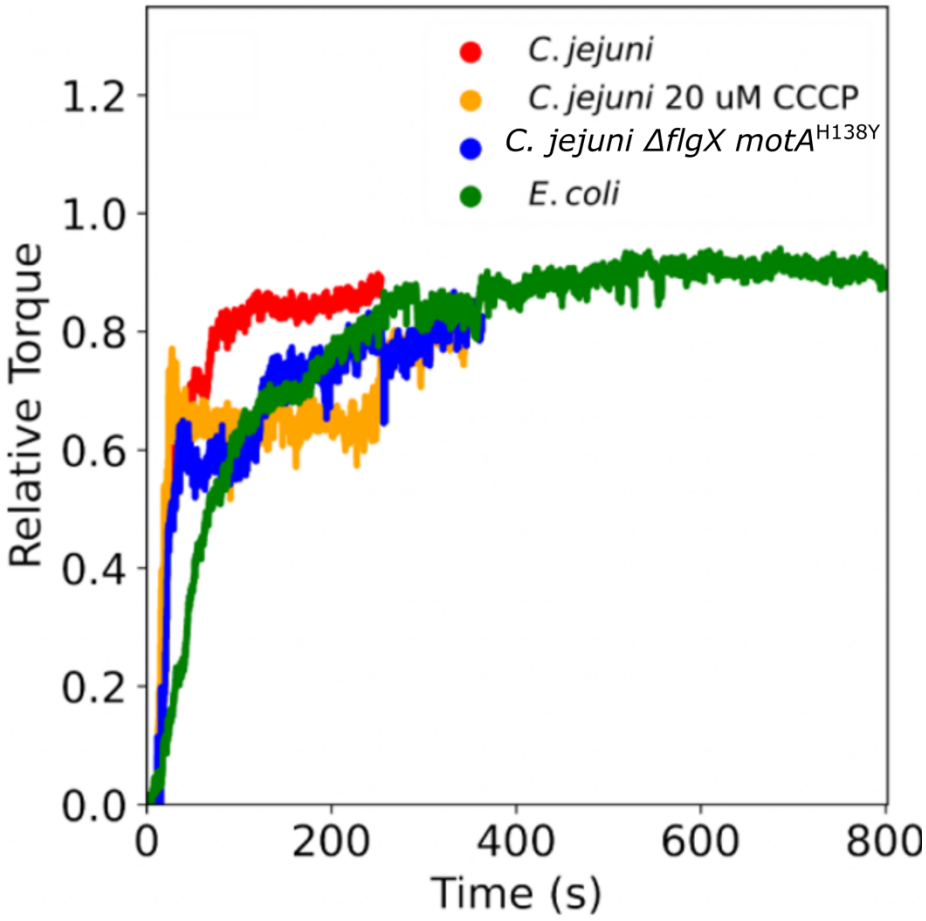


Figure 3.6 Resurrection experiments on *C. jejuni ΔflgX motA*^{H138Y} exhibit faster incorporation of stator units compared to *E. coli* but slower incorporation speeds compared to wild type *C. jejuni*.

3.4.7 Locating FlgX using AlphaFold2 CollabFold (v1.5.5) and Cryo-tomography

Since the subtomogram average of the motile *C. jejuni* mutant *ΔflgX motA*^{H138Y} did not show the location of FlgX, I designed a tag bound to FlgX and used cryo-electron tomography and subtomogram average to find the location of FlgX. I used AlphaFold2 CollabFold (v1.5.5) to predict a structure of FlgX with the tag to see if the tag would clash with surrounding proteins and whether the tags were suggestive of success.

3.4.7.1 Tag Design

Since deleting FlgX was suggestive of its location, I decided to design rigid tags fused to FlgX that would confirm its location in the motor. To design a tag for cryo-electron tomography and

Subtomogram averaging it had to be 1) a rigid density so it was positioned in the same place in each tomogram and therefore when the tomograms were averaged it would be visible 2) the tag should be large enough to be visible by cryo-tomography since I was limited by resolution. Therefore, the N-terminal alpha helix of lysozyme from hen (Gallus Gallus) was chosen to fuse to the C-terminal alpha helix of FlgX (Figure 3.7).

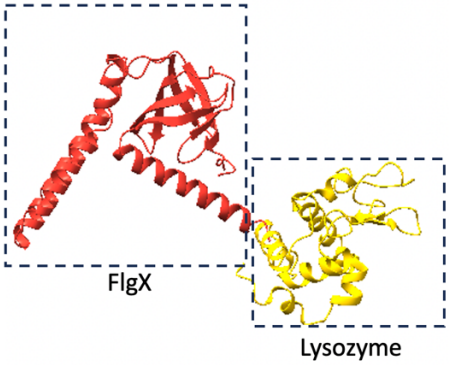


Figure 3.7 The designed tag included FlgX in red with its extended alpha helix at the C-terminal fused to Lysozyme in yellow.

The AlphaFold2 CollabFold (v1.5.5) model of FlgX that I fit into the extra density under MotA has an extended alpha helix that points outwards away from the C-ring. This placement of the alpha helix made it a good candidate for a tag to be fused without potentially affecting the rotational function of the motor. The last four residues of FlgX C-terminus (KGQE) and the first three residues of lysozyme N-terminus (KVF) which were flexible in FlgX and Lysozyme were deleted to ensure a rigid tag. Eight mutants were designed, the protein sequences for these mutants were inserted into AlphaFold2 CollabFold (v1.5.5) to check what the predicted structure would look like as shown in Figure 3.8 (a) highlighted in red FlgX on the right and on the left FlgX with a rigid tag fitted into the single particle structure of the stator ring *in situ*. The predicted structure of five of the eight mutants looked like it would not clash with the structure of the C-ring in the motor as the fused lysozyme tag faced outwards rather than inwards towards the motor. Professor Dave Hendrixson (UT Southwestern Medical Center) cloned four mutants, Fusion 1 is the C-terminal of FlgX (removed flexible sequence KGQE) fused to the N-terminal of Lysozyme (removed flexible sequence KVF) (Figure 3.8 b) where lysozyme faced up because of the orientation of alpha helix but did not clash with surrounding proteins; Fusion 3 (removed sequence NKKGQE to change orientation of the Lysozyme) fused to N-terminal of Lysozyme (removed flexible sequence KVF) where lysozyme was facing inwards towards the ring between two stators but not clashing with any proteins (Figure 3.8 c). Two other mutants were cloned (named Fusion 7 and Fusion 9), in which part of the C-terminal helix was duplicated to extend the alpha helix which would form a rigid linker to fuse Lysozyme for fusion 7 the extension was slightly longer (protein sequence PEDKMAFDAFV) (Figure 3.8 d) compared to fusion 9 (protein sequence PEDKMAFDA) to have

lysozyme at different positions (Figure 3.8 e). Instead of the alpha helix acting like an extended alpha helix the helix turned 90° upwards, AlphaFold2 CollabFold (v1.5.5) showed that there was a possibility this could cause a clash between proteins.

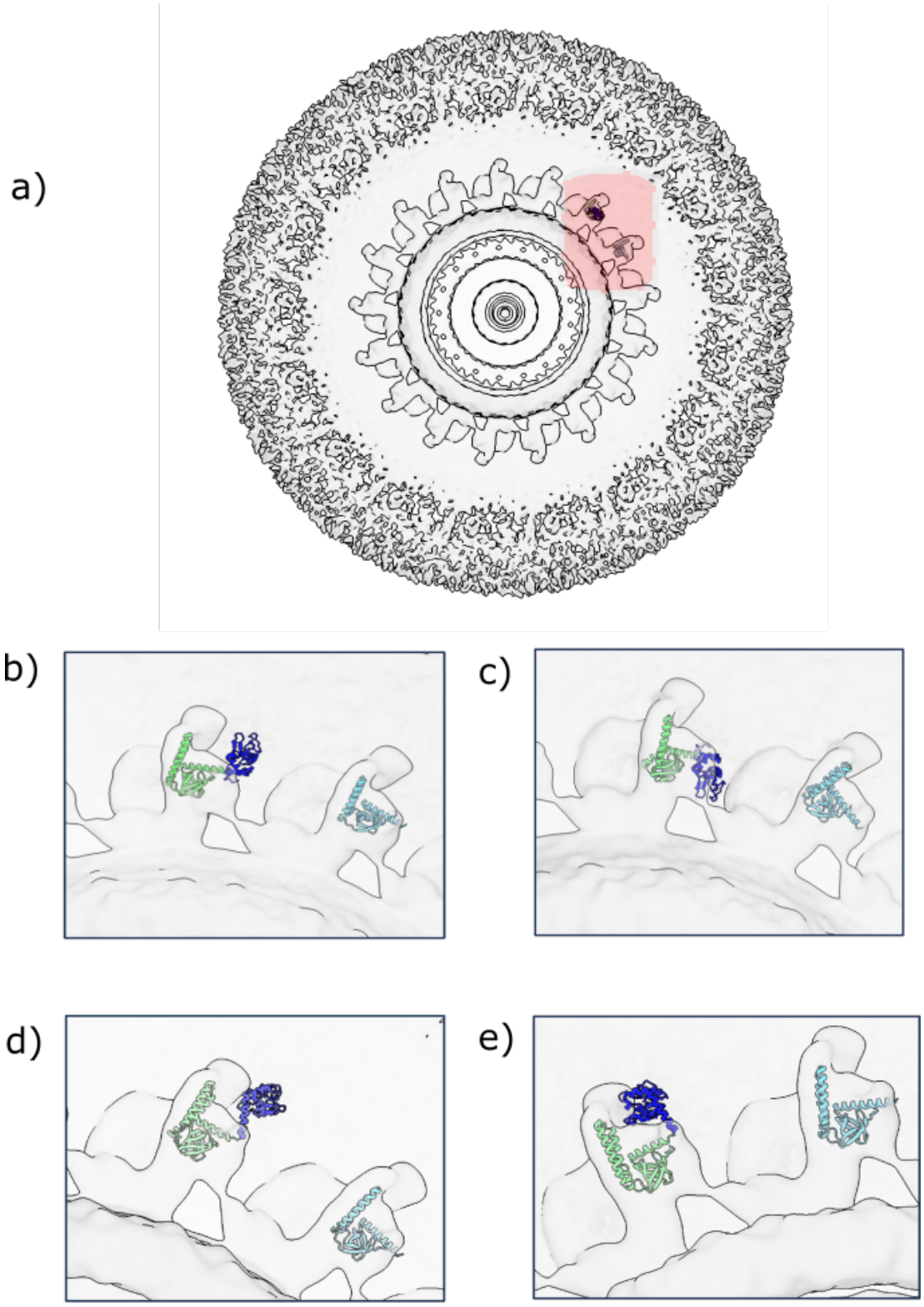


Figure 3.8 Different tag designs of FlgX fused to lysozyme. FlgX density: green is FlgX, blue is lysozyme, light blue is FlgX without the tag. a) the SPA structure of motor in situ with FlgX with tag (left) and without tag (right)

highlighted in red. b) Fusion 1 fitted into putative FlgX density. c) Fusion 3 fitted into putative FlgX density. d) Fusion 7 fitted into putative FlgX density. e) Fusion 9 fitted into putative FlgX density.

The tags were fused to FlgX in *C. jejuni* by our collaborator (David Henderixson, UTSouthwestern). *C. jejuni* with the tags were put on motility plates to check if the mutants could still swim, this is a good indication of the stators still being present around the motor. The motility plates showed that Fusion 1 and Fusion 9 swam comparably to wild type *C. jejuni* and Fusion 3 and Fusion 7 swam less well (Figure 3.9). Table 3.1 shows the diameter of each growth halo in the motility plate.

Table 3.1 Diameter of growth on 0.4% w/v agarose gel (motility plate).

Mutant	Diameter in mm
DRH837(81-176 rpsLSm/pECO102)	17
DRH5026 (81-176 rpsLSm ΔflgX/pECO102::flgX-FLAG)	2
DRH5031(81-176 rpsLSm ΔflgX/pECO102::flgX)	19
pDRH8743 (Fusion 1)	16.5
pDRH8745 (Fusion 3)	10
pDRH8746 (Fusion 7)	12
pDRH8747 (Fusion 9)	15

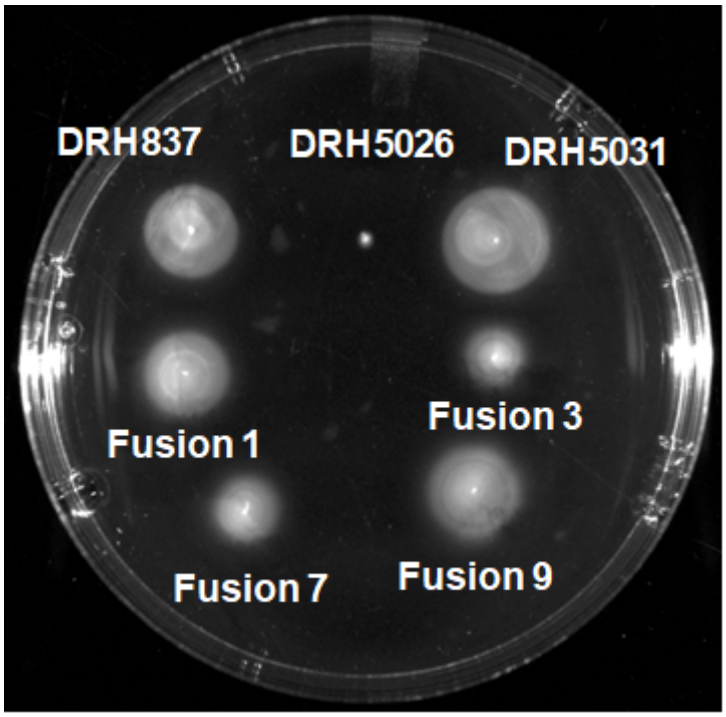


Figure 3.9 *C. jejuni* mutants with the designed tags were grown on motility agar to measure swimming abilities. The following mutants are DRH837 – 81-176 rpsLSm/pECO102; DAR5031 - 81-176 rpsLSm DflgX/pECO102, DAR5026 - 81-176 rpsLSm DflgX/pECO102::flgX-FLAG, DRH8752 - 81-176 rpsLSm DflgX/pECO102::flgX-

lysozyme fusion 1, (pDRH8743), DRH8754 - 81-176 rpsLSm DflgX/pECO102::flgX-lysozyme fusion 3,(pDRH8745), DRH8756 - 81-176 rpsLSm DflgX/pECO102::flgX-lysozyme fusion 7, (pDRH8746), DRH8758 - 81-176 rpsLSm DflgX/pECO102::flgX-lysozyme fusion 9, (pDRH8747) (Professor David Hendrixson, UT Southwestern Medical Center).

3.4.8 Stators and putative FlgX missing densities in FlgX-tagged C. jejuni subtomogram average

To investigate the location of FlgX in the motor I chose to image FlgX-lysozyme fusion 1 mutant using cryo-electron tomography (as seen in schematic image Figure 3.10 b). This mutant was chosen because its motility was comparable to wild type suggesting that the tag was not affecting stator function therefore all 17 stators and FlgX should be present. Subtomogram averages from 192 particles showed that FlgX and stator units were not visible. Subtomogram average of the mutant looked comparable to the subtomogram average of Δ*motB* mutant (Figure 3.10 a) To check whether stator units could be observed in a subset of the dataset the data was classified in PEET by my supervisor Dr. Morgan Beeby (Imperial College London). Classification showed that a hint of MotB was observed in one class suggesting that stators are present but are dynamic or low occupancy (processed by my supervisor Dr. Morgan Beeby, Imperial College London) (Figure 3.10 c). Since stator units were present around the motor less frequently, the C-ring was oriented in fewer conformations. This allowed us to find the symmetry of the C-ring which is shown to be 38-fold symmetric (Figure 3.10 d) (processed by my supervisor Dr. Morgan Beeby, Imperial College London).

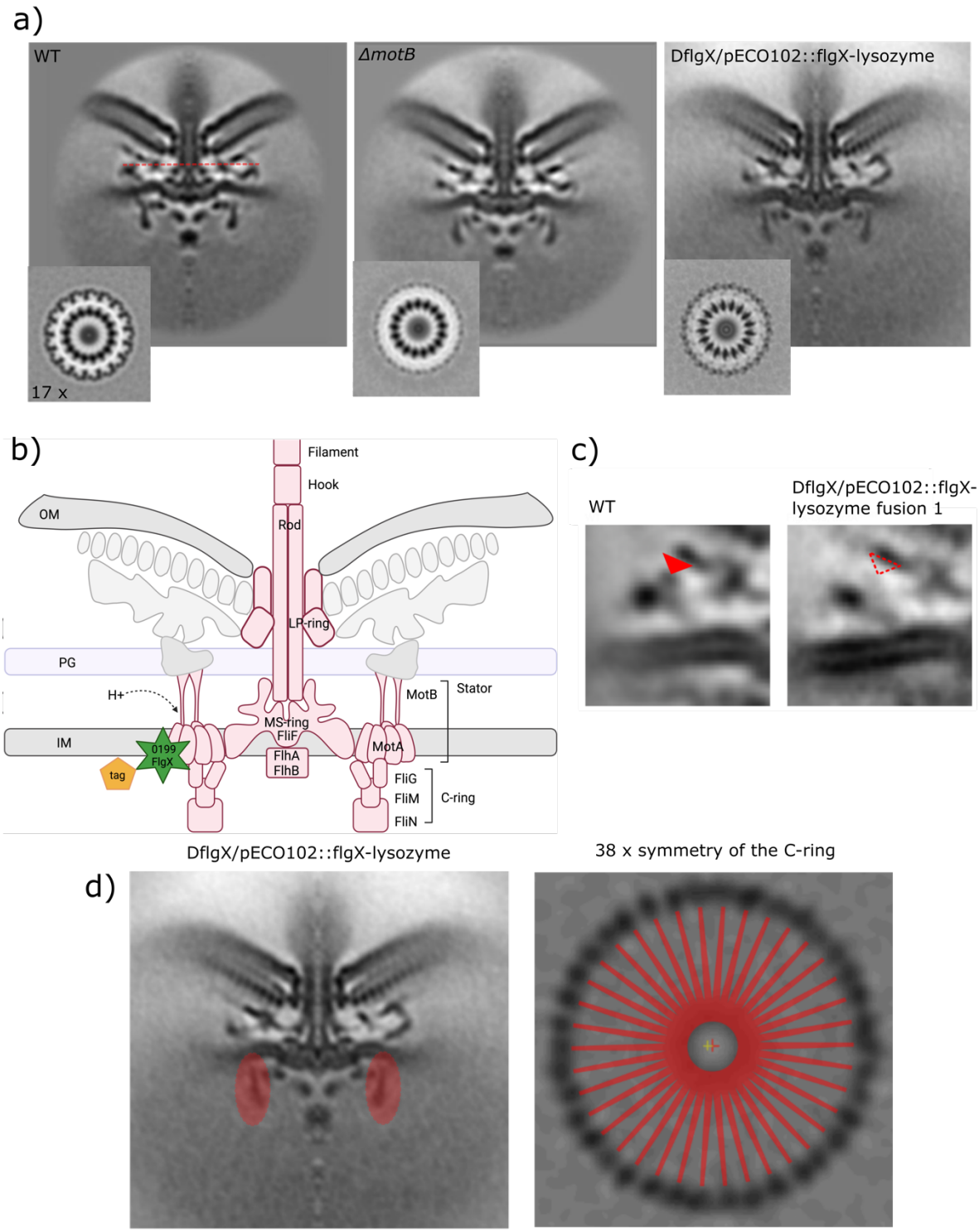


Figure 3.10 Subtomogram average of the tagged FlgX mutant lacked the presence of stators but the mutant is motile which suggests dynamic stator units. a) subtomogram averages comparing wild type *C. jejuni* Δ*motB* mutant and *C. jejuni* flgX-lysozyme fusion 1. Subtomogram average of wild type *C. jejuni* taken from Beeby *et al.,* 2016. Red dotted line in wild type subtomogram average highlights the placement of MotB. Section across the Z axis shows that 17 x MotB units are visible which is absent in Δ*motB* mutant and *C. jejuni* flgX-lysozyme fusion 1. b) schematic image of a motor highlighting a tagged FlgX. c) Classification shows a hint of MotB suggesting low occupancy stators compared to wild type motor (Dr. Morgan Beeby, Imperial College London).

d) red highlights the C-ring in the motor and the image on the right shows the C-ring is 38-fold symmetric (Dr. Morgan Beeby, Imperial College London).

3.5 Discussion

3.5.1 Summary of results

In this Chapter I show that stators in *C. jejuni* are statically placed around the motor as opposed to high occupancy. I showed that even when no load is imposed on the motor *C. jejuni* retains all of its stators which means stators are statically placed around the motor. Results suggest that stators are held in place by a protein called FlgX which is situated under MotA in the cytoplasmic region of the motor.

3.5.2 Stators are statically placed around the motor

In this project I investigated the dynamics of stator units in *C. jejuni*. To check whether stators dissociate once there is no load on the motor, I added protonophore CCCP to *C. jejuni* cells. Subtomogram average of the motor exposed to CCCP showed that stator units remained statically placed around the motor when no load is present on the motor (Figure 3.2). My results show that dynamics in *C. jejuni* (high torque motor) is different from dynamics in *E. coli* and *S. enterica* (low torque motors) due to evolutionary recruitment of additional proteins most importantly FlgX. When the motors in *E. coli* and *S. enterica* are exposed to high load (i.e. high viscosity medium) the stators incorporate and at low load the stators dissociate (Lele et al., 2013; Tipping et al., 2013). The amount of time the stator unit is engaged to the motor increases with the amount of force that is applied on the stator, also known as the catch bond mechanism (Nord et al., 2017). In *C. jejuni* the stators remain permanently attached to the motor. Subtomogram average of *C. jejuni* with CCCP show 17 stator units attached to the motor and MotB interacting with the peptidoglycan layer (Figure 3.2). As opposed to dynamic stators low-torque motors which cannot be seen using cryo-electron tomography and subtomogram averaging (Leake et al., 2006). In addition to this, changes in the membrane were observed, there was a partial drop in the inner membrane above FlgV (Figure 3.2, green arrow), however, it is not yet known what causes changes in the membrane as this has previously not been observed in bacterium motors as per my knowledge, however changes in membrane morphology have been observed in mitochondria due to the collapse of membrane potential (Miyazono et al., 2018).

Our result is consistent with previous literature which shows that stators in *Borrelia burgodorferi* remained associated when exposed to CCCP (Chang et al., 2019). However, stators *Borrelia burgodorferi* were shown to be high occupancy by making a point mutation in MotB and performing

classification on the stators. Classification showed fewer stators in some classes compared to others suggesting that the stators that remain associated to motor have a stronger interaction with the motor. Thus, the bacterium is high occupancy and when fewer stators are needed in a low viscosity environment some stators dissociate. Although it may be that high-torque motors are further divided into high-occupancy and static stators where *C. jejuni* has evolved further to keep its stators in place.

3.5.3 Biophysical assays support statically placed stators

Resurrection experiments performed by our collaborator Dr. Francesco Pedaci's lab show that stators do not dissociate in *C. jejuni* which is not comparable with *E. coli* where stator units re-engage with the motor in a stepwise manner once the CCCP is washed off (Figure 3.5). In *C. jejuni*, once CCCP is washed away the cells rapidly increase in speed and then plateau. The semi-log x plots show a higher increase in angular speed for *C. jejuni* compared to *E. coli*. Results from resurrection assays support our structural results which suggest that stator units are attached to the motor in *C. jejuni* when no load is present and are kept in place by scaffolding around each stator unit. Once the motor senses load the stator units which are already attached to the motor, rotate to generate torque. Whereas in *E. coli* stator units first need to be incorporated into the motor, more time is required to apply torque, which leads to a more gradual increase in speed compared to *C. jejuni*. In *E. coli*, stator unit steps are visible because stator activation after CCCP is removed takes more time and as each stator incorporates it shows a stepwise pattern.

A biological reason for changes in stators in low torque versus high torque motors could be that polar motors such as those of *C. jejuni* and *Helicobacter pylori* and spirochetal flagellated motors such as *Borrelia burgodorferi* have adapted to swim at high viscous environments (Beeby et al., 2016; Chen et al., 2011; Kudryashev et al., 2012; Liu et al., 2009; Murphy et al., 2006). These bacteria have motors which are far more complex compared to enteric model organisms such as *E. coli* and *S. enterica*. Even though bacterial motors have core proteins which are conserved in all motors, the addition of proteins that facilitate function optimizes the function of the already conserved proteins.

3.5.4 Additional proteins keep stators in place in *C. jejuni*

The mechanism of generating rotation is thought to be conserved in motors. But stators incorporating into the motor to produce high torque has evolved. Stator units in *C. jejuni* have somehow evolved to be statically placed around the rotor or are high occupancy and dissociate from the rotor infrequently. These differences could be explained by the architectural differences found in *C. jejuni.* The additional proteins observed in the *C. jejuni* motor contribute to holding stator units in place. Genetic screening and co-immunoprecipitation assays identified proteins important for motility specific to *C. jejuni* many

of which have not been characterised. MotA has been shown to interact with an uncharacterized protein cjj81176_0199, also known as FlgX, also known as a chaperone for stator units and prevents degradation of stators from FtsH. (Gao et al., 2014; Ribardo et al., 2019). In this project I identified FlgX as a protein which contributes to holding MotA in place (statically) in *C. jejuni*. Since there was not a structure available of FlgX, AlphaFold2 CollabFold (v1.5.5) was used to generate an *in silico* structure of FlgX. The FlgX structure fit in the density under MotA which suggested its placement (Figure 3.3). This is the first time to our knowledge that any idea of the structure of FlgX was formed.

3.5.5 Stator motility without FlgX is restored by a mutation in MotA

FlgX is important for the retention of stators. When FlgX is deleted *C. jejuni* cannot swim, but a point mutation in $motA^{H138Y}$ can restore motility which is comparable to wild type *C. jejuni* (Ribardo *et al.*, 2019). I confirmed this using motility plates, the diameter suggested it does not swim as well as wild type but does form a halo suggesting the presence of stators. This suggests that when FlgX is not present stators cannot be incorporated into the motor however the point mutation allows some stators to be incorporated again. The small density hypothesized to be FlgX was also missing. By imaging the *C. jejuni* motor with this point mutation and the deletion of FlgX, I showed that stator units were not visible without FlgX even though stators were functional. This suggests that stators might be dynamic or only a few stators remain and are averaged out in the motor therefore not visible. We hypothesized that *C. jejuni* Δ*flgX* $motA^{H138Y}$ would incorporate stator units in a stepwise manner since it swims but STA shows that stator units are not anchored to the motor. Resurrection experiments partly supported our hypothesis since *C. jejuni* Δ*flgX* $motA^{H138Y}$ was slower than wild type *C. jejuni* but faster than *E. coli*. This suggests that stator units in *C. jejuni* Δ*flgX* $motA^{H138Y}$ have been de-stabilized and partly exhibits similar stator dynamics to *E. coli* (Figure 3.6).

3.5.6 Locating FlgX *in situ* using a tag did not confirm its placement in the flagellar motor

Since imaging the mutant did not confirm the placement of FlgX I added a tag to FlgX. The tag was an extended alpha helix with a lysozyme at the end to add an extra density. The reason I added lysozyme was because it was a rigid structure which also had an extended alpha helix. The flexible residues from both FlgX and lysozyme were removed to make sure the structure was fully rigid. In tomography, usually other tags such as metallotag which are very dense or DNA origami tags, or normal fluorescent tags like GFP are used but these tags could interfere with the motor. The structures were then confirmed in AlphaFold2 CollabFold (v1.5.5) and inserted into the density in the motor to check for any clashes with the C-ring as this would prevent the motor from swimming. Of the 12 mutants 5 were chosen as they looked like they would not clash according to what we thought was how FlgX fit into the structure. These designs were sent to our collaborator to be made Professor David Hendrixson (UT Southwestern

Medical Center). He made the mutants and checked whether these mutants swam on motility plates, the first 2 mutants (Fusion 1 and Fusion 3) swam comparably to wild type Fusion 2 could not be made and Fusion 7 and 9 swam less well. Therefore mutant 1 was imaged, it was the most promising from the AlphaFold2 CollabFold (v1.5.5) model and motility plates.

Cryo-electron tomography and subtomogram averaging were used to image FlgX fusion 1 to find the exact location of FlgX. Subtomogram average of the *C. jejuni* fusion mutant showed no presence of stator units or FlgX. By classifying the dataset in PEET we observed a class with stators and a class without stators suggesting that stators are incorporating into the motor. Since the mutant is motile, we know that stators are present, but cryo-electron tomography suggests that the fusion mutant has dynamic stator units. The addition of the tag has most likely de-stabilized FlgX which means MotA is degraded by FtsH which leads to MotA incorporating more frequently into the motor as opposed to high-occupancy or static stator units. The addition of protein tags has generally been unsuccessful because they tend to be flexible or bulky and affect the native state of the protein of interest. The lack of continuous presence of stators meant that the cytoplasmic ring was less disoriented. This led to finding the symmetry of the C-ring which is 38-fold symmetric. Although the location of FlgX could not be confirmed provides convincing evidence that the density under MotA could be FlgX which stabilizes stator units.

In this chapter I show that stator units in *C. jejuni* are statically placed around the flagellar motor using cryo-electron tomography and subtomogram averaging by imaging *C. jejuni* after its exposed to a protonophore. This result is supported by biophysical experiments performed by our collaborators. I further investigated a protein FlgX which keeps MotA statically in place. I show that without FlgX the stator units are not visible in subtomogram averages which suggests dynamic stator units. Biophysical experiments by our collaborators confirm that stator units exhibit more of a dynamic pattern once FlgX is not present. I imaged a tagged version of FlgX to confirm its location under MotA but the tag de-stabilised FlgX and the stator units. In this mutant we also suggest that stator units exhibit a dynamic behaviour because after classification stator units are seen in one class and not the other. De-stabilising stator units meant that there was less movement in the C-ring which means we could find the symmetry of the C-ring. Although there is still work to be done to confirm the location of FlgX we now have a better understanding for how *C. jejuni* has evolved its flagellar motor to swim a high viscous environment.

3.6 Methods

3.6.1 Cell growth

C. jejuni 81-176 was grown from a freezer stock on Mueller Hinton medium/ agar plates (24 g/L) with 10 µg/ml Trimethoprim at 37 °C under microaerobic conditions for 48 hours, the *C. jejuni* colonies were then re-streaked on a new Mueller Hinton medium/ agar plate (24 g/L) with 10 µg/ml Trimethoprim for 24 hours for sufficient colonies to grow. The mutant strains sent by David Hendrixson's lab were grown on Mueller Hinton medium/ agar plates (24 g/L) with 10 µg/ml Trimethoprim and 15 µg/ml Chloromphenicol.

Table 3.2 Strains used for this project

Strain name	Mutant	Source
C. jejuni wild type	*C. jejuni* 81-176	
Minicell-producing strain	*C. jejuni* Δ*flhG* Δ*flaAB*	This study (Eli Cohen, Imperial College London)
DRH8752	81-176 *rpsL*^{Sm} D*flgX*/pECO102::*flgX-lysozxyme fusion 1*	David Henderixson, UT Southwestern
DRH8754	81-176 *rpsL*^{Sm} D*flgX*/pECO102::*flgX-lysozxyme fusion 3*	David Henderixson, UT Southwestern
DRH8756	81-176 *rpsL*^{Sm} D*flgX*/pECO102::*flgX-lysozxyme fusion 7*	David Henderixson, UT Southwestern
DRH8758	81-176 *rpsL*^{Sm} D*flgX*/pECO102::*flgX-lysozxyme fusion 9*	David Henderixson, UT Southwestern
DAR5112	C. jejuni (DRH212 derivative), (motA H138Y; DFlgX)	Deborah Ribardo, UT Southwestern

3.6.2 Swimming speed videos

To compare bacterial swimming speeds, *C. jejuni* 81-176 (wild type) and the mutant strains (Table 3.2) were grown for 24 hours and then re-streaked and grown for another 24 hours. *C. jejuni* colonies were washed off from the plate using 1mL Mueller Hinton medium. 2 µl of the 2 mL washed cells was added to 100 µl of MH broth to get a final OD of 0.2. *C. jejuni* (WT and mutants) were visualised under the microscope. Cells were imaged at 100x oil immersion on a MT4000 series light microscope (Meiji

Techno) with a DMK23G618 digital camera connected to IC Capture software. Bacterial cells were tracked for 30 seconds using Fiji.

3.6.3 Motility Plates

C. jejuni mutant and wild type were stabbed into soft agar plates (0.4% agar w/v) at 37 °C under microaerobic conditions for 24 hours. An image of the plate was taken on The ChemiDoc XRS+ System (BioRad) The next day, halo of each mutant and wild type were measured.

3.6.4 Preparing *C. jejuni* for freezing grids

The plate was washed with 5mL of Mueller Hinton medium (24 g/L) and centrifuged at 5000 *x g* for 10 minutes. The supernatant was removed, pellets were pooled together and resuspended in 50 µl of Mueller Hinton medium. Separately, 10 nm gold fiducials were prepared by adding 133 µl to a 1.5 mL Eppendorf tube to which 33 µl of 5% BSA was added and vortexed for 30 seconds to mix the BSA with the gold fiducials 10 nm diameter suspended in PBS (ALDRICH). The fiducials were then centrifuged at 18,000 *x g* for 15 minutes to pellet the gold fiducials. 30 µl of resuspended *C. jejuni* pellet was then resuspended with the pelleted 10 nm gold fiducials once the supernatant from the fiducials was removed. R 2/200 quantifoil grids were glow discharged for one minute to which 3 µl of *C. jejuni* with gold fiducials mixture was pipetted. The grids were plunge frozen on the Vitrobot Mark IV at blot force 10 seconds, blot time 30 seconds, wait time 10 seconds. Grids were screened on the FEI Tecnai T12 transmission electron microscope to check for vitreous ice and optimal sample quantity and a tilt series was then collected on the Glacios™ with Falcon 4 DED and Selectris energy filter Cryo-Transmission Electron Microscope (Thermo Scientific™) with Falcon 4 DED and Selectris energy filter.

3.6.5 Cryo -Electron Tomography Data Acquisition

Tilt series of *C. jejuni* mutants (table 3.2) were collected on the Glacios™ Cryo-Transmission Electron Microscope (Thermo Scientific™) with Falcon 4 DED and Selectris energy filter operating at 200 keV with a total fluence of 120e-/ Å2 was used and a defocus of -2 to -5 µm. Tomograms were collected a tilt range of ± 60 with 3° tilt increments and a pixel size of 1.9 Å. Tilt series were collected using Leginon and tomo5 using a dose symmetric tilt scheme.

3.6.6 Tomogram Reconstruction and Processing

Tomogram reconstruction was done using personal scripts (written by Morgan). Each tilt stack was first binned by 4 times. This achieved a pixel size of 7.6 and a box size of 1024 with a Z height of 700. Each tilt series stack was auto-reconstructed using ETOMO which auto-reconstructs using fiducial-tracking based tilt series alignment in IMOD to align the tilt series. Tomograms were picked manually using IMOD. Subtomogram averaging was carried once in Dynamo using a custom mask to be focussed on

the rod to allow for optimal alignment and 17-fold symmetry because a clear 17 fold symmetry was observed in C1 alignments.

3.6.7 AlphaFold2 CollabFold (v1.5.5) Models

To find the *In silico* structure of FlgX and the structure of the FlgX: MotA complex, the sequence of FlgX was entered into AlphaFold2 Collab (Jumper et al., 2021).

Chapter 4

Additional proteins are incorporated into the motor to control rotor speed.

4.1 Chapter summary

Campylobacter jejuni is a polarly flagellated, pathogenic bacterium that swims in highly viscous environments of the intestinal epithelium. *C. jejuni* has adapted certain features which make it more favourable to swim in highly viscous environments compared to other flagellated bacteria such as *E. coli* and *S. enterica*. One curious characteristic is *C. jejuni*'s ability to increase its swimming speeds in high viscosity and slow down at lower viscosities. This characteristic is driven by differences in the architecture of *C. jejuni*'s flagellar motor compared to other bacterial species. *C. jejuni* harbours a more complex flagellar motor with more protein components compared to *E. coli* and *S. enterica*. For example, transmembrane proteins which power the flagellar motor remain statically attached to the motor in contrast to *E. coli* and *S. enterica* which helps *C. jejuni* maintain sufficient energy to power the motor at high viscosities. Although, *E. coli* serves as a model system for biophysical studies to study the mechanics of flagellar motors, it does not provide an explanation for *C. jejuni*'s ability to swim in high viscosity and limit speeds at lower viscosities. Previous studies have identified flagellar motor proteins which help modulate velocity. To contribute to the understanding of how *C. jejuni* controls motor output, I solve subtomogram averages of deletion mutants in the *C. jejuni* flagellar motor to locate proteins important for controlling velocity. My results in combination with our collaborators results (Professor David Hendrixson, UT Southwestern Medical Center) strongly suggest that previously identified motility proteins in *C. jejuni* flagellar motor make up a ring between the MS-ring and C-ring to modulate flagellar motor output. Whereas a different transient protein which interacts with the inner ring to reduce motility acting as a 'brake'.

4.2 Introduction

4.2.1 *C. jejuni'* s flagellar motor modulates viscosity dependent motor output

Campylobacter jejuni is a pathogenic bacterium that swims in high viscous environments of the intestine. *C. jejuni* is a flagellated bacterium, each flagellum is made up of a motor embedded in the membrane which spins an extracellular filament to move the bacterium forward. The flagellar motor entirely drives swimming in flagellated bacteria. Previous studies have observed *C. jejuni*'s ability to control swimming speeds. At high viscosity *C. jejuni* is known to swim faster whereas at low viscosity *C. jejuni* slows down (Ferrero and Lee, 1988; Shigematsu et al., 1998). Interestingly, the swimming speeds at low viscosity are comparable to bacteria with less powerful flagellar motors such as *E. coli/ S. enterica*. This type of swimming was originally described as corkscrewing through non-Newtonian fluids (Berg and Turner, 1979; Martinez et al., 2014; Schneider and Doetsch, 1974). But more recent discoveries show that *C. jejuni* has incorporated proteins in its flagellar motor to help it swim in high and low viscous environments (Ribardo et al., 2024).

The ability to increase swimming speeds in a high viscous environment is not common in flagellated bacteria. Usually, flagellated bacteria such as *E. coli* slow down and eventually stall at higher viscosities (Chen and Berg, 2000; Ryu et al., 2000). These differences in flagellar motor outputs are likely due to architectural differences in the flagellar motor which lead to mechanistic differences between *C. jejuni* and *E. coli*. Biophysical experiments to study the flagellar motor are generally conducted using *E. coli* as a model bacterium, but *E. coli* flagellar motors behave differently to *C. jejuni* flagellar motors. Therefore, to understand how high torque motors operate we need to conduct biophysical experiments on bacteria such as *C. jejuni*.

4.2.2 *C. jejuni*'s flagellar motor structure is built to favour a high viscous environment

The core structures of the flagellar motor can be divided into three parts which are the basal body, a central rod, and the universal joint known as the hook which connects the extracellular filament to the rotor. The basal body is composed of the MS-ring (Membrane and Supra-membrane ring) and a C-ring (Cytoplasmic ring) (Francis et al., 1994; Johnson et al., 2020; Lowenthal et al., 2009; Morimoto et al., 2014). To power the flagellar motor, transmembrane proteins called stator complexes (5MotA:2MotB per stator unit) take in protons and interact with the cytoplasmic ring to generate torque (Deme et al., 2020; Santiveri et al., 2020). As each stator is activated, MotB reaches up to bind to the peptidoglycan layer allowing protons into MotA. To drive rotation MotA interacts with the 'torque helix' of FliG in the C-ring. FliG then interacts with FliF which is located in the MS-ring to transport torque upwards towards the rest of the flagellar motor.

The core structures of a flagellar motor largely remain the same. But in bacteria whose flagellar motors produce high torque (section 1.9) differences in the behaviour of core subunits have been observed. For example, *C. jejuni* has a wider cytoplasmic ring in comparison to *S. enterica/E. coli* which increases the radial distance to which force is applied, this in turn generates high torque (Beeby et al., 2016) (Chapter 1, section 1.10). *C. jejuni* also has more stator units compared to *S. enterica/E. coli* and other species of bacterium. More stator units mean more ions can be used to power the flagellar motor. In Chapter 3 I show that stator units are statically present around the motor unlike *S. enterica/E. coli* where stator units are dynamic. This means stator units are readily present to power the motor at high viscosity and do not have to continuously re-associate into the motor. This is beneficial since *C. jejuni* mostly live in high viscous environments.

Cryo-electron microscopy has revealed diverse architectures of different flagellar motors in different species (section 1.6). In the subtomogram averages and single particle structure of the *C. jejuni* flagellar motor we observe additional scaffold structures and motility proteins which are not present in flagellar motors that produce low torque such as *S. enterica/E. coli* (Chaban et al., 2018; Drobnič et al., 2023). These additional structures have most likely contributed to *C. jejuni*'s ability to modulate its speed. The flagellar motor in *C. jejuni* has adapted to swim predominantly in a high viscous environment. Additional proteins could contribute to both speeding up and slowing down the motor when necessary. Novel motility proteins in *C. jejuni* have been identified using genetic screening but their location and interaction with other proteins is not fully understood (Gao et al., 2014). Here, I focus on a subset of proteins which are known to somehow play a role in modulating motor output. By identifying the locations of these proteins in *C. jejuni*'s flagellar motor we gain an understanding of how these proteins work together to modulate motor output.

4.2.3 A subset of motility proteins in the flagellar motor control velocity of *C. jejuni*

Previous studies have investigated identified motility proteins in *C. jejuni* (Gao et al., 2014). A subset of these proteins is known to contribute to motor output. An identified transmembrane protein called FlgV interacts with FliF as observed in co-immunoprecipitation assays. Previous research suggests that FlgV interacts with FliF to control torque output. FlgV also interacts two other lesser-known motility proteins VidA and CJJ81176_1732 (Gao et al., 2014). Cryo-electron tomography and STA were used to locate FlgV (Botting et al., 2022). Authors imaged a FlgV deletion mutant in a highly motile variant ($\Delta flgV_{G27M}$) of *Helicobacter pylori* which is also a member of the Campylobacterota. Deleting FlgV reduced swimming in motility agar and resulted in hypo-flagellation. Subtomogram averages of the mutants ($\Delta flgV_{B12}$ and $\Delta flgV_{G27M}$) and wild type *H. pylori* showed that a density located between the MS-ring and the C-ring are missing. (Figure 4.1).

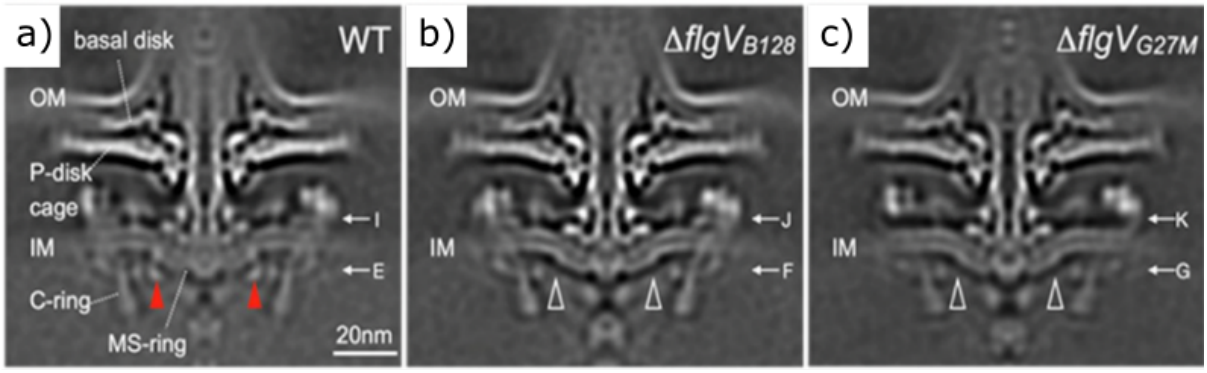


Figure 4.1 Subtomogram averages of *H. pylori*. a) *H. pylori* wild type b) *H. pylori* Δ*flgV*$_{B128}$ c) *H. pylori* Δ*flgV*$_{G27M}$. Figure and subtomogram averages adapted from (Botting et al., 2022).

VidA (viscosity-dependent determinant A) and VidB were identified by our collaborators (Professor Dave Hendrixson, Dr. Deborah Ribardo, UT Southwestern Medical Center). Both VidA and VidB are required for modulating speed at low viscosity. Although, the structure of VidA has been solved no biological context was provided for how it functions in the flagellar motor (Yokoyama et al., 2008). A previous study showed that deleting VidA reduces entry in mammalian cells suggesting it is required for colonization in hosts (Goon et al., 2006). Co-immunoprecipitation assays showed that VidA and FlgV somehow interact, but their exact function is unknown (Gao et al., 2014).

VidB was identified when looking for suppressor mutants in *C. jejuni* 81-176 Δ*vidA* to allow swimming at low viscosity. VidA and VidB somehow interact to control motor output at low viscosity. In a most recent study by our collaborators (Professor David Hendrixson, UT Southwestern Medical Center) VidA is known as an 'anti-brake' and helps *C. jejuni* increase speed by counteracting VidB which is known as the 'brake' protein (Ribardo et al., 2024). VidA and VidB are both essential for motility at low viscosity (below 1cP) but only VidA is required (to a lesser extent) at high viscosity (40cP). At low viscosity Δ*vidA C. jejuni* 81-176 swims badly but at high viscosity *C. jejuni* 81-176 Δ*vidA* regains motility but not as well as wild type *C. jejuni*. To regain motility at low viscosity in *C. jejuni* 81-176 Δ*vidA*, VidB must be inactive which suggests it partly inhibits the activity of VidA, therefore, acting as a brake. Although the *C. jejuni* 81-176 Δ*vidA* has reduced ability to colonize chick ceca, *C. jejuni* 81-176 Δ*vidB* does not impact chick ceca compared to wild type therefore is only required as a 'brake' but not for colonization.

The predicted protein structure of VidB has a GGDEF domain which is known as a regulatory domain. In most cases it acts a diguanylate cyclase which synthesizes cyclic di-GMP. Although, *C. jejuni*'s regulatory mechanism does not involve cyclic di-GMP. This domain is also found in another *C. jejuni* protein CbrR which is related to biofilm formation and also interacts with chemotaxis protein cheA (Cox et al., 2021; Elgamoudi et al., 2022). To investigate whether VidB supresses motility in *C. jejuni*

Δ*vidA*, our collaborators measured velocity in *C. jejuni* Δ*vidA* Δ*vidB*. Compared to *C. jejuni* Δ*vidA*, *C. jejuni* Δ*vidA* Δ*vidB* swam significantly faster at low viscosity (Ribardo et al., 2024). *C. jejuni* Δ*vidA* Δ*vidB* had a measured velocity of 27.8 μm/s whereas *C. jejuni* Δ*vidA* only had a velocity of 2.6 μm/s which shows that VidB does act as a 'brake' and limits motility at low viscosity. *C. jejuni* Δ*vidA* Δ*vidB* also swam 2.5 times faster than wild type *C. jejuni* which shows that both VidA and VidB work together to control motor output at low viscosity. At high viscosity *C. jejuni* Δ*vidA* Δ*vidB* swims comparably to low viscosity and swims to the same levels as wild type *C. jejuni* which shows that VidA and VidB are primarily required for swimming at low viscosity.

Lastly, a protein CJJ81176_1732 was found to interact with both VidA and FlgV in co-immunoprecipitation assays (Gao et al., 2014). Motility assays by our collaborators Dave Hendrixson showed that *C. jejuni* swims at a constant velocity when CJJ81176_1732 is deleted (unpublished data). CJJ81176_1732 may act as a bridge between FlgV and VidA.

In summary, *C. jejuni* swims faster at high viscosity and slows down at low viscosity. To control speed *C. jejuni* depends on its flagellar motor. *C. jejuni* rotates using a filament attached to a motor to move the bacterium forward. The flagellar motor constitutes proteins that help control motor output. A subset of proteins has been identified which interact with core flagellar motor to control rotation in the motor. Of these proteins, FlgV interacts with the MS-ring and supposedly acts as a bridge between the MS-ring and C-ring. VidA and VidB modulate motor output at low viscosity. VidA interacts with FlgV and is an 'anti-brake'; VidB counteracts VidA and acts as a 'brake' but VidA is required to make sure VidB does not completely stop motility at low viscosity. CJJ81176_1732 somehow interacts with FlgV to control rotation (Figure 4.2). By finding the locations of these proteins we could gain an understanding of how they work together to control motor output.

4.2.4 Aims

The aim of this project was to gain an understanding of the mechanism required to control flagellar motor output in *C. jejuni* under high and low viscosities. I did this by finding the location of already identified motility proteins (FlgV, VidA, VidB, CJJ81176_1732) required for controlling flagellar motor output to better understand how these proteins work together to control velocity of *C. jejuni*.

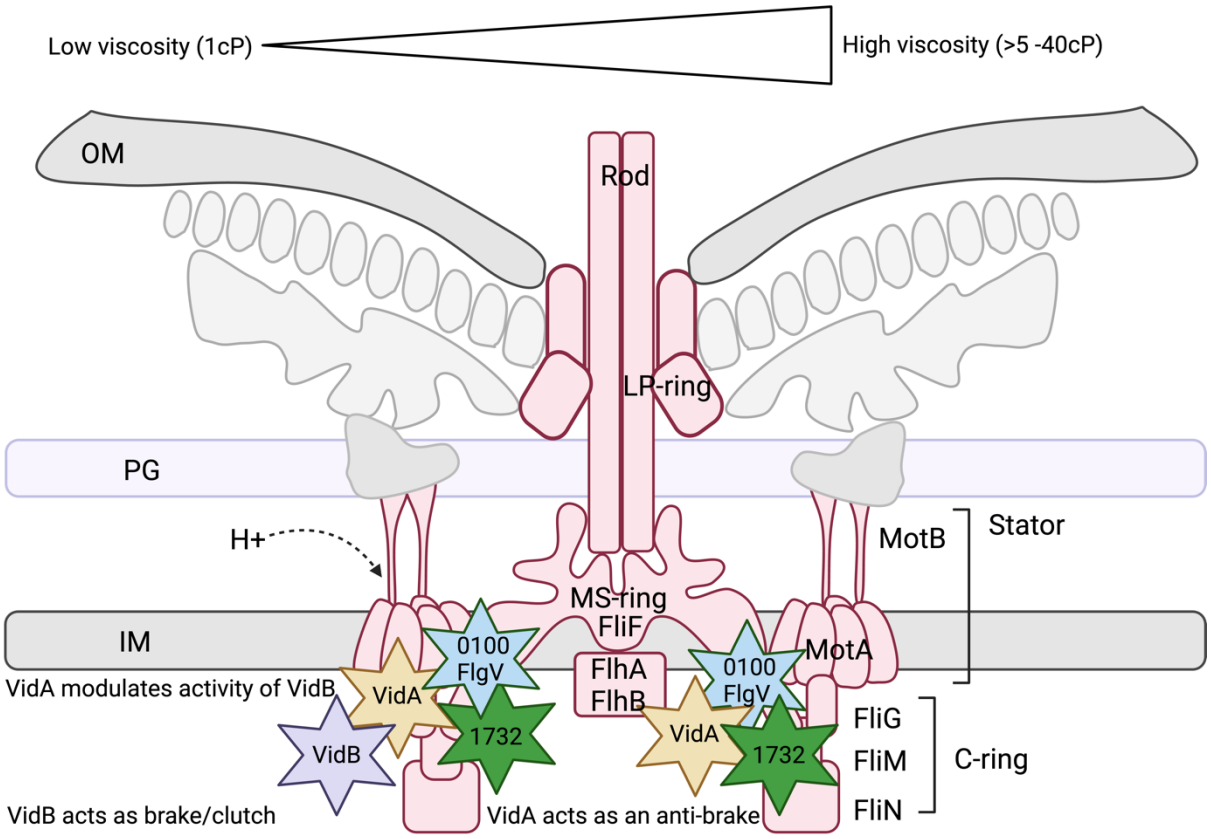


Figure 4.2 Shows the putative location of proteins FlgV (CJJ81176_0100), VidA (CJJ81176_0996), VidB (CJJ81176_1107) and CJJ81176_1732 and their potential interactions in the motor to control velocity.

4.3 Results

4.3.1 Initial Screening of Mutants

To investigate each mutant for differences in cell morphology, I froze grids of mutants *C. jejuni* 81-176 Δ*vidA*, Δ*vidA* Δ*vidB* and Δ*1732* on R2/2 200 and R2/2 100 grids. I screened the grids on the FEI Tecnai T12 transmission electron microscope. Images captured on the microscope showed that *C. jejuni* cells had filaments on both poles and there was no change in the morphology of the cell (Figure 4.3).

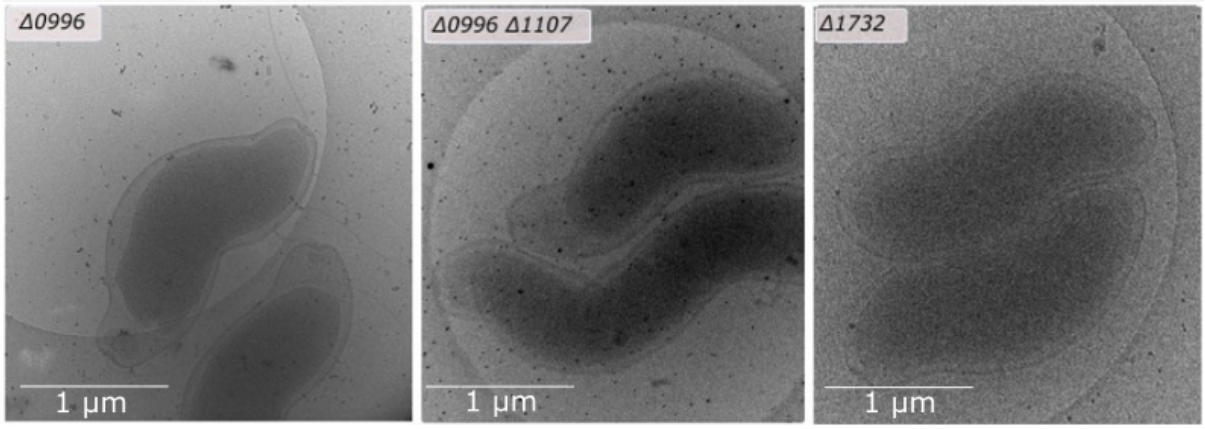


Figure 4.3 *C. jejuni* cells were screened on the T12 microscope (Thermofisher Scientific™) before data collection. Left to Right - *C. jejuni* 81-176 Δ*vidA*, *C. jejuni* 81-176 Δ*vidA* Δ*vidB* and *C. jejuni* 81-176 Δ*1732*.

4.3.2 VidA deletion reduces the size of the density between the MS- and N-terminus of FliG

Cryo-electron tomography and subtomogram averaging was used to locate VidA. *C. jejuni* 81-176 Δ*vidA* was obtained from our collaborator Professor Dave Hendrixson (UT Southwestern Medical Center) and imaged. At the final stages of STA 17-fold symmetry was imposed. The 17-fold symmetrised *C. jejuni* 81-176 Δ*vidA* subtomogram average was compared to wild type (Figure 4.4 a) *C. jejuni* 81-176 Δ*vidA* (Figure 4.4 b) showed that the ring between the MS-ring and MS ring and N-terminus of FliG reduced in size. This result suggests that the density between the MS-ring and N-terminus of FliG originally thought to be just FlgV is suggested to be a complex of VidA and FlgV.

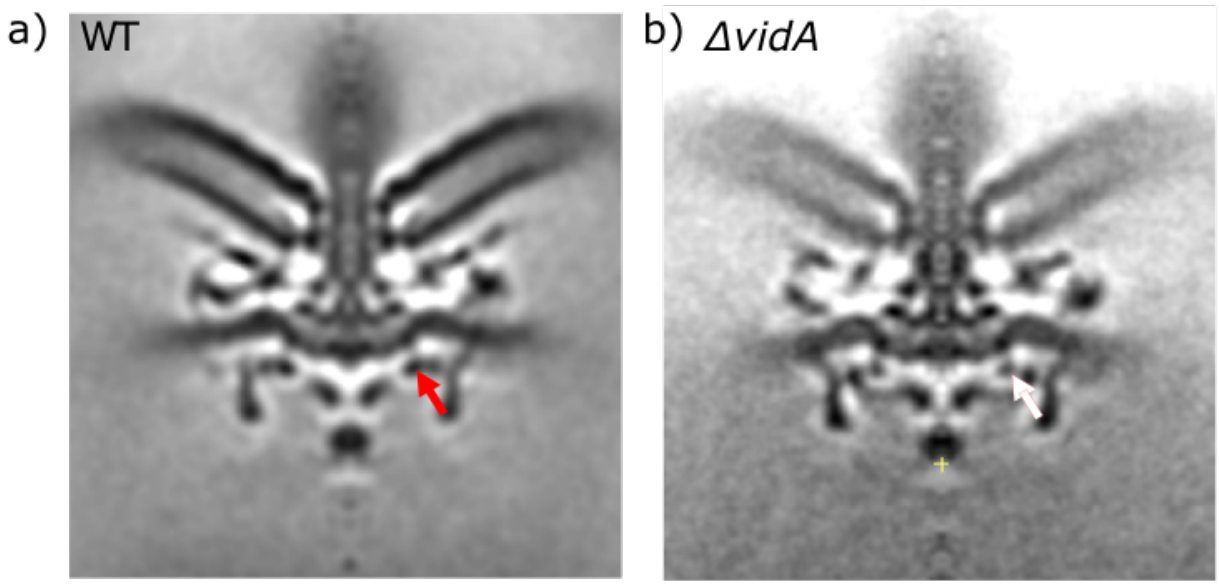


Figure 4.4 Subtomogram average of *C. jejuni* Δ*vidA* reveals a smaller density between the MS-ring and C-ring compared to *C. jejuni* wild type. a) Subtomogram average of wild type *C.* jejuni (Beeby et al., 2016), C17, the red arrow highlights a larger density between the MS-ring and FliG. b) Subtomogram average of C17 symmetrized *C. jejuni* 81-176 Δ*vidA*, the arrow highlights a decrease in the density between the MS-ring and FliG.

Compared to wild type (Figure 4.5 a), the C17 symmetric motor of *C. jejuni* Δ*vidA* showed the presence of an extra 'bridge' like density between FlhA and FliG (Figure 4.5 b). The C1 structure of Δ*vidA* shows a density interacting with the C-ring (Figure 4.5 c, d). Suggesting, the presence of VidA could inhibit a protein and when Δ*vidA* is deleted the protein re-attaches itself to the motor. Since our collaborators (Professor David Hendrixson, UT Southwestern Medical Center) suggests that deleting VidA means VidB is more active and affects *C. jejuni*'s swimming abilities, VidB could be the 'bridge' density between FlhA and FliG.

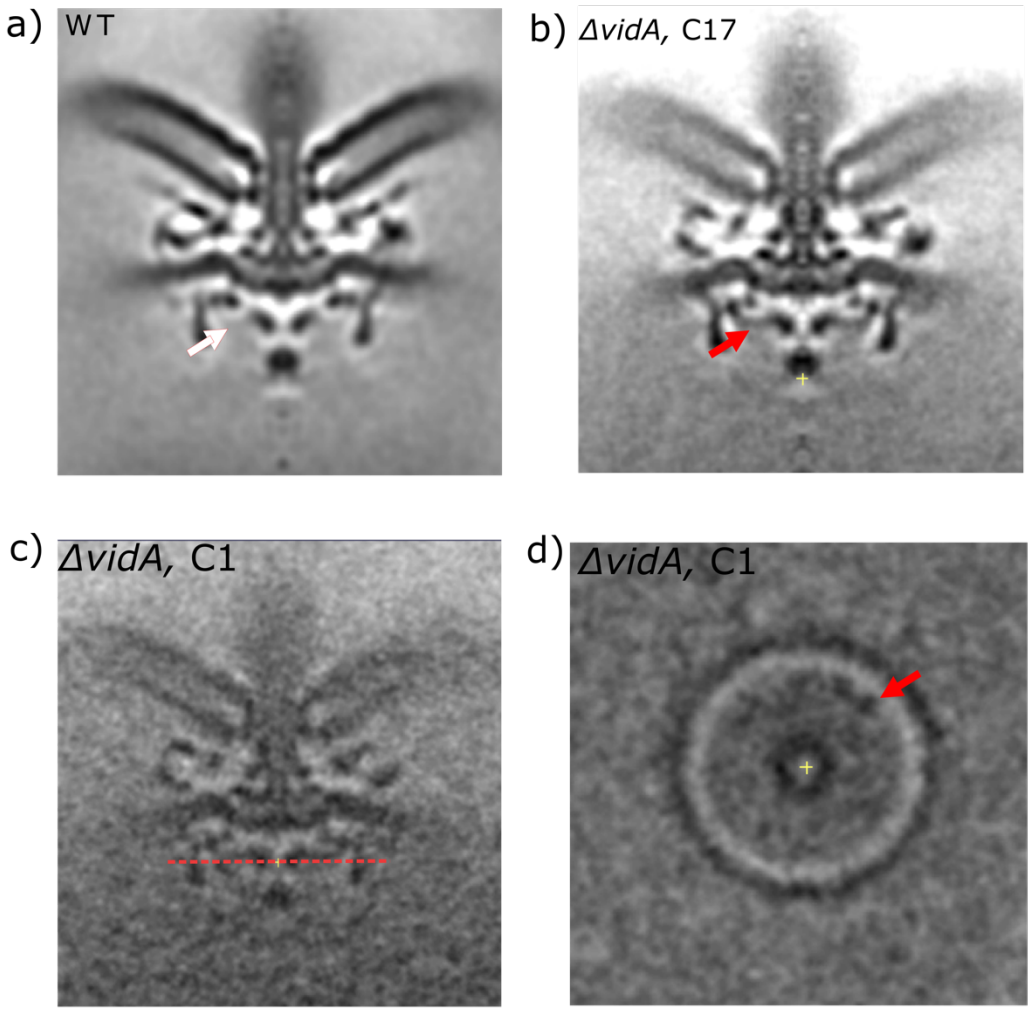


Figure 4.5 Subtomogram average of *C. jejuni* ΔvidA reveals unknown density interacting with the C-ring. Subtomogram average of wild type *C. jejuni* (Beeby et al., 2016)., C17 symmetry, arrow highlights there is no 'bridge' present between FlhA and FliG; b) Subtomogram average of *C. jejuni* 81-176 Δ*vidA* mutant, C17 symmetry to provide higher contrast, the red arrow highlights the 'bridge' density which is now more visible; c) Subtomogram average of *C. jejuni* 81-176 Δ*vidA* mutant, C1 symmetry, the red arrow highlights the extra 'bridge' density found between FlhA and the FliG; d) Subtomogram average of *C. jejuni* 81-176 Δ*vidA* mutant, C1 symmetry, the red arrow highlights the extra 'bridge' density which corresponds to e) view which interacts with the C-ring.

4.3.3 Deleting VidA and VidB does not remove the density between FlhA and FliG

Next, I investigated the location of VidB. To investigate if the putative density between FlhA and FliG is VidB, I imaged a *C. jejuni* 81-176 Δ*vidA* Δ*vidB* mutant (mutant was provided by Professor David Hendrixson, UT Southwestern Medical Center) to check whether the 'bridge' density is missing. In the

C17 symmetrized subtomogram averages the 'bridge' density interacting with the C-ring was still present (Figure 4.6 b, green arrow), the VidA density was also missing (Figure 4.6 b, white-red arrow). The 'bridge' density was not VidB and no other densities were missing in the motor when compared to wild type (Figure 4.6 a, white-green arrow).

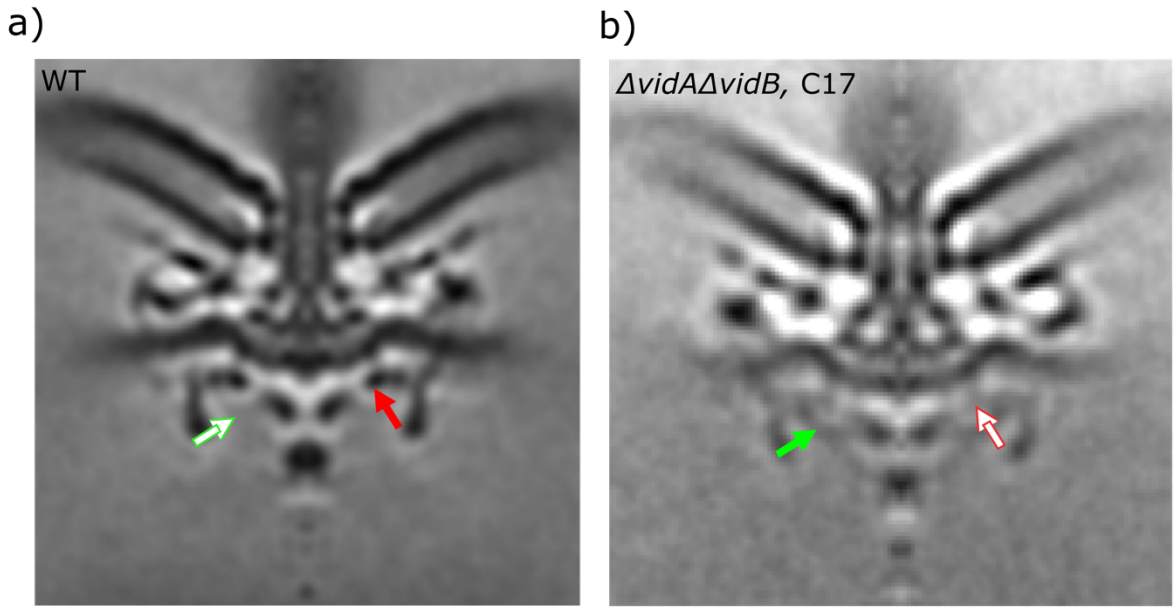


Figure 4.6 Subtomogram average of *C. jejuni* Δ*vidA* Δ*vidB* reveals the same missing density as observed in *C. jejuni* Δ*vidA* but the hypothesized VidB density remains. a) wild type *C. jejuni* (Beeby et al., 2016). The green arrow shows VidA density, and the red arrow shows the missing bridge density. b) C17 symmetrized subtomogram average of *C. jejuni* 81-176 Δ*vidA* Δ*vidB*. The green arrow shows the missing VidA density and red arrow shows the 'bridge density' between the C-ring and FlhA.

4.3.4 CJJ81176_1732 deletion removes the FlgV density in *C. jejuni*

I investigated the location of CJJ81176_1732 in the *C. jejuni* flagellar motor which is known to interact with FlgV. Our collaborators (Professor David Hendrixson, UT Southwestern Medical Center) showed that *C. jejuni* 81-176 Δ*1732* mutant swims at a constant velocity regardless of viscosity (unpublished data). The *C. jejuni* 81-176 Δ*1732* mutant was imaged by cryo-electron tomography and subtomogram averaging (mutant was provided by Professor David Hendrixson, UT Southwestern Medical Center). When compared to a subtomogram average of wild type *C. jejuni* (Figure 4.7 a) C17 symmetrized subtomogram average of *C. jejuni* 81-176 Δ*1732* showed the inner density between MS-ring and FliG N-terminus was missing (Figure 4.7 b). This density was originally thought to be FlgV (section 4.2.4, Figure 4.1). Therefore, either CJJ81176_1732 is essential in the recruitment of FlgV/ VidA (CJJ81176_0996) or it is part of the FlgV density. To compare, a deletion of FlgV in *C. jejuni* was also collected which shows the inner ring to be missing as expected (dataset collected by Dr. Trishant Umrekar, Imperial College London) (Figure 4.7 c). Although, after focused refinement on the C-ring,

an extra density was observed in *C. jejuni* 81-176 Δ*flgV* that was not observed in *C. jejuni* 81-176 Δ*1732* (Figure 4.7 d). In the C1 symmetric structure a similar density was observed interacting with the C-ring as observed in *C. jejuni* 81-176 Δ*VidA* (Figure 4.5 d compared to Figure 4.7 e).

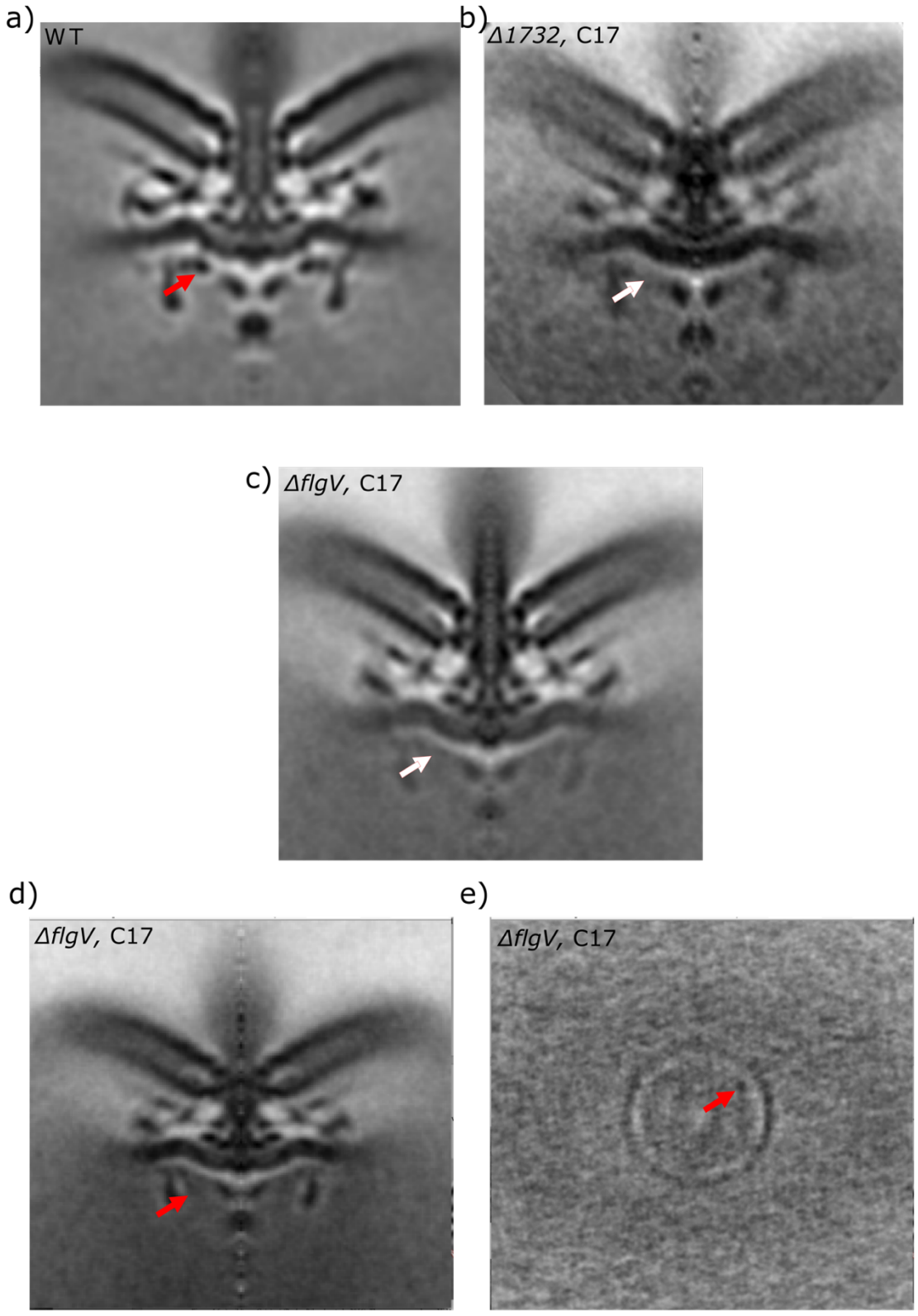


Figure 4.7 Subtomogram average of *C. jejuni* Δ*flgV* reveals part-ring formation between the MS-ring and C-ring and a density interacting with the C-ring. Subtomogram average of wild type *C. jejuni* (Beeby et al., 2016). B) subtomogram average of *C. jejuni 81-176 Δ1732* c) subtomogram average of *C. jejuni 81-176* Δ*flgV*. D) focused refined structure of *C. jejuni 81-176* Δ*flgV,* red arrow points to extra density. E) C1 structure of *C. jejuni 81-176* Δ*flgV*, red arrow shows extra density interacting with the C-ring.

4.3.5 The putative FlgV ring is 20-fold symmetric in *C. jejuni*

The lab previously collected a minicell dataset for another project where over 1000 tilt series were collected. My supervisor Dr. Morgan Beeby used PEET for subtomogram averaging with a focused mask around FlgV with randomized searches around the Z-axis to find symmetry. The final C1 symmetric subtomogram averaged showed a 20-fold symmetric FlgV ring (Figure 4.8).

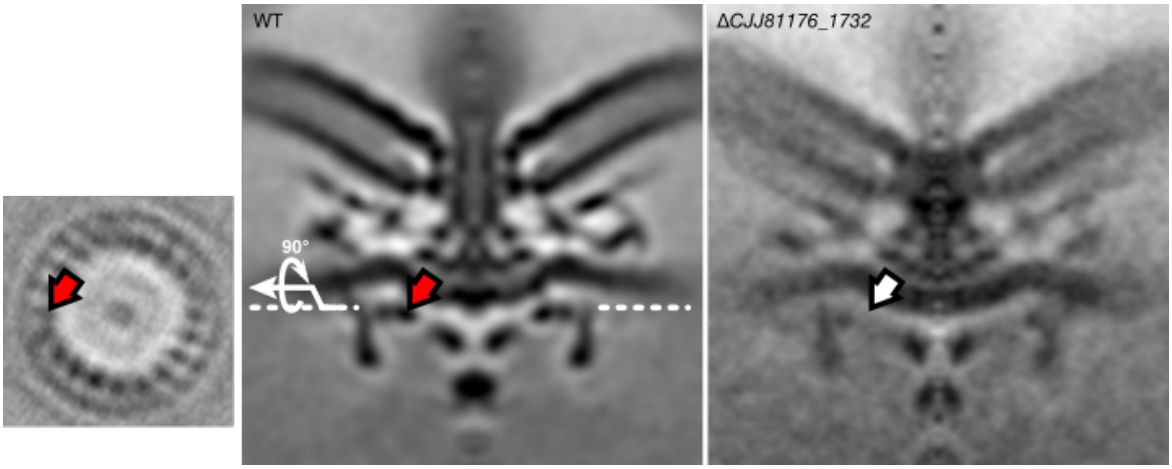


Figure 4.8 Subtomogram average of wild type *C. jejuni* reveals 20-fold symmetric ring between the MS-ring and C-ring. Left to right - subtomogram average of wild type *C. jejuni* rotated 90° to show 20-fold symmetry of the putative FlgV ring (density between MS-ring and FliG). Subtomogram average of *C. jejuni 81-176 Δ1732* the density between the MS-ring and FliG is missing (highlighted by the arrow) (figure made by Dr. Morgan Beeby).

4.3.6 Attempting to obtain a 20-fold symmetric ring in the single particle flagellar motor structure in *C. jejuni*

Subtomogram average of *C. jejuni* minicells showed that the FlgV ring in the cytoplasm is 20-fold symmetric (section 4.3.5) albeit at low resolution. To decipher the proteins that constitute the inner ring (including FlgV) the structure needed to be solved at a higher resolution (<10 Å). Therefore, a previously collected dataset of *C. jejuni* minicells was re-processed. As introduced in Chapter 2 (section 2.2.4 - 2.2.5), minicells are smaller cells that are a product of mis-localization of the septum during cell division. Minicells are smaller than wild type and are thinner and therefore the final resolution of the minicell flagellar motor when processed by single particle analysis is higher than that of a STA flagellar motor structure. The *C. jejuni* minicell dataset was re-processed in RELION 3.1 to focus on the inner ring of the motor (dataset from Chapter 2).

To find other symmetries in the motor an existing 'data.star' file corresponding to a C17 refined motor with the appropriate Psi, Tilt and Rot coordinates was edited to randomise the Rot values. Rot is rotation around the z-axis, tilt is the rotation around the new y-axis (after applying rot) and Psi is a final z-axis rotation. By using my best high-resolution C17 structure I was able to keep accurate Rot and Tilt values for parts of the motor that were not 17-fold symmetric such as the FlgV ring (scripts for this were written by Josh Parks, undergraduate student, Imperial College London). Restricted searches were performed in Psi to find symmetry mismatched components.

As observed in Chapter 2, the *C. jejuni* minicell single particle structure (Figure 4.9 a) was much higher resolution compared to subtomogram average (Figure 4.9 b). The inner ring in the single particle structure of the motor reveals more distinct features compared to subtomogram average of *C. jejuni* (Figure 4.9 c). Core structures of the flagellar motor are highlighted in Figure 4.9 (d). To investigate the conformations of these densities in the inner ring I re-processed the dataset in attempts to obtain a 20-fold symmetric ring.

The single particle *C. jejuni* minicell dataset was processed in RELION 3.1, first the Rot Priors were randomised using specialised scripts (written by Josh Park, Imperial College London). A 3D classification was run with new offsets (sigma rot =1, sigma tilt = 1, sigma psi = 60), this was used as an input for future runs. Results were compared to the *C. jejuni* refined motor structure (Figure 4.9 a). As observed in Figure 4.9 (e), a larger offset range (20 pix) and a randomised reference map yielded a motor with no symmetry in top view but a full motor structure in size view. When the reference map was changed to a subtomogram average with 20-fold symmetric inner ring, the final motor was lower in resolution compared to wild type and increasing the search range did not improve the motor (Figure 4.9 f, g, h). As a control, a 3D classification job was performed with a C17 symmetric reference map, but no symmetry was imposed. Relion could not 'find' the 17-fold symmetry without it being imposed on the motor (Figure 4.9 i). Lastly 3D refinement was attempted with a mask in the cytoplasmic region of the motor and C20 symmetry was imposed but this produced an artefact 20-fold symmetric ring. Decreasing or increasing the search range did not improve the result (Figure 4.9 j, k). Although the C-terminal regions of CJJ81176_0996 are still not well resolved, perhaps they are in contact with proteins of the membrane.

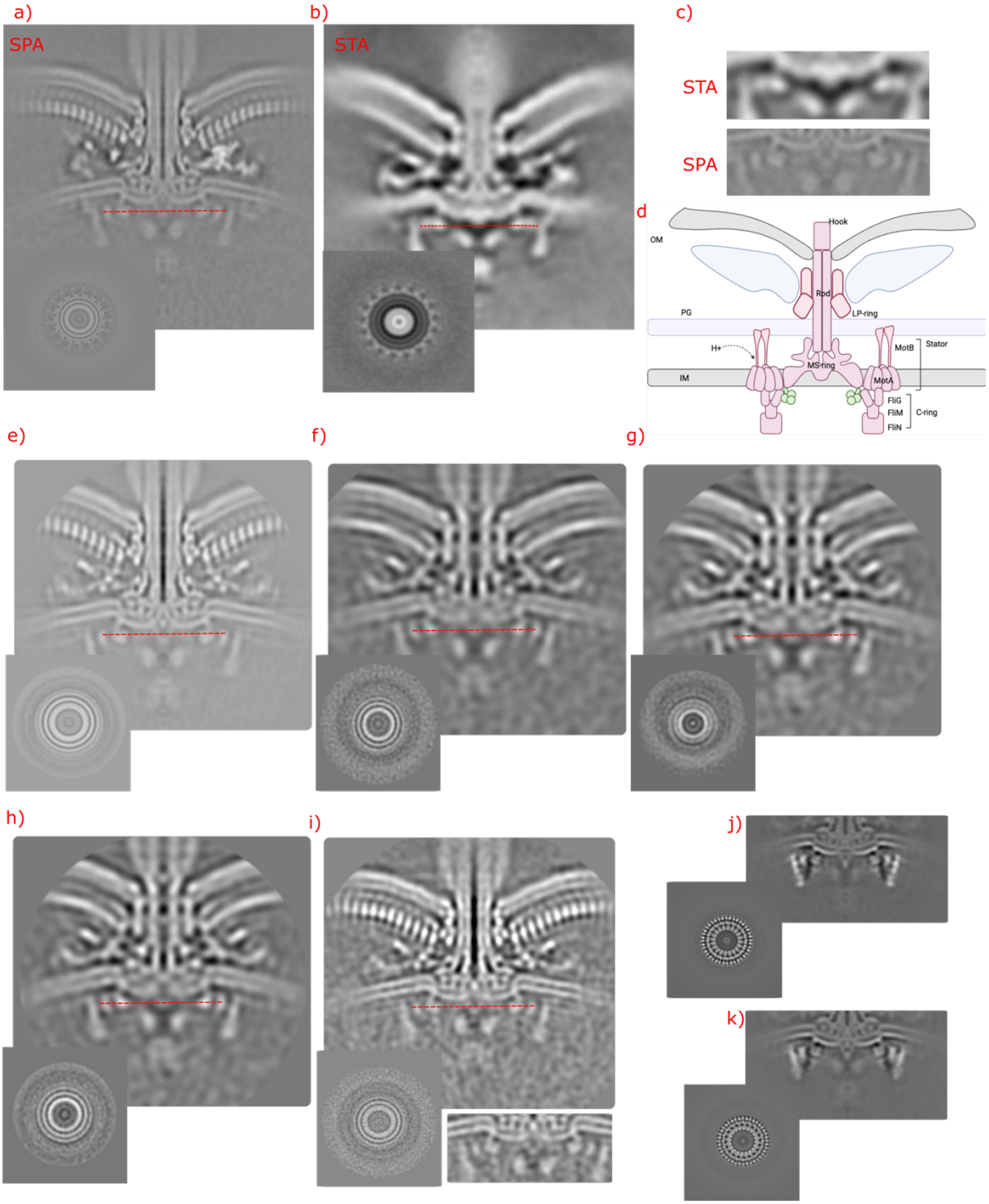
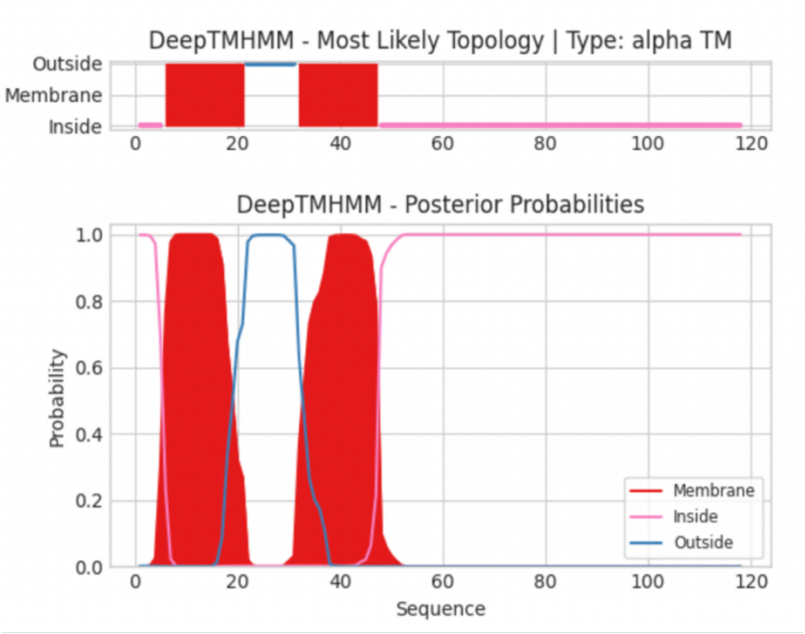


Figure 4.9 Single Particle analysis of minicells shows the density between MS-ring and C-ring encompasses 4 subunits. a) SPA structure of *C. jejuni* minicell flagellar motor, b) STA structure of *C. jejuni* minicell flagellar motor, c) comparison of the cytoplasmic region of the motor using STA versus SPA, d) schematic image of a motor, green area highlights the inner ring made of four proteins, e) 3D classification using randomised map and wider offset range. *C. jejuni* flagellar motor maps in f), g), h) are 3D wider increased search ranges to find symmetry of the inner ring, i) 3D classification in C1 using C17 reference map without symmetry being imposed. j) k) C-20 symmetry imposed with increasing search ranges.

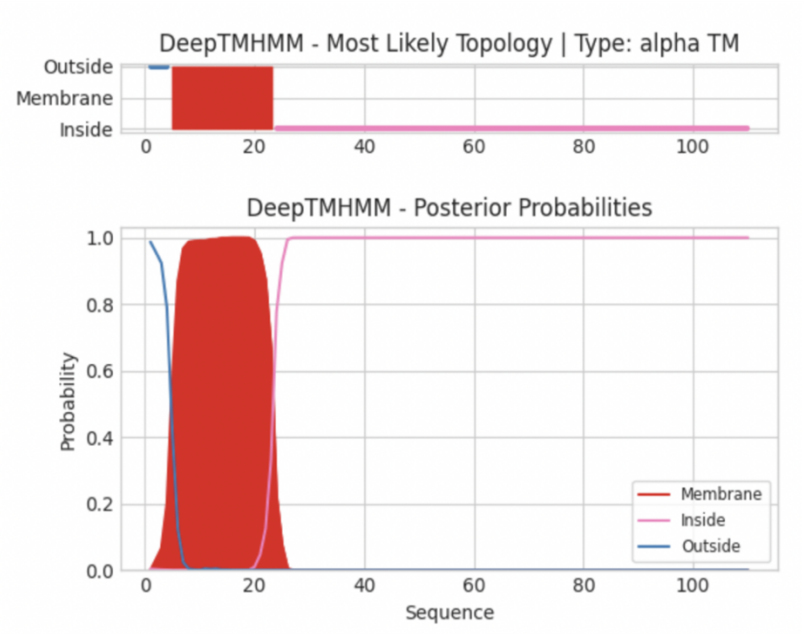
In attempt to understand the stoichiometry of proteins that make up the inner ring I used AlphaFold2 (ColabFold v1.5.1) to predict individual protein structures and protein complexes between FlgV, VidA, VidB, CJJ81176_1732 and CJJ81176_1107. This would be useful to gain a biological understanding of how these proteins could fit together in the flagellar motor and I could then validate these complexes using genetic studies and cryo-electron microscopy. ColabFold provided a predicted protein structure and a Predicted Aligned Error (PAE) plot measured in Angstroms which measures confidence in orientations of the two proteins in a complex. The PAE plots and the predicted protein structures (data not shown) showed low confidence predictions. Although a few residues had a high confidence score most of the structure was not reliable. Membrane proteins are challenging to predict, as shown using DeepTMHMM, proteins FlgV and CJJ81176_1732 are partly embedded in the membrane (Figure 4.10).

a)



>CJJ81176_0100
MRPENYVAFFTVCGFFIGLTFSIISIDEAFDILIFTCFITFMFYVFVHIAIMNFIDVKKISGRIF
NKHDYEKTSNNIINDLVIREKKMDIILEKLNEEREELKKNEFKERRRNAKRAA

b)



>CJJ81176_1732
MFTNWLVLTILICATIYLIVMLFYYKTLLNKEKTSKDFIKNNLDDTEIVIRKLQIQLQRSLGNI
DILTEELNKIKADLTSLRTRNSQYRLENDKLRQRIKELEAKIEALL

Figure 4.10 DeepTMHMM transmembrane topology plots of a) FlgV and b) CJJ81176_1732.

4.4 Discussion

4.4.1 Summary of previous research and results

C. jejuni is a polarly flagellated bacterium which predominantly swims in a high viscous environment (Ferrero and Lee, 1988; Karim et al., 1998; Shigematsu et al., 1998). Evolutionary adaptations that allow for *C. jejuni* to swim in high viscosity are not fully understood. *C. jejuni* can modulate its swimming speeds to swim slower at low viscosity and speed up at high viscosity. Studies have identified specific proteins located in the flagellar motor of *C. jejuni* that allow it to fine-tune its motor output to control swimming speeds (Gao et al., 2014). I investigated this mechanism using cryo-electron tomography and subtomogram averaging to find the location of previously identified proteins.

Co-immunoprecipitation assays showed that VidA interacts with FliF. This suggests that VidA could interact with FliF to directly control flagellar motor output (Gao et al., 2014; Ribardo et al., 2024). Our collaborators showed that VidA is required when the cell swims at low viscosity to maintain swimming speeds. VidA can be partly inhibited by VidB which acts as a 'brake' at low viscosity. Both VidA and VidB are essential for *C. jejuni*'s flagellar motor output at low viscosity. Another protein CJJ81176_1732 also interacts with FlgV to somehow fine-tune velocity (Gao et al., 2014). Deleting CJJ81176_1732 in *C. jejuni*'s flagellar motor output produces constant velocity at any viscosity.

To identify the location of each of these proteins I imaged deletion mutants of VidA, VidB, FlgV and CJJ81176_1732. I found that FlgV, VidA and CJJ81176_1732 are located in the 'inner ring' between the MS-ring and the N-terminal region of FliG. In contrast to previous research which showed that the inner ring consists of only FlgV subunits (Botting et al., 2022). I present work by my supervisor Dr. Morgan Beeby showing that *C. jejuni*'s inner ring is 20-fold symmetric. Here, I discuss each finding leading to these results.

4.4.2 VidA interacts with FlgV to control velocity

Subtomogram average of a VidA deletion in *C. jejuni* showed that the density between the MS-ring and N-terminal region of FliG becomes smaller (Figure 4.4 b). This result suggests that the inner ring between FliF and FliG is composed of VidA and FlgV. The single particle structure of *C. jejuni* shows that each spoke in the inner ring is made of four domains which supports this finding (Figure 4.9 c).

Our collaborators show that VidA interacts with the flagellar motor mainly at low viscosity to maintain swimming. Previous research showed that VidA directly interacts with FlgV (Gao et al., 2014; Ribardo

et al., 2024). FlgV itself is shown to interact with FliF a core flagellar protein in the MS-ring. My findings suggest that VidA and FlgV permanently interact and VidA simply changes conformation once the flagellar motor senses low viscosity. This changes a conformation in FlgV which interacts with FliF to change flagellar motor output.

The crystal structure of VidA where the HotDog domain of dimer was resolved but the disordered regions of VidA which are possible interacting regions did not resolve (Yokoyama et al., 2008). Although no biological function was associated with the structure in the paper by Yokoyama and co-authors, site-directed mutagenesis and invasion assays showed acyl-CoA binding sites in VidA are important for invading hosts. But catalytic sites that are usually required for a thioesterase are lacking in VidA even though both have hotdog-domains and similar structures. This paper suggests that the N-terminal domain is the major structural domain whereas the smaller C-terminal domain is the disordered functional domain which changes conformation to a more ordered state once it's bound to a yet unknown protein. I used AlphaFold2 to predict a complex between the dimeric VidA and FlgV but the final structure and PAE plot was predicted to very low confidence (data not shown). Possibly, because the interacting sites in VidA are disordered and the transmembrane regions of FlgV are challenging to predict.

4.4.3 CJJ81176_1732 is important for the stability of FlgV and VidA

CJJ81176_1732 is a membrane protein that interacts with VidA and FlgV as shown in co-immunoprecipitation assays. A CJJ81176_1732 deletion mutant swims at a constant velocity in liquid media which implies it somehow controls velocity. Subtomogram average of the CJJ81176_1732 deletion mutant shows that similarly to a FlgV deletion the inner ring is a missing density (Figure 4.7 b; Figure 4.7 c). This result suggests that CJJ81176_1732 is required for the stability of the inner ring. Although, CJJ81176_1732 was shown to be important for the inner ring, its exact role in the motor remains unknown.

4.4.4 FlgV is important for the stability of CJJ81176_1732 and VidA

Subtomogram average of the FlgV deletion mutant in *C. jejuni* showed that the 'inner-ring' density was missing in *C. jejuni* (Figure 4.7 c). A small protein interacting with the C-ring was identified in the subtomogram average *C. jejuni* 81-176 Δ*flgV* (Figure 4.7 e) which was also identified in the subtomogram average of *C. jejuni* 81-176 Δ*vidA.*

The missing 'inner ring' result is supported by Botting and co-authors who found that deleting FlgV in *H. pylori* also removes the inner ring between FliF and FliG N-terminus (Figure 4.1) (Botting et al.,

2022). *H. pylori* is a member of the Campylobacterota, members of this phylum do not have a sequence similarity for FlgV, but they do have conserved GxxxG domain which is usually important for protein-protein interactions. Botting and co-authors suggested GFFxG in the first transmembrane helix of *H. pylori* FlgV may be important for the interaction between FliF and FlgV.

AlphaFold2 prediction of *C. jejuni* FlgV with FliF was also predicted by Botting *et al.* The co-authors modelled conserved transmembrane residues Phe-15 and Phe-16 in *H. pylori* FlgV and Phe-466 and Tyr-467 in FliF, located in the transmembrane helix near the C-terminus. Their predicted model showed chains were 4.4 Å of each other (so high confidence) but the overall protein complex was low confidence. The conserved residues Phe-15 and Phe-16 in FlgV and Phe-459 and Tyr-460 in FliF are also present in *C. jejuni* (Figure 4.11). Since, the overall predicted model is low confidence in the paper and my research, the predicted interacting residues are not reliable.

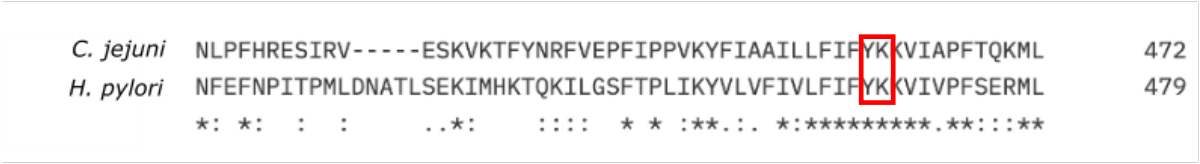


Figure 4.11 Region of sequences from *C. jejuni* and *H. pylori* from an MSA analysis highlighting residues in FliF which are hypothesized to interact with FlgV.

4.4.5 The inner ring between the MS-ring and FliG N-terminus is 20-fold symmetric

Subtomogram averages of wild type *C. jejuni* showed that the inner ring is 20-fold symmetric, and a previous mutant (fusion 1, Chapter 3) showed that the C-ring in *C. jejuni* is 38-fold symmetric. This is comparable to a paper which showed that FlgV in *H. pylori* is 21-fold symmetric and *H. pylori*'s C-ring is 39-fold symmetric. The paper by Botting and colleagues is consistent with my research since motors incorporate wider C-ring's as well as other core motor components to provide higher torque. The torque for *C. jejuni* is estimated to be similar to that of *H. pylori* around ~3600 pN·nm since both are from the Campylobacterota phylum (Celli et al., 2009). Therefore, it is expected that both have similar stoichiometries of core protein subunits.

4.4.6 20-fold symmetric structure could not be imposed on the single particle structure of the flagellar motor in *C. jejuni* minicells

The single particle structure of the flagellar motor in *C. jejuni* minicells revealed multiple protein densities that form the inner ring between the MS-ring and the C-ring. Subtomogram averages of wild type *C. jejuni* processed by Morgan showed a 20-fold symmetric inner ring. I imposed 20-fold

symmetry on the single particle structure of the motor imaged in *C. jejuni* minicells to aim for a higher resolution structure of the inner ring. But the final 3D refinement was an artefact of imposing 20-fold symmetry as opposed to a 'true' 20-fold symmetric structure. I attempted to resolve the structure of *C. jejuni*'s flagellar motor in C1 symmetry (as did other members of the lab), but we were unable to do so. The reason for this could be high symmetry mismatch in the motor structure and high orientation bias because the filament and hook determine the position of the bacterium flagellar motor on the grid (Drobnič et al., 2023; Johnson et al., 2020).

Limitations in resolving the symmetry of FlgV include fewer views of the motor which were obtained by single particle analysis compared to tomography providing lesser information in the Z axis, thus angular distribution is not well spread. Although the stoichiometry could not be achieved, we know that multiple proteins make up the inner ring. To study this further we would either need a higher resolution subtomogram average of the flagellar *C. jejuni* motor which allows us to obtain more views of the flagellar motor or somehow prevent orientation bias in SPA of the *C. jejuni* flagellar motor.

4.4.7 VidB's location is unknown

The location of VidB was thought to be the 'bridge' density between FlhA and FliG observed in the subtomogram average of C. jejuni 81-176 Δ*vidA* (Figure 4.4 b). The subtomogram average of *C. jejuni* 81-176 Δ*vidA* Δ*vidB* did not remove the bridge density and no other densities were observed to be missing Figure 4.6 b) therefore the location of VidB is yet unknown. Our Collaborators showed that VidB acts like a brake to prevent *C. jejuni* from swimming at high velocity in a low viscous environment (Ribardo et al., 2024). My subtomogram average results of *C. jejuni* 81-176 Δ*vidA*Δ*vidB* suggest that VidB could be a transient protein that acts as a brake when it 'senses' low viscosity therefore it is not visible in subtomogram averages. Since VidB is only required at low viscosity it may not be as visible at high viscosity if it is not permanently bound to the motor. During sample preparation in cryo-electron microscopy it is difficult to control the viscosity of the sample when the sample is frozen on the grid therefore VidB may be 'lost' in this process.

Previous research and Uniprot predicts VidB to be a 55 kDa protein with a GGDEF domain ("GGDEF domain-containing protein - Campylobacter jejuni subsp. jejuni serotype O:23/36 (strain 81-176) | UniProtKB | UniProt," n.d.; Schirmer, 2016). The GGDEF domain is generally related to proteins that are associated with the c-di-GMP signalling system. This domain is also found in another *C. jejuni* protein CbrR which is related to biofilm formation and also interacts with chemotaxis protein cheA (Cox et al., 2021; Elgamoudi et al., 2022). Results from our collaborator showed that deleting CbrR in *C. jejuni* 81-176 Δ*vidA* did not affect its velocity at 1 cP or 40 cP. Whereas deleting CbrR in wild type showed a slight decrease in velocity although this result was significant it was not consistent in each *C.*

jejuni bacterium measured. Overexpression of CbrR slightly increased speed at 40 cP. Although VidB shares weak homology to genes encoding diguanylate cyclases but our collaborators did not observes any diguanylate cyclase activity in VidB which did not synthesize any c-di-GMP. Therefore, VidB works in c-di-GMP independent manner. Overall, *C. jejuni* has fewer signalling systems compared to other bacteria such as the *Sulfurospirillum* genus (Mo *et al.*, 2022). Since these GGDEF domains may not be used as part of c-di-GMP signalling system, they are likely to have other roles that are yet unknown.

4.4.8 Conclusion

In this project I attempt to show the location of proteins required for regulating flagellar motor output. I show that VidA directly interacts with FlgV in the inner ring located in the cytoplasm. My results indicate that CJJ81176_1732 is also located in the cytoplasm. The location of VidB is unknown and is suggested to be transient within the flagellar motor. VidB is specific to low viscosity and since it does not seem to be permanently attached to the flagellar motor it is difficult to image and subtomogram average. This limitation can be addressed by using other protein assays or possibly adding a tag to VidB. *C. jejuni* has evolved proteins which slow down the flagellar motor at low viscosity. I show these proteins belong in the cytoplasm, possibly to interact with core flagellar motor proteins such as the MS ring and C-ring to slow down motility. Further experiments are required to understand the exact mechanism of flagellar motor output.

4.5 Methods

4.5.1 Cell Growth and Freezing Conditions

C. jejuni 81-176 was grown from a freezer stock on Mueller Hinton medium/ agar plates (24 g/L) with 10 µg/ml trimethoprim at 37 °C under microaerobic conditions for 48 hours, the *C. jejuni* colonies were then re-streaked on a new Mueller Hinton medium/ agar plate (24 g/L) with 10 µg/ml trimethoprim for 24 hours for sufficient colonies to grow. To grow *C. jejuni* in liquid media, cells were streaked from a -80°C stock were first grown on a plate for 48 hours, cells were re-streaked on a new MH plate and grown for 16 hours. *C. jejuni* was washed from an MH plate using MH broth to an OD600 of 0.8. 20 mL of culture was grown in 125 mL flask. Cells were grown overnight ~18-24hr as standing cultures (no shaking). Cells were pelleted at 4000 *x g* for 20 minutes. In a separate Eppendorf 133µL of 10 nm gold fiducials (Sigma-Aldrich) and 33 µL of 5% BSA were vortexed together and pelleted at *18000 x g*, 30 µL of sample was mixed with the pelleted fiducials, cells were frozen at blot force of 6, wait time of 30 seconds and blot time of 10 seconds on R2/2 200 mesh Quantifoil grids. Table 4.1 shows the mutants used for this project.

Table 4.1: Mutants of *C. jejuni* used for imaging.

Construct	**Strain**	**Mutant**
ABT501	*C. jejuni* (DRH212 derivative)	Δ*cjj0996 (ΔvidA)*
DRH6836	*C. jejuni* (DRH212 derivative)	Δ*flgV*
DAR6357	*C. jejuni* (DRH212 derivative)	Δ*cjj1107*Δ*cjj0996 (ΔvidA ΔvidB)*
	C. jejuni (DRH212 derivative)	Δ*1732*
DRH212	*C. jejuni* (DRH212 derivative)	wild type

4.5.2 Cryo -Electron Tomography Data Acquisition

Tilt series of *C. jejuni* mutants (Table 4.1) were collected on the Glacios™ Cryo-Transmission Electron Microscope (Thermo Scientific™) with Falcon 4 DED and Selectris energy filter operating at 200 keV with a total fluence of 140e-/ Å2 was used and a defocus of -2 to -5 µm. Tomograms were collected a

tilt range of ± 60 with 3° tilt increments and a pixel size of 1.9 Å. Tilt series were collected using Leginon and tomo5 using a dose symmetric tilt scheme.

4.5.3 Tomogram Reconstruction and Processing

4.5.3.1 Data Prep and Reconstruction:

To reconstruct the data each tilt stack was first binned by four which provided a final pixel size of 7.6, X and Y heights of 1024 and a Z height of 700. Each binned tilt series of 35 stacks was reconstructed using ETOMO using semi-automated scripts written by Dr. Morgan Beeby.

4.5.3.2 Picking particles and Subtomogram averaging:

C. jejuni motors were picked in IMOD. A text file was created to feed in the picked motors (.mod files), reconstructed tomograms (.mrc files) and tilt series information (.tlt files) into PEET and Dynamo. Subtomogram averages of VidA, CJJ81176_1732 and low viscosity *C. jejuni* were averaged in Dynamo. Whereas the subtomogram average for VidA VidB double deletion was averaged in PEET. Both C1 and C17 symmetries were obtained, C1 symmetric subtomogram average was used for finding extra densities.

4.5.3.3 Further Processing:

For each subtomogram average, customised masks were made in the cytoplasmic region of the motor encompassing the C-ring, FlgV and stator region to focus/better alignment in those specific regions.

4.5.3.4 Resolving 20-fold symmetry in the FlgV ring:

Dr. Tina Drobnic (Previous PhD Student) collected and processed a tomography dataset of *C. jejuni* minicells. Dr. Morgan Beeby (Supervisor) further processed this dataset to find the 20-fold symmetry FlgV ring. PEET and customised scripts were used to randomise rotation in the Z axis with focused mask to find other symmetries.

4.5.4 Single Particle Analysis and subtraction of the FlgV ring

RELION 3.1 was used to process the minicell dataset as shown in Chapter 3. To find other symmetries in the motor, the searches were restricted in the Z axis and the orientation remained the same in the X and Y axis (scripts for this were written by Josh Parks, undergraduate student, Imperial College London). To find other symmetries in the motor, previously imposed symmetry is removed from the

structure. A data.star file with accurate coordinates in Psi, Rot and Tilt was edited to randomise Rot. A series of 3D classification and 3D refinement jobs were run with the edited 'data.star' file, flags (--sigma_psi 1; --sigma_rot; and --sigma_tilt 60), increased T-value and angular searches. To find the 20-fold symmetry of the ring in Relion without imposing 'C20' symmetry on the motor I provided relion with a subtomogram average of the motor with an already resolved 20-fold symmetric FlgV ring.

Chapter 5

Locating flagellar signalling suppressor (fss) proteins required for holdfast in *C. crescentus*

5.1 Chapter Summary

Bacteria sense their surrounding environments using chemotaxis. Chemotactic signalling is important for movement, colonisation and surface adhesion. In flagellated bacteria, chemotactic signalling works in synchronisation with the flagellum to direct the movement of a cell. Some bacteria have evolved complex developmental cycles to grow and colonize solid surfaces. For example, *Caulobacter crescentus* starts its life-cycle as a flagellated bacterium and in later stages after surface colonisation it transitions to a sessile state and switches its flagellum for a stalk. The transformation from a swarmer cell to a cell in sessile state involves a holdfast which prepares the cell for adhesion to a solid surface. A holdfast is a structure used by an organism to anchor itself to a substrate. Holdfast can be generated by two different mechanisms one of these mechanisms targets later stages of the swarmer cell life cycle. Previous studies have noted important proteins required for the signalling of holdfast. Identified proteins include trans-membrane protein complexes called stators which power the flagellar motor. More recently identified proteins FssA and FssB are also known to play a role in this mechanism. In this project I attempt to locate FssA and FssB proteins in *C. crescentus* in the flagellar motor using cryo-electron tomography and subtomogram averaging to gain a better understanding of the mechanism by which *C. crescentus* colonizes solid surfaces.

5.2 Introduction

5.2.1 Bacteria have advanced developmental cycles for colonization of solid surfaces

Bacteria can sense their surrounding environments which is important for detecting nutrients and surface colonisation. Bacteria sense chemicals using chemoreceptors and respond by chemotaxis which determines its direction of swimming, surface adhesion and other cell responses. Surface attachment is beneficial for bacteria because it provides protection against the surrounding environment and xenobiotic stress (Dunne, 2002). Solid surfaces are generally heterogeneous and contain many different compounds adsorbed on the surface which makes it an optimal environment for cell nutrition. Bacteria attach to solid surfaces in two ways, either by passive transport or by active swimming (Berne et al., 2018). In many bacteria, such as *C. crescentus*, chemotaxis and the flagellum work together to sense the surrounding environment, navigate itself in the right direction and to attach itself to solid surfaces (Laub et al., 2002, 2000). *C. crescentus* is a dimorphic bacterium, at the beginning of its life cycle, the cell starts as a flagellated cell which allows it to swim, also known as a swarmer cell (Shapiro et al., 1971). These cells explore their surroundings until they find a suitable environment for surface adhesion. The cell can then generate a holdfast and the swarmer cell prepares for attachment to the surface using a polysaccharide adhesin (Levi and Jenal, 2006; Radhakrishnan et al., 2008). In this process, the flagellum is lost, and a stalk takes its place transforming into a sessile state to strongly attach itself to the substrate and absorb nutrients. DNA-replication starts, and the cell begins to divide which results in a new swarmer cell and the original stalked cell.

5.2.2 Holdfast promotes adhesion by a yet unknown mechanism.

The mechanism by which holdfast is initiated remains elusive. Epistasis analysis was used to study the interactions between different genes and how they phenotypically affect *C. crescentus*. Two main pathways were identified using epistasis analysis of flagellar signalling suppressor (fss) genes which promote holdfast and cell adhesion (Hershey et al., 2021). The first pathway works to disrupt early and late stages of flagellar assembly to stop swimming and promote adhesion. The second pathway disrupts later stages of flagellar assembly and involves stator complexes (Motility protein A and Motility protein B also known as MotA and MotB) and its associated diguanylate cyclase (DgcB). MotB and another fss gene called PleD regulate holdfast production under certain conditions and MotB is specifically required for holdfast synthesis (Hug et al., 2017; Paul et al., 2004).

In this project I focus on the stator-dependent pathway. In the stator-dependent pathway the cell first senses mechanical stimuli from its surroundings. The cell prepares for holdfast by disrupting flagellar

motor assembly of a flagellar motor that is already fully assembled. It does this using stator complexes which are able to sense mechanical load in the surrounding environment. Generally, the load-sensing flagellar motor can recruit additional stator complexes when it experiences higher load for example, a high viscous environment to generate additional power for swimming (Partridge et al., 2015; Tipping et al., 2013). Studies have suggested that this same mechanism is involved in initiating disassembly of the flagellar motor when transitioning from swarmer cell to a sessile state.

5.2.3 FssA and FssB contribute to late stage flagellar disassembly

Two genes known as flagellar signalling suppressor (fss) A and B contribute to late-stage flagellar disassembly prior to holdfast in the stator dependent pathway. The genes *fssA* and *fssB* were identified using epistasis and adhesion profiling (Hershey et al., 2021). The gene *fssA* (CC_1064; CCNA_01117) translate to a protein which has a secretion (Sec) / Signal peptidase I (SPI) domain but no predicted functional domains and gene *fssB* (CC_2058; CCNA_02137) translates to a protein which also has Sec /SPI secretion signal domain but has a predicted tetratricopeptide repeat (TPR) domain.

Our collaborator (David Hershey, Department of Bacteriology, University of Wisconsin Madison) showed that deleting *fssA* and *fssB* in *C. crescentus* did not affect adhesion but suppressed hyper adhesive phenotypes which suggests that *fssA* and *fssB* play a role in the mechanism that disrupts late stages of flagellar motor assembly therefore the stator-dependent pathway (Hershey et al., 2021). In both *fssA* and *fssB* deletions, motility was impaired, but the filament was intact which shows that *fssA* and *fssB* contribute to disrupting flagellar assembly once the flagellum is assembled.

Both *fssA* and *fssB* deletions in *C. crescentus* affect motility as measured in soft agar. Although ΔfssA retained some motility in soft agar, Δ*fssB* cells were nonmotile. To recover full motility in Δ*fssA* the mutant gained missense mutations. 14 mutants were suppressors of which 3 were found in MotA and 11 were found in MotB. The most striking mutation was MotB serine 52 to cysteine which was found in 9 of the 11 missense mutations. The mutations found in MotB disrupt a dimeric MotB plug which prevents protons from entering MotA (Hershey et al., 2021). By disrupting the MotB plug protons enter the stator complex and continue powering the flagellar motor thus regaining motility as observed in other studies (Brenzinger et al., 2016). By deleting both *fssA* and *fssB* genes the cell becomes immotile suggesting that both genes are required for stator function and holdfast (Hershey et al., 2021).

In summary, the mechanical and developmental pathway work together to start holdfast production with contributing proteins being *motB*, *dgcB*, *fssA* and *fssB*. Furthermore, the load sensing ability of the flagellar motor is also harnessed when cells move from a swarmer state to an adhesive state resisting external forces of solid surfaces (Partridge et al., 2015; Tipping et al., 2013). We know that *fssA* and

fssB are required for holdfast stimulation, but their exact location and function is not fully understood. By studying proteins FssA and FssB we can develop an understanding of the stator-dependent holdfast mechanism.

5.2.4 Subtomogram averages of *C. crescentus* reveal yet unknown densities

A previous structure of *C. crescentus* was solved (Rossmann et al., 2020). The flagellar motor structure provided clearly unresolved structures which had not been visualised before. More specifically, a 13-fold symmetric cogwheel structure in the periplasm and a 11-fold symmetric less prominent structure above the inner membrane and above the stator complexes was found. The 11-fold structure had also been observed before (Chen et al., 2011), but the proteins that form these structures have no yet been identified. It is possible that these structures correspond to FssA and FssB since these proteins are in close proximity to stator complexes.

By using cryo-electron tomography we can visualise protein complexes and deleted proteins *in situ.* By averaging many identical flagellar motors by STA we can resolve high sub-nanometre resolution structure of the flagellar motor to distinguish (Rossmann and Beeby, 2018; Zhao et al., 2014). In this project, I use cryo-electron tomography and subtomogram averaging to image deletion mutants Δ*fssA* and Δ*fssB C. crescentus* to find their location in the flagellar motor. This will provide a better understanding of how these proteins work together in holdfast.

5.2.5 Aims

In this study I examine the location of FssA and FssB in *C. crescentus* to determine their location to better understand the holdfast mechanism in the stator-dependent pathway.

5.3 Results

5.3.1 NA1000 cells versus CB15 cells for cryo-electron tomography

I investigated two different strains of *C. crescentus* cells CB15 and NA1000. CB15 strain is the wild type strain of *C. crescentus* isolated from a freshwater environment. NA1000 strain is an engineered more genetically stable variant of CB15 cells. CB15 cells form rosettes making it 'sticky' whereas NA1000 cells do not form rosettes which means they could be easier to work with. To investigate which strain of cells (CB15 or NA1000) would provide the most optimal grids, I froze the deletion mutants Δ*fssA* and Δ*fssB* in both strains CB15 and NA1000 on R2/2 200 copper grids and screened the grids on the FEI Tecnai T12 transmission electron microscope. Images captured on the microscope showed that CB15 cells were clumped together which led to thicker ice and difficulty in seeing filaments in swarmer cells (Figure 5.1 a). Since NA1000 cells do not adhere to each other the cells were evenly separated across the grid and I was able to obtain thinner ice on the grid (Figure 5.1 b).

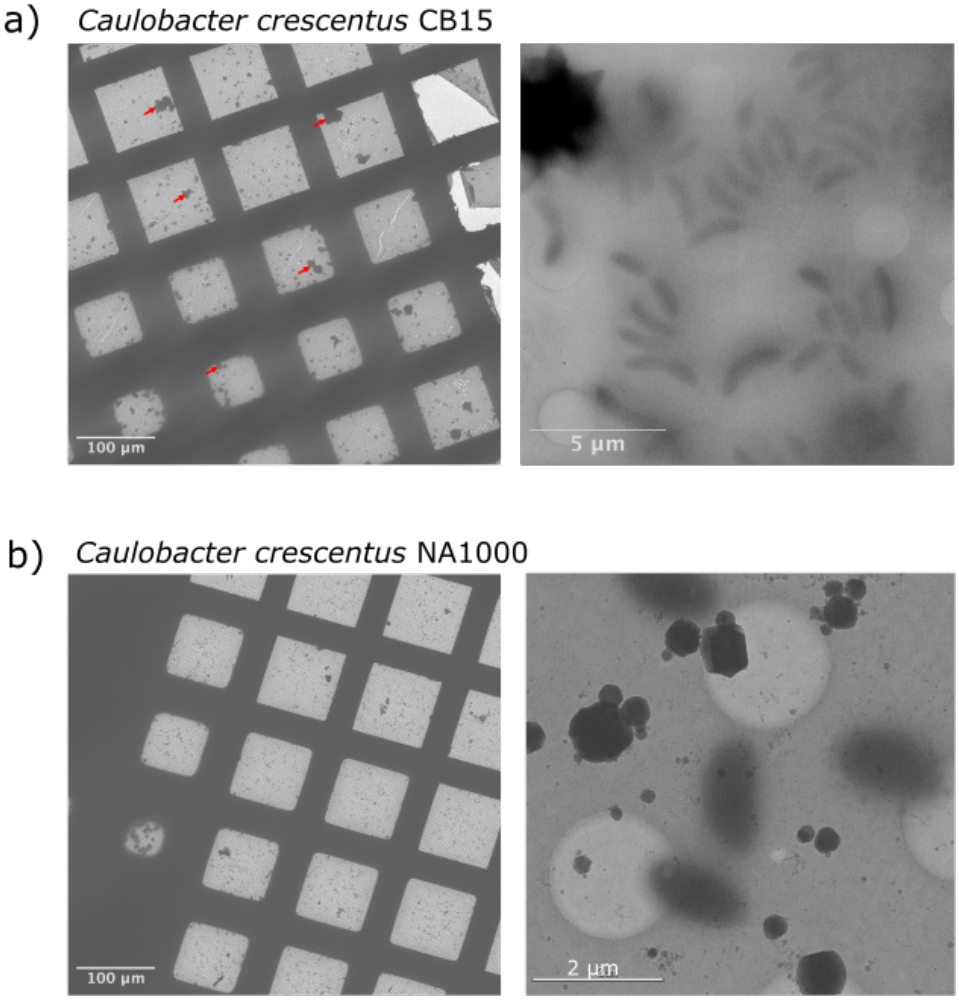


Figure 5.1 Cryo-electron microscopy images comparing CB15 cells with NA1000 cells. Cells were frozen on R2/2 200 copper mesh grids and images were taken on FEI Tecnai T12 transmission electron microscope. a) Low

magnification image of *C. crescentus* CB15 cells which clump together (left). High magnification image of *C. crescentus* CB15 cells which clumped cells (right). b) Low magnification image of *C. crescentus* NA1000 cells which do not clump (left). High magnification image of *C. crescentus* NA1000 cells which do not clump and are optimal for data collection (right).

5.3.2 Synchronization separates pre-divisional cells from swarmer cells

C. crescentus NA1000 Δ*fssA* and Δ*fssB* cells were stained using uranyl acetate for negative stain and imaged on the FEI Tecnai T12 transmission electron microscope to check for filaments. Negative stain images of both Δ*fssA* and Δ*fssB* showed the presence of filaments in some cells (Figure 5.2).

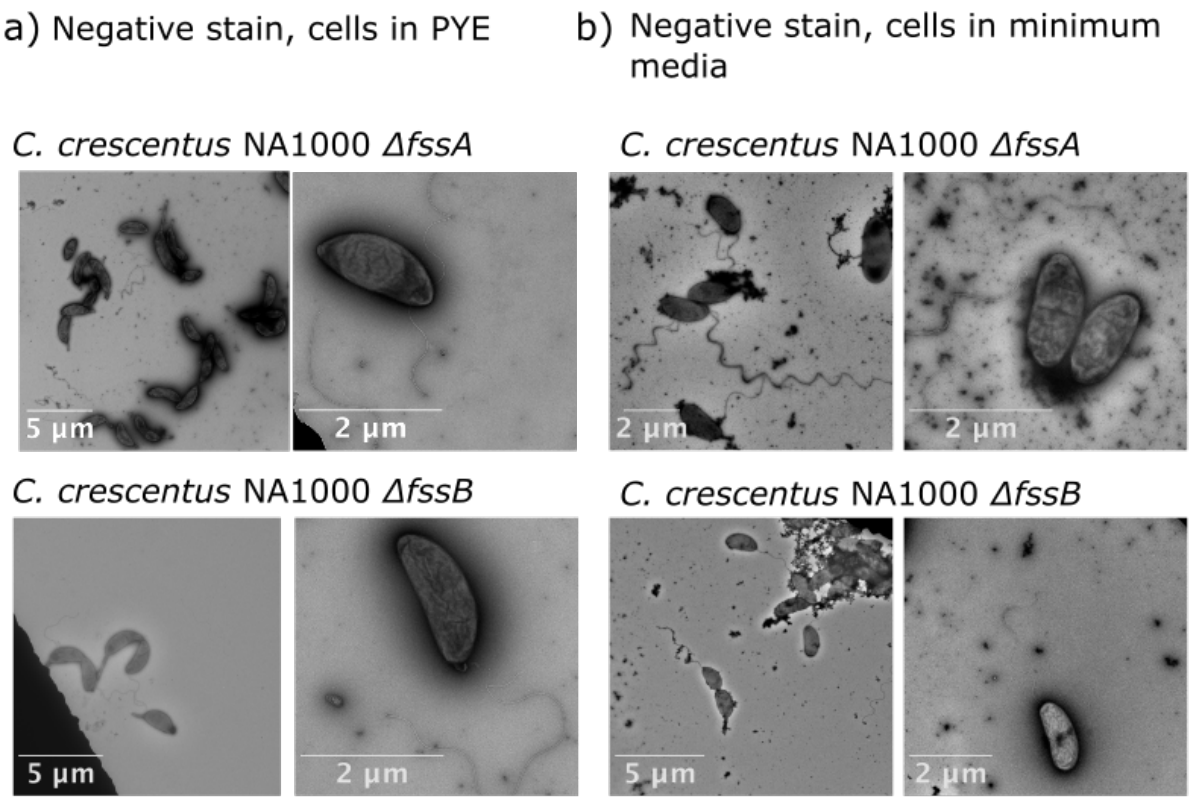


Figure 5.2 Negative stain images to check for filaments in *C. crescentus* NA1000 Δ*fssA* and Δ*fssB* cells. a) Low magnification and high magnification images of Δ*fssA* and Δ*fssB* in PYE medium. b) Low magnification and high magnification images of Δ*fssA* and Δ*fssB* in M2X medium required for synchronization. Both grids had a mixture of swarmer cells and stalked cells.

After checking for filaments in *C. crescentus* NA1000 Δ*fssA* and Δ*fssB* cells, I separated swarmer cells (with filament) from pre-divisional and stalked cells using synchronization. In synchronization Percoll® beads are used to form a gradient to separate pre-divisional cells from swarmer cells. The pre-divisional cells remain at the top and the dense swarmer cells form a second band further down the gradient (Figure 5.3 a). Once swarmer cells are isolated, they are washed in M2 buffer and frozen on R2/2 200 copper mesh grids. Images captured from these grids showed that after several washes, Percoll® remained attached to the outer-membrane of the cell (Figure 5.3 b, c, d) which increased ice-thickness around the

cell lowering the resolution and increasing noise of the final image future subtomogram averages. This proved difficult for picking targets for data collection because there were no filaments and in some cases no motors observed. Although the number of washes were kept the same, there was batch to batch variation in the levels of Percoll® per grid which meant it was not reproducible for data collection. When centrifuging at lower speeds during synchronization, the Percoll® remained at higher levels therefore not suitable for data collection.

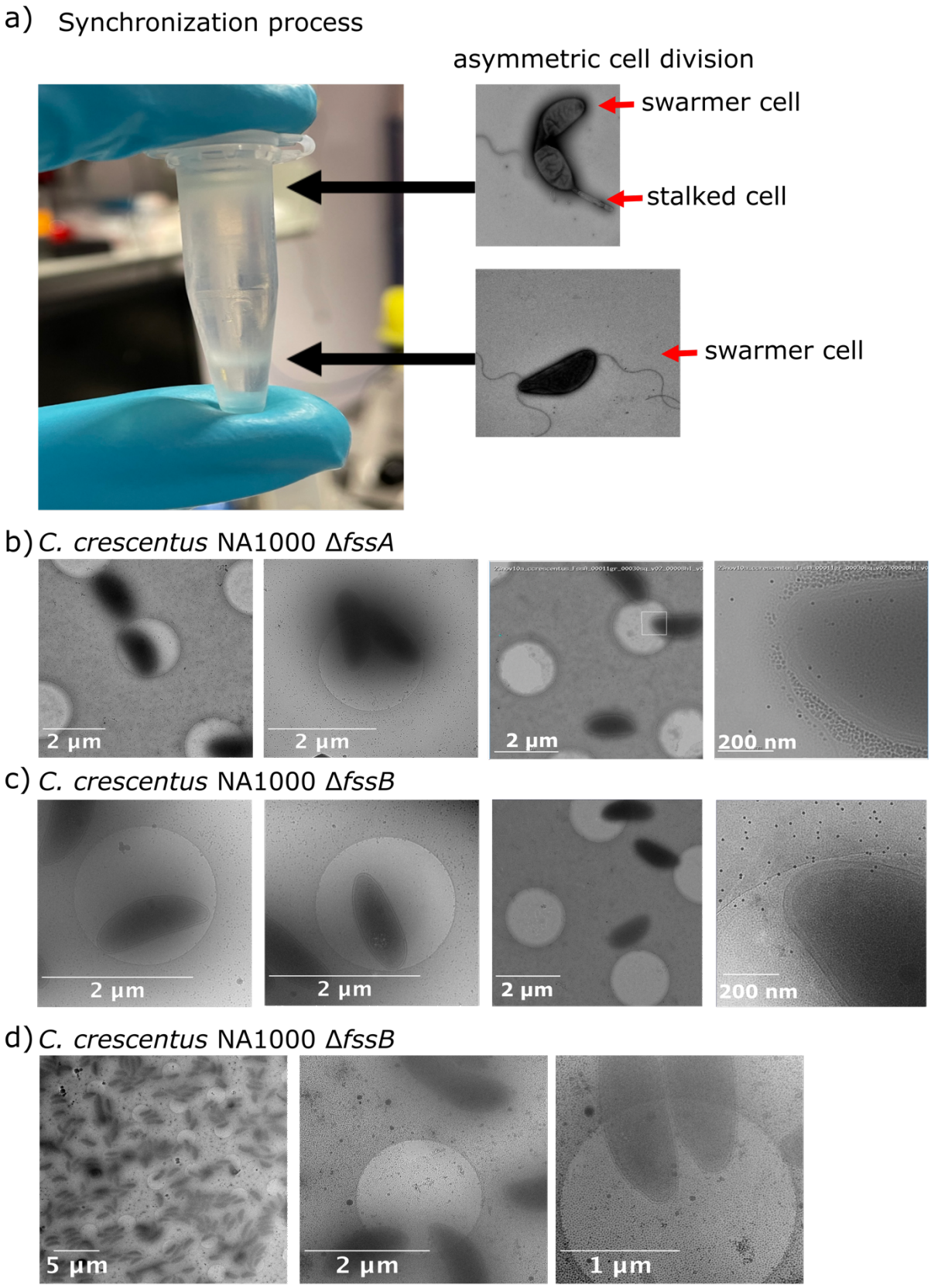


Figure 5.3 Synchronization separates swarmer cells from stalked cells but residual Percoll® remains in the samples. Synchronization process shows two bands, the top band has pre-divisional and stalked cells, and the bottom band has the swarmer cells with filaments. B) *C. crescentus* Δ*fssA* previously treated with Percoll®

captured on grid. Harsh methods of repeated washing in a Percoll® gradient presented most cells without a filament. Percoll® remained in the sample surrounding the cell body and filament. C) *C. crescentus* Δ*fssB* previously treated with Percoll® captured on grid. Similarly, to (b) Percoll® remained on the grid. D) *C. crescentus* Δ*fssB* cells on grid. After multiple washes Percoll® large amounts of Percoll® remained in the sample which increased ice thickness and contributes to noise during data processing.

5.3.3 Subtomogram averaging of mutants reveals flagellar motor without the cogwheel

Since the process of synchronization led to grids with Percoll® for data collection, we also collected a dataset without synchronization which consisted of a mixture of swarmer cells and stalked cells. Particles were picked from both datasets for subtomogram averaging. Figure 5.4 shows an example of a tomogram of *C. crescentus* Δ*fssA* (Figure 5.4 a) and a tomogram of *C. crescentus* Δ*fssB* (Figure 5.4 b) where the flagellar motor is visible.

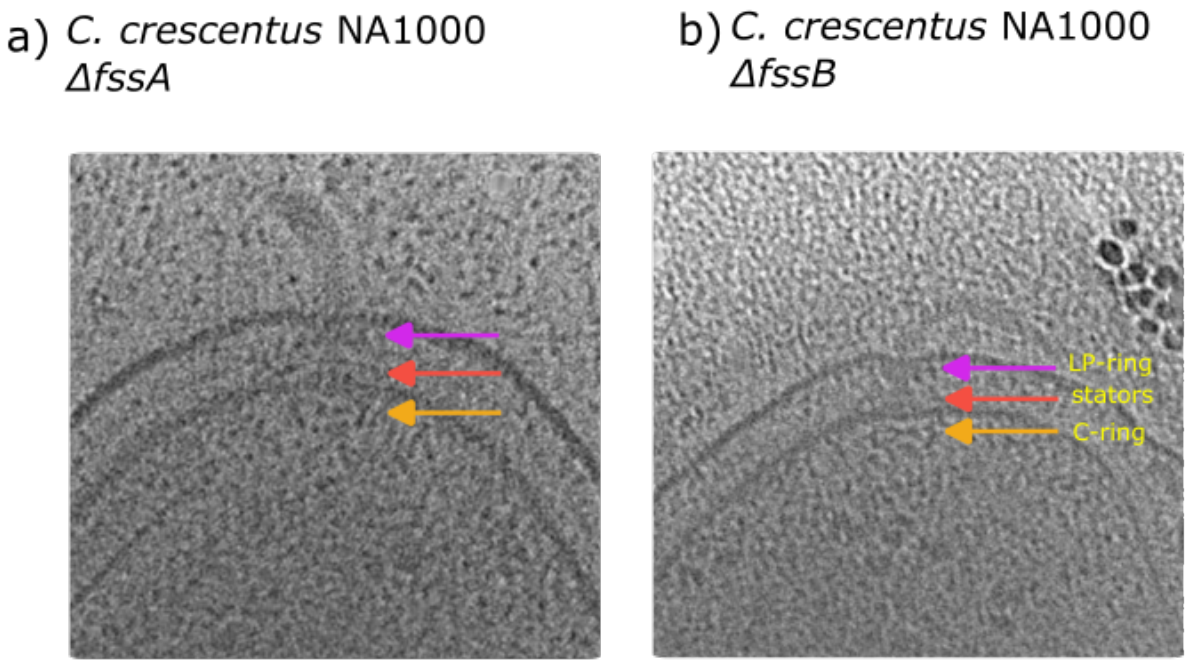


Figure 5.4 Tomograms of *C. crescentus* Δ*fssA* (a) and Δ*fssB* (b) were collected on the Glacios 200 keV cryo-transmission electron microscope. Tomograms showed the flagellar motor with low resolution densities of the cytoplasmic ring, stators and LP-ring.

Subtomogram averages of these mutants when compared to *C. crescentus* wild type motor showed that for both *C. crescentus* Δ*fssA* and Δ*fssB* a density under the outer-membrane previously identified as the 'cogwheel' structure was either missing, partially disrupted or partially assembled (Figure 5.5 a). Figure 5.5 (b) provides a rendered structure of wild type *C. crescentus* highlighting structures in *C. crescentus'* flagellar motor including the cogwheel.

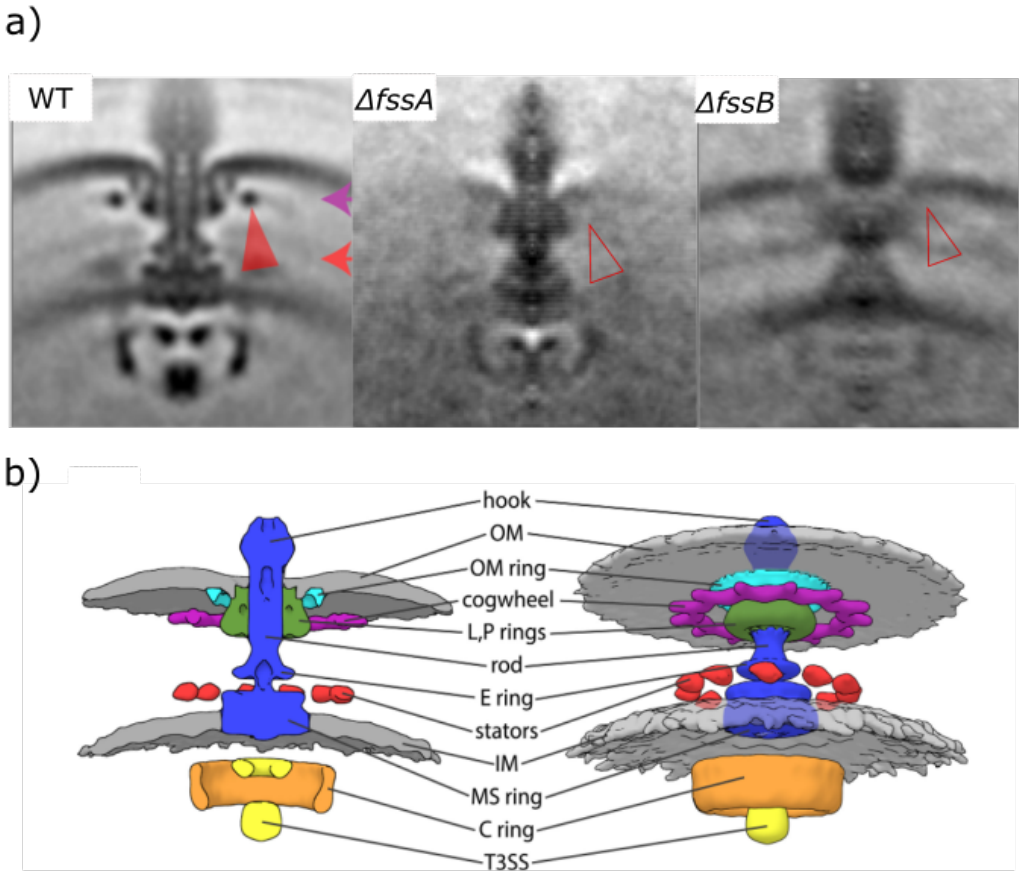


Figure 5.5 Subtomogram averages of Δ*fssA* and Δ*fssB* lack the cogwheel structure. a) Left to right – wild type *C. crescentus.* The red arrow highlights the cogwheel structure; *C. crescentus* Δ*fssA*. The arrow highlights missing density; *C. crescentus* Δ*fssB*. The arrow highlights missing density. b) rendered structure of *C. crescentus* CB15 taken from Rossmann *et al*., 2020. Each component of the flagellar motor is labelled.

5.4 Discussion

Bacteria use chemotaxis as a means to navigate their surrounding environment, control cellular processes and adhesion. In flagellated bacteria, chemotaxis and the flagellum work together to navigate the cell and perform cell adhesion. An example of this mechanism is seen in *C. crescentus*' which can adhere to solid surfaces by switching its flagellum for a stalk. The process starts with a flagellated swarmer cell which together with the cell's chemotactic abilities 'sense' its surroundings. Once it finds a solid surface the cell loses its flagellum and replaces it with a stalk using a holdfast for which there are two independent mechanisms. Previous studies have shown that in stator-dependent holdfast two proteins FssA and FssB required but their location is yet unknown (Hershey et al., 2021). In subtomogram averages of *C. crescentus* there are two prominent un-identified structures, a 13-fold symmetric cogwheel structure and an 11-fold structure above the stator units (Rossmann et al., 2020) which could correspond to FssA and FssB.

To investigate the location of FssA in *C. crescentus* a Δ*fssA* mutant was imaged using cryo-electron microscopy. A density under the outer membrane known as the 'cogwheel' is missing (Figure 5.5 a). The cogwheel structure was replaced by a small, faded density (Figure 5.5 a). Previous studies showed that deleting FssA in *C. crescentus* reduces motility, but the cell is not completely immotile (Hershey et al., 2021). My results together with previous research suggests that FssA might be required to stabilize the cogwheel structure providing optimal motility.

Our collaborators work which shows that *C. crescentus fssA* deletion regained its motility comparably to wild type by gaining suppressor mutants in MotB which suggests that these proteins indeed do interact with each other. The AlphaFold predicted structure of FssA and MotB dimer had mostly no interacting residues except for Phenylalanine 63 in MotB which could interact with the inner alpha helix of FssA. But the overall predicted complex was very low confidence and does not provide a valid structure.

To investigate the location of FssB in *C. crescentus* a Δ*fssB* mutant was imaged using cryo-electron microscopy (Figure 5.5 a). Since the final resolution was quite low it was difficult to find smaller densities that might still be present. Previous research has shown that deleting FssB is analogous to deleting MotB, both are immotile (Hershey et al., 2021). The exact function of FssB is still unknown. But FssB has a predicted TPR domain which has also previously been found in BB0236, a protein which assembles a collar structure in *Borrelia burgdorferi.* BB0236 is in a similar position to the cogwheel structure in *C. crescentus* (Moon et al., 2018).

In conclusion, the structures of FssA and FssB both correspond to the cogwheel structure and are most likely required for the stability of the flagellar motor in *C. crescentus*. Although more evidence and a higher resolution subtomogram average would be required to decipher smaller details in the flagellar motor. It could be that the cogwheel structure itself is required for holdfast and is disrupted during the process. Previous research shows that deleting both FssA and FssB in *C. crescentus* rendered the bacterium to be non-motile. Which showed that deletion of FssB is epistatic and overrides the semi-motile FssA deletion mutant. Since the stator dependent pathway involves FssA and FssB and are also required for stator activity, it could be that the deletion of FssA and FssB disrupts scaffold structures that allow stators to maintain torque, although further studies need to be done to confirm this.

5.5 Methods

5.5.1 Cell Growth and Synchronization process

C. crescentus CB15 and NA1000 cells (Δ*fssA* and Δ*fssB*) were grown in PYE medium for 24 hours. 2-5 mL of this culture was subcultured into 20 mL of new PYE medium and grown for 5-6 hours. The culture was then centrifuged at 15,000 *x g*. The supernatant was removed, and the pellet was kept on ice prior to freezing on grids. In the case, of synchronization. The initial 2-5 mL culture was grown in PYE medium for 24 hours, then this culture was diluted by 1/256 in M2X medium, the final volume was between 10 – 50 mL. The M2X culture was grown until 0.3-0.4 OD (around 12 hours). To separate stalked and pre-divisional cells from swarmer cells, M2X culture, M2 salts and Percoll (Cytivia) were required. All components were chilled on ice prior to use and during the synchronization process. M2X culture was harvested at OD 0.3-0.4. The cells were spun down for 30 minutes at 4000 *x g* at 4 °C. The supernatant was discarded including the loosely pelleted cells which are mostly stalked and pre-divisional cells. The pellet was resuspended in 750 µL of cold M2 salts and transferred to an Eppendorf tube. 750 µL of Percoll (Cytivia) was added to the Eppendorf tube and the mixture was resuspended. The Eppendorf tube was centrifuged for 20 minutes at 20,000 *x g* at 4 °C to separate swarmer cells. The Stalked and pre-divisional cells remain at the top of the Eppendorf tube whereas the swarmer cells form a separate band of cells nearer to the centre of the Eppendorf tube (Figure 5.3 a).

5.5.2 Freezing cells for cryo-electron tomography

To prepare samples for freezing fiducials were prepared by adding 133µL of 10 nm gold fiducials (Sigma-Aldrich) and 33 µL of 5% BSA to an Eppendorf tube which was vortexed together with the cell pellet and pelleted at *18000 x g*, 30 µL of sample was mixed with the pelleted fiducials, cells were frozen at blot force of 6, wait time of 30 seconds and blot time of 10 seconds on R2/2 200 mesh Quantifoil grids. Table 5.1 shows the mutants used for this project.

Table 5.1: Mutants of *C. crescentus* used for imaging.

Construct	**Strain**	**Mutant**
DH783	*C. crescentus* (CB15)	ΔfssA
DH845	*C. crescentus* (CB15)	ΔfssB
AKC71	*C. crescentus* (NA1000)	ΔfssA
AKC72	*C. crescentus* (NA1000)	ΔfssB

5.5.3 Cryo -Electron Tomography Data Acquisition

Tilt series of *C. crescentus* mutants (Table 5.1) were collected on the Glacios™ with Falcon 4 DED and Selectris energy filter. Cryo-Transmission Electron Microscope (Thermo Scientific™) operating at 200 keV with a total fluence of 140e-/ Å2 was used and a defocus of -2 to -5 µm. Tomograms were collected a tilt range of ± 60 with 3° tilt increments and a pixel size of 1.9 Å. Tilt series were collected using Leginon and tomo5 using a dose symmetric tilt scheme.

5.5.4 Tomogram Reconstruction and Processing

5.5.4.1 Data Preparation and Reconstruction

To reconstruct the data each tilt stack was first binned by four which provided a final pixel size of 7.6, X and Y heights of 1024 and a Z height of 700. Each binned tilt series of 35 stacks was reconstructed using ETOMO using semi-automated scripts written by Dr. Morgan Beeby.

5.5.4.2 Picking particles and Subtomogram averaging

C. crescentus motors were picked in IMOD. A text file was created to feed in the picked motors (.mod files), reconstructed tomograms (.mrc files) and tilt series information (.tlt files) into PEET and Dynamo. Subtomogram averages of *C. crescentus* ΔfssA and *C. crescentus* ΔfssB were averaged in Dynamo. Both C1 and C11 and C13 symmetries were obtained.

5.5.4.3 Further Processing

For each subtomogram average, customised masks were made in the cytoplasmic region of the motor encompassing the cogwheel structure rod and C-ring to focus/better alignment in those specific regions.

Chapter 6

Conclusions

6.1 Summary

The evolution of macromolecular complexes and how they structurally adapt to evolutionary changes has been a long-standing question in evolutionary biology. The bacterial flagellar motor is good model system to study these evolutionary changes in large macromolecular complexes. Bacterial flagellar motors are known to be complex and there is huge diversity in flagellar motors between species. This makes the flagellar motor an interesting case study to study the evolution of macromolecular complexes providing an explanation for proteins being adapted and re-purposed as a part of a large molecular system. The flagellar motor has a conserved core, but additional structures have incorporated into the flagellar motor that differ between lineages. *C. jejuni* has one of the most complex flagellar motors. Why these novel proteins have incorporated into the flagellar motor is still uncertain. I also looked at *C. crescentus* which goes through structural changes using its own unique set of proteins in the flagellar motor so the cell can switch from a flagellated state to an adhesive state in the appropriate environment. My work brings together structural biology, biophysics and genetics which has furthered the understanding of new flagellar components.

6.2 Present conclusions and future work

6.2.1 A higher resolution flagellar motor structure provides insight into molecular evolution

The purpose of the flagellar motor is to generate torque so the cell can swim to different locations. Since flagellar motors in different species have evolved and incorporated specific proteins, we need to first understand how the flagellar motor rotates and then how these proteins contribute to generating torque. Usually cryo-electron tomography and subtomogram averaging have been used to solve the structure of flagellar motors but this has limited our resolution to 30-50 Å. To gain an understanding on how additional proteins interact with each other to generate torque we need a higher resolution structure. In Chapter 2, I used hyperflagellated *C. jejuni* minicells to solve a higher resolution flagellar motor structure. As a group we solved the highest resolution sub-nanometre structure of the *C. jejuni* flagellar motor. The minicell approach showed that it is possible to solve the structure of large membrane-associated complexes to nanometre resolution. By processing this dataset further a previous PhD student in our lab showed that in certain regions of the motor the resolution could be pushed to a molecular level (Drobnič et al., 2023). I further processed the data to obtain the first *in situ* structure of stator units where we could see pentameric stators. Previously, the structure of purified stator complexes was resolved which revealed that stator units were pentameric but structural information about interacting proteins was lost during the purification process (Deme et al., 2020; Santiveri et al., 2020). By visualising pentameric stator units *in situ* we gain an understanding of how these stator units could interact with surrounding proteins to drive rotation.

I attempted to resolve different conformational states of a stator unit to provide visual snapshot of the mechanism of interaction between stator units and the C-ring, but it was not possible to decipher these conformational states. Limitations in this dataset included conformational bias which meant there were not enough 'views' of the flagellar motor and only encompassed side views. The initial model showed stator units rotating against the C-ring, but it could be possible that stator units move back and forth in a switching motion once protons move into each stator unit. Although stator unit conformations could not be resolved 3D classification in Scipion resulted in one class with a density next to the stator unit and one class without the density next to the stator unit which could indicate changes in stator unit conformation.

6.2.2 A step forward in understanding stator dynamics in *C. jejuni*

The pentameric stator ring imaged *in situ* using hyper flagellated *C. jejuni* minicells provided sufficient resolution (~15 Å) to model the already solved stator unit structure (Santiveri et al., 2020). Once stator units were modelled into the stator ring new densities around each stator unit became more apparent. In

Chapter 3 I identified a protein called FlgX which is located under stator units to keep stator units statically in place. FlgX was previously shown work as a chaperone to stabilise the stator units and prevent it from degradation by FtsH (Ribardo et al., 2019). Deleting FlgX caused the cell to become immotile and stator units in a FlgX deletion mutant are not visible in subtomogram averages. FlgX is a key protein which highlights how *C. jejuni* has diverged from simpler flagellar motors to maintain a high torque by keeping stator units incorporated in the flagellar motor. In Chapter 3 I also show that stator units are statically attached to the flagellar motor by adding a protonophore (CCCP) to wild type *C. jejuni* and solving its structure by cryo-electron tomography and subtomogram averaging which shows the presence of stators even after the ion-gradient has dissipated. These results are supported by biophysical data from our collaborators.

In the last year three papers have solved the structure of the *Salmonella* C-ring with the MS-ring to a resolution between 3 to 5 Å, by purifying the ring as a complex from the bacterium. This led to a major advancement in understanding the flagellar switch complex (Johnson et al., 2024; Singh et al., 2024; Tan et al., 2024). The three papers found that the MS-ring together with the C-ring in *Salmonella* are made of 203 subunits this can be categorised into 33 FliF subunits, 34 FliG subunits, 34 FliM subunits and around 102 FliN subunits. Each paper highlighted the conformational changes that occur once the flagellar motor switches from counterclockwise (swimming) to clockwise (tumbling) in order to switch direction. To switch direction a chemotaxis protein CheY binds to FliM which promotes CW rotation. The C-terminal of FliF and the FliG subunit rotate ~180°. The central region of FliG switches domains as a part of a conformational change to reverse the orientation of the FliG torque helix so that the torque helix faces outwards and MotA moves inside the C-ring. In counterclockwise rotation, MotA interacts with the outer surface of the C-ring. (Johnson et al., 2024) showed by adding a linker between MotA and FliG subunits that around three FliG subunits are in contact with MotA. The change from CCW involves not just the rotational switch from FliG but also a change in location of MotA which was previously thought to be static. Although these papers have provided molecular details to the understanding of torque generation, *Salmonella* has dynamic stators. It is still unknown whether high-torque flagellar motors possess a similar mechanism and how additional scaffolds present in these high-torque motors contribute to stator-rotor interaction. Therefore, additional experiments need to be done to confirm protein interactions in high torque motors such as *C. jejuni*.

6.2.3 STA to locate novel proteins

Campylobacter jejuni swims in high viscous environments of the intestine. Previous research has shown that *C. jejuni* can swim faster in high viscous environments and slows down in low viscous environments. As shown in Chapter 3, *C. jejuni* has a protein FlgX which keeps stator units in place. *C. jejuni* has diverged to swim predominantly in high viscous environments and reduces its swimming

speeds in low viscous environments. In Chapter 4 I investigated four proteins required to fine-tune *C. jejuni*'s velocity when it senses its surrounding viscosity using cryo-electron tomography and subtomogram averaging. I found that proteins VidA, FlgV and CJJ81176_1732 are located under the MS-ring and form a separate ring. The location of VidB is still unknown. A limitation of this study was the low resolution of the subtomogram average which does not provide details of the conformation of each protein in the ring. Deletion assays are useful but sometimes additional proteins that are dependent on the protein of interest also disappear due to lack of protein stability. Single particle structure of the flagellar motor showed four proteins which make up the ring between the MS-ring and the C-ring. But limitations in imposing other symmetries within the ring in our single particle dataset meant that we could not resolve the conformational states. Although we know the ring is 20-fold symmetric from subtomogram averages of wild type *C. jejuni*, more information is needed to decipher exact conformational states of these proteins to gain an understanding of how these proteins work together to control velocity.

In Chapter 5, I show that two previously identified proteins in *C. crescentus* could contribute to a 'cogwheel' structure which is located just under the outer membrane of the flagellar motor *in C. crescentus*. These proteins FssA and FssB are important for one pathway that allows *C. crescentus* to move from a swarmer state to a sessile state. AlphaFold models could not predict protein complexes between these proteins. Therefore, having purified protein structures of these proteins could be useful for determining the full structure of the cogwheel.

6.2.4 Limitations

In Chapter 2 and 3, I show that we can image large, dynamic macromolecular complexes which are embedded in the membrane. The use of minicells has provided a useful higher resolution structure of the *C. jejuni* flagellar motor. Minicells can be used to provide higher resolution structures of other bacterium species. Successful imaging of minicells would require minicells that are small and are hyperflagellated. For example, minicells of *Salmonella* and *E. coli* and bigger and not as thin making them not suitable for imaging. However, minicells for *in situ* single particle imaging depending on the species is still a step forward in obtaining a higher resolution *in situ* structure of large complexes. Higher resolution structures provide information for novel proteins in which *in silico* structures can be docked into. Although methods to validate the location of these proteins such as tagging proteins is not always successful. In Chapter 3 I imaged a tagged FlgX protein. The tag and FlgX as well as stator complexes were not visible in the subtomogram average. Tags often de-stabilize protein complexes therefore finding better methods of designing tags which will not interfere in protein interactions will be a step forward in validating the location of novel proteins *in situ*.

In Chapter 4 and 5 I show that co-immunoprecipitation assays (as done by our collaborators) are useful for detecting interactions between complexes and subtomogram averaging can be used to verify the location of these proteins by deletion analysis. Improvements in resolution can provide us with the location of smaller proteins that are not visible at 30-40 Å. In future studies, using minicells and single particle imaging for deletion analysis could provide a more informative approach to locating proteins.

7 Bibliography

Abby, S.S., Rocha, E.P.C., 2012. The Non-Flagellar Type III Secretion System Evolved from the Bacterial Flagellum and Diversified into Host-Cell Adapted Systems. PLOS Genetics 8, e1002983. https://doi.org/10.1371/journal.pgen.1002983

Abrishami, V., Ilca, S.L., Gomez-Blanco, J., Rissanen, I., de la Rosa-Trevín, J.M., Reddy, V.S., Carazo, J.-M., Huiskonen, J.T., 2021. Localized reconstruction in Scipion expedites the analysis of symmetry mismatches in cryo-EM data. Progress in Biophysics and Molecular Biology, CryoEM microscopy developments and their biological applications 160, 43–52. https://doi.org/10.1016/j.pbiomolbio.2020.05.004

Abrusci, P., Vergara–Irigaray, M., Johnson, S., Beeby, M.D., Hendrixson, D., Roversi, P., Friede, M.E., Deane, J.E., Jensen, G.J., Tang, C.M., Lea, S.M., 2013. Architecture of the major component of the type III secretion system export apparatus. Nat Struct Mol Biol 20, 99–104. https://doi.org/10.1038/nsmb.2452

Agulleiro, J.I., Fernandez, J.J., 2011. Fast tomographic reconstruction on multicore computers. Bioinformatics 27, 582–583. https://doi.org/10.1093/bioinformatics/btq692

Baker, L.A., Rubinstein, J.L., 2010. Chapter Fifteen - Radiation Damage in Electron Cryomicroscopy, in: Jensen, G.J. (Ed.), Methods in Enzymology, Cryo-EM Part A Sample Preparation and Data Collection. Academic Press, pp. 371–388. https://doi.org/10.1016/S0076-6879(10)81015-8

Balaban, M., Hendrixson, D.R., 2011. Polar flagellar biosynthesis and a regulator of flagellar number influence spatial parameters of cell division in Campylobacter jejuni. PLoS Pathog 7, e1002420. https://doi.org/10.1371/journal.ppat.1002420

Beeby, M., 2019. Evolution of a family of molecular Rube Goldberg contraptions. PLOS Biology 17, e3000405. https://doi.org/10.1371/journal.pbio.3000405

Beeby, M., Deborah A. Ribardo, Brennan, C.A., Ruby, E.G., Jensen, G.J., Hendrixson, D.R., 2016a. Diverse high-torque bacterial flagellar motors assemble wider stator rings using a conserved protein scaffold. Proceedings of the National Academy of Sciences 113, E1917–E1926. https://doi.org/10.1073/pnas.1518952113

Beeby, M., Ribardo, D.A., Brennan, C.A., Ruby, E.G., Jensen, G.J., Hendrixson, D.R., 2016b. Diverse high-torque bacterial flagellar motors assemble wider stator rings using a conserved protein scaffold. Proc Natl Acad Sci U S A 113, E1917–E1926. https://doi.org/10.1073/pnas.1518952113

Berg, H.C., 2003. The Rotary Motor of Bacterial Flagella. Annual Review of Biochemistry 72, 19–54. https://doi.org/10.1146/annurev.biochem.72.121801.161737

Berg, H.C., Turner, L., 1979. Movement of microorganisms in viscous environments. Nature 278, 349–351. https://doi.org/10.1038/278349a0

Berne, C., Ellison, C.K., Ducret, A., Brun, Y.V., 2018. Bacterial adhesion at the single-cell level. Nat Rev Microbiol 16, 616–627. https://doi.org/10.1038/s41579-018-0057-5

Bharat, T.A.M., Russo, C.J., Löwe, J., Passmore, L.A., Scheres, S.H.W., 2015. Advances in Single-Particle Electron Cryomicroscopy Structure Determination applied to Sub-tomogram Averaging. Structure 23, 1743–1753. https://doi.org/10.1016/j.str.2015.06.026

Blair, D.F., 2003. Flagellar movement driven by proton translocation. FEBS Letters, Protonmotive Mechanisms of Energy Transducing Enzymes 545, 86–95. https://doi.org/10.1016/S0014-5793(03)00397-1

Blair, D.F., Berg, H.C., 1988. Restoration of torque in defective flagellar motors. Science 242, 1678–1681. https://doi.org/10.1126/science.2849208

Botting, J.M., Tachiyama, S., Gibson, K.H., Liu, J., Starai, V.J., Hoover, T.R., 2022. Helicobacter pylori FlgV forms a flagellar motor ring structure required for optimal motility. https://doi.org/10.1101/2022.10.24.513468

Bouvette, J., Liu, H.-F., Du, X., Zhou, Y., Sikkema, A.P., da Fonseca Rezende e Mello, J., Klemm, B.P., Huang, R., Schaaper, R.M., Borgnia, M.J., Bartesaghi, A., 2021. Beam image-shift

accelerated data acquisition for near-atomic resolution single-particle cryo-electron tomography. Nat Commun 12, 1957. https://doi.org/10.1038/s41467-021-22251-8

Branon, T.C., Bosch, J.A., Sanchez, A.D., Udeshi, N.D., Svinkina, T., Carr, S.A., Feldman, J.L., Perrimon, N., Ting, A.Y., 2018. Efficient proximity labeling in living cells and organisms with TurboID. Nat Biotechnol 36, 880–887. https://doi.org/10.1038/nbt.4201

Brenzinger, S., Dewenter, L., Delalez, N.J., Leicht, O., Berndt, V., Paulick, A., Berry, R.M., Thanbichler, M., Armitage, J.P., Maier, B., Thormann, K.M., 2016. Mutations targeting the plug-domain of the Shewanella oneidensis proton-driven stator allow swimming at increased viscosity and under anaerobic conditions. Mol Microbiol 102, 925–938. https://doi.org/10.1111/mmi.13499

Carroll, B.L., Nishikino, T., Guo, W., Zhu, S., Kojima, S., Homma, M., Liu, J., 2020. The flagellar motor of Vibrio alginolyticus undergoes major structural remodeling during rotational switching. eLife 9, e61446. https://doi.org/10.7554/eLife.61446

Carter, C.B., Williams, D.B., 2016. Transmission Electron Microscopy: Diffraction, Imaging, and Spectrometry. Springer.

Celli, J.P., Turner, B.S., Afdhal, N.H., Keates, S., Ghiran, I., Kelly, C.P., Ewoldt, R.H., McKinley, G.H., So, P., Erramilli, S., Bansil, R., 2009. Helicobacter pylori moves through mucus by reducing mucin viscoelasticity. Proc Natl Acad Sci U S A 106, 14321–14326. https://doi.org/10.1073/pnas.0903438106

Chaban, B., Coleman, I., Beeby, M., 2018. Evolution of higher torque in Campylobacter-type bacterial flagellar motors. Sci Rep 8, 97. https://doi.org/10.1038/s41598-017-18115-1

Chang, Y., Moon, K.H., Zhao, X., Norris, S.J., Motaleb, M.A., Liu, J., 2019. Structural insights into flagellar stator-rotor interactions. Elife 8, e48979. https://doi.org/10.7554/eLife.48979

Chang, Y., Xu, H., Motaleb, M.A., Liu, J., 2021. Characterization of the Flagellar Collar Reveals Structural Plasticity Essential for Spirochete Motility. mBio 12, e0249421. https://doi.org/10.1128/mBio.02494-21

Che, Y.-S., Nakamura, S., Morimoto, Y.V., Kami-Ike, N., Namba, K., Minamino, T., 2014. Load-sensitive coupling of proton translocation and torque generation in the bacterial flagellar motor. Mol Microbiol 91, 175–184. https://doi.org/10.1111/mmi.12453

Chen, S., Beeby, M., Murphy, G.E., Leadbetter, J.R., Hendrixson, D.R., Briegel, A., Li, Z., Shi, J., Tocheva, E.I., Müller, A., Dobro, M.J., Jensen, G.J., 2011a. Structural diversity of bacterial flagellar motors. EMBO J 30, 2972–2981. https://doi.org/10.1038/emboj.2011.186

Chen, S., Beeby, M., Murphy, G.E., Leadbetter, J.R., Hendrixson, D.R., Briegel, A., Li, Z., Shi, J., Tocheva, E.I., Müller, A., Dobro, M.J., Jensen, G.J., 2011b. Structural diversity of bacterial flagellar motors. EMBO J 30, 2972–2981. https://doi.org/10.1038/emboj.2011.186

Chen, X., Berg, H.C., 2000. Torque-speed relationship of the flagellar rotary motor of Escherichia coli. Biophys J 78, 1036–1041.

Cheng, Y., Grigorieff, N., Penczek, P.A., Walz, T., 2015. A primer to single-particle cryo-electron microscopy. Cell 161, 438–449. https://doi.org/10.1016/j.cell.2015.03.050

Cohen, E.J., Nakane, D., Kabata, Y., Hendrixson, D.R., Nishizaka, T., Beeby, M., 2020. Campylobacter jejuni motility integrates specialized cell shape, flagellar filament, and motor, to coordinate action of its opposed flagella. PLoS Pathog 16, e1008620. https://doi.org/10.1371/journal.ppat.1008620

Coulton, J.W., Murray, R.G., 1978. Cell envelope associations of Aquaspirillum serpens flagella. Journal of Bacteriology 136, 1037–1049. https://doi.org/10.1128/jb.136.3.1037-1049.1978

Cox, C.A., Bogacz, M., El Abbar, F.M., Browning, D.D., Hsueh, B.Y., Waters, C.M., Lee, V.T., Thompson, S.A., 2021. The Campylobacter jejuni Response Regulator and Cyclic-Di-GMP Binding CbrR Is a Novel Regulator of Flagellar Motility. Microorganisms 10, 86. https://doi.org/10.3390/microorganisms10010086

Crowther, R.A., DeRosier, D.J., Klug, A., 1970. The Reconstruction of a Three-Dimensional Structure from Projections and its Application to Electron Microscopy. Proceedings of the Royal Society of London. Series A, Mathematical and Physical Sciences 317, 319–340.

Crowther, R.A., Klug, A., 1971. ART and science or conditions for three-dimensional reconstruction from electron microscope images. J Theor Biol 32, 199–203. https://doi.org/10.1016/0022-5193(71)90147-0

De Rosier, D.J., Klug, A., 1968. Reconstruction of Three Dimensional Structures from Electron Micrographs. Nature 217, 130–134. https://doi.org/10.1038/217130a0

Deme, J.C., Johnson, S., Vickery, O., Aron, A., Monkhouse, H., Griffiths, T., James, R.H., Berks, B.C., Coulton, J.W., Stansfeld, P.J., Lea, S.M., 2020. Structures of the stator complex that drives rotation of the bacterial flagellum. Nat Microbiol 5, 1553–1564. https://doi.org/10.1038/s41564-020-0788-8

Denise, R., Abby, S.S., Rocha, E.P.C., 2020. The Evolution of Protein Secretion Systems by Co-option and Tinkering of Cellular Machineries. Trends in Microbiology 28, 372–386. https://doi.org/10.1016/j.tim.2020.01.005

Dobro, M.J., Melanson, L.A., Jensen, G.J., McDowall, A.W., 2010. Chapter Three - Plunge Freezing for Electron Cryomicroscopy, in: Jensen, G.J. (Ed.), Methods in Enzymology, Cryo-EM Part A Sample Preparation and Data Collection. Academic Press, pp. 63–82. https://doi.org/10.1016/S0076-6879(10)81003-1

Drobnič, T., Cohen, E.J., Alzheimer, M., Froschauer, K., Svensson, S., Singh, N., Garg, S.G., Henderson, L., Umrekar, T., Nans, A., Ribardo, D., Hochberg, G., Hendrixson, D.R., Sharma, C.M., Rosenthal, P., Beeby, M., 2023a. Molecular model of a bacterial flagellar motor *in situ* reveals a "parts-list" of protein adaptations to increase torque. https://doi.org/10.1101/2023.09.08.556779

Drobnič, T., Cohen, E.J., Alzheimer, M., Froschauer, K., Svensson, S., Singh, N., Garg, S.G., Henderson, L., Umrekar, T., Nans, A., Ribardo, D., Hochberg, G., Hendrixson, D.R., Sharma, C.M., Rosenthal, P., Beeby, M., 2023b. Molecular model of a bacterial flagellar motor in situ reveals a "parts-list" of protein adaptations to increase torque. https://doi.org/10.1101/2023.09.08.556779

Dubochet, J., Mcdowall, A., 1981. Vitrification of Pure Water for Electron-Microscopy. J. Microsc.-Oxf. 124, RP3–RP4.

Dunne, W.M., 2002. Bacterial adhesion: seen any good biofilms lately? Clin Microbiol Rev 15, 155–166. https://doi.org/10.1128/CMR.15.2.155-166.2002

Egan, F., Barret, M., O'Gara, F., 2014. The SPI-1-like Type III secretion system: more roles than you think. Front Plant Sci 5, 34. https://doi.org/10.3389/fpls.2014.00034

Egerton, R.F., 2014. Choice of operating voltage for a transmission electron microscope. Ultramicroscopy 145, 85–93. https://doi.org/10.1016/j.ultramic.2013.10.019

Elgamoudi, B.A., Starr, K.S., Korolik, V., 2022. Extracellular c-di-GMP Plays a Role in Biofilm Formation and Dispersion of Campylobacter jejuni. Microorganisms 10, 2030. https://doi.org/10.3390/microorganisms10102030

Ewing, C.P., Andreishcheva, E., Guerry, P., 2009. Functional Characterization of Flagellin Glycosylation in Campylobacter jejuni 81-176. J Bacteriol 191, 7086–7093. https://doi.org/10.1128/JB.00378-09

Farley, M.M., Hu, B., Margolin, W., Liu, J., 2016. Minicells, Back in Fashion. J Bacteriol 198, 1186–1195. https://doi.org/10.1128/JB.00901-15

Fernández, J.J., Li, S., Crowther, R.A., 2006. CTF determination and correction in electron cryotomography. Ultramicroscopy 106, 587–596. https://doi.org/10.1016/j.ultramic.2006.02.004

Ferreira, J.L., Matthews-Palmer, T.R.S., Beeby, M., 2018. Electron Cryo-Tomography, in: Hanssen, E. (Ed.), Cellular Imaging: Electron Tomography and Related Techniques. Springer International Publishing, Cham, pp. 61–94. https://doi.org/10.1007/978-3-319-68997-5_3

Ferrero, R.L., Lee, A., 1988a. Motility of Campylobacter jejuni in a viscous environment: comparison with conventional rod-shaped bacteria. J Gen Microbiol 134, 53–59. https://doi.org/10.1099/00221287-134-1-53

Ferrero, R.L., Lee, A., 1988b. Motility of Campylobacter jejuni in a viscous environment: comparison with conventional rod-shaped bacteria. J Gen Microbiol 134, 53–59. https://doi.org/10.1099/00221287-134-1-53

Finnigan, G.C., Hanson-Smith, V., Stevens, T.H., Thornton, J.W., 2012. Evolution of increased complexity in a molecular machine. Nature 481, 360–364. https://doi.org/10.1038/nature10724

Francis, N.R., Sosinsky, G.E., Thomas, D., DeRosier, D.J., 1994. Isolation, characterization and structure of bacterial flagellar motors containing the switch complex. J Mol Biol 235, 1261–1270. https://doi.org/10.1006/jmbi.1994.1079

Gao, B., Lara-Tejero, M., Lefebre, M., Goodman, A.L., Galán, J.E., 2014. Novel Components of the Flagellar System in Epsilonproteobacteria. mBio 5, e01349-14. https://doi.org/10.1128/mBio.01349-14

Gao, Y., Neubauer, M., Yang, A., Johnson, N., Morse, M., Li, G., Tang, J.X., 2014. Altered motility of Caulobacter Crescentus in viscous and viscoelastic media. BMC Microbiol 14, 322. https://doi.org/10.1186/s12866-014-0322-3

GGDEF domain-containing protein - Campylobacter jejuni subsp. jejuni serotype O:23/36 (strain 81-176) | UniProtKB | UniProt [WWW Document], n.d. URL https://www.uniprot.org/uniprotkb/A0A0H3PAJ5/entry (accessed 4.2.24).

Goon, S., Ewing, C.P., Lorenzo, M., Pattarini, D., Majam, G., Guerry, P., 2006. A sigma28-regulated nonflagella gene contributes to virulence of Campylobacter jejuni 81-176. Infect Immun 74, 769–772. https://doi.org/10.1128/IAI.74.1.769-772.2006

Guo, S., Liu, J., 2022. The Bacterial Flagellar Motor: Insights Into Torque Generation, Rotational Switching, and Mechanosensing. Front Microbiol 13, 911114. https://doi.org/10.3389/fmicb.2022.911114

Hagen, W.J.H., Wan, W., Briggs, J.A.G., 2017. Implementation of a cryo-electron tomography tilt-scheme optimized for high resolution subtomogram averaging. J Struct Biol 197, 191–198. https://doi.org/10.1016/j.jsb.2016.06.007

Hamaguchi, T., Maki-Yonekura, S., Naitow, H., Matsuura, Y., Ishikawa, T., Yonekura, K., 2019. A new cryo-EM system for single particle analysis. J Struct Biol 207, 40–48. https://doi.org/10.1016/j.jsb.2019.04.011

Hazell, S.L., Lee, A., Brady, L., Hennessy, W., 1986. Campylobacter pyloridis and gastritis: association with intercellular spaces and adaptation to an environment of mucus as important factors in colonization of the gastric epithelium. J Infect Dis 153, 658–663. https://doi.org/10.1093/infdis/153.4.658

Heel, M. van, Gowen, B., Matadeen, R., Orlova, E.V., Finn, R., Pape, T., Cohen, D., Stark, H., Schmidt, R., Schatz, M., Patwardhan, A., 2000. Single-particle electron cryo-microscopy: towards atomic resolution. Quarterly Reviews of Biophysics 33, 307–369. https://doi.org/10.1017/S0033583500003644

Henderson, R., 1995. The potential and limitations of neutrons, electrons and X-rays for atomic resolution microscopy of unstained biological molecules. Q Rev Biophys 28, 171–193. https://doi.org/10.1017/s003358350000305x

Hendrixson, D.R., Akerley, B.J., DiRita, V.J., 2001. Transposon mutagenesis of Campylobacter jejuni identifies a bipartite energy taxis system required for motility. Mol Microbiol 40, 214–224. https://doi.org/10.1046/j.1365-2958.2001.02376.x

Hershey, D.M., Fiebig, A., Crosson, S., 2021. Flagellar Perturbations Activate Adhesion through Two Distinct Pathways in Caulobacter crescentus. mBio 12, e03266-20. https://doi.org/10.1128/mBio.03266-20

Herzik, M.A., Wu, M., Lander, G.C., 2017. Achieving better-than-3-Å resolution by single-particle cryo-EM at 200 keV. Nat Methods 14, 1075–1078. https://doi.org/10.1038/nmeth.4461

Hochberg, G.K.A., Liu, Y., Marklund, E.G., Metzger, B.P.H., Laganowsky, A., Thornton, J.W., 2020. A hydrophobic ratchet entrenches molecular complexes. Nature 588, 503–508. https://doi.org/10.1038/s41586-020-3021-2

Hu, B., Morado, D.R., Margolin, W., Rohde, J.R., Arizmendi, O., Picking, W.L., Picking, W.D., Liu, J., 2015. Visualization of the type III secretion sorting platform of Shigella flexneri. Proc Natl Acad Sci U S A 112, 1047–1052. https://doi.org/10.1073/pnas.1411610112

Hug, I., Deshpande, S., Sprecher, K.S., Pfohl, T., Jenal, U., 2017. Second messenger-mediated tactile response by a bacterial rotary motor. Science 358, 531–534. https://doi.org/10.1126/science.aan5353

Ilca, S.L., Kotecha, A., Sun, X., Poranen, M.M., Stuart, D.I., Huiskonen, J.T., 2015. Localized reconstruction of subunits from electron cryomicroscopy images of macromolecular complexes. Nat Commun 6, 8843. https://doi.org/10.1038/ncomms9843

Inoue, T., Barker, C.S., Matsunami, H., Aizawa, S.-I., Samatey, F.A., 2018. The FlaG regulator is involved in length control of the polar flagella of Campylobacter jejuni. Microbiology (Reading) 164, 740–750. https://doi.org/10.1099/mic.0.000648

Johnson, S., Deme, J.C., Furlong, E.J., Caesar, J.J.E., Chevance, F.F.V., Hughes, K.T., Lea, S.M., 2024. Structural basis of directional switching by the bacterial flagellum. Nat Microbiol 9, 1282–1292. https://doi.org/10.1038/s41564-024-01630-z

Johnson, S., Fong, Y.H., Deme, J.C., Furlong, E.J., Kuhlen, L., Lea, S.M., 2020. Symmetry mismatch in the MS-ring of the bacterial flagellar rotor explains the structural coordination of secretion and rotation. Nat Microbiol 5, 966–975. https://doi.org/10.1038/s41564-020-0703-3

Joslin, S.N., Hendrixson, D.R., 2009. Activation of the Campylobacter jejuni FlgSR two-component system is linked to the flagellar export apparatus. J Bacteriol 191, 2656–2667. https://doi.org/10.1128/JB.01689-08

Jumper, J., Evans, R., Pritzel, A., Green, T., Figurnov, M., Ronneberger, O., Tunyasuvunakool, K., Bates, R., Žídek, A., Potapenko, A., Bridgland, A., Meyer, C., Kohl, S.A.A., Ballard, A.J., Cowie, A., Romera-Paredes, B., Nikolov, S., Jain, R., Adler, J., Back, T., Petersen, S., Reiman, D., Clancy, E., Zielinski, M., Steinegger, M., Pacholska, M., Berghammer, T., Bodenstein, S., Silver, D., Vinyals, O., Senior, A.W., Kavukcuoglu, K., Kohli, P., Hassabis, D., 2021. Highly accurate protein structure prediction with AlphaFold. Nature 596, 583–589. https://doi.org/10.1038/s41586-021-03819-2

Karim, Q.N., Logan, R.P., Puels, J., Karnholz, A., Worku, M.L., 1998. Measurement of motility of Helicobacter pylori, Campylobacter jejuni, and Escherichia coli by real time computer tracking using the Hobson BacTracker. J Clin Pathol 51, 623–628. https://doi.org/10.1136/jcp.51.8.623

Khan, S., Dapice, M., Reese, T.S., 1988. Effects of mot gene expression on the structure of the flagellar motor. Journal of Molecular Biology 202, 575–584. https://doi.org/10.1016/0022-2836(88)90287-2

Kojima, S., Blair, D.F., 2004. Solubilization and Purification of the MotA/MotB Complex of Escherichia coli. Biochemistry 43, 26–34. https://doi.org/10.1021/bi035405l

Kojima, S., Blair, D.F., 2001. Conformational Change in the Stator of the Bacterial Flagellar Motor. Biochemistry 40, 13041–13050. https://doi.org/10.1021/bi011263o

Kojima, S., Furukawa, Y., Matsunami, H., Minamino, T., Namba, K., 2008. Characterization of the Periplasmic Domain of MotB and Implications for Its Role in the Stator Assembly of the Bacterial Flagellar Motor. J Bacteriol 190, 3314–3322. https://doi.org/10.1128/JB.01710-07

Kojima, S., Imada, K., Sakuma, M., Sudo, Y., Kojima, C., Minamino, T., Homma, M., Namba, K., 2009. Stator assembly and activation mechanism of the flagellar motor by the periplasmic region of MotB. Mol Microbiol 73, 710–718. https://doi.org/10.1111/j.1365-2958.2009.06802.x

Kojima, S., Takao, M., Almira, G., Kawahara, I., Sakuma, M., Homma, M., Kojima, C., Imada, K., 2018. The Helix Rearrangement in the Periplasmic Domain of the Flagellar Stator B Subunit Activates Peptidoglycan Binding and Ion Influx. Structure 26, 590-598.e5. https://doi.org/10.1016/j.str.2018.02.016

Kremer, J.R., Mastronarde, D.N., McIntosh, J.R., 1996. Computer visualization of three-dimensional image data using IMOD. J Struct Biol 116, 71–76. https://doi.org/10.1006/jsbi.1996.0013

Kudryashev, M., Münter, S., Lemgruber, L., Montagna, G., Stahlberg, H., Matuschewski, K., Meissner, M., Cyrklaff, M., Frischknecht, F., 2012. Structural basis for chirality and directional motility of Plasmodium sporozoites. Cell Microbiol 14, 1757–1768. https://doi.org/10.1111/j.1462-5822.2012.01836.x

Laub, M.T., Chen, S.L., Shapiro, L., McAdams, H.H., 2002. Genes directly controlled by CtrA, a master regulator of the Caulobacter cell cycle. Proc Natl Acad Sci U S A 99, 4632–4637. https://doi.org/10.1073/pnas.062065699

Laub, M.T., McAdams, H.H., Feldblyum, T., Fraser, C.M., Shapiro, L., 2000. Global analysis of the genetic network controlling a bacterial cell cycle. Science 290, 2144–2148. https://doi.org/10.1126/science.290.5499.2144

Leake, M.C., Chandler, J.H., Wadhams, G.H., Bai, F., Berry, R.M., Armitage, J.P., 2006. Stoichiometry and turnover in single, functioning membrane protein complexes. Nature 443, 355–358. https://doi.org/10.1038/nature05135

Lee, L.K., Ginsburg, M.A., Crovace, C., Donohoe, M., Stock, D., 2010. Structure of the torque ring of the flagellar motor and the molecular basis for rotational switching. Nature 466, 996–1000. https://doi.org/10.1038/nature09300

Lele, P.P., Hosu, B.G., Berg, H.C., 2013. Dynamics of mechanosensing in the bacterial flagellar motor. Proc Natl Acad Sci U S A 110, 11839–11844. https://doi.org/10.1073/pnas.1305885110

Levi, A., Jenal, U., 2006. Holdfast formation in motile swarmer cells optimizes surface attachment during Caulobacter crescentus development. J Bacteriol 188, 5315–5318. https://doi.org/10.1128/JB.01725-05

Li, H., Sourjik, V., 2011. Assembly and stability of flagellar motor in Escherichia coli. Mol Microbiol 80, 886–899. https://doi.org/10.1111/j.1365-2958.2011.07557.x

Li, X., Mooney, P., Zheng, S., Booth, C.R., Braunfeld, M.B., Gubbens, S., Agard, D.A., Cheng, Y., 2013. Electron counting and beam-induced motion correction enable near-atomic-resolution single-particle cryo-EM. Nat Methods 10, 584–590. https://doi.org/10.1038/nmeth.2472

Liu, J., Lin, T., Botkin, D.J., McCrum, E., Winkler, H., Norris, S.J., 2009. Intact flagellar motor of Borrelia burgdorferi revealed by cryo-electron tomography: evidence for stator ring curvature and rotor/C-ring assembly flexion. J Bacteriol 191, 5026–5036. https://doi.org/10.1128/JB.00340-09

Lloyd, S.A., Whitby, F.G., Blair, D.F., Hill, C.P., 1999. Structure of the C-terminal domain of FliG, a component of the rotor in the bacterial flagellar motor. Nature 400, 472–475. https://doi.org/10.1038/22794

Lowenthal, A.C., Hill, M., Sycuro, L.K., Mehmood, K., Salama, N.R., Ottemann, K.M., 2009. Functional analysis of the Helicobacter pylori flagellar switch proteins. J Bacteriol 191, 7147–7156. https://doi.org/10.1128/JB.00749-09

Macnab, R.M., 2003. How bacteria assemble flagella. Annu Rev Microbiol 57, 77–100. https://doi.org/10.1146/annurev.micro.57.030502.090832

Martinez, V.A., Schwarz-Linek, J., Reufer, M., Wilson, L.G., Morozov, A.N., Poon, W.C.K., 2014. Flagellated bacterial motility in polymer solutions. Proc Natl Acad Sci U S A 111, 17771–17776. https://doi.org/10.1073/pnas.1415460111

Minamino, T., 2014. Protein export through the bacterial flagellar type III export pathway. Biochimica et Biophysica Acta (BBA) - Molecular Cell Research, Protein trafficking and secretion in bacteria 1843, 1642–1648. https://doi.org/10.1016/j.bbamcr.2013.09.005

Minamino, T., Imada, K., 2015. The bacterial flagellar motor and its structural diversity. Trends in Microbiology 23, 267–274. https://doi.org/10.1016/j.tim.2014.12.011

Minamino, T., Kinoshita, M., Namba, K., 2019. Directional Switching Mechanism of the Bacterial Flagellar Motor. Computational and Structural Biotechnology Journal 17, 1075–1081. https://doi.org/10.1016/j.csbj.2019.07.020

Miyazono, Y., Hirashima, S., Ishihara, N., Kusukawa, J., Nakamura, K., Ohta, K., 2018. Uncoupled mitochondria quickly shorten along their long axis to form indented spheroids, instead of rings, in a fission-independent manner. Sci Rep 8, 350. https://doi.org/10.1038/s41598-017-18582-6

Mo, R., Liu, Y., Chen, Y., Mao, Y., Beile Gao, n.d. Evolutionary Principles of Bacterial Signaling Capacity and Complexity. mBio 13, e00764-22. https://doi.org/10.1128/mbio.00764-22

Moon, K.H., Zhao, X., Manne, A., Wang, J., Yu, Z., Liu, J., Motaleb, M.A., 2016. Spirochetes flagellar collar protein FlbB has astounding effects in orientation of periplasmic flagella, bacterial shape, motility, and assembly of motors in Borrelia burgdorferi. Mol Microbiol 102, 336–348. https://doi.org/10.1111/mmi.13463

Moon, K.H., Zhao, X., Xu, H., Liu, J., Motaleb, M.A., 2018. A Tetratricopeptide Repeat Domain Protein has Profound Effects on Assembly of Periplasmic Flagella, Morphology, and Motility of the Lyme disease spirochete Borrelia burgdorferi. Mol Microbiol 110, 634–647. https://doi.org/10.1111/mmi.14121

Morimoto, Y.V., Ito, M., Hiraoka, K.D., Che, Y.-S., Bai, F., Kami-Ike, N., Namba, K., Minamino, T., 2014. Assembly and stoichiometry of FliF and FlhA in Salmonella flagellar basal body. Mol Microbiol 91, 1214–1226. https://doi.org/10.1111/mmi.12529

Motaleb, M.A., Corum, L., Bono, J.L., Elias, A.F., Rosa, P., Samuels, D.S., Charon, N.W., 2000. Borrelia burgdorferi periplasmic flagella have both skeletal and motility functions. Proceedings

of the National Academy of Sciences 97, 10899–10904. https://doi.org/10.1073/pnas.200221797
Murphy, G.E., Leadbetter, J.R., Jensen, G.J., 2006. In situ structure of the complete Treponema primitia flagellar motor. Nature 442, 1062–1064. https://doi.org/10.1038/nature05015
Nakane, T., Kotecha, A., Sente, A., McMullan, G., Masiulis, S., Brown, P.M.G.E., Grigoras, I.T., Malinauskaite, L., Malinauskas, T., Miehling, J., Uchański, T., Yu, L., Karia, D., Pechnikova, E.V., de Jong, E., Keizer, J., Bischoff, M., McCormack, J., Tiemeijer, P., Hardwick, S.W., Chirgadze, D.Y., Murshudov, G., Aricescu, A.R., Scheres, S.H.W., 2020. Single-particle cryo-EM at atomic resolution. Nature 587, 152–156. https://doi.org/10.1038/s41586-020-2829-0
Newell, D.G., 2002. The ecology of Campylobacter jejuni in avian and human hosts and in the environment. Int J Infect Dis 6 Suppl 3, 3S16-20; discussion 3S20-21, 3S53-58. https://doi.org/10.1016/s1201-9712(02)90179-7
Nirody, J.A., Berry, R.M., Oster, G., 2016. The Limiting Speed of the Bacterial Flagellar Motor. Biophysical Journal 111, 557–564. https://doi.org/10.1016/j.bpj.2016.07.003
Nirody, J.A., Sun, Y.-R., Lo, C.-J., 2017. The biophysicist's guide to the bacterial flagellar motor. Advances in Physics: X 2, 324–343. https://doi.org/10.1080/23746149.2017.1289120
Nishino, Y., Onoue, Y., Kojima, S., Homma, M., 2015. Functional chimeras of flagellar stator proteins between E. coli MotB and Vibrio PomB at the periplasmic region in Vibrio or E. coli. Microbiologyopen 4, 323–331. https://doi.org/10.1002/mbo3.240
Nord, A.L., Biquet-Bisquert, A., Abkarian, M., Pigaglio, T., Seduk, F., Magalon, A., Pedaci, F., 2022. Dynamic stiffening of the flagellar hook. Nat Commun 13, 2925. https://doi.org/10.1038/s41467-022-30295-7
Nord, A.L., Pedaci, F., 2020. Mechanisms and Dynamics of the Bacterial Flagellar Motor. Adv Exp Med Biol 1267, 81–100. https://doi.org/10.1007/978-3-030-46886-6_5
Ogawa, R., Abe-Yoshizumi, R., Kishi, T., Homma, M., Kojima, S., 2015. Interaction of the C-terminal tail of FliF with FliG from the Na+-driven flagellar motor of Vibrio alginolyticus. J Bacteriol 197, 63–72. https://doi.org/10.1128/JB.02271-14
Orlova, E.V., Saibil, H.R., 2011. Structural Analysis of Macromolecular Assemblies by Electron Microscopy. Chem Rev 111, 7710–7748. https://doi.org/10.1021/cr100353t
Palma, V., Gutiérrez, M.S., Vargas, O., Parthasarathy, R., Navarrete, P., 2022. Methods to Evaluate Bacterial Motility and Its Role in Bacterial–Host Interactions. Microorganisms 10, 563. https://doi.org/10.3390/microorganisms10030563
Park, S.-Y., Lowder, B., Bilwes, A.M., Blair, D.F., Crane, B.R., 2006. Structure of FliM provides insight into assembly of the switch complex in the bacterial flagella motor. Proceedings of the National Academy of Sciences 103, 11886–11891. https://doi.org/10.1073/pnas.0602811103
Partridge, J.D., Nieto, V., Harshey, R.M., 2015. A new player at the flagellar motor: FliL controls both motor output and bias. mBio 6, e02367. https://doi.org/10.1128/mBio.02367-14
Paul, R., Weiser, S., Amiot, N.C., Chan, C., Schirmer, T., Giese, B., Jenal, U., 2004. Cell cycle-dependent dynamic localization of a bacterial response regulator with a novel di-guanylate cyclase output domain. Genes Dev 18, 715–727. https://doi.org/10.1101/gad.289504
Penczek, P.A., 2010. Fundamentals of three-dimensional reconstruction from projections. Methods Enzymol 482, 1–33. https://doi.org/10.1016/S0076-6879(10)82001-4
Pereira, L., Hoover, T.R., 2005. Stable accumulation of sigma54 in Helicobacter pylori requires the novel protein HP0958. J Bacteriol 187, 4463–4469. https://doi.org/10.1128/JB.187.13.4463-4469.2005
Perez-Carrasco, R., Franco-Oñate, M.-J., Walter, J.-C., Dorignac, J., Geniet, F., Palmeri, J., Parmeggiani, A., Walliser, N.-O., Nord, A.L., 2022. Relaxation time asymmetry in stator dynamics of the bacterial flagellar motor. Science Advances 8, eabl8112. https://doi.org/10.1126/sciadv.abl8112
Punjani, A., Rubinstein, J.L., Fleet, D.J., Brubaker, M.A., 2017. cryoSPARC: algorithms for rapid unsupervised cryo-EM structure determination. Nat Methods 14, 290–296. https://doi.org/10.1038/nmeth.4169
Radhakrishnan, S.K., Thanbichler, M., Viollier, P.H., 2008. The dynamic interplay between a cell fate determinant and a lysozyme homolog drives the asymmetric division cycle of Caulobacter crescentus. Genes Dev 22, 212–225. https://doi.org/10.1101/gad.1601808

Reid, S.W., Leake, M.C., Chandler, J.H., Lo, C.-J., Armitage, J.P., Berry, R.M., 2006. The maximum number of torque-generating units in the flagellar motor of Escherichia coli is at least 11. Proc Natl Acad Sci U S A 103, 8066–8071. https://doi.org/10.1073/pnas.0509932103

Ribardo, D.A., Johnson, J.J., Hendrixson, D.R., 2024. Viscosity-dependent determinants of Campylobacter jejuni impacting the velocity of flagellar motility. mBio 15, e0254423. https://doi.org/10.1128/mbio.02544-23

Ribardo, D.A., Kelley, B.R., Johnson, J.G., Hendrixson, D.R., 2019a. A Chaperone for the Stator Units of a Bacterial Flagellum. mBio 10, e01732-19. https://doi.org/10.1128/mBio.01732-19

Ribardo, D.A., Kelley, B.R., Johnson, J.G., Hendrixson, D.R., 2019b. A Chaperone for the Stator Units of a Bacterial Flagellum. mBio 10. https://doi.org/10.1128/mBio.01732-19

Rohou, A., Grigorieff, N., 2015. CTFFIND4: Fast and accurate defocus estimation from electron micrographs. J Struct Biol 192, 216–221. https://doi.org/10.1016/j.jsb.2015.08.008

Rosenthal, P.B., Henderson, R., 2003. Optimal determination of particle orientation, absolute hand, and contrast loss in single-particle electron cryomicroscopy. J Mol Biol 333, 721–745. https://doi.org/10.1016/j.jmb.2003.07.013

Rossmann, F.M., Beeby, M., 2018. Insights into the evolution of bacterial flagellar motors from high-throughput in situ electron cryotomography and subtomogram averaging. Acta Crystallogr D Struct Biol 74, 585–594. https://doi.org/10.1107/S2059798318007945

Rossmann, F.M., Hug, I., Sangermani, M., Jenal, U., Beeby, M., 2020. In situ structure of the Caulobacter crescentus flagellar motor and visualization of binding of a CheY-homolog. Molecular Microbiology 114, 443–453. https://doi.org/10.1111/mmi.14525

Roujeinikova, A., 2008. Crystal structure of the cell wall anchor domain of MotB, a stator component of the bacterial flagellar motor: Implications for peptidoglycan recognition. Proceedings of the National Academy of Sciences 105, 10348–10353. https://doi.org/10.1073/pnas.0803039105

Ryu, W.S., Berry, R.M., Berg, H.C., 2000. Torque-generating units of the flagellar motor of Escherichia coli have a high duty ratio. Nature 403, 444–447. https://doi.org/10.1038/35000233

Santiveri, M., Roa-Eguiara, A., Kühne, C., Wadhwa, N., Hu, H., Berg, H.C., Erhardt, M., Taylor, N.M.I., 2020. Structure and Function of Stator Units of the Bacterial Flagellar Motor. Cell 183, 244-257.e16. https://doi.org/10.1016/j.cell.2020.08.016

Scheres, S.H.W., 2012. RELION: implementation of a Bayesian approach to cryo-EM structure determination. J Struct Biol 180, 519–530. https://doi.org/10.1016/j.jsb.2012.09.006

Schirmer, T., 2016. C-di-GMP Synthesis: Structural Aspects of Evolution, Catalysis and Regulation. J Mol Biol 428, 3683–3701. https://doi.org/10.1016/j.jmb.2016.07.023

Schneider, W.R., Doetsch, R.N., 1974. Effect of Viscosity on Bacterial Motility. J Bacteriol 117, 696–701.

Shapiro, L., Agabian-Keshishian, N., Bendis, I., 1971. Bacterial differentiation. Science 173, 884–892. https://doi.org/10.1126/science.173.4000.884

Sharpe, P.T., 1988. Methods of Cell Separation. Elsevier.

Shigematsu, M., Umeda, A., Fujimoto, S., Amako, K., 1998. Spirochaete-like swimming mode of Campylobacter jejuni in a viscous environment. J Med Microbiol 47, 521–526. https://doi.org/10.1099/00222615-47-6-521

Singh, P.K., Sharma, P., Afanzar, O., Goldfarb, M.H., Maklashina, E., Eisenbach, M., Cecchini, G., Iverson, T.M., 2024. CryoEM structures reveal how the bacterial flagellum rotates and switches direction. Nat Microbiol 9, 1271–1281. https://doi.org/10.1038/s41564-024-01674-1

Sowa, Y., Berry, R.M., 2008. Bacterial flagellar motor. Q Rev Biophys 41, 103–132. https://doi.org/10.1017/S0033583508004691

Stader, J., Matsumura, P., Vacante, D., Dean, G.E., Macnab, R.M., 1986. Nucleotide sequence of the Escherichia coli motB gene and site-limited incorporation of its product into the cytoplasmic membrane. Journal of Bacteriology 166, 244–252. https://doi.org/10.1128/jb.166.1.244-252.1986

Tachiyama, S., Skaar, R., Chang, Y., Carroll, B.L., Muthuramalingam, M., Whittier, S.K., Barta, M.L., Picking, W.L., Liu, J., Picking, W.D., 2021. Composition and Biophysical Properties of the Sorting Platform Pods in the Shigella Type III Secretion System. Front Cell Infect Microbiol 11, 682635. https://doi.org/10.3389/fcimb.2021.682635

Tan, J., Zhang, L., Zhou, X., Han, S., Zhou, Y., Zhu, Y., 2024. Structural basis of the bacterial flagellar motor rotational switching. Cell Res 34, 788–801. https://doi.org/10.1038/s41422-024-01017-z

Thanbichler, M., Shapiro, L., 2006. MipZ, a spatial regulator coordinating chromosome segregation with cell division in Caulobacter. Cell 126, 147–162. https://doi.org/10.1016/j.cell.2006.05.038

Thompson, R.F., Walker, M., Siebert, C.A., Muench, S.P., Ranson, N.A., 2016. An introduction to sample preparation and imaging by cryo-electron microscopy for structural biology. Methods 100, 3–15. https://doi.org/10.1016/j.ymeth.2016.02.017

Tipping, M.J., Delalez, N.J., Lim, R., Berry, R.M., Armitage, J.P., 2013. Load-Dependent Assembly of the Bacterial Flagellar Motor. mBio 4, e00551-13. https://doi.org/10.1128/mBio.00551-13

Umrekar, T.R., Cohen, E., Drobnič, T., Gonzalez-Rodriguez, N., Beeby, M., 2021. CryoEM of bacterial secretion systems: A primer for microbiologists. Molecular Microbiology 115, 366–382. https://doi.org/10.1111/mmi.14637

Van Vliet, A.H.M., Wood, A.C., Wooldridge, K., Ketley, J.M., Henderson, J., 1998. 7.7 Genetic Manipulation of Enteric Campylobacter Species, in: Williams, P., Ketley, J., Salmond, G. (Eds.), Methods in Microbiology, Bacterial Pathogenesis. Academic Press, pp. 407–419. https://doi.org/10.1016/S0580-9517(08)70301-5

Wade, R.H., 1992. A brief look at imaging and contrast transfer. Ultramicroscopy 46, 145–156. https://doi.org/10.1016/0304-3991(92)90011-8

Wallis, M.R., 1994. The pathogenesis of Campylobacter jejuni. Br J Biomed Sci 51, 57–64.

Wilson, M.L., Macnab, R.M., 1990. Co-overproduction and localization of the Escherichia coli motility proteins motA and motB. J Bacteriol 172, 3932–3939.

Yokoyama, T., Paek, S., Ewing, C.P., Guerry, P., Yeo, H.-J., 2008. Structure of a σ28-regulated Non-flagella Virulence Protein from Campylobacter jejuni. J Mol Biol 384, 364–376. https://doi.org/10.1016/j.jmb.2008.09.036

Zhao, X., Norris, S.J., Liu, J., 2014. Molecular architecture of the bacterial flagellar motor in cells. Biochemistry 53, 4323–4333. https://doi.org/10.1021/bi500059y

Zhao, X., Zhang, K., Boquoi, T., Hu, B., Motaleb, M.A., Miller, K.A., James, M.E., Charon, N.W., Manson, M.D., Norris, S.J., Li, C., Liu, J., 2013. Cryoelectron tomography reveals the sequential assembly of bacterial flagella in Borrelia burgdorferi. Proc Natl Acad Sci U S A 110, 14390–14395. https://doi.org/10.1073/pnas.1308306110

Zheng, S.Q., Palovcak, E., Armache, J.-P., Verba, K.A., Cheng, Y., Agard, D.A., 2017. MotionCor2: anisotropic correction of beam-induced motion for improved cryo-electron microscopy. Nat Methods 14, 331–332. https://doi.org/10.1038/nmeth.4193

Zhou, J., Blair, D.F., 1997. Residues of the cytoplasmic domain of MotA essential for torque generation in the bacterial flagellar motor. J Mol Biol 273, 428–439. https://doi.org/10.1006/jmbi.1997.1316

Zhou, J., Lloyd, S.A., Blair, D.F., 1998a. Electrostatic interactions between rotor and stator in the bacterial flagellar motor. Proceedings of the National Academy of Sciences 95, 6436–6441. https://doi.org/10.1073/pnas.95.11.6436

Zhou, J., Sharp, L.L., Tang, H.L., Lloyd, S.A., Billings, S., Braun, T.F., Blair, D.F., 1998b. Function of Protonatable Residues in the Flagellar Motor of Escherichia coli: a Critical Role for Asp 32 of MotB. Journal of Bacteriology 180, 2729–2735. https://doi.org/10.1128/jb.180.10.2729-2735.1998

Zivanov, J., Nakane, T., Forsberg, B.O., Kimanius, D., Hagen, W.J., Lindahl, E., Scheres, S.H., 2018. New tools for automated high-resolution cryo-EM structure determination in RELION-3. Elife 7, e42166. https://doi.org/10.7554/eLife.42166